Perforated Current Collectors and the Concept of Relithiation in Lithium-Ion Batteries

Dissertation

zur Erlangung des Doktorgrades Dr. rer. nat.

der Fakultät für Naturwissenschaften der Universität Ulm

Vorgelegt von

Jan Hettig

aus Frankfurt am Main

2026

Dekan der Fakultät	**:** Prof. Dr. Jan Tuckermann
Erstgutachter	**:** Prof. Dr. Markus Hölzle
Zweitgutachter	**:** Prof. Dr. Mika Lindén
Tag der Promotion	**:** 5. Oktober 2026

“Everything that happens once can never happen again. But everything that happens twice will surely happen a third time.”

- Paulo Coelho, "The Alchemist"

Abstract

The lithium-ion battery (LIB) industry and research landscape is expanding rapidly on a global scale. To meet future demand, continuous improvement of key performance indicators such as energy and power density, cycle life, safety, resource efficiency, sustainability and cost-effectiveness is crucial. Substantial and continuous efforts are dedicated to optimizing these indicators, which necessitates addressing all components at different levels, from materials to electrodes, cells, and battery packs. However, in this context, relatively few advancements have focused on current collectors over the last three decades, with a major trend being to reduce their thickness.

This work discusses and demonstrates the application and potential of an innovative, perforated current collector design for LIB electrodes from both theoretical and practical perspectives. The straightforward integration of the perforated current collector design introduced here (with a hole diameter of ~1 mm and a perforation degree of ~27.5%) into standard laboratory and pilot line electrode manufacturing processes is demonstrated, highlighting its viability as a drop-in technology. Single-layer (~60 mAh), bi-layer (~120 mAh) and stacked (~180 mAh) Graphite‖LFP or SiC‖LFP demonstrator pouch cells are assembled and examined.

In brief, perforated current collectors can enhance the specific energy and energy density of LIBs in two ways: by reducing inactive components at the electrode level and through anodic prelithiation treatment at the cell level. Furthermore, Graphite‖LFP cells with perforated current collectors exhibited improved long-term cycling stability and maintained similar rate performance compared to reference cells with standard current collector foils.

Moreover, this work provides a fundamental understanding of an innovative, less-explored prelithiation approach at the cell level. This approach mandatorily requires lithium-ion permeable electrodes and a sacrificial Li-donor electrode within the assembled cell. Initial capacity losses (ICLs), which are caused by anodic solid electrolyte interphase (SEI) formation, can be offset by replenishing the cell's active lithium deficit with the additional Li-donor electrode. Furthermore, this study expands upon the prelithiation concept by introducing a well-controlled anodic lithium reservoir equivalent to 10% of the cell's total capacity. This anodic lithium reservoir compensates for a defined portion of active lithium losses (ALL) during cycling, preserving cell capacity and boosting the cell's cycle life.

A qualitative and quantitative analysis is provided to evaluate the initial state of the cells' active lithium inventory (i.e., deficit, prelithiated, or reservoir) by considering the cathode's reversible specific capacity, the degree of anodic lithiation in the discharged and charged states, as well as the

cell's voltage profiles. Accurately determining the cells' active lithium inventory is critical to ensure safe operation, as an overabundance of active lithium in the cell after prelithiation can cause lithium plating on the anode's surface. Demonstrator cells reveal the impact of active lithium inventory size on the rate and cycling performance of Graphite‖LFP and SiC‖LFP single-layer pouch cells with a capacity of ~60 mAh.

Furthermore, the prelithiation approach at the cell level was complemented by a novel relithiation strategy. This strategy replenished the active lithium inventory of aged Graphite‖LFP single-layer pouch cells (~60 mAh) via the incorporated Li-donor electrode. A comparison of the cell's first 600 cycles after assembly and its first 600 cycles after relithiation demonstrated that the relithiated cell utilizes full reversible cathode capacity with a slower aging rate during its second life. These initial results highlight the potential of relithiation at the cell level as a novel approach for ALL aged Graphite‖LFP cells that could eliminate the need for costly recycling, while significantly extending the usable lifespan and energy of LIBs for second-life applications.

Finally, the relithiation approach is applied and demonstrated as an alternative to the prelithiation approach in stacked Graphite‖LFP pouch cells (~180 mAh) to compensate for their ICLs after cell formation. Relithiation at the cell level is emerging as a promising alternative to prelithiation strategies, as it allows for accurate management of the cell's active lithium inventory at every stage of its operational life.

Table of Contents

Abstract vii

Table of Contents xi

Theoretical Background 1

1. Introduction **2**

1.1 The Shift from Fossil Fuels to Renewable Energy Sources 2

1.2 Energy Storage Systems 4

2. Lithium-Ion Batteries **6**

2.1 General Working Principle 6

2.2 Electrochemical Fundamentals 8

2.3 From Materials to Cells 14

2.4 Prelithiation Concept and Strategies 26

Motivation and Objectives 31

3. The Role of Perforated Current Collectors in LIBs **32**

4. Scope of this Thesis **38**

5. Summary **39**

Results and Discussion 41

6. Proof of Concept **42**

6.1 Perforation Design in This Study 42

6.2 Predicted Effects at the Electrode and at the Cell Level 46

6.3 Initial Lab Scale Electrode Development 53

6.4 Single-Layer Demonstrator Pouch Cells 62

6.5 From Prediction to Demonstration 70

7. Prelithiation and Beyond **71**

7.1 Predicted Impact on LIB Performance 72

7.2 Lab Scale Electrode Development 78

7.3 Single-Layer Demonstrator Pouch Cells 87

7.4 Relithiation of Aged Cells 103

8. Scale Up **106**

8.1 Upscaled Roll-to-Roll Electrode Development 106

8.2 Bi-Layer and Stacked Demonstrator Pouch Cells 126

9. Transfer to High Capacity SiC Anode Active Material 145
9.1 Single-Layer Pouch Cells 147

Conclusion and Outlook 159

10. Conclusion 160
11. Outlook 167

Materials and Methods 169

12. Materials 170
12.1 Electrode Materials 170
12.2 Cell Materials 171
13. Instrumentals 172
14. Procedures 175
14.1 Theoretical Calculations 175
14.2 Pre-Mix Preparation 177
14.3 Slurry Preparation 179
14.4 Rheological Measurements 181
14.5 Coating 182
14.6 Cell Assembly 184
14.7 Battery Testing 184

Appendix 185

15. Appendix: Proof of Concept 186
16. Appendix: Prelithiation and Beyond 187
17. Appendix: Scale Up 188
18. Appendix: Transfer to High Capacity SiC Anode Active Material 189

References I

Table of Figures XIX

Table of Tables XXIX

List of Abbreviations XXXI

Curriculum Vitae XXXIII

Conference Contributions XXXV

Declaration of Authorship XXXVII

Theoretical Background

1. Introduction

1.1 The Shift from Fossil Fuels to Renewable Energy Sources

Modern societies depend on accessible and affordable energy.

In 2025, fossil fuels such as coal, oil, and natural gas remained the dominant energy sources worldwide.[1–3] It is well known that burning fossil fuels releases the greenhouse gas (GHG) carbon dioxide (CO_2), which significantly drives global warming. In 2024, global GHG emissions reached a new high of 53.2 Gt CO_2-equivalent.[4] The majority of these emissions consisted of CO_2 (74.5%), primarily resulting from fossil fuel combustion. Methane (CH_4, 17.9%), nitrous oxide (N_2O; 4.8%), and Fluorine (F) containing gases (2.8%) constituted the remaining GHG emissions, predominantly originating from the agricultural sector.[4,5]

Naturally occurring GHGs make life on earth possible by creating a comfortable climate, with an average temperature of 14 °C instead of approximately -20 °C in their absence.[6–8] However, GHGs released to power modern human society further amplify the greenhouse effect, potentially causing irreversible anthropogenic climate change. From 1957 to 2025, atmospheric CO_2 concentrations increased from approximately 315 ppm to 430 ppm, and the average global temperature rose by about 1.2 °C over the same period.[9–16]

An increase of a few degrees in the global temperature should not be underestimated.[17,18] The impacts are already evident today in the form of more frequent extreme weather events, retreating glaciers, increased wildfires, biodiversity loss, and many other related effects. Readers of *The Uninhabitable Earth* by David Wallace-Wells gain a clear understanding of the urgency of addressing potential future climate risks.[19] In 2015, nearly all countries in the world committed under the Paris Climate Agreement to the goal of limiting global warming to well below 2 °C relative to the preindustrial level.[20,21]

To achieve this goal, GHG emissions must be drastically reduced. While, unfortunately, still the opposite trend is currently observable on a global scale (with global GHG emissions continuing to rise even in 2024, largely driven by developing and emerging economies), a significant decline in emissions is already evident in many industrialized countries. For instance, between 2015 and 2024, greenhouse gas emissions decreased by 19% in the EU-27 and by 25% in Germany.[4]

This reduction is largely due to the substitution of fossil energy and mainly electricity with renewable energy sources such as wind, solar, and hydropower. From 2015 to 2024, the share of

renewable energy sources in electricity generation increased globally from 23% to 32%, in the EU-27 from 30% to 45%, and in Germany from 29% to 58%.[3,22] Today, renewable energy sources are already economically competitive with fossil fuels, and further cost reductions are expected.[23]

In 2009, David JC MacKay published the comprehensive book *Sustainable Energy – Without the Hot Air*, in which he evaluated whether a transition from fossil fuels to renewable energy sources was physically feasible for the United Kingdom.[24] MacKay presented his analysis in straightforward language and unraveled the potentials and challenges of renewable energy sources when considering country-specific landscapes, energy demands, and weather conditions. In 2018, Christian Holler and Joachim Gaukler adapted the book concept for Germany in *Erneuerbare Energien ohne heisse Luft*.[25] The resulting scenarios are highly promising: renewable energy sources have the potential to not only meet the energy demands of the example countries, but also those of the entire planet.[26] The remaining challenge is the implementation of decisive measures by all countries.

Indeed, replacing fossil fuels with renewable energy sources is not trivial. One major challenge with renewable energy sources, such as wind and solar, is their fluctuation over time.[27,28] Electricity from solar energy can, by definition, not be generated at night or on cloudy days. Electricity from wind energy cannot be produced on windless days. These fluctuations in energy supply pose a challenge to maintaining a stable electric grid. For this reason, large-scale energy storage systems are required to enable a reliable shift from fossil fuels to renewable energy sources.

1.2 Energy Storage Systems

Energy storage systems are defined by their ability to perform three processes: charging, storage, and discharging. These processes can be carried out within a single device or distributed across multiple devices. For the power sector, energy storage systems can store electrical energy directly (e.g., capacitors) or convert it into mechanical (e.g., pumped storage plants, flywheel storage facilities), chemical (e.g., power-to-gas), thermal, or electrochemical (e.g., batteries) forms. There are two subcategories of energy storage systems: i) primary, which can be charged and discharged only once, and ii) secondary, which can be charged and discharged multiple times.[26]

A pumped-storage hydroelectric plant converts electrical energy into potential energy by pumping water from a lower reservoir to higher one when excess electricity is generated. During periods of power demand, the water flows back through a turbine, converting the potential energy – via kinetic energy – into usable electrical energy. Thus, a pumped-storage plant is a secondary energy storage system, in which charging, storage, and discharging are performed by three distinct devices at a single location. Although these systems can have a large storage capacity and be efficient (75 – 85%), they have low energy density (1 – 2 Wh L^{-1}) and require specific geological conditions.[26,29]

Power-to-gas energy storage systems are a promising alternative that uses high-energy-density carriers, such as hydrogen. Electrical energy is converted into chemical binding energy through electrolysis, in which water (H_2O) is decomposes into hydrogen (H_2) and oxygen (O_2). The hydrogen gas can be stored in large caverns or transported via pipelines to smaller tanks or facilities. When needed, this chemical energy can be converted back into electrical or thermal energy. Electrical energy can be produced in a fuel cell, and thermal energy can be produced as an additional component in gas networks. Thus, hydrogen power-to-gas energy storage systems can function as primary (via direct combustion) or secondary (e.g., via a combination of electrolyzers and fuel cells) energy storage systems, in which charging, storage, and discharging are performed by three distinct devices at different locations. They provide high energy density (500 – 3,000 Wh L^{-1}) and flexibility as they can be used in all areas inclunding electricity, heating, and transport.[26] However, their relatively low efficiency (20 – 66%) and high costs currently limit their widespread application.[26,29–31]

Batteries are another type of energy storage system that offers high operational flexibility. They already have numerous applications, ranging from powering small electronic devices to electric vehicles, and from residential to large-scale energy storage installations. In general, batteries convert chemical energy stored in their active materials into electrical energy through an electrochemical redox reaction. Primary batteries are assembled in a charged state and can only be discharged once, whereas secondary batteries can be recharged multiple times due to a reversible electrochemical process. Charging, storage, and discharging all occur within a single device.[26,32]

Perhaps the best-known battery system is the lead acid battery, which was invented over 150 years ago.[26] Its main applications include starter batteries in vehicles, as well as emergency and backup power supplies. The technology's widespread use and long development history have made it a prime example of effective recycling, with recycling rates of above 90%.[30,33] However, its relatively low energy density (50 – 80 Wh L^{-1}) limit its use in advanced applications.[26,29,30]

Lithium-ion batteries (LIBs), commercialized in the early 1990s, offer a higher energy density (200 – 500 Wh L^{-1}) compared to lead acid batteries, along with high efficiency and a long cycle life.[26,30,31,34,35] Today, LIBs power not only portable electronic devices, but also play a key role in the electrification of the transportation sector. LIBs are also a promising technology for electric grid stabilization. Despite the industry's rapid growth and improvements in efficiency and cost of LIBs over the past decades, they are still not fully mature.[34,35] There are still many challenges and opportunities of the technology that need to be addressed.

2. Lithium-Ion Batteries

2.1 General Working Principle

LIBs are secondary batteries consisting of one or more electrochemical cells. A LIB cell contains two electrodes, one negative (-) and one positive (+), which are separated by an ionically conductive electrolyte and an electrically insulating separator, as illustrated in **Figure 2.1** using a graphite negative electrode and lithium iron phosphate ($LiFePO_4$, LFP) positive electrode.[36]

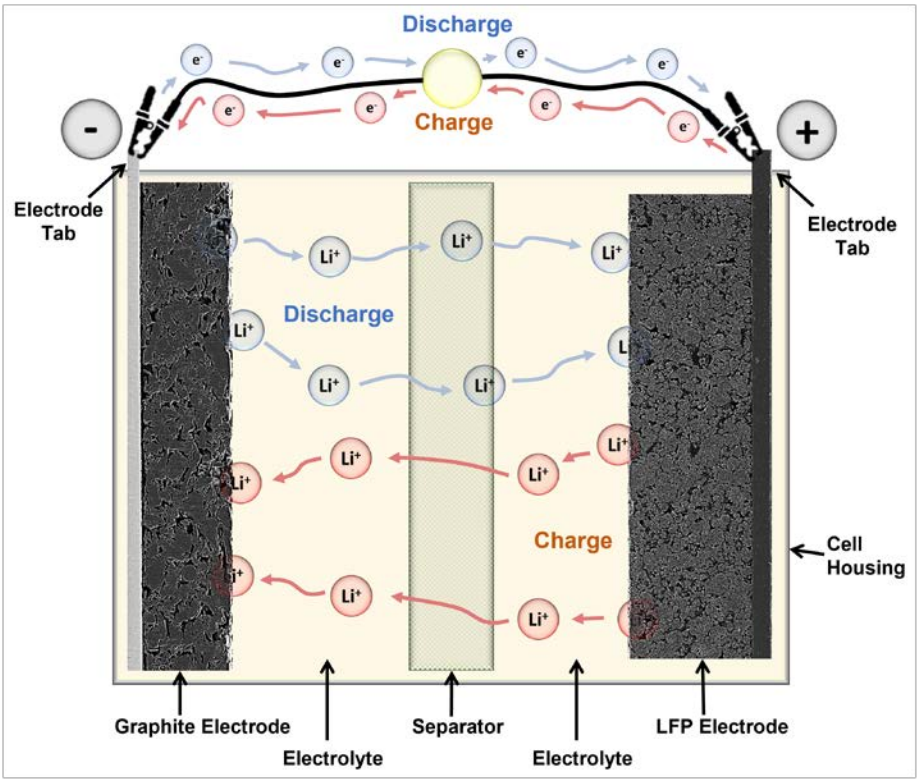

Figure 2.1 Schematic illustration of a Graphite‖LFP LIB cell. The graphite electrode acts as the negative electrode, and the LFP electrode acts as the positive one. The electron and lithium-ion flow during charging is shown in red; during discharging, it's shown in blue.

Charging a LIB cell converts electrical energy into chemical energy. This process can only be forced and is driven by applying an external voltage. The cell functions as an electrolytic cell: oxidation of the positive's electrode active material (AM) releases electrons, that flow through the external circuit to the negative's electrode AM, where reduction occurs. To maintain electroneutrality, the external electronic current must be balanced by an equal internal ionic current, as illustrated in **Figure 2.1**.[37]

Discharging a LIB cell converts chemical energy into electrical energy. This process is occurring spontaneous and is driven by the electrochemical potential difference of both electrodes. The cell functions as a galvanic cell: oxidation of the negative's electrode AM releases electrons, that flow through the external circuit to the positive's electrode AM, where reduction occurs. Electroneutrality must again be maintained, as illustrated in **Figure 2.1**.[37]

Lithium ions "rock" between the two electrodes, being released from one and taken up by the other. For this, it is necessary that the LIB contains an active lithium inventory, which is typically provided by the positive electrode in the cell's initial state.[38,39]

Electrode and cell reactions at a single active site, exemplified by a Graphite‖LFP cell chemistry, are as follows:

Negative Electrode	$C_6 + Li^+ + e^-$	$\underset{Discharge}{\overset{Charge}{\rightleftharpoons}}$	LiC_6	**2.1**
Positive Electrode	$LiFePO_4$	$\underset{Discharge}{\overset{Charge}{\rightleftharpoons}}$	$FePO_4 + Li^+ + e^-$	**2.2**
Cell	$C_6 + LiFePO_4$	$\underset{Discharge}{\overset{Charge}{\rightleftharpoons}}$	$LiC_6 + FePO_4$	**2.3**

According to electrochemical definitions, during charging, the negative electrode acts as the cathode, where reduction occurs, and the positive electrode acts as the anode, where oxidation occurs.[37] However, in the battery community, the negative electrode is always called the anode and the positive electrode is always called the cathode, regardless of the redox reaction occurring at each electrode. This convention will also be used in this thesis.

2.2 Electrochemical Fundamentals

2.2.1 Cell Voltage *U* (V)

In general, the potential of a single electrode ($E_{electrode}$) can be obtained by the **Nernst-Equation 2.4**,

$$E_{electrode} = E^0_{electrode} + \frac{RT}{nF} ln\left(\frac{\alpha_{Ox}}{\alpha_{Red}}\right) \quad \textbf{2.4}$$

where E^0 is the standard electrode potential, R is the universal gas constant (≈ 8.314 J mol^{-1} K^{-1}), T is the temperature, n is the number of transferred electrons, F is the Faraday constant (≈ 96,485 C mol^{-1}), and α_{Ox} and α_{Red} are the activity coefficents of oxidized and reduced species, respectively. The standard electrode potential (E^0) is referred against the standard hydrogen electrode (SHE) under standard conditions.[26,37,40]

The cell potential (E_{cell}) at equilibrium, when no current is flowing, is also called the open-circuit voltage (OCV). It is determined by the potential difference between the cathode and the anode, as described by **Equation 2.5**.[26,37,40]

$$E_{cell} = E_{cathode} - E_{anode} \quad \textbf{2.5}$$

It can also be described in terms of the electrochemical potential of electrons $\tilde{\mu}_{e^-}$, or equivalently the chemical potential of lithium μ_{Li} in the electrodes, according to **Equation 2.6**.[41–43]

$$E_{cell} = -\frac{1}{F}\left(\tilde{\mu}_{e^-}^{cathode} - \tilde{\mu}_{e^-}^{anode}\right) = -\frac{1}{F}\left(\mu_{Li}^{cathode} - \mu_{Li}^{anode}\right) \quad \textbf{2.6}$$

In an operating cell, when current is flowing, the cell voltage (U_{Cell}) varies from its OCV (U_{OCV}) due to polarization effects of each electrode ($\Delta\varphi^{electrode}$), as described by **Equation 2.7** and **2.8**.[42]

$$U_{cell} = U_{OCV} + \Delta\varphi^{cathode} + \Delta\varphi^{anode} \quad \textbf{2.7}$$

$$\Delta\varphi^{electrode} = \Delta\varphi_{AM}^{electrode} + \Delta\varphi_{CT}^{electrode}\ \Delta\varphi_{EL}^{electrode} \quad \textbf{2.8}$$

The total overpotential of each electrode ($\Delta\varphi^{electrode}$) can be considered as the sum of the overpotentials required for solid-state diffusion in the electrode active materials ($\Delta\varphi_{AM}^{electrode}$), charge transfer between the electrode and electrolyte ($\Delta\varphi_{CT}^{electrode}$), and ionic transport in the electrolyte phase within a porous electrode ($\Delta\varphi_{EL}^{electrode}$).[42]

Ohm's law 2.9 provides an additional relationship between voltage U (in this case $\Delta\varphi^{electrode}$), current I, and resistance R.[36]

$$\Delta U = I \cdot R \quad \textbf{2.9}$$

As a result of overpotentials, the operating cell voltage is higher than the OCV during charging ($U_{cell} > U_{OCV}$) and lower than the OCV during discharging ($U_{cell} < U_{OCV}$).[37,44] Only at very low operating currents, where polarization effects are negligible, the cell operates close to its OCV ($U_{cell} \approx U_{OCV}$).[36] At high operating current densities, electrode overpotentials can become critical for cell operation, as they may trigger unwanted side reactions that alter the electrodes and the cell.[44–47] For example, during charging, the anode potential can drop below 0 V vs. Li^+/Li, making lithium plating thermodynamically favorable, leading to active lithium losses (ALL) and safety concerns.[47–51] On the cathode side, high potentials can induce structural changes and degradation of the AM.[45,46,52] Since electrode overpotentials are largely driven by the kinetics of electron and ion transport,[42] they can be mitigated through the optimization of materials (e.g., morphology[53–57], particle size[58,59], and surface modifications[60–62]), electrodes (e.g., coating design[63–66], surface structuring[67,68], current collector design[69,70], and tab design[71–73]), and cells (e.g., cell design[74–76] and electrolyte design[77–79]), as well as through carefully chosen operating conditions (temperature, cut-off voltages, current density, etc.).[42,47,48]

2.2.2 Cell Capacity *Q* (Ah)

The cell capacity, Q_{cell} (Ah), determines the amount of electrical charge a LIB cell can store or deliver.[40] Each electrode has its own capacity ($Q_{electrode}$). In the initial state, the cathode generally contains all active lithium, thereby determining the cells active lithium inventory and overall capacity ($Q_{cathode} = Q_{cell}$).[80] The anode must have sufficient capacity to uptake all the active lithium available in the cell. Excess active lithium can lead to metallic lithium plating at the anode, which is associated with ALL and safety concerns.[48,52] Therefore, proper electrode balancing, expressed as an N/P-ratio greater than 1, is crucial for safe cell operation.[76,80] As an additional safety measure and to minimize edge effects, negative electrodes are often made slightly larger than positive ones, a configuration referred to as an anode edge overhang.[81,82]

The electrode capacity can be normalized to the electrode area, resulting in the areal capacity, $Q_{areal,electrode}$ (mAh cm^{-2}), to the mass, resulting in specific capacity, $Q_{spec,electrode}$ (mAh g^{-1}), or to the volume, resulting in volumetric capacity, $Q_{vol,electrode}$ (mAh cm^{-3}). This reveals important characteristics of the electrodes, allowing a better comparison.

Specific capacity values of the AMs, $Q_{spec,AM}$ (mAh g^{-1}), consider only the mass of the AM in the electrodes and are also commonly used. Theoretical specific capacity values of AMs ($Q_{theor,spec,AM}$) can be calculated using Faraday's law according to **Equation 2.10**,

$$Q_{theor,spec,AM} = \frac{n\,F}{3.6\,M_W} \qquad \textbf{2.10}$$

where M_w is the molar weight of the AM, n is the number of electrons transferred and F is the Faraday constant, and 3.6 the conversion factor (A s to mA h).[40] For example, the theoretical

calculated specific capacities of LFP ($M_w(LiFePO_4)$ = 157.757 g mol^{-1}) and graphite ($M_w(C_6)$ = 72.06 g mol^{-1}) are 170 mAh g^{-1} and 372 mAh g^{-1}, respectively (**Figure 2.2**).

However, it is important to critically assess the theoretically calculated values of AMs because they may differ from the values that can be practically used. While almost the full theoretical capacity of graphite and LFP can be utilized for reversible energy storage, only half of the lithium can be reversibly deintercalated from the lithium cobalt oxide ($LiCoO_2$, LCO), structure.[83,84] This results in a practical specific capacity of approximately 150 mAh g^{-1} for LCO, which is only about 55% of the theoretical value.[34]

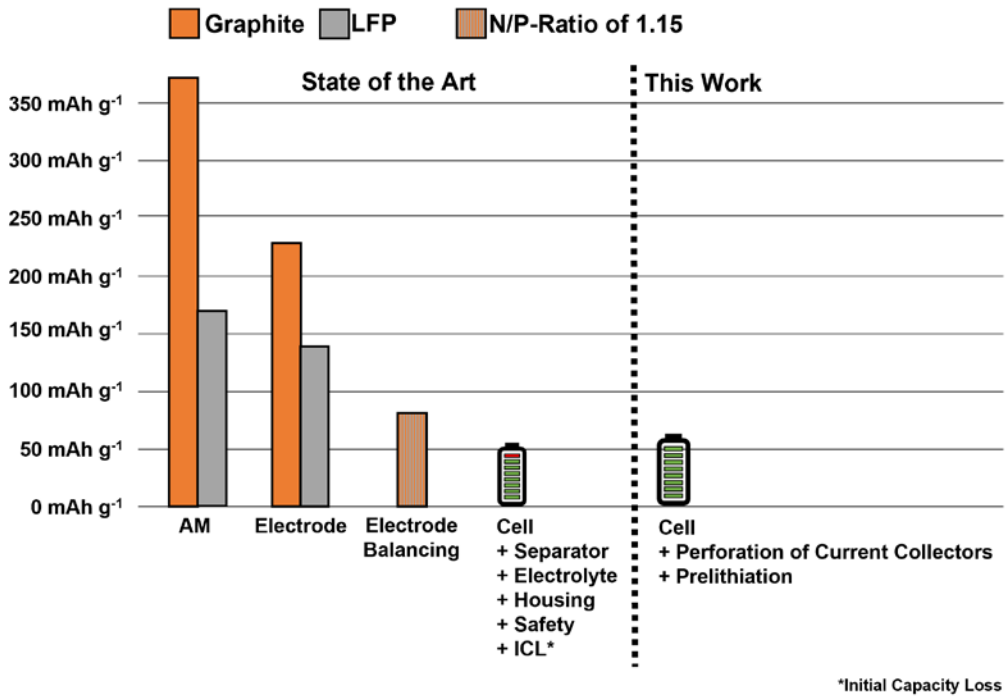

Figure 2.2 Simplified illustration of the theoretical specific capacity evolution from the material level to the electrode level to cell level. The calculations are based on double-sided coated LFP electrodes with an areal capacity of 2.6 mAh cm^{-2} per side, double-sided coated graphite electrodes with an areal capacity of 3.0 mAh cm^{-2} per side, together with the use of standard current collector foils (10 µm copper foil, 15 µm aluminum foil) and coating compositions (92 wt.% LFP, 94 wt.% graphite).

Figure 2.2 clearly shows that the overall specific capacity decreases from the AM level to the electrode level and then again from the electrode level to the cell level. This is because the cell requires the presence of inactive components in both the electrode (e.g., current collector, tabs, binder, and conductive additives) and the cell itself (e.g., separator, electrolyte, housing, and safety components) in order to function properly. Furthermore, during the initial charge/discharge cycles, referred to as cell formation, the instability of the electrolyte at low potentials results in the formation of a protective solid-electrolyte interphase (SEI) on the anode surface (described in detail in **Chapter 2.3.4**, page 23).[85–88] This reaction irreversibly consumes active lithium, causing initial capacity losses (ICLs) and reducing the cell's active lithium inventory.

Moreover, the usable capacity of an operating cell largely depends on conditions such as the cut-off voltages (U_{charge} and $U_{discharge}$), current density and temperature. To facilitate comparisons between cells, the applied current is often expressed as a so-called C-rate, which normalizes the current to the cell's capacity (**Equation 2.11**).

$$C - rate = \frac{I}{Q_{cell}} \qquad \textbf{2.11}$$

For example, a C-rate of C/10, 1C, and 2C correspond to currents at which Q_{cell} is utilized in 10 h, 1 h, and 0.5 h, respectively.

As described above, electron and ion transport become increasingly limited as current density increases or temperature decreases, leading to electrode overpotentials.[42] Consequently, the cells' defined cut-off voltages, can be reached before the full active lithium inventory of the cell is transferred from one electrode to the other. Only at low operating currents, where polarization effects are negligible, does the usable capacity correspond to the available active lithium inventory. Therefore, in addition to a constant-current (CC) step, during which overpotentials may limit the cell's charge/discharge capacity, cell charging protocols often includes an additional constant-voltage (CV) step. This step transfers the remaining active lithium to the other electrode without inducing excessive overpotentials. The applied current is reduced and the voltage is kept constant in this step to prevent unwanted reactions, such as lithium plating, that could damage the cell. The capacity retention during the CC step at different C-rates reflects the cell's rate performance. This is determined in so-called rate capability tests, in which the charge or discharge C-rate increases every three to five cycles. The CC capacities measured at each C-rate are then compared to the cell's maximum practical capacity, which is measured at low C-rates.

2.2.3 State-of-Health and End-of-Life

The state-of-health, SOH (%), of a cell is defined as the ratio of its usable capacity to its initial capacity (**Equation 2.12**).

$$SOH_{cycle\ x} = \frac{Q_{cell,cycle\ x}}{Q_{cell,cycle\ 1}} \cdot 100 \qquad \textbf{2.12}$$

The cycle life of a cell is defined as the number of charge/discharge cycles it can undergo before its usable capacity falls below 80% of the initial value. This point is referred to as the end-of-life (EOL), as expressed by **Equation 2.13**.

$$EOL \rightarrow SOH_{cycle\ x} < 80\% \qquad \textbf{2.13}$$

The coulombic efficiency, *CE* (%), indicates the capacity loss per cycle and is defined as the ratio of the released to the stored capacity (**Equation 2.14**).

$$CE_{cycle\ x} = \frac{Q_{discharge,cycle\ x}}{Q_{charge,cycle\ x}} \cdot 100 \qquad \textbf{2.14}$$

Maintaining a high CE of 99.99%, for example, corresponds to a long cycle life of about 2,231 cycles before reaching EOL, whereas lower values, such as 99.95%, reflect rapid capacity fade and short cycle life of about 446 cycles.

Aging mechanisms in LIBs are inherently complex because all components interact with each other and with the operating conditions. ALL summarizes all processes which decrease the active lithium inventory of the cell, including parasitic reactions (e.g., SEI formation, lithium plating, and electrolyte decomposition), lithium trapping, and AM disconnection.[89] ALL (without AM disconnection) primarily causes capacity fade, whereas other, more severe aging mechanisms, such as structural or mechanical degradation of the AMs or the electrodes may also significantly alter the cell's voltage profile.[52,90]

2.2.4 Cell Energy *J* (Wh) and Power *P* (W)

The combination of cell capacity (Q_{cell}) and the average working voltage ($U_{\emptyset,cell}$) determines the amount of energy (J_{cell}) that can be stored or delivered, as described in **Equation 2.15**.[40]

$$J_{cell} = Q_{cell} \times U_{\emptyset,cell} \qquad \textbf{2.15}$$

Considering Graphite‖LFP ($U_{\emptyset,cell}$ *= 3.35 V*) and Graphite‖LCO ($U_{\emptyset,cell}$ *= 3.8*) cells with the same capacity (Q_{cell}), the energy (J_{cell}) of the two cell chemistries differs significantly, with the latter exhibiting approximately 13.4% higher energy.[34] The cell energy can also be normalized to the cell mass, specific energy $J_{spec,cell}$ (Wh kg^{-1}), or cell volume, energy density $J_{vol,cell}$ (Wh L^{-1}), to provide an even more comprehensive value for comparison.

Equation 2.15 represents only a simplified estimate of a cell's maximum energy, as both, Q_{cell} and $U_{\emptyset,cell}$, vary in practice with operating conditions (e.g., current density, temperature, cut-off voltages, etc.) and SOH, as discussed above. The practical delivered energy depends strongly on the cell's overall output power, P_{cell} (W), over time, *t* (h), as expressed by **Equation 2.16** and **2.17**.[91]

$$P_{cell} = I \cdot U_{cell} \qquad \textbf{2.16}$$

$$J(t)_{cell} = \int_0^{\Delta t} P(t)_{cell}\, dt \approx J(I)_{cell} = Q(I)_{cell} \cdot U(I)_{\emptyset,cell} \qquad \textbf{2.17}$$

The overall electrochemical fundamentals of LIBs imply that all components and operating conditions must be carefully designed to ensure safe operation and a long cycle life while maintaining high energy and high power.[92–94] Unfortunately, there is a trade-off between high energy and high power: high-energy cells require minimizing inactive materials, resulting in dense,

thick electrodes, whereas high-power cells aim to reduce overpotentials, favoring porous, thin electrode designs.

2.3 From Materials to Cells

LIB cell manufacturing comprises multiple components and processing steps, as illustrated in **Figure 2.3**.[34,82,95–97] First, the active and inactive coating components are mixed in a defined ratio with a solvent to form a homogeneous suspension, typically called slurry. Next the slurry is accurately coated onto a current collector to achieve the desired coating loading (mg cm^{-2}) after drying. Next, the coating is calendared to the target coating density (g cm^{-3}) and slit into the required electrode format, including tabs. Finally, the cathodes, anodes, and separators are stacked or wound and packed into a housing. Before sealing the cell, the electrolyte is added.

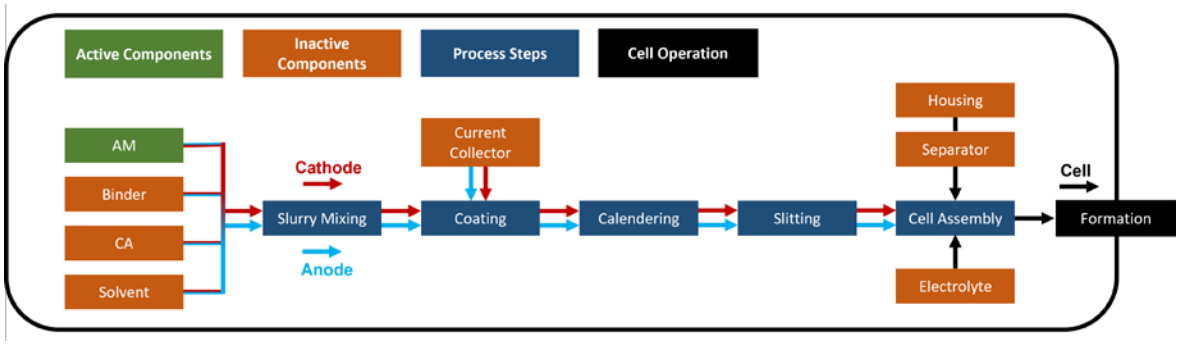

Figure 2.3 Simplified block diagram illustrating the basic LIB manufacturing process, from materials to cells (based on Li et al., 2021[82]).

The selection, design and implementation of both active and inactive components must be carefully aligned with their respective functions. Accordingly, processing steps, instruments and parameters must to be precisely adjusted to the components involved and the targeted cell characteristics (energy, power, cycle life, and cost). To this end, rigorous quality control of cell components and intermediate products after each process step is essential to understand cell performance and, more importantly, to ensure safe operation and prevent failures that cannot be traced in the inherently complex LIB system.

2.3.1 Active Materials

Electrochemical active materials determine key electrode properties, including its capacity and voltage, as discussed in ***Chapter 2.2*** (page 8). Ideal AMs combine high specific and volumetric electrical capacities, excellent electronic and ionic conductivities, structural stability, and are made from abundant, non-critical raw materials. Furthermore, they should be produced in an environmentally friendly manner and are low cost. Cathode AMs should operate at high potentials, while anode AMs should operate at low potentials to ensure a high overall cell voltage.

From an electrochemical perspective, lithium metal is a promising anode candidate due to its low reduction potential (-3.04 V vs. SHE) and high theoretical specific capacity (3,862 mAh g^{-1}).[98,99] However, lithium metal batteries are not safe for practical secondary battery operation, as their operating mechanism relies on lithium plating and stripping, which poses safety risks due to dendrite formation and internal short circuits.[100,101] Nevertheless, lithium metal is widely used in half-cell measurements and as a reference electrode (V vs. Li^+/Li) to evaluate AMs and electrode characteristics in LIB research and development.[102] Caution is advised with the former, as Li‖Electrode cell operation under standard loadings and current densities should be evaluated as a full-cell rather than as a half-cell measurement.[102–104]

A breakthrough in the transition from primary lithium metal batteries to secondary lithium-ion batteries was triggered by the substitution of lithium metal with graphite as the anode's AM.[91,99,101,105–107] Graphite consists of sp^2-hybridized graphene layers that are linked by relatively weak van der Waals forces and π-π interactions between delocalized electron orbitals in hexagonal (ABAB, thermodynamically favored) or rhombohedral (ABCABC) stacking symmetries. Its layered structure serves as a lithium host.[108–111] Graphite exhibits a moderate theoretical specific capacity of 372 mAh g^{-1}, together with a low average working voltage (0.1 V vs. Li^+/Li), high electronic conductivity and low cost.[34,112] The lithium intercalation/deintercalation mechanism is commonly described in four stages, with stage 1 corresponding to the fully lithiated structure (LiC_6).[99,111,113] During intercalation, the graphene layers undergo slight relative sliding, resulting in a structural transition from ABAB stacking in pristine graphite to AIAI stacking in the fully lithiated state (I = intercalant layer).[99,114] This process causes a modest volume expansion of approximately 10%, which highlights graphite's high structural stability and long cycle life.[112,115,116] Lithiation of graphite is also accompanied by a characteristic color changes in the individual particles, progressing from black (C_6) to dark blue, red (LiC_{12}), and finally to golden (LiC_6).[116,117] Only moderate ICLs arises from anodic SEI formation, which is primarily affected by the material's morphology and surface area, as well as the electrolyte composition chosen.[85,86,118] Graphite's exceptional properties have made it the dominant anode material since the commercialization of LIBs.[34,101,112] However, graphite anodes are prone to lithium plating at high currents and low temperatures because their operating voltage is close to 0 V vs. Li^+/Li. This poses significant performance and safety concerns in the event of pronounced electrode polarization.[47,48]

Lithium titanate ($Li_4Ti_5O_{12}$, LTO) is a commercially available alternative anode AM that exhibits a significantly higher operating voltage (1.55 V vs. Li^+/Li) than graphite.[119] Its voltage profile exhibits a single well-defined plateau that corresponds to the phase transition from $Li_4Ti_5O_{12}$ to $Li_7Ti_5O_{12}$.[120] LTO is considered a "zero strain" material in terms of lithium intercalation/deintercalation, resulting in minimal volume expansion (~0.2%) and long cycle life.[121] Its low electronic conductivity[122] and moderate ionic conductivity[123–125] can be mitigated through doping[122], nanosizing[126,127], morphology control[128], and surface modifcation[129,130], thereby also enabling high-rate performance. However, although one mole of LTO can host three moles of lithium, its high molecular weight (459.193 g mol^{-1}) results in a low theoretical capacity of 175 mAh g^{-1}. Combined with its high operating voltage, this limits its application as an anode AM.[34,131,132]

Last but not least, silicon (Si) is also a widely investigated anode AM due to its low operating voltage (0.2 V vs. Li^+/Li), exceptionally high theoretical specific capacity (3,579 mAh g^{-1}), and raw material abundance, as well as its eco-friendly and non-toxic nature.[34] However, severe volume expansion (~280%) during lithiation from Si to $Li_{15}Si_4$ leads to poor cycle life, as neither the AM particles nor the electrode structure (including the anodic SEI) can accommodate the resulting mechanical stress.[133–135] This causes pulverization of the particles, loss of electronic contact, formation of cracks within the electrode coating, loss of active lithium due to SEI formation, and eventual complete delamination from the current collector.[136] Particle pulverization can be mitigated by nanosizing the silicon particles[137–139] and limiting the degree of lithiation[140,141], while structural stability and cycle life can be further enhanced by embedding silicon in a carbon matrix[142–145], forming so-called silicon–carbon composites (SiCs), as well as by appropriate selection of electrode coating[146–148] and electrolyte[149,150] composition.[151] In addition, Si and SiC electrodes suffer from high ICLs, which limits the achievable energy in a full-cell setup.[142] Despite significant progress in recent years, the use of silicon in commercial LIB anodes remains limited to low weight fractions.[152]

Figure 2.4 presents the electrochemical data of the graphite and SiC active materials used in this work.

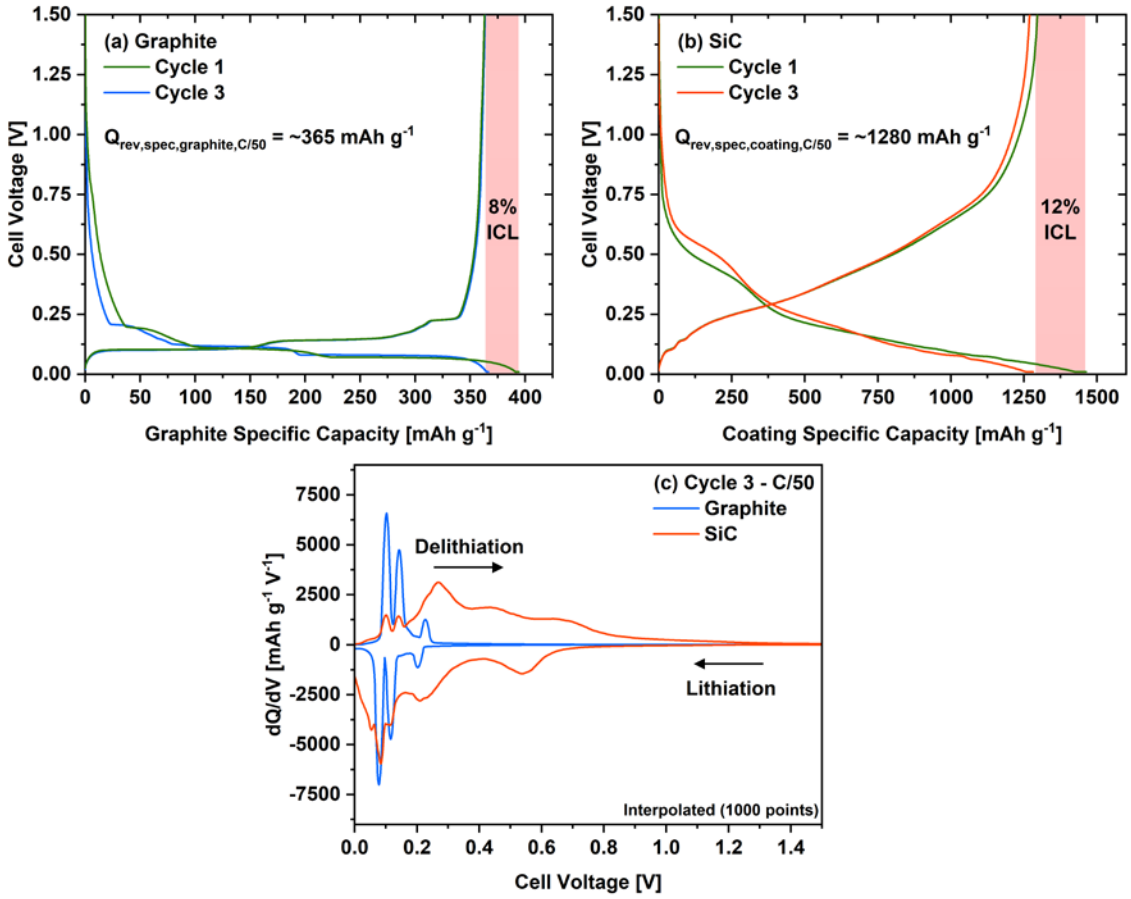

Figure 2.4 2032-coin half-cell (Li‖Electrode) formation data of graphite and SiC electrodes: a, b) voltage profile and c) derivative analysis. The formation protocol involves three CCCV-lithiation and CC-delithiation cycles of the electrode AMs at a current density of C/50 in the potential window 0.05 – 1.50 V. All cells contain electrodes with an areal capacity of ~3.0 mAh cm^{-2}. The electrolyte formulation depends on the anode AM, with LP10VC02 used for graphite and LP10VC02FEC10 for SiC.

Already in the early stages of alkali metal battery research, it was understood that optimal electrode reversibility requires that the AM crystal structure remain intact during cycling, with no bonds broken or formed.[153] On this basis, the intercalation compound lithium titanium disulfid ($LiTiS_2$, $Q_{theor,spec}$ = 225 mAh g^{-1}, $U_{\emptyset}$ = 2.1 V vs. Li$^+$/Li) was initially established as a cathode AM for lithium batteries.[83,153,154] However, its relatively low operating voltage limited its energy density. The search for alternative intercalation cathode AMs progressed from chalcogenides (M_nS_m) to metal oxides (M_nO_m), resulting in the adoption of lithium cobalt oxide ($LiCoO_2$, LCO), which served as the cathode AM in the first LIB commercialized by Sony in 1991.[83,105,154]

LCO exhibits a layered oxide structure and features good reversible specific capacity with high operating voltage (3.9 V vs. Li$^+$/Li).[34,83,84] However, cobalt's high cost and limited availability restrict its application primarily to small LIB cells, such as those used in portable electronic devices.[155,156] Substitution of cobalt with nickel results in lithium nickel oxide ($LiNiO_2$, LNO), which provides comparable energy characteristics ($Q_{rev,spec}$ = 200 mAh g^{-1}; $U_{\emptyset}$ = 3.75 V vs. Li$^+$/Li) while relying on more abundant and less expensive raw materials.[157–159] Unfortunately, LNO shows poor cycling

stability, as nickel and lithium tend to exchange lattice positions within the crystal structure.[159,160] The breakthrough was achieved by partially substituting nickel with cobalt, along with additional substituents, such as manganese or aluminum, to stabilize the crystal lattice, forming nickel manganese cobalt oxides ($LiNi_xMn_yCo_zO_2$, NMC) or lithium nickel cobalt aluminum oxides ($LiNi_xCo_yAl_zO_2$, NCA). The energy density, cycle life, safety, and cost of these AMs can be balanced by adjusting the stoichiometric ratio of transition metals; for clarity this information is added to the material name, *e.g.,* $LiNi_{0.8}Mn_{0.1}Co_{0.1}O_2$, NMC811. NMC and NCA are widely used as cathode AMs in large-format LIB cells today.[34]

Lithium iron phosphate ($LiFePO_4$, LFP) is a commercially utilized alternative cathode AM for large-format LIB cells, offering low cost at high raw material abundance, together with enhanced safety and cycling stability, at the expense of energy density.[161] LFP exhibits an olivine crystal structure and features a moderate theoretical specific capacity (170 mAh g^{-1}), along with a suitable operating voltage (3.45 V vs. Li^+/Li).[161,162] Nanosizing and carbon coating of LFP materials mitigate its intrinsically low electronic and ionic conductivity, enabling also good rate performance.[162–166]

Figure 2.5 presents the electrochemical data of the LFP and NMC811 AMs employed in this work. LFP exhibits a well-defined voltage plateau, reflecting its two-phase reaction, along with a high first cycle CE. In contrast, NMC811 shows a sloping voltage profile, reflecting its solid-state diffusion reaction, along with lower first cycle CE, which is typical for this material class. Unlike anodic ICLs caused by SEI formation, nearly 75% of the cathodic ICLs are only kinetically hindered and reversible at very low currents, while the remaining losses are irreversible and associated with structural changes or parasitic surface reactions.[80,167]

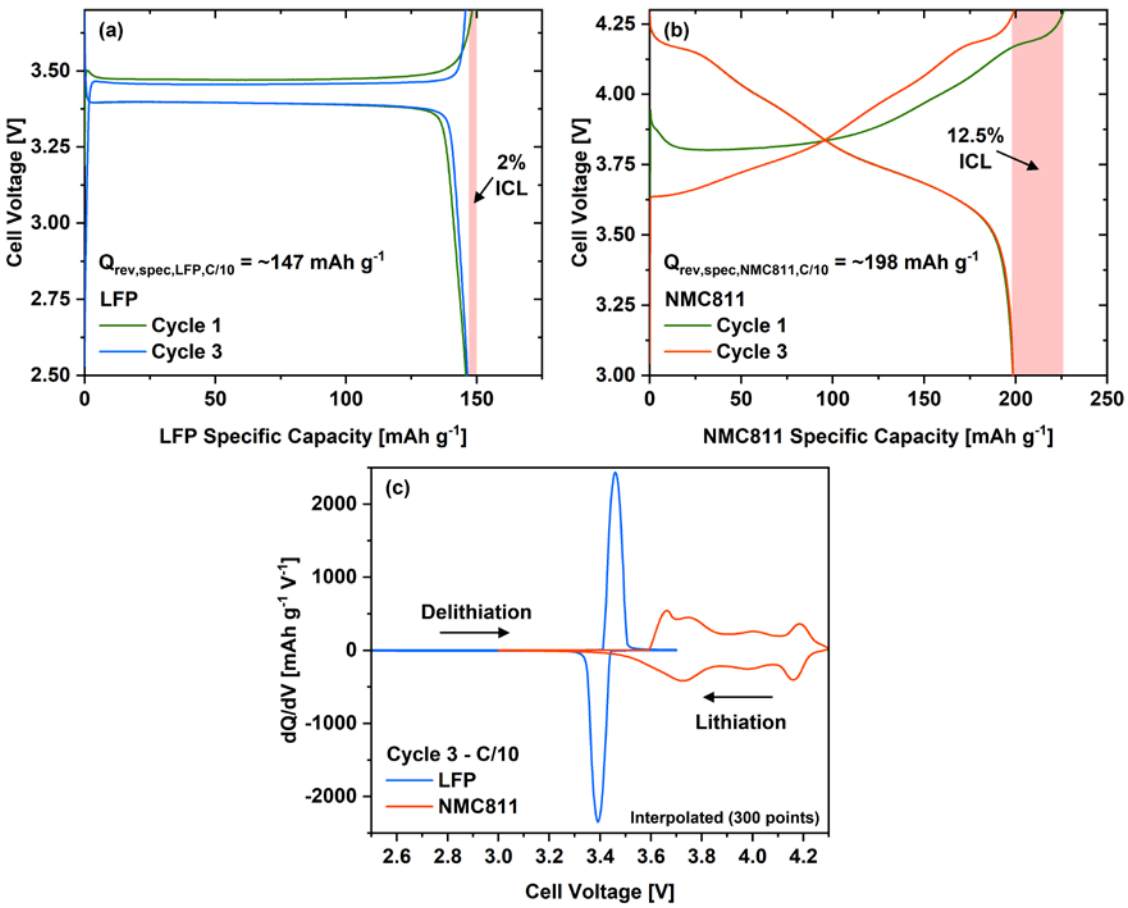

Figure 2.5 2032-coin half-cell (Li‖Electrode) formation data of LFP and NMC811 electrodes: a, b) voltage profile and c) derivative analysis. The formation protocol involves three CC-delithiation and CC-lithiation cycles of the electrode active materials at a current density of C/10 in the potential window 2.5 – 3.7 V and 3.0 – 4.3 V for LFP and NMC811 electrodes, respectively. All cells contain electrodes with an areal capacity of ~2.55 mAh cm^{-2} and LP10VC02 as electrolyte.

2.3.2 Inactive Materials

Electrochemically inactive materials are equally important, as they ensure proper cell functionality. Conductive additives (CAs), binders, and current collectors, together with the previously described AMs, form the LIB electrodes, while electrolyte, separators, and housing make up the rest of the cell. As inactive components reduce the specific energy and energy density of LIBs, their overall mass and volume have to be kept as low as possible while maintaining safe and stable operation, along with high-rate performance. In general, they should remain chemically and electrochemically stable during both cell manufacturing and operation, regardless of their function.

CAs form a conductive network throughout the electrode coating, facilitating efficient electron transfer between the current collector and the AM particles.[168] CAs are typically carbon-based materials, such as carbon black (CB), carbon nanotubes (CNTs), or graphite, which combine high electronic conductivity with a large specific surface area.[169–171]

Binders provide mechanical stability of electrodes, including adhesion of the coating to the current collector and cohesion between the coating components. In general, binders are selected to match the chemical (slurry solvent) and electrochemical (operating voltage) stability of the AM. Polyvinylidene fluoride (PVDF) with N-methyl-2-pyrrolidone (NMP) was long the state-of-the-art system for both anodes and cathodes.[172] However, NMP-based electrode processing poses health risks and is costly, as the solvent must be recovered during drying.[82,173] Moreover, PVDF belongs to the critically considered group of per- and polyfluoroalkyl substances (PFAS).[174] For this, over the last decades, water-based binders such as carboxymethyl cellulose (CMC), styrene-butadiene rubber (SBR), and poly(acrylic acid) (PAA) have been investigated and are now also widely used.[97,175–178] Nevertheless, water-sensitive AMs, such as high nickel NMC, or high-operating-voltage AMs, still require PVDF and NMP for their processing, and research continues to adapt them also for cheaper and more environmentally friendly binder-solvent systems by maintaining electrode functionality.[179–182]

2.3.3 Electrode and Cell Manufacturing Process

AMs, CAs, and binders are mixed together in a solvent to form the electrode slurry. Mixing is conducted to break up agglomerates and to homogenize all components within the slurry. During this process, all components interact physically with each other to form a wet-state matrix, which depends on morphology, particle size, and surface interactions. This wet-state matrix will later shape the microstructure of the electrode.[95,183] Caution must be taken because overly vigorous mixing can lead to irreversible changes in the slurry components.[184]

It has been found that electrode performance can be enhanced by sequential slurry mixing.[185] First, the binder is completely dissolved in the solvent (binder solution), followed by the addition of CAs (PreMix solution). In subsequent steps, AMs are added, and, if present, mixing-sensitive components are introduced last under gentle mixing to complete the electrode slurry. Slurry mixing is generally followed by degassing and, often, filtration.[82] The mixing conditions – including instrumentation, sequence, intensity, duration, and temperature – must be carefully selected to ensure the production of a reproducible, scalable, high-quality slurry that is compatible with the subsequent coating process.[82,95,97,168] Slurry mixing is typically performed as a batch process with cowles dispersers or planetary mixers, or as a continuous process with extruders.[82]

A grindometer can be used to detect unwanted agglomeration, while a rheometer can be used to investigate rheological properties of the final slurry.[183] Shear-thinning behavior is particularly favorable for electrode slurries.[186] At low shear rates, a high viscosity is preferable, as particle motion is limited and sedimentation is reduced (suspension stability). At high shear rates, a low viscosity is desirable, as this promotes improved flow and a more uniform wet-coating layer (suspension coatability). Rheological properties of slurries can be tuned by adjusting the coating components, formulation, and total solid content (TSC).[187–189]

Next, the electrode slurry is cast onto a current collector to obtain a uniform wet coating of a controlled thickness (which determines the final coating loading) with sharp edges.[82] Copper and aluminum foils are the preferred current collectors for anodes and cathodes, respectively.[190] At the lab-scale, doctor blade coating is used, and the wet-film thickness is controlled by the gap between the blade and the substrate. At larger scales, slot-die coating is employed, allowing even more precise control of the wet-film quality by adjusting slot-die geometry, slurry flow (regulated with a pump), coating width, and line speed. Slot-die coating is typically processed in a roll-to-roll system, in either continuous or intermittent mode.

Immediately after coating, the wet-film layer is dried by evaporating the slurry solvent. Excessive drying conditions can cause binder migration to the electrode surface, reducing mechanical stability. Insufficient drying, on the other hand, can leave behind unwanted solvent residues.[82] Traditionally, both sides of the current collector foil are coated and dried sequentially; nowadays, both sides can also be coated and dried simultaneously.

Finally, single- or double-sided coated electrodes are calendered to the targeted coating density and slit to the desired electrode format.[82] It is paramount to understand: all electrode fabrication steps – from material selection to slurry mixing to electrode calendering – shape the electrode's microstructure, consequently affecting its electrochemical performance. Parameters such as tortuosity, porosity, and homogeneity distribution must be carefully designed to enable efficient electronic and ionic transport, as well as mechanical stability of the electrode.[42,168,191]

Cathodes, anodes and separator are stacked or wound and assembled into the cell housing.[82] The separator is a thin, porous, electrically insulating membrane that prevents short circuits between the electrodes while remaining permeable to lithium ions.[82] Glass microfiber and polyolefins – specifically polypropylene (PP) and polyethylene (PE) – are mainly used in battery research and industry.

Before sealing the cell, the electrolyte is added.[82] The electrolyte enables lithium-ion transport between the electrodes during charge and discharge. Typically, the electrolyte consists of lithium salts, such as lithium hexafluorophosphate ($LiPF_6$), dissolved in organic solvents including dimethyl carbonate (DMC), ethyl methyl carbonate (EMC), and diethyl carbonate (DEC), ethylene carbonate (EC), along with small amounts of SEI-forming additives, such as fluoroethylene carbonate (FEC) or vinylene carbonate (VC).[34,192] The electrolyte composition must be tailored to the AMs and the cell's operating conditions. As $LiPF_6$ containing electrolytes are moisture-sensitive, all cell components must be thoroughly dried before its addition.[193–195]

2.3.4 SEI Formation

After sealing, the cell is left resting without any applied current to allow the electrolyte to uniformly wet the electrodes and separator.

LIB cells are assembled in a discharged state, with the full active lithium inventory located in the cathode. During the first charge, the cathode is delithiated, which increases the cathodic electrode potential, while the anode is lithiated, which decreases the anodic electrode potential. The overall cell voltage rises. For this to occur, the electrodes and electrolyte must interact to enable the transport of lithium ions between the cathode and the anode. The contact area where the electrode meets the electrolyte is called an interface.[88] At this interface, electron transfer between electrode and electrolyte can occur. Therefore, electrodes should operate only within the electrolyte's electrochemical stability window. If this condition is not met, the electrolyte decomposes at the electrode surface, forming an interphase at the electrode–electrolyte interface.[86,88]

However, LIB electrolytes are electrochemically unstable at very low potentials, as is the case with graphite or silicon electrodes, which operate far below 1 V vs. Li^+/Li.[34,112] It has been found that using an appropriate electrolyte formulation leads to the formation of a stable protective layer, known as the solid electrolyte interphase (SEI), on the anode surface. This layer impedes further electrolyte decomposition while remaining permeable to lithium ions.[87] The anodic SEI is a complex multicomponent layer consisting of mixed organic (semi-carbonates) and inorganic (oxides, carbonates, fluorides) electrolyte reduction products and its thickness is determined by the electron tunneling range.[85,87,88]

The ideal SEI combines high ionic conductivity and electrical resistance with strong mechanical stability, tolerance to expansion and contraction stresses, insolubility in the electrolyte, and overall stability across a wide range of operating conditions, including temperature. Its final structure depends highly on the electrolyte composition, the anode surface characteristics, and its formation conditions (e.g., current density, temperature). In fact, switching from propylene carbonate (PC)-based to EC-based electrolyte mixtures was key to achieving electrochemically reversible full lithiation and delithiation of graphite, thanks to the formation of a stable anodic SEI. This breakthrough paved the way for graphite's use as an anode AM in the early 1990s.[87,196]

As illustrated in **Figure 2.6**, the anodic SEI acts as a solid electrolyte, enabling the reversible operation of LIBs by preventing continued electrolyte reduction at the electrode–electrolyte interface. However, its formation irreversibly consumes active lithium from the cell's active lithium inventory, resulting in ICLs during cell formation.[85,87,88]

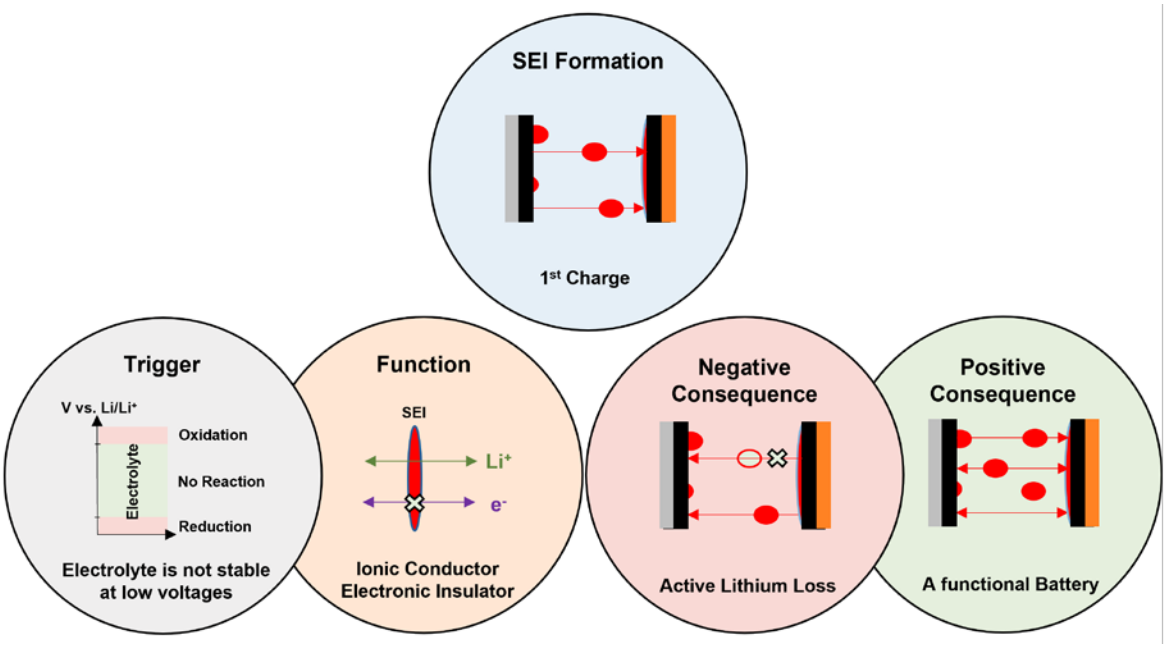

Figure 2.6 Schematic illustration of anodic SEI formation and its function in LIBs.

Figure 2.7 shows the formation data of Graphite‖LFP, Graphite‖NMC, and SiC‖LFP cell chemistries considered in this work. It's clearly oberveable, that the first-cycle CE, ICLs, and voltage profiles vary strongly with the chosen cell chemistry.

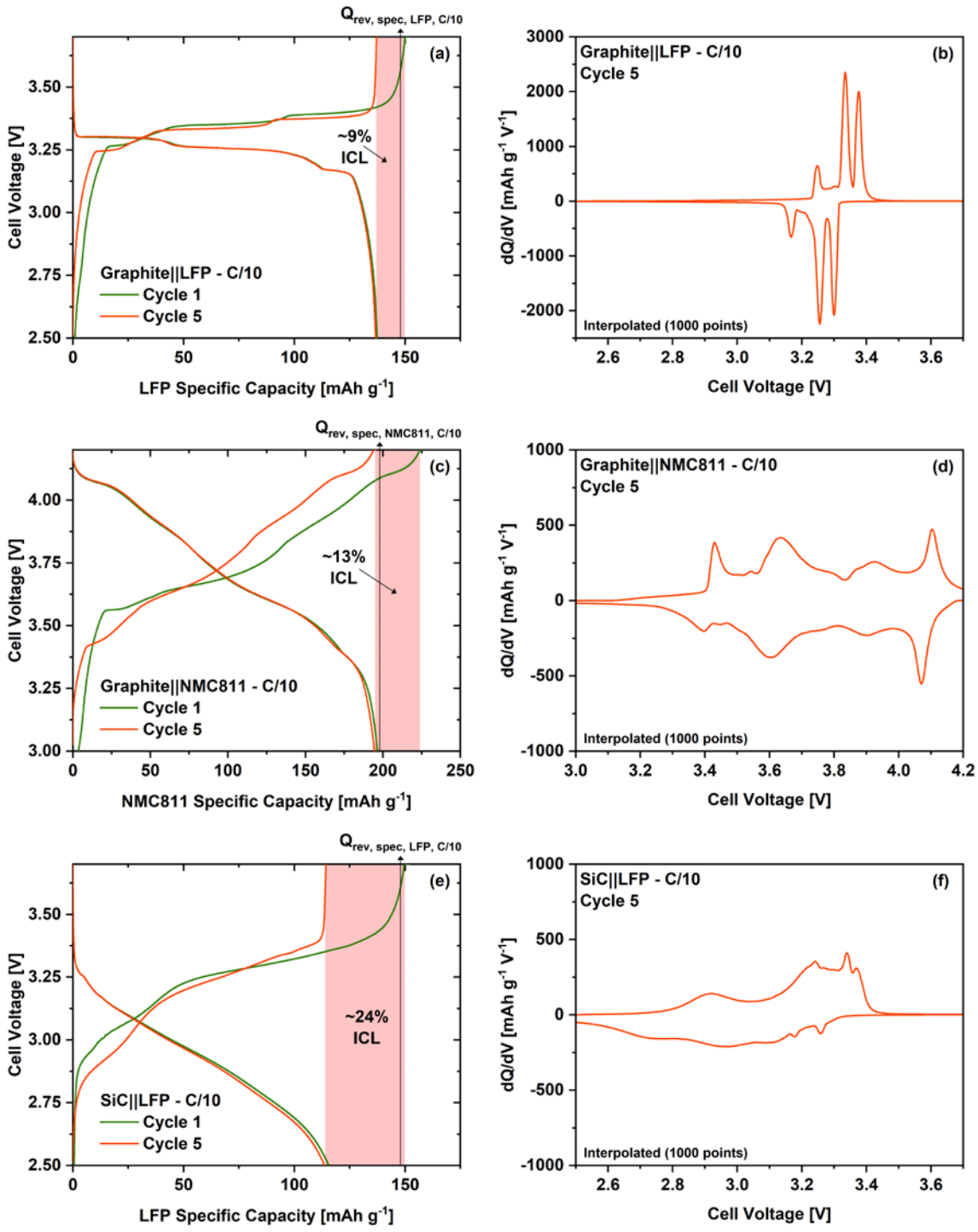

Figure 2.7 Single-layer pouch cell (Anode‖Cathode) formation data of a, b) Graphite‖LFP, c, d) Graphite‖NMC811, and d, e) SiC‖LFP cell chemistries: a, c, e) voltage profile and b, d, e) derivative analysis. The formation protocol involves five CCCV-charge and CC-discharge cycles at a current density of C/10 in the voltage window 2.5 – 3.7 V and 3.0 – 4.2 V for LFP and NMC811 cathode AM chemistries, respectively. All cells include a total initial cathode capacity of ~60 mAh, with a cathodic reversible areal capacity of ~2.5 mAh cm^{-2} and a N/P-balancing of ~1.15. The electrolyte formulation depends on the anode AM, with LP10VC02 used for graphite and LP10VC02FEC10 for SiC.

2.4 Prelithiation Concept and Strategies

The concept of prelithiation can be defined as follows: compensation of anodic ICLs through additional active lithium sources to enable full use of reversible cathode capacity in the operating cell.[197–200]

A more concrete understanding of the general prelithation principle can be obtained from the formation data shown in **Figure 2.7** (page 25), which directly addresses the cell chemistries considered in this work.

Graphite‖LFP cells exhibit a first cycle CE of 91%, resulting in a usable LFP specific capacity of ~136 mAh g^{-1} after cell formation. This value is ~8% below its practical reversible specific capacity measured in half-cells (147 mAh g^{-1}, **Figure 2.5** on page 19). In other words, 8% of the cathode AM remains inactive in the electrode after anodic SEI formation due to a deficiency in the cell's active lithium inventory. This effect is even more pronounced in SiC‖LFP cells, where the first-cycle CE is only 76%, yielding a usable LFP specific capacity of 114 mAh g^{-1} (~23% below its practical capacity). This data proves that active lithium deficiencies arising from anodic initial irreversible capacity losses cause the accumulation of inactive active materials in LIBs after cell formation, which drastically reduces their practical energy density.

Interestingly, Graphite‖NMC811 cells exhibit markedly different behavior, even if it may not be immediately apparent to the untrained eye. Although these cells also display a relatively low first cycle CE (~87%), the usable NMC811 specific capacity after formation in the full-cell (195 mAh g^{-1}) still matches its practical reversible specific capacity measured in half-cells (198 mAh g^{-1}). This behavior is characteristic of a prelithiated cell.[198]

But why does Graphite‖NMC811 exhibit the characteristics of a prelithiated cell, while Graphite‖LFP shows a deficiency in active lithium after cell formation?

In contrast to LFP, NMC811 showed a relatively low first cycle CE in half-cell measurements (**Figure 2.5** on page 19). Kasnatscheew et al. (2016) attributed such low first-cycle CEs in NMC111 to slow lithium uptake at high lithiation levels.[167] In brief, most ICLs of NMC111 are reversible: active lithium is not irreversibly consumed, unlike in anodic SEI formation, but, due to kinetic limitations, cannot be reintercalated into the AM structure. Thus, NMC electrodes initially contain more active lithium than they can reversibly utilize under standard operating conditions, representing an intrinsic active lithium surplus in their initial state. In a subsequent study, Kasnatscheew et al. (2017) further considered the impact of half-cell AM first-cycle CEs on full-cell performance.[80] They concluded that the full-cell active lithium inventory after anodic SEI formation is governed by the difference and nature of anode and cathode ICLs. If $ICL_{anode} > ICL_{cathode}$, cell formation results in an active lithium deficiency and reduced reversible capacity. If $ICL_{anode} = ICL_{cathode}$, then anodic ICLs are balanced by the cathode's active lithium surplus (typical of prelithiation). When $ICL_{anode} < ICL_{cathode}$, the cathode's

active lithium surplus balances the anodic ICLs and forms an anodic lithium reservoir. The anodic lithium reservoir can compensate for ALL in subsequent cycles until it is depleted. According to these papers, the here discussed Graphite‖LFP cells are predicted to exhibit a ~6% active lithium deficiency, while Graphite‖NMC811 cells possess a ~4% anodic lithium reservoir. These predictions are largely in agreement with the formation data discussed above. However, the formation data provided still can't validate the presence or size of an anodic lithium reservoir in Graphite‖NMC811 cells. Therefore, while additional prelithiation can improve the energy of Graphite‖LFP cells, it may pose safety risks in Graphite‖NMC811 cells. In these cells, excess active lithium that cannot be accommodated by the anode anymore will plate on its surface, potentially causing short circuits in the worst case.[48]

It is obvious, evaluating a cell's initial state of active lithium inventory from only full-cell formation data is not straightforward. As discussed above, first-cycle CEs and full-cell capacity values, which are often reported in prelithiation studies, provide only part of the picture. Studies should be critically considered, as active lithium oversupply is difficult to detect. In general, extra active lithium supply in LIBs must be handled cautiously with high control and proper N/P-balancing, as otherwise it can result in safety risks during cell operation as explained above.[48,198]

This work focuses on studying controlled anodic prelithiation and lithium reservoir formation using a cell-level prelithiation strategy. Accordingly, Anode‖LFP cell chemistries were chosen as the best option in this study based on the formation data discussed above.

2.4.1 Prelithiation Strategies

Prelithiation strategies have been widely investigated across all stages of LIB manufacturing, including the material, electrode, and cell levels.[197–200]

On the cathode side, prelithiation at the material level can be realized by overlithiation of cathode AMs or by adding sacrificial prelithiation additives into the cathode, as illustrated in **Figure 2.8**.[197–200]

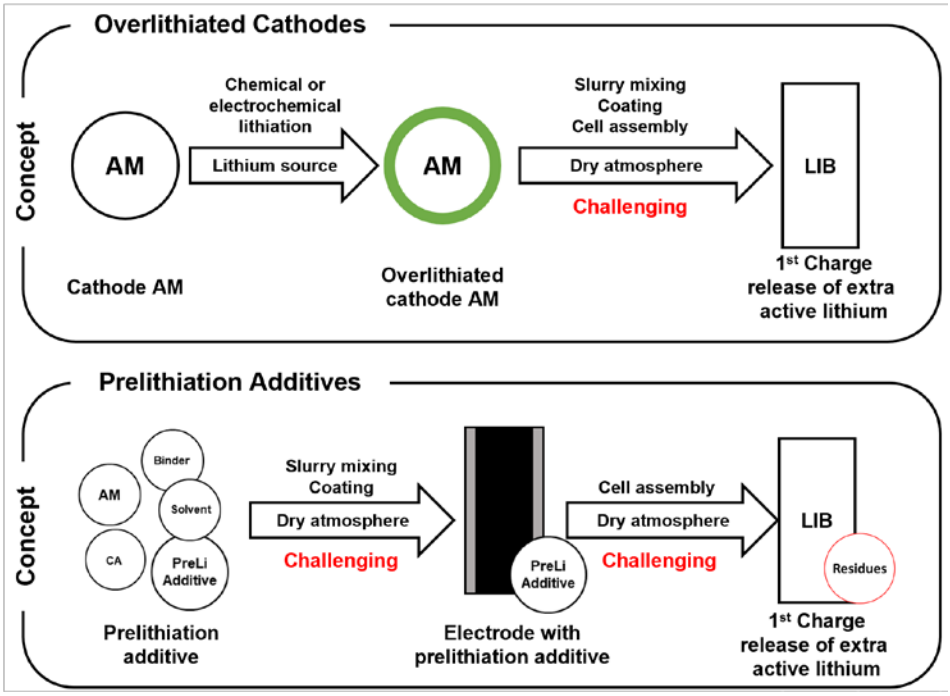

Figure 2.8 Simplified illustration of prelithiation strategies at the material level on the cathode side.

Chemical or electrochemical overlithiation of cathode AMs such as $Li_{1+x}Mn_2O_4$ or $Li_{1+x}Ni_{0.5}Mn_{1.5}O_4$ result in materials with a well-controlled intrinsic extra active lithium surplus.[201–203] Alternatively, prelithiation additives such as Li_3N, Co/Li_2O or Li_3P can be incorporated into the positive electrode in well-defined amounts.[204–207] As prelithiation additives contribute to electrode mass, they should exhibit high specific capacity.[198] In both concepts, extra active lithium release during first charge offsets anodic ICLs without depleting the cathode's reversible lithium reservoir. The latter results in the formation of residues (gaseous or solid), which may increase safety risks or impair cell performance.[197–199]

On the anode side, prelithitiation at the material or at the electrode level can be realized through reaction with lithium containing reagents or small amounts of lithium metal, as illustrated in **Figure 2.9**.[197–200]

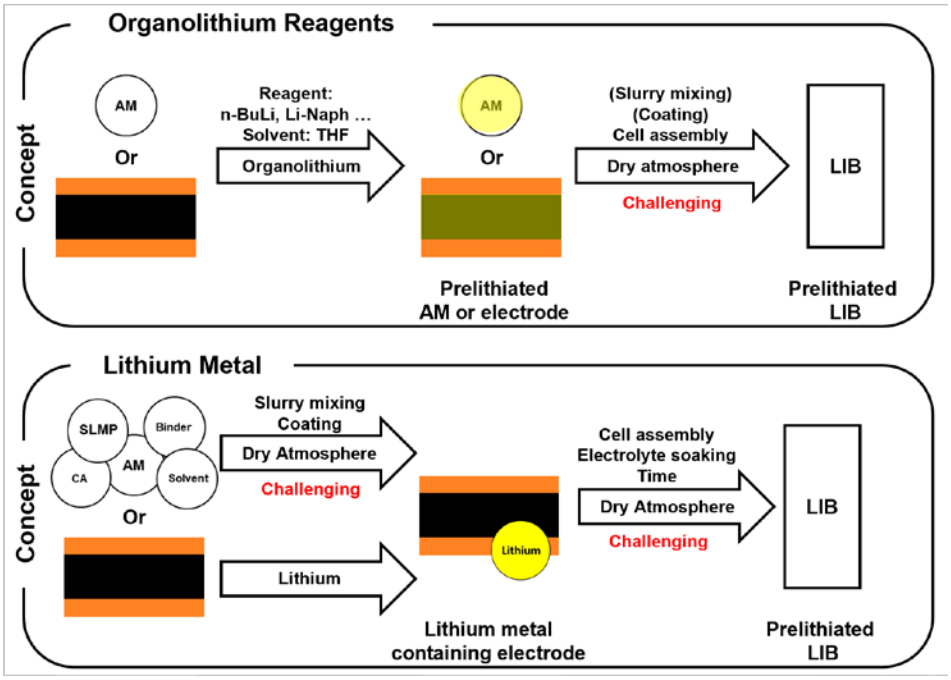

Figure 2.9 Simplified illustration of prelithiation strategies at the material or at the electrode level on the anode side.

Exposing anode AMs or electrodes to organolithium solutions, such as n-butyl lithium (n-BuLi) or lithium naphthalene (Li-Naph), or directly to metallic lithium (e.g. stabilized lithium metal powder, SLMP) in the presence of electrolyte, results in chemical redox reaction.[208–212] Organolithium solutions and metallic lithium are strong reducing agents capable to form an anodic SEI or even an anodic lithium reservoir.[210,212] The degree of prelithiation can be controlled by adjusting the exposure time and reagent concentration or lithium metal mass. However, chemical prelithiation is time-consuming and the resulting SEI may differ in thickness, stability, and composition from an electrochemical formed SEI due to variations in reaction conditions, solvents, and reagents.[197–200]

Both prelithiation strategies at the material or electrode level require complex processing, costly additives/components, or produce highly reactive intermediates, making most of them incompatible with current industrial LIB manufacturing.[197–200]

Lastly, at the cell level, prelithiation can be realized by introducing lithium-ion permeable electrodes and a sacrificial lithium donor electrode into the cell, as illustrated in **Figure 2.10**.[213–215]

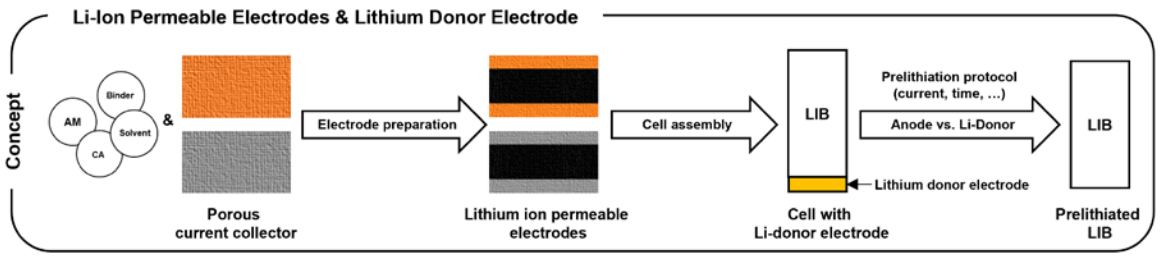

Figure 2.10 Simplified illustration of prelithiation strategy at the cell level using lithium-ion permeable electrodes and a sacrificial lithium donor electrode.

ICLs from anodic SEI formation are compensated by a current-controlled active lithium transfer between a lithium-donor electrode and the anode layers in the cell. The lithium-ion permeability of electrodes is essential, as it enables lithium-ion diffusion pathways throughout the entire cell.[213–215] This approach avoids handling of reactive intermediates, as prelithiation is performed in the final step of LIB manufacturing – during cell formation. However, application of this method in LIB literature is still limited to the best of the author's knowledge;[213–215] constraints in technology, including porous current collector and cell design, are hindering its development.

Motivation and Objectives

3. The Role of Perforated Current Collectors in LIBs

The commercialization of LIBs in the early 1990s revolutionized portable electronic devices and paved the way for modern lifestyles. In recent decades, LIB applications have expanded to include stationary energy storage systems and traction batteries, establishing LIBs as key technologies for addressing contemporary challenges such as renewable energy integration and decarbonization.[91,105,106,216]

However, the growing demand for LIBs has raised concerns about the availability of the critical raw materials required for their production, including copper, cobalt, nickel, manganese, graphite, and lithium.[33,35,217] Furthermore, as market expectations evolve, it is crucial to continuously optimize several key LIB performance indicators, such as energy density, power density, cycle life, safety, efficient resource usage, sustainability, and cost, while taking into account technical, legislative, economic, and ecological factors. Consequently, a variety of innovation-driven strategies that address all stages of LIB development, from materials to electrodes, cells, and packs, have emerged in recent decades.

This work focuses on an innovative electrode design that uses perforated current collector foils. Design-related opportunities to improve several key LIB performance indicators, including energy density, cycle life, and efficient material utilization, are discussed in detail.

Anticipations at the Electrode Level

In general, a LIB electrode consists of a thin, dense layer composed of AMs, CAs and binder, coated on a current collector foil.[34] AMs determine the specific capacity and working potential.[34,82] Inactive components ensure the electrode's functionality. CAs ensure sufficient electron conductivity and binder provides adhesion, cohesion, and mechanical stability.[82] Copper and aluminum are the preferred materials for current collectors for anode and cathode, respectively, due to their electrochemical stability and good electronic conductivity.[190] In addition to the electrode components, the electrode microstructure is equally important for ensuring good cell performance.[42,168,191]

A straightforward approach to enhancing the specific capacity of an electrode is maximizing the AM content in the coating composition by reducing inactive materials in the coating layer.[82,97] However, the AM content in state-of-the-art LIB electrode coatings already exceeds 94 wt.%.[34,218] Further increases in AM content are desirable but introduce practical constraints on maintaining electrode processability and functionality. Additionally, as shown in **Figure 3.1b**, only a marginal increase in electrode specific capacity can be achieved even when this approach is pushed to its limits.

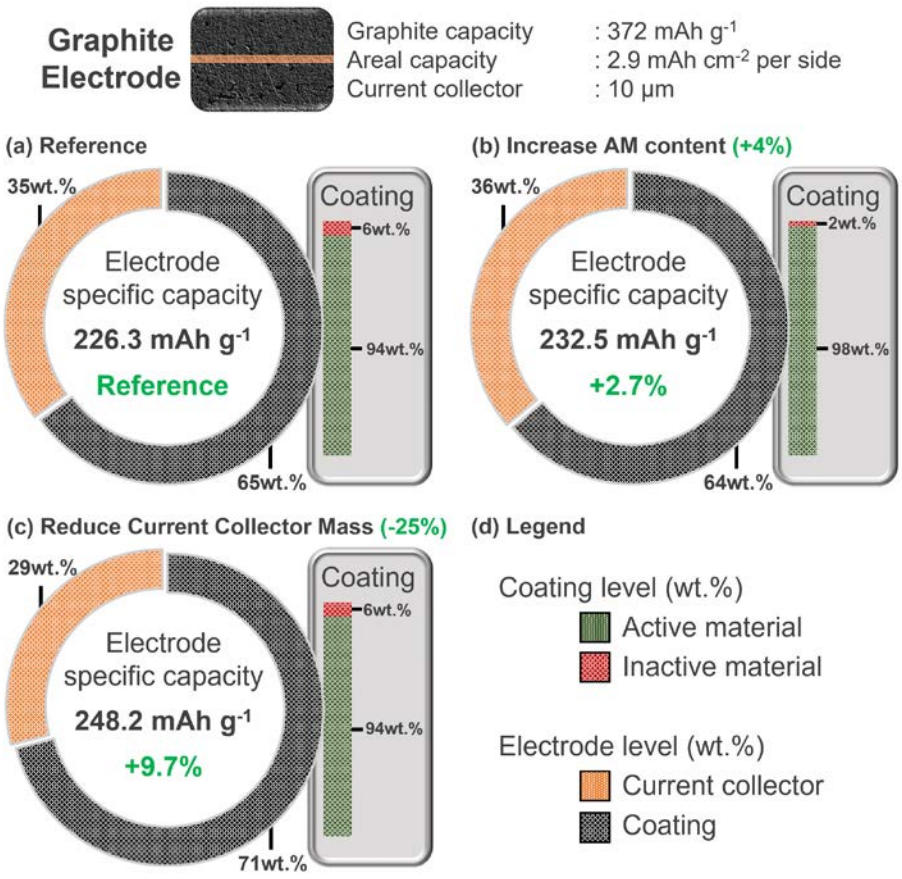

Figure 3.1 A comparison of different strategies to increase the specific capacity of graphite electrodes, focusing on electrode design: a) reference, b) increase of AM content in the coating layer, c) reduction of current collector mass/volume, and d) the color legend. The calculations are based on a double-sided coated graphite electrode with an areal capacity of 2.9 mAh cm^{-2} per side.

Another approach to enhancing the specific capacity of electrodes is to maximize the overall coating loading/areal capacity (mg cm^{-2}/mAh cm^{-2}), thereby reducing the relative mass of the current collector in proportion to the overall mass of the coating layer per unit area. However, high loadings result in thick electrodes, which introduce practical constraints on maintaining electrode processability and functionality.[219]

Modifying the current collector foil is a smart alternative approach to increasing the electrode's specific capacity. This approach reduces the relative mass of the current collector in proportion to the overall mass of the coating layer per unit area. As **Figure 3.1c** shows, reducing the mass of the copper current collector by 25 wt.% can significantly improve the specific capacity of the graphite electrode (+9.7%), thereby avoiding the aforementioned drawbacks associated with thick electrodes.

This fact is, is well-known in the LIB industry. Nevertheless, despite three decades of efforts to reduce the thickness of current collectors in LIB manufacturing (Al thickness reduced from 25 µm

to 10 µm, and Cu thickness reduced from 18 µm to 10 µm from 1998 to 2019), innovative current collector designs have been surprisingly disregarded.[82,190]

In battery research, metal foils, metal meshes, metal foams, etched metals, structured metals, and coated metals, as well as carbonaceous materials, have been investigated to improve the properties of current collector, such as electrochemical stability, electrical conductivity, mechanical strength, material density, sustainability, and cost.[190,220,221] Nonetheless, these attempts have not achieved a commercial breakthrough due to concerns about the material density, industrial processability, electrical resistance and mechanical stability of the proposed current collectors. Thus, standard copper and aluminum foils are still mainly used in LIB production.

In the lithium-ion capacitor (LIC) industry, JM Energy (nowadays Musashi Energy Solutions, Japan) developed and commercialized perforated current collectors to achieve a lower anode potential through prelithiation.[213,214,222] Caizán-Juanaren et al. reported on the design of a frontrunner LIC (ULTIMO, Musashi Energy Solutions). The LIC cell contained anodes coated with graphite on perforated copper foil (with a hole diameter of ~80 µm) as the current collector; cathodes coated with activated carbon on chemically etched aluminum foil as the current collector; and a "prelithiation plate", all of which were separated by separators and electrolyte.[223]

Inspired by developments in the LIC industry, Tsuda et al. fabricated "through-holed" LIB electrodes using a picosecond pulsed laser.[213] Later, Watanabe et al. reported the first successful application of JM Energy's prelithiation at the cell level method in a LIB cell.[214] They employed "through-holed" electrodes together with a sacrificial Li-donor electrode. The concept involved structuring the current collector and coating layer using laser processing to create unobstructed lithium-ion diffusion channels throughout the electrode. Their final approach resulted in an "opening rate" of 1% across the entire electrode surface; the electrode specific capacity remained effectively unchanged, while the electrode capacity density decreased compared to unstructured electrodes.[224] Thus, excluding prelithiation, this innovative electrode structuring approach cannot directly enhance cell energy density. However, recent research shows that laser structuring of electrodes can improve cell power density and is beneficial for fast-charging applications.[67]

Recently, VARTA Microbattery GmbH registered a patent for LIBs with enhanced energy density, which is achieved solely through a perforated current collector design.[225] Over the course of this study (2022 – 2026), perforated current collectors have become commercially available.[226]

In 2025, the electrochemical performance of graphite electrodes coated on a perforated copper current collector foil with a thickness of 9 µm and a hole diameter of 250 µm was reported in the literature for the first time, to the best of the author's knowledge.[227] The lab-scale coating procedure involved placing the perforated current collector foil on a flat glass plate covered with a polytetrafluoroethylene (PTFE) film and using alcohol to temporarily adhere the foil to the glass surface. Both sides of the perforated copper foil were consecutively coated and dried in this

manner. Graphite‖LFP bi-layer pouch cells incorporating the perforated current collector system in the anode exhibited improved specific capacity, cycling stability, and lower impedance.[227]

These initial results of perforated current collectors in LIBs suggest that they may offer advantages beyond simply enhancing the electrodes' specific capacity. However, this data should be interpreted with caution, as there is currently no independent confirmation of it, to the best of the author's knowledge. From a theoretical standpoint, changes in cycle life and impedance are not entirely unexpected since a perforated current collector design may affect the final microstructure of the electrode.

Anticipation at the Cell Level

Moreover, using perforated current collectors results in lithium-ion permeable electrodes, which allow "communication" (or, more technically, "interaction") between parallel electrode layers across the entire LIB system. In other words, lithium-ion movement is no longer confined to the space between the facing anode and cathode layers.[215] The implementation of perforated current collectors could enable a "smart" electrode stack, in which lithium ions distribute to the thermodynamically most stable active sites during battery operation. This could enhance the safety, rate performance, and cycle life of LIBs. The initial LIB performance data of graphite electrodes with a perforated current collector system, as reported by Zou et al.[227] (described above), would be consistent with this theory.

Moreover, the ability of lithium ions to migrate through an entire electrode stack enables an innovative prelithiation strategy at the cell level.[214,215]

As explained in **Chapter 2.3** (page 23), during initial cell charging, active lithium is irreversibly consumed in forming the anodic SEI[87,88] due to the electrochemical decomposition of electrolyte components at potentials below 1 V vs. Li^+/Li.[85] This decomposition leads to the formation of a protective layer that impedes further electrolyte decomposition while remaining permeable to lithium ions.[86] The irreversible nature of these reactions consume active lithium supplied by the cathode AM, rendering it unavailable for reversible storage in subsequent cycles.[198] Especially, using anode AMs with relatively high ICLs, such as Si and SiCs, limits the reversible capacity of the resulting cells.[34,112]

As detailed in **Chapter 2.4** (page 26), prelithiation of LIBs offsets the impact of ICLs by providing additional active lithium sources for anodic SEI formation, which enables the full utilization of the cathode capacity for reversible energy storage afterwards. This enhances the specific energy and energy density of LIBs and may contribute to more efficient raw material utilization in resulting cells. Prelithiation approaches have been studied at every stage of LIB manufacturing, including the material, electrode, and cell levels (detailed in **Chapter 2.4.1** on page 28). However, the reactivity of intermediate products, difficulty controlling the degree of prelithiation, and lack of technology still limit its industrialization.[197–200]

Recent advancements in electrochemical prelithiation at the cell level demonstrate that this approach relies on two fundamental practical conditions: i) the lithium-ion permeability of the electrodes, and ii) the presence of a Li-donor electrode or source.[214,215] ICLs can be compensated by lithium ions from a Li-donor source within the fully assembled cell. Consequently, prelithiation concept at the cell level avoids the need to handle reactive intermediate products during manufacturing, as it is performed in the final stage of LIB production, either before or after cell formation. Very few studies have been published on applying this prelithiation strategy to LIBs.

In 2019, Watanabe et al. reported the first application of this approach in LIBs using "through-holed" electrodes, as described above.[214] In a pouch cell setup, they stacked three LFP electrodes (with an areal capacity of ~0.8 mAh cm^{-2} per side) with three graphite electrodes (with an areal capacity of ~0.8 mAh cm^{-2} per side) and a sacrificial Li-donor electrode. The electrode size was 3.5 × 2.5 cm, the total cell capacity was ~35 mAh. Laser structuring of the electrodes (with hole diameters of 20, 100, and 200 µm) made them permeable to lithium ions. ICLs could be compensated for by selecting appropriate prelithiation conditions, such as the charge amount, hole diameter, and lithium-ion balancing time.[214] Furthermore, it was shown that lithium-ion migration across the cell during the prelithiation treatment did not affect the quality of inactive interlayer cathodes.[222]

In 2020, Zensen published a comprehensive study on the same topic using expanded metals as current collectors that were double-sided coated simultaneously with a vertical coating laboratory device. The permeable nature of the expanded metals facilitated lithium-ion mobility through the electrodes. Zensen expanded on the concept of simple prelithiation by adding an extra active lithium reservoir to silicon anodes. An anodic Li-reservoir buffers ALL during cell operation and enhances the cell's cycle life. Prelithiated multilayer Si‖NMC622 demonstrator pouch cells (total cell capacity: ~0.5 Ah; cathode areal capacity: ~4 mAh cm^{-2} per side; anodic Li-reservoir: 20% SOC_{anode}) achieved over 250 cycles until end of life (EOL: usable cell capacity < 80% of initial capacity), whereas reference cells without prelithiation treatment reached EOL in fewer than 100 cycles. Additionally, Zensen reported and demonstrated the concept of a removable Li-donor source for the first time in a LIB pouch cell setup.[215]

Both, the "through-holed" electrode approach and the expanded metal current collector approach, demonstrate the feasibility of a novel and promising prelithiation strategy at the cell level.[214,215] However, the overall concept can only be adapted to LIB industry if the following three conditions are met: i) a lightweight, lithium-ion permeable current collector system must be available that can be directly processed using standard manufacturing equipment, ii) an appropriate Li-donor source and cell design must be engineered and iii) a fundamental understanding of the underlying prelithiation process and its impact on final cell performance must be achieved.

From Concept to Industrial Application: Remaining Challenges

From this point of view, perforating commercial current collector foils to enable the transition from closed to lithium-ion permeable electrodes represents a promising, incremental, drop-in technology. This technology can improve multiple key LIB performance indicators while supporting more efficient material utilization. It achieves this by reducing the proportion of inactive materials at the electrode level and fully exploiting the capacity of AMs through prelithiation at the cell level.

However, the lack of available data limits the assessment of the concept's overall feasibility in terms of lab- and pilot-scale manufacturing integration and its actual impact on LIB performance. Furthermore, a fundamental understanding of the controllability of the underlying prelithiation process and its impact on cell performance compared to reference cells is lacking. Therefore, in-depth research on electrode development and cell performance is essential to explore the role of perforated current collectors in LIBs and pave the way for their use in commercial cells.

4. Scope of this Thesis

This thesis explores the role of perforated current collectors and the concept of prelithiation at the cell level in LIBs, from theoretical concepts to experimental validation. Several aspects are of primary relevance, including slurry and electrode development at both laboratory and pilot-line scales, prelithiation treatment in single-layer and multi-layer pouch cells, and the electrochemical investigation of prelithiated cells relative to reference cells.

The electrode parameters and manufacturing processes in this work are set as close as possible to industrial standards. This allows the results to be applied to realistic industrial use scenarios as an incremental, drop-in technology. Additionally, electrochemical results, particularly those related to prelithiated cells, are presented in the clearest possible manner. The goal is to demonstrate, discuss, and ultimately understand the complete measurement profile and characteristics of cells differing only in their active lithium inventory size.

Throughout the thesis, only one perforation design is used and investigated. Furthermore, the design of the prototype cells for prelithiation at the cell level is kept as simple as possible and serves only for demonstration purposes. Optimizing the perforation design and other relevant topics, such as advanced engineering of the lithium donor electrode and cell design, is beyond the scope of this work.

5. Summary

The first chapter, ***Proof of Concept*** (**Chapter 6** on page 42), introduces the perforated current collector design used in this study and discusses its straightforward integration into standard, laboratory scale electrode manufacturing procedures. It begins with theoretical predictions of the benefits and limitations of the study's concept of perforated current collectors and prelithiation at the electrode and cell levels, considering different state-of-the-art AM chemistries (Graphite, SiC, LFP, and NMC), and ends with a practical demonstration in Graphite‖LFP single-layer pouch cells.

The second chapter, ***Prelithiation and Beyond*** (**Chapter 7** on page 71), provides a fundamental understanding of the management of a cell's active lithium inventory size and its impact on the cell's electrochemical performance. To this end, Graphite‖LFP single-layer pouch cells which differ only in their initial active lithium inventory size, are assembled and investigated. The chapter presents a qualitative and quantitative analysis to assess the size of a cell's active lithium inventory. Furthermore, it introduces and demonstrates a novel relithiation strategy at the cell level, allowing full reversible cathode capacity utilization for the prelithiated Graphite‖LFP cell's second life.

The third chapter, ***Scale Up*** (**Chapter 8** on page 106), demonstrates the scalability of electrode production using a perforated current collector system and standard pilot-line electrode manufacturing equipment. The impact of current collector substitution on cell performance is investigated using Graphite‖LFP bi-layer pouch cells. Lastly, the scalability and benefits of the overall concept of this study – perforated current collectors and relithiation – are demonstrated in stacked Graphite‖LFP pouch cells with a capacity of 180 mAh.

In the final chapter, ***Transfer to High Capacity SiC Anode Active Material*** (**Chapter 9** on page 145), the fundamental knowledge acquired throughout this work is applied to a more complex SiC‖LFP cell chemistry.

Results and Discussion

6. Proof of Concept

6.1 Perforation Design in This Study

Commercial state-of-the-art LIB current collector coils (copper foil: 10 µm thick, 150 mm width; aluminum foil: 15 µm thick, 150 mm width) were mechanically perforated by Bender GmbH-Siegen. The foil length in the coils was over 100 m.

The perforation design is shown **Figure 6.1**. It consists of round holes that are arranged in a hexagonal, staggered pattern along the entire length and width of the foil. The hole diameter is 1.0 mm, the horizontal hole distance from center to center is 1.9 mm, and the vertical hole distance from center to center is 3.4 mm. The perforation degree was determined to be 27.5% using optical microscopy and gravimetric analysis. Consequently, the perforation pattern reduces the mass and volume of the current collector's metal by 27.5%, compared to the unmodified foil.

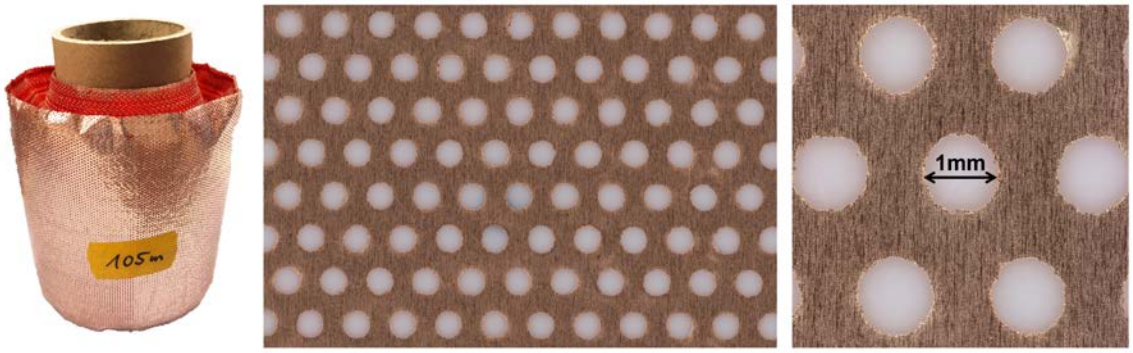

Figure 6.1 Photographs and microscopic images of the perforated current collector coil and foil.

The mechanical perforation process leaves burrs on the opposite side of the foil where the punch impacts. These burrs create thickness inhomogeneities of up to 30 µm on the foil surface. This negatively impacts the quality of the resulting electrode, particularly in the coating and calendering process (detailed in **Chapter 6.3** on page 53). Therefore, it is crucial to flatten the foil surface in advance for its use in LIB electrode applications.

Single sheets of perforated copper foil (approx. 30 cm in length) were flattened using a small tabletop calender with low line pressure (5 N mm^{-1}). This pretreatment yielded a homogeneous foil thickness of 10 µm. **Figure 6.2** shows microscopic images of single perforations in their initial and flattened states.

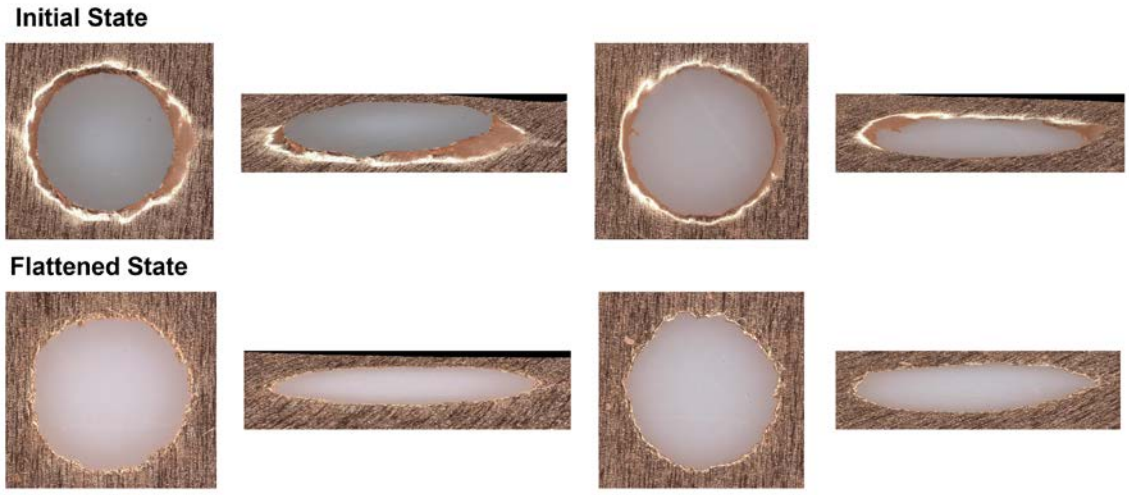

Figure 6.2 2D and 3D microscopic images of a single perforation in the copper current collector foil, shown from the front and back sides in both the initial and flattened states.

The same flattening process was applied to sheets of perforated aluminum foil (approx. 30 cm in length). A homogeneous foil thickness of 15 µm was achieved, identical to that of the pristine aluminum foil. **Figure 6.3** shows images of single holes under a microscope in their initial and flattened states.

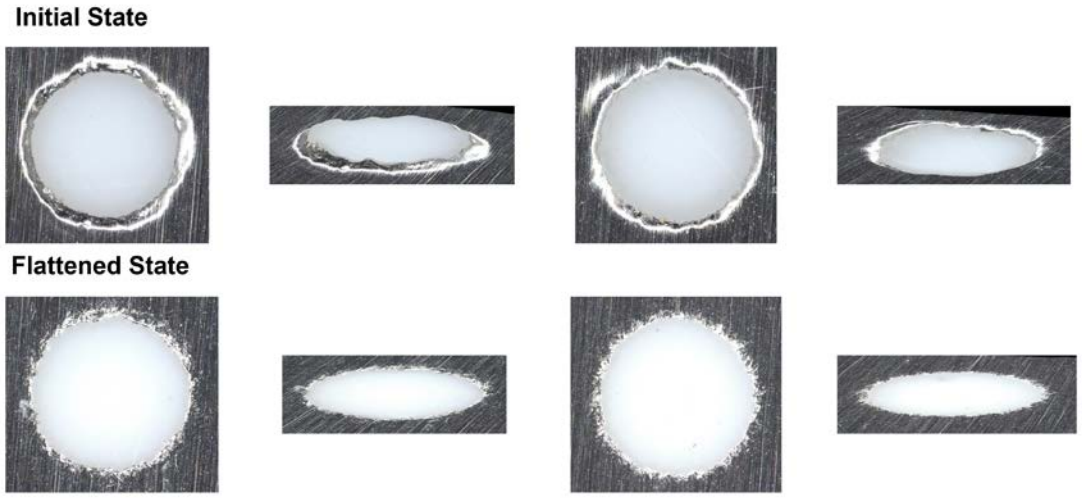

Figure 6.3 2D and 3D microscopic images of a single perforation in the aluminum current collector foil, shown from the front and back sides in both the initial and flattened states.

Considering the scaling up battery electrode manufacturing from the laboratory scale (10 – 100 cm) to the pilot line scale (10 – 500 m), the flattening process needs to be applied to longer lengths of perforated current collector foil.

The foil flattening pretreatment was scaled accordingly: the initial perforated current collector coil was manually unwound, flattened at low line pressure using a small tabletop calender, and then manually rewound onto a new core. **Figure 6.4** (left) visualizes this procedure. The result was a coil

of perforated copper current collector foil, 10 m long, with a flattened surface (**Figure 6.4**, center). As shown in **Figure 6.4** (right), the pretreated coil is well suited for roll-to-roll processing. The further processing of this coil is described in **Chapter 8.1.1** (page 110) in detail.

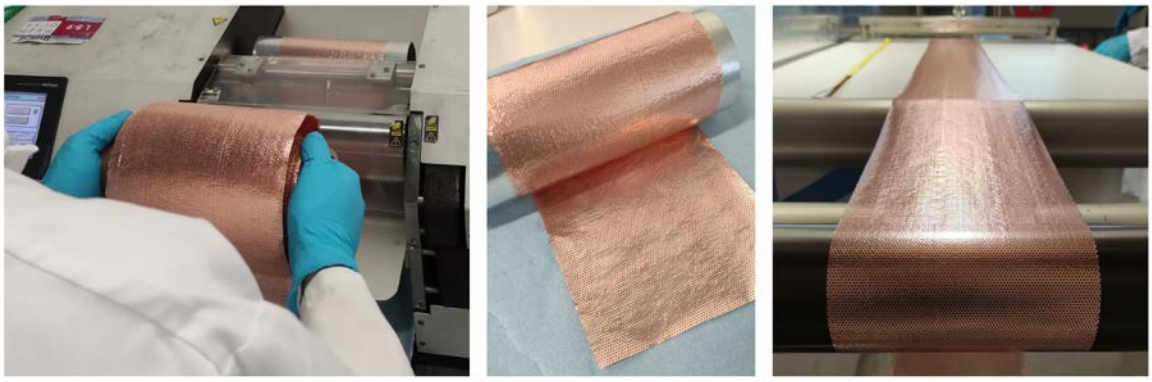

Figure 6.4 Photographs of the initial scale up of the foil flattening pretreatment process: process visualization (left), resulting coil of perforated current collector foil with a flattened surface (center), and subsequent roll-to-roll processing of the pretreated coil (right).

The same process was used to obtain a coil of a 10-meter-long perforated aluminum current collector foil with a flattened surface. The further processing of this coil is described in **Chapter 8.1.2** (page 117).

Of course, manually unwinding and rewinding foil coils is a time-consuming and delicate intermediate step. Often, it results in current collector coils that require additional pretreatment due to misaligned winding and uneven tension. In **Chapter 8** (page 106) the challenges associated with these manually preprocessed coils is discussed in detail. Most of these coil preparation issues can be effectively avoided by using a state-of-the-art pilot line calender equipped with edge and tension control, as shown in **Figure 6.5**. The automatic roll-to-roll flattening pretreatment yielded a 40-meter-long coil of perforated aluminum current collector foil with a flattened surface. This high-quality, perforated current collector coil is suitable for direct use with state-of-the-art roll-to-roll battery electrode manufacturing equipment. However, it was not used further in this study and serves only as proof of feasibility for industrial application.

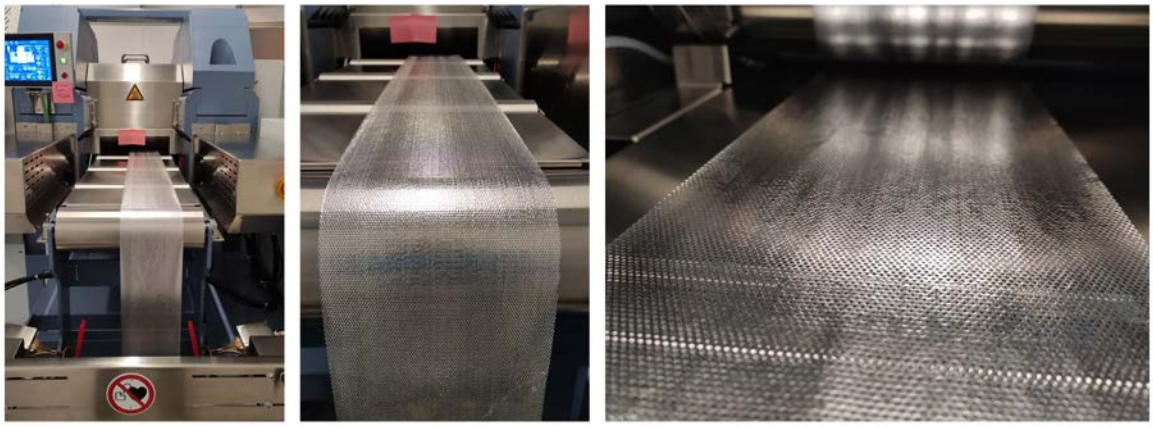

Figure 6.5 Photographs of the advanced scale-up of the foil-flattening pretreatment process using the ZSW roll-to-roll pilot-line calender with edge and tension control.

6.2 Predicted Effects at the Electrode and at the Cell Level

The current collector perforation design used in this study reduces the metal mass and volume by 27.5% compared to unmodified foils. Theoretical calculations are employed to quantify advantages and limitations of this current collector design across various LIB electrode and cell chemistries.

The following calculations at the electrode level consider double-sided coated electrodes, while neglecting the current collector tab size and mass, as illustrated in **Figure 6.6**. The material and electrode parameters selected for each electrode chemistry are summarized in the **Chapter 14.1** (page 175).

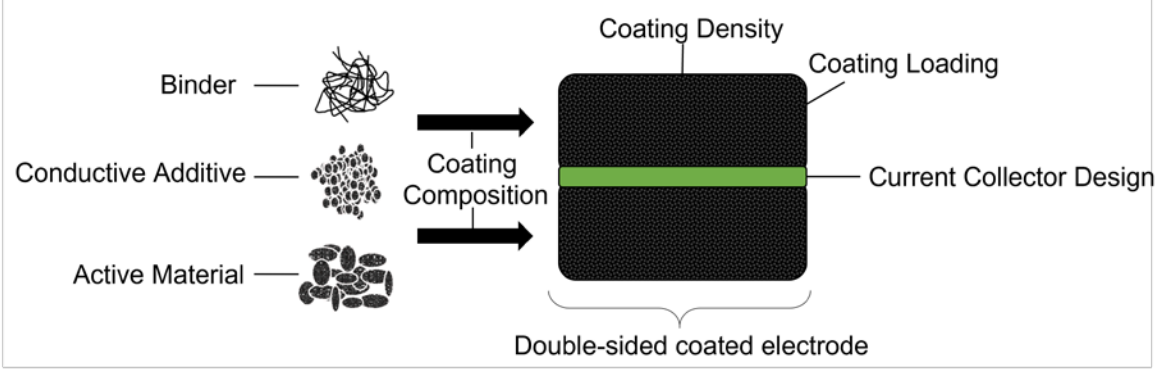

Figure 6.6 Illustration of a double-sided coated electrode used to calculate specific and volumetric capacity values at the electrode level.

Figure 6.7 and **Figure 6.8** quantify the impact of coating loading on the specific and volumetric capacities at the electrode level for various cathode and anode chemistries, respectively. In addition to standard current collectors (black lines), the calculations also include perforated current collectors (blue lines) within the electrodes.

In general, the specific and volumetric capacity of electrodes increases with increasing coating loading. These improvements are achieved by maximizing the fraction of AM while minimizing the mass and volume fraction of the current collector within the electrodes. The contribution of the current collector to the electrode overall mass and volume is significant for low-loading electrodes and becomes negligible for high-loading ones.

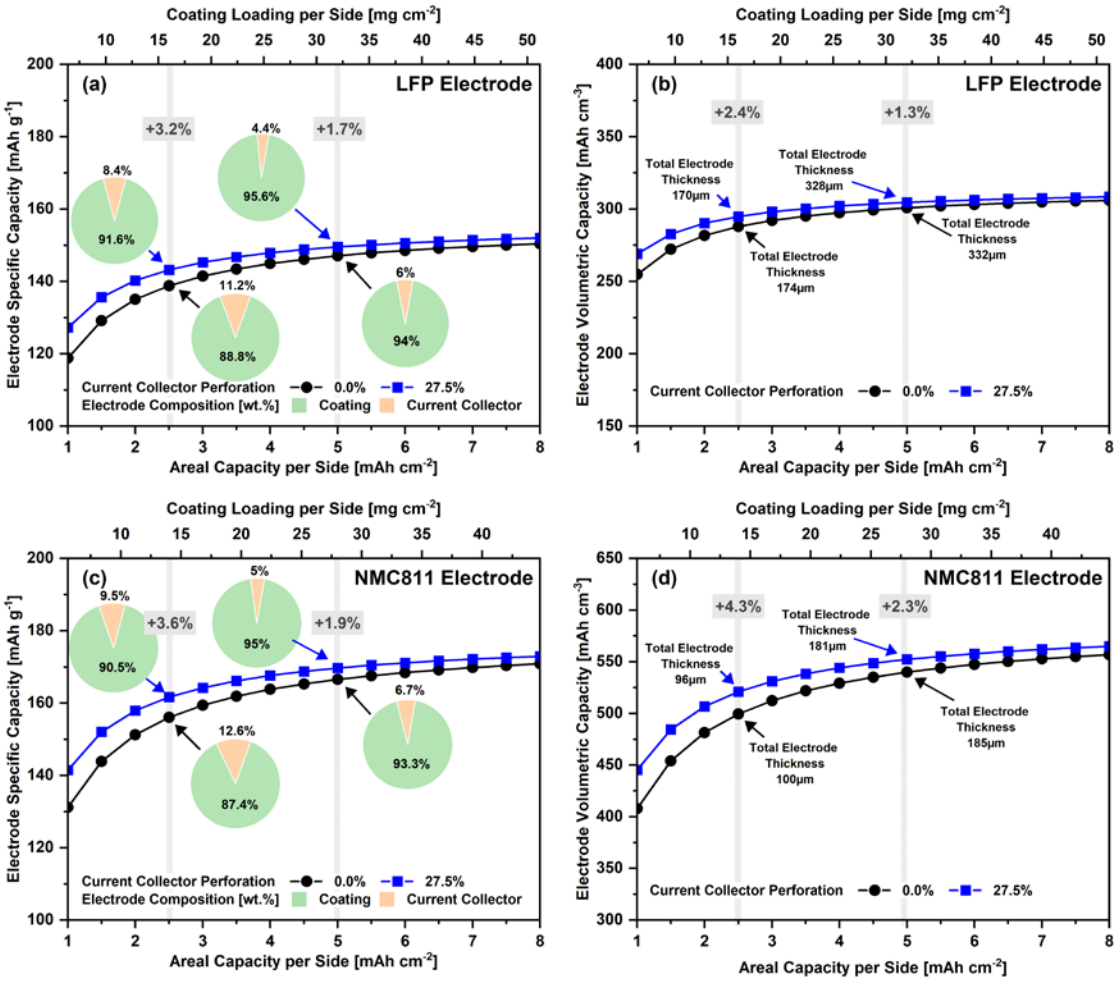

Figure 6.7 Calculated specific and volumetric capacity as a function of areal capacity per side of double-sided coated a, b) LFP and c, d) NMC811 electrodes. The black and blue lines represent electrodes with standard and perforated current collectors, respectively.

Figure 6.7 (black lines) shows the specific and volumetric capacities as a function of areal capacity per side of LFP and NMC electrodes. An increase in the coating loading up to 28 – 32 mg cm^{-2} (~5 mAh cm^{-2}) on each side of the current collector leads to a significant increase of the electrode's specific and volumetric capacity values. These improvements are achieved by minimizing the fraction of current collector mass and volume within the electrodes. For double-sided coated LFP electrodes, the current collector mass corresponds to 11 wt.% of the total electrode mass at an areal capacity of 2.5 mAh cm^{-2} per side, and only to 6 wt.% at a higher areal capacity of 5 mAh cm^{-2} per side. Similar trends are observed for NMC811 electrodes. Besides the practical constraints of thick electrodes,[219] boosting the cathode loadings further leads to a plateau-like behavior in electrode specific and volumetric capacities, providing no more significant improvements after a certain point.

As shown in **Figure 6.8**, the increase in electrode specific and volumetric capacity with higher coating loadings is even more drastic for anode AMs. This is due to the higher specific capacity of

the anode AMs (372 mAh g^{-1} for graphite and 1550 mAh g^{-1} for the SiC composite) compared to that of the cathode AMs (170 mAh g^{-1} for LFP and 190 mAh g^{-1} NMC811): lower loadings are required to achieve the same areal capacity values. In addition, the contribution of the current collector to the overall electrode mass and volume is more pronounced in anodes because copper is denser than aluminum. Copper has a density of 8.96 g cm^{-3}, while aluminum has a density of 2.70 g cm^{-3}.

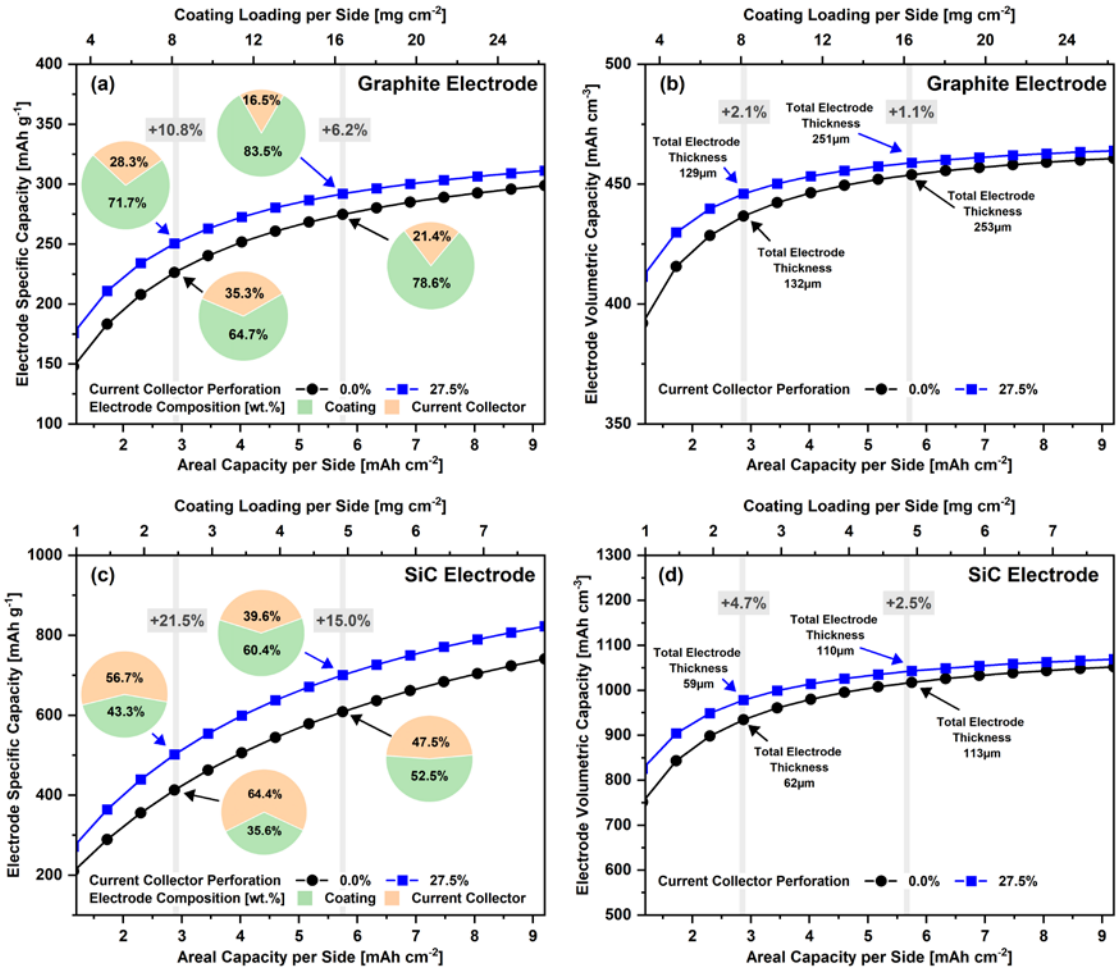

Figure 6.8 Calculated specific and volumetric capacity as a function of areal capacity per side of double-sided coated a, b) graphite and c, d) SiC electrodes. The black and blue lines represent electrodes with standard and perforated current collectors, respectively.

For double-sided coated graphite electrodes, the current collector mass corresponds to 35 wt.% of the total electrode mass at an areal capacity of 2.9 mAh cm^{-2} per side, and to 21 wt.% at a higher areal capacity of 5.8 mAh cm^{-2} per side (**Figure 6.8a**). Even more pronounced trends are observed for SiC electrodes, as shown in **Figure 6.8c**.

Replacing the standard current collector foil with a perforated one reduces the overall mass of the foil in the electrode and at the same time provides additional volume for the coating layer within the holes, all without changing the coating loading.

Figure 6.7 and **Figure 6.8** quantify the effect of current collector substitution on the electrode's specific and volumetric capacities. On the cathode side, an increase of 3% to 4% in the specific capacity of the electrode is expected, considering an areal capacity of 2.5 mAh cm^{-2} (**Figure 6.7**). Even more significant enhancements are evident on the anode side **(Figure 6.8**). Namely, an increase of 11% and 22% is calculated for graphite and SiC AMs, respectively, when considering an areal capacity of 2.9 mAh cm^{-2} per side. The improvements on the electrode volumetric capacity are less pronounced across all electrode chemistries.

Based on these findings, the calculations were extended to assess the advantages and limitations of the perforated current collector design on the specific energy (Wh kg^{-1}) and the energy density (Wh L^{-1}) across different anode‖cathode LIB cell chemistries. The smallest cell-unit was used as the basis for these calculations, as illustrated in **Figure 6.9**.

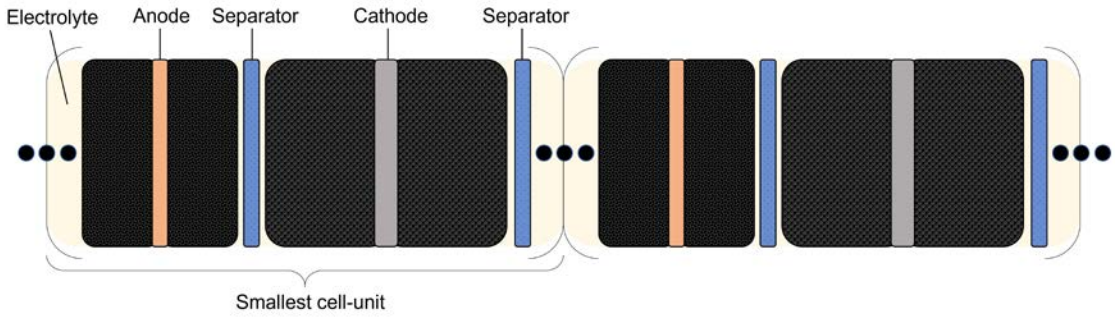

Figure 6.9 Illustration of a LIB cell-unit used to calculate specific energy and energy density values at the cell level.

The smallest cell-unit consists of a double-sided coated anode, a double-sided coated cathode, two separators, and electrolyte. It is stackable and can be used to predict the energy characteristics of unknown LIB cell formats by excluding the cell housing, tab design, and anode edge overhang. The N/P-ratio was set at 1.15 for all anode‖cathode chemistries, and the electrolyte volume was adjusted to equal the total free pore volumes of the anode, cathode, and separators. The material and electrode parameters selected are summarized in **Chapter 14.1** (page 175).

Figure 6.10 shows the specific energy as a function of cathode areal capacity per side of different cell chemistries. The substitution of standard current collector foils (black lines) with perforated ones (blue lines) within both electrodes results in an 4.5% – 6.5% increase of specific energy for all cell chemistries under investigation, when considering a cathode areal capacity of 2.5 mAh cm^{-2} per side.

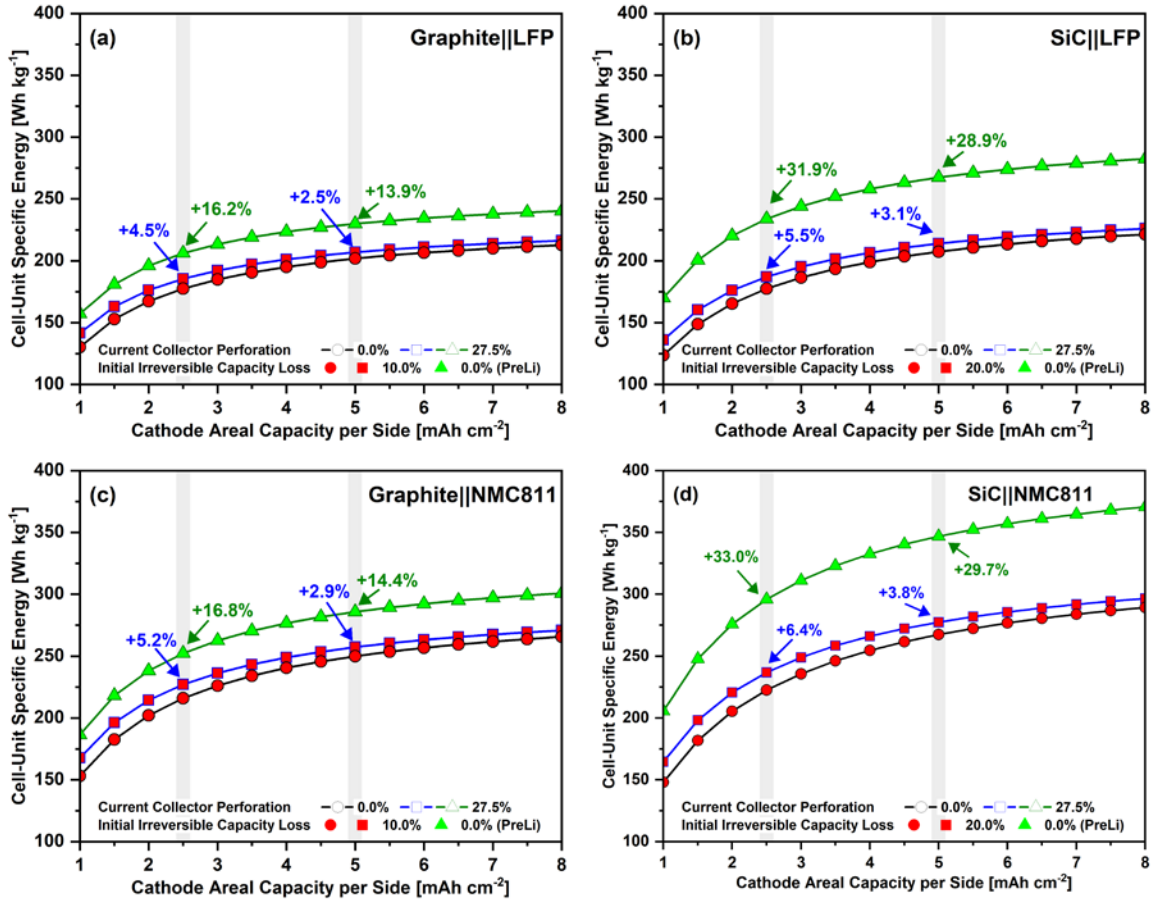

Figure 6.10 Calculated specific energy as a function of cathode areal capacity per side of a) Graphite‖LFP, b) SiC‖LFP, c) Graphite‖NMC811, and d) SiC‖NMC811 cell-units.

As noted in the theoretical background and introduction of this thesis, the use of perforated current collectors results in electrodes permeable to lithium ions, which enable a prelithiation strategy at the cell level (illustrated in **Figure 6.11**).[213–215] Prelithiation offsets anodic ICLs. From an industrial design perspective, the additional lithium source should either be removable or carefully designed so that no excess lithium or inactive components remain in the cell after the process is complete. Accordingly, the weight and volume of the extra lithium source are excluded in the calculations presented here.

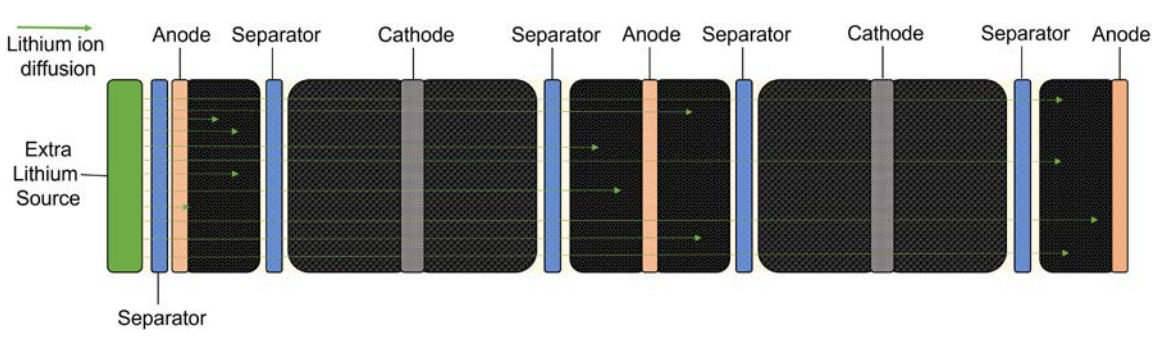

Figure 6.11 Illustration of the LIB prelithiation approach at the cell level. This approach requires lithium-ion permeable electrodes and an extra Li-donor source.

Figure 6.10 also quantifies specific energy values of prelithiated cells (green line). Significant improvements in energy density across all cell chemistries can be seen. Specifically, combination of perforated current collectors and prelithiation increase the specific energy of graphite‖cathode and SiC‖cathode cell chemistries by 16% – 17% and 32% – 33%, respectively, when considering a cathode areal capacity of 2.5 mAh cm^{-2} per side.

Figure 6.12 allows a direct comparison of the different cell chemistries considering a cathode areal capacity of 2.5 mAh cm^{-2} per side. Interestingly, when excluding data of prelithiated cells, the cathode chemistry seems to primarily determine the overall cell energy, regardless of the anode chemistry involved (175 – 190 Wh kg^{-1} for anode‖LFP and 215 – 240 Wh kg^{-1} for anode‖NMC). This is partly due to the different working potentials of the cathode and anode chemistries, but predominantly due to the different ICLs associated with each anode chemistry. Thus, the calculations presented here highlight the well-known practical limitations of high silicon content in LIB anodes. Prelithiation of the cells buffers this negative effect, allowing cells with silicon anodes to achieve significant higher energy than those with graphite anodes.

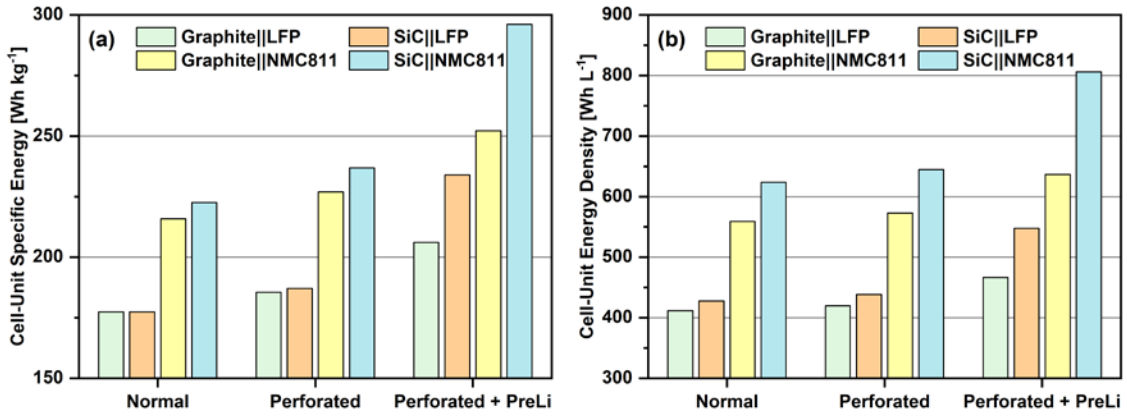

Figure 6.12 Calculated a) specific energy and b) energy density of different anode‖cathode cell-units, assuming a cathode areal capacity of 2.5 mAh cm^{-2} per side.

From this theoretical perspective, perforated current collectors and prelithiation treatment could achieve high energy densities for next-generation LIBs as summarized in **Table 6.1**.

Table 6.1 Comparison of the maximum anticipated specific energy and energy density of LIB chemistries of this study with state-of-the-art (2020) and target (2030) values for automotive applications, as reported by Armand et al. (2020)[34].

Cell Level (Targets)[34]	Specific Energy [Wh kg^{-1}]	Energy Density [Wh L^{-1}]
2020	**160-260**	**450-730**
2030	**275-320**	**750-900**
Cell Unit (Standard)[This study]		
Graphite‖LFP	**177**	**411**
SiC‖LFP	**177**	**428**
Graphite‖MC811	**215**	**559**
SiC‖NMC811	**223**	**624**
Cell-Unit (Prelithiated)[This study] (The extra lithium source is assumed to be removed in the operating cell)		
Graphite‖LFP	**206**	**466**
SiC‖LFP	**234**	**548**
Graphite‖MC811	**252**	**637**
SiC‖NMC811	**296**	**806**

Of course, the expected performance indicators of the overall concept are promising. However, its practical implementation has still to be demonstrated.

6.3 Initial Lab Scale Electrode Development

6.3.1 Initial graphite electrode development

A standard graphite electrode formulation of AM:CB:CMC:SBR – 94:2:2:2 was chosen. **Figure 6.13** provides a schematic overview of the processing steps and instruments used to coat graphite electrodes.

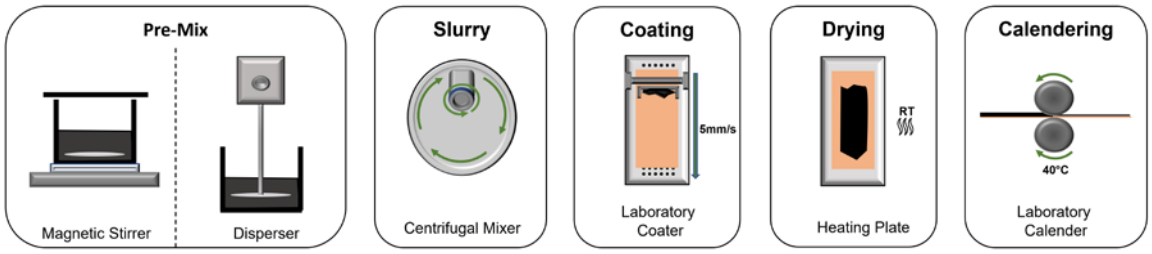

Figure 6.13 Schematic overview of the processing steps and instruments used to manufacture graphite electrodes.

Initially, the pre-mix (Water:CB:CMC – 96:2:2) was prepared using a magnetic stirrer. In general, pre-mix preparation ensures complete binder dissolution and the formation of a homogeneous dispersion of deagglomerated CAs. Only binders that remain stable under higher shear rates should be included in the pre-mix. SBR, which is shear sensitive, is therefore added in the final step of slurry preparation under more gentle mixing conditions.

Rheological measurements in **Figure 6.14** show that mixing time with a magnetic stirrer significantly affects the viscosity of the pre-mix. Mixing for one day results in a higher viscosity (27.1 Pa s at 1 s^{-1}), whereas mixing for three days reduces the viscosity substantially (0.8 Pa s at 1 s^{-1}). These differences in pre-mix viscosity also impact the final slurry viscosity (59.1 Pa s for the high-viscosity pre-mix and 3.5 Pa s for the low-viscosity pre-mix at 1 s^{-1}), despite an identical slurry formulation and total solid content (TSC) of 45 wt.%.

Regardless of the final viscosity, both slurries demonstrate stable coating performance when applied to standard copper current collector foil (**Figure 6.14**). However, on perforated substrates, slurry viscosity is a more critical factor: only the high-viscosity slurry produced stable wet and dry coating layers.

As shown in **Figure 6.14**,the low-viscosity slurry either form droplets or simply seep through the perforations instead of covering them. On the one hand, it seems to be too fluid. On the other hand, its surface tension appears too high to form a stable wet film layer capable of handling multiple 1 mm holes on the substrate's surface. Consequently, the wet film layer coalesces into several drops on the perforated substrate's surface. In contrast the high-viscosity slurry forms a stable wet film layer which is capable of covering the perforations of the substrate's surface without to contract into droplets. Moreover, the coating layer of the high-viscosity slurry remains stable even

after drying. The resulting graphite coating on the perforated current collector foil exhibits good mechanical stability and it can be wound around a cylinder of ~10 mm diameter without mechanical failure, as also shown in **Figure 6.14**.

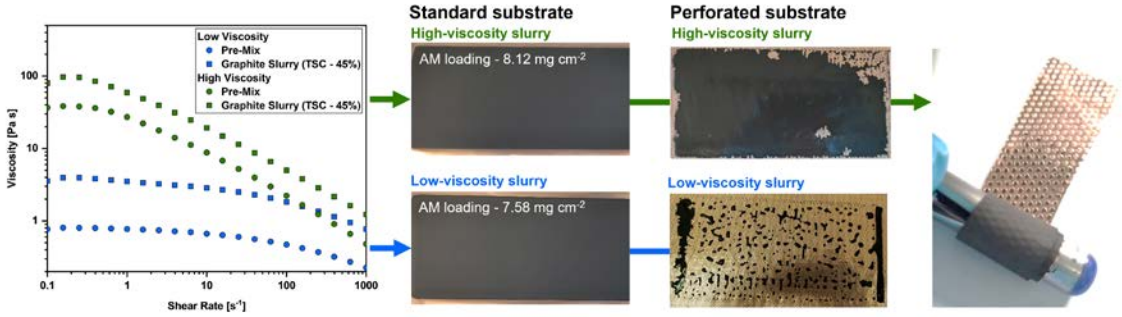

Figure 6.14 Rheological flow curves of the pre-mix and graphite slurries, together with images of their coating process on standard and perforated current collector foils, and a photograph of a single-sided coated graphite electrode with a perforated current collector wound around a cylinder of ~10 mm diameter.

Figure 6.15 shows microscopic images of the dried coatings on perforated current collector foil in their initial (0.9 g cm^{-3}) and calendered (1.4 g cm^{-3}) states. It is important to note that the current collector foils have not been flattened in advance at this initial stage of the work. The top view images of the front and back in the initial state of the coating indicate a homogeneous layer with only the holes filled. However, the 3D side view recording clearly shows the copper burrs on the backside of the current collector and reveals that the coating layer has significantly infiltrated through the perforations. Calendering the coating produces a distinct segmentation of hole and land regions on the coating surface, as visible in the corresponding top view images shown in **Figure 6.15**.

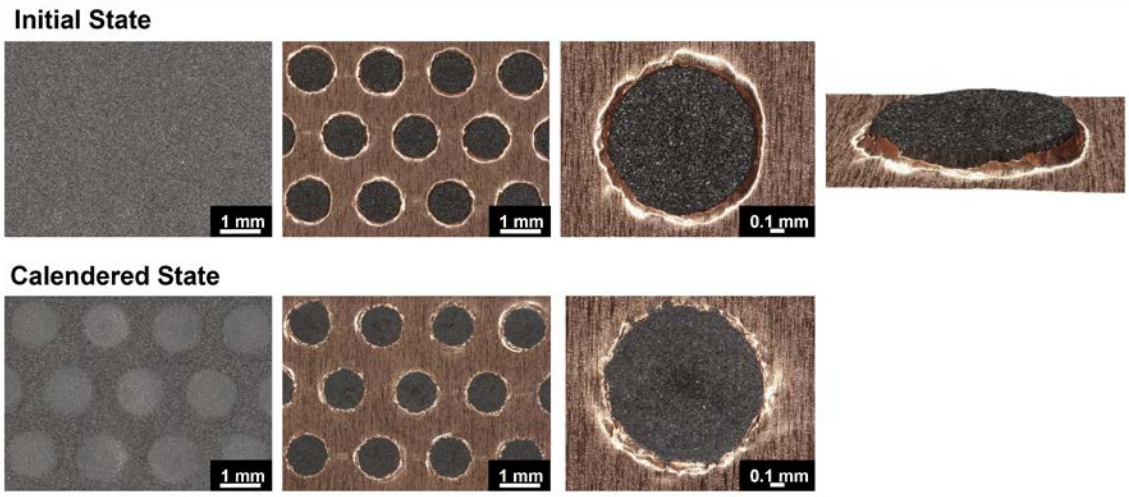

Figure 6.15 2D and 3D microscopic images of a graphite coating on a perforated copper current collector foil in the initial and calendered states.

The pronounced segmentation between the hole and land regions can be attributed to differences in the degree of coating densification. This unusual phenomenon is attributed to the novel design of the current collector and the coating technique employed, as schematically illustrated in **Figure 6.16**.

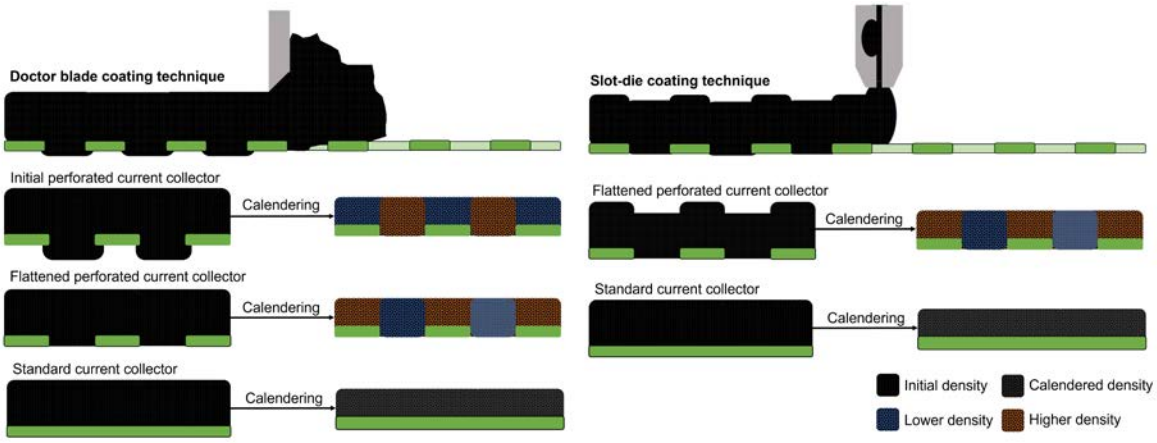

Figure 6.16 Illustration of the formation of distinct coating loading and density segments, depending on the current collector design and applied coating technique.

During the doctor blade coating process, a defined coating gap is used to apply electrode slurry on the surface of the current collector. This typically results in a uniform, homogeneous coating layer. The amount of slurry per unit area, which determines the coating loading, can be controlled by adjusting the coating gap.

However, when this process is applied to perforated current collectors, the outcome changes significantly, as illustrated in **Figure 6.16**. Due to the presence of perforations, the surface of the substrate is no longer uniform. During coating, additional slurry can be pushed downwards into the holes. This results in different coating loadings in the hole and land regions. Consequently, calendering these electrodes to a defined thickness results in a visible segmentation of regions with varying coating densification, particularly when loading variations are significant.

As can be seen in the microscopic image in **Figure 6.15**, the coating overhang on the back of the electrode appears to be intensified by the copper burrs around the perforations. These burrs likely enhance capillary forces, thereby exacerbating the undesired effect of loading inhomogeneity. To minimize these effects, it is essential to flatten the current collector foil and fine-tune the slurry viscosity.

Interestingly, from a purely theoretical standpoint, eliminating coating overhang on the backside of the electrode would reverse the previously described densification effect, resulting in a denser coating layer in the land regions than in the hole regions. If an optimized electrode slurry is used and burrs are removed, thus eliminating the coating overhang, the amount of additional slurry entering the holes would be negligible. In this case, uniform coating loading across the entire electrode surface can be expected. During calendering, the land areas offer less available volume

for the coating layer, as they are constrained by the presence of the current collector foil. Consequently, the coating in the land regions becomes minimally denser than in the hole regions, as also illustrated in **Figure 6.16**.

In practice, the second scenario can be fully achieved using the slot-die coating technique, where a precisely controlled slurry flow ensures uniform coating loading across the entire substrate surface, regardless of the substrate design.

Electrodes with a coating that varies in density across the electrode could be an interesting approach for high-power applications. However, this coating structure was only an initial, unexpected finding in this work. In fact, such density variations are highly unusual in LIB electrodes, and the goal of this study is not to create or investigate controlled density gradients within LIB electrodes. Therefore, this coating feature on perforated current collectors was minimized and not systematically studied.

The here presented initial data revealed that slurry viscosity and substrate surface properties are critical for obtaining good quality coatings on perforated foils. Therefore, only flattened perforated current collector foils are used from now on. The flattening process is described in **Chapter 6.1** (page 42). The next crucial milestones are ensuring the reproducibility of the electrode slurry and achieving precise control of its viscosity.

The mixing device used for preparing the pre-mix solution was changed from a magnetic stirrer to a disperser with a cowles blade, as illustrated in **Figure 6.13**.

Two pre-mix formulations were tested: Water:CMC:CB – 96:2:2 and Water:CMC:CB – 97:1.5:1.5. Rheological measurements in **Figure 6.17a** show that the more concentrated pre-mix has a higher viscosity (163 Pa s at 1 s^{-1}) than the less concentrated one (38 Pa s at 1 s^{-1}). Using the two pre-mixes as a starting point, graphite slurries with a TSC of 40% were prepared. Rheological measurements in **Figure 6.17a** demonstrate that the final slurry viscosity is highly reproducible (85 – 95 Pa s at 1 s^{-1}) and is determined solely by the slurry formulation and TSC. The pre-mix processing parameters or composition no longer influences the final slurry viscosity.

Next, two slurry batches were prepared for each TSC (37.5%, 40.0%, and 42.5%), resulting in a total of six graphite slurries. Rheological measurements in **Figure 6.17b** and **c** demonstrate that the slurry preparation process is highly reproducible, as data from batches of the same formulation show excellent agreement. These tests also show that slurry viscosity can be precisely adjusted by varying the TSC while keeping the electrode formulation and materials constant.

One slurry from each batch was coated onto standard copper current collector foils using the doctor blade technique at three different wet thicknesses: 240 µm, 280 µm, and 320 µm. A linear relationship between coating wet thickness and areal capacity was observed and quantified for each slurry TSC (**Figure 6.17d**).

Finally, the graphite slurry, with a TSC of 40%, was coated onto both standard and perforated copper current collectors at the specified wet thickness of 260 µm to produce graphite coatings with an areal capacity of 3.0 mAh g^{-1}. The electrodes were calendered to a coating density of 1.4 g cm^{-3} and cut into pouch cell format.

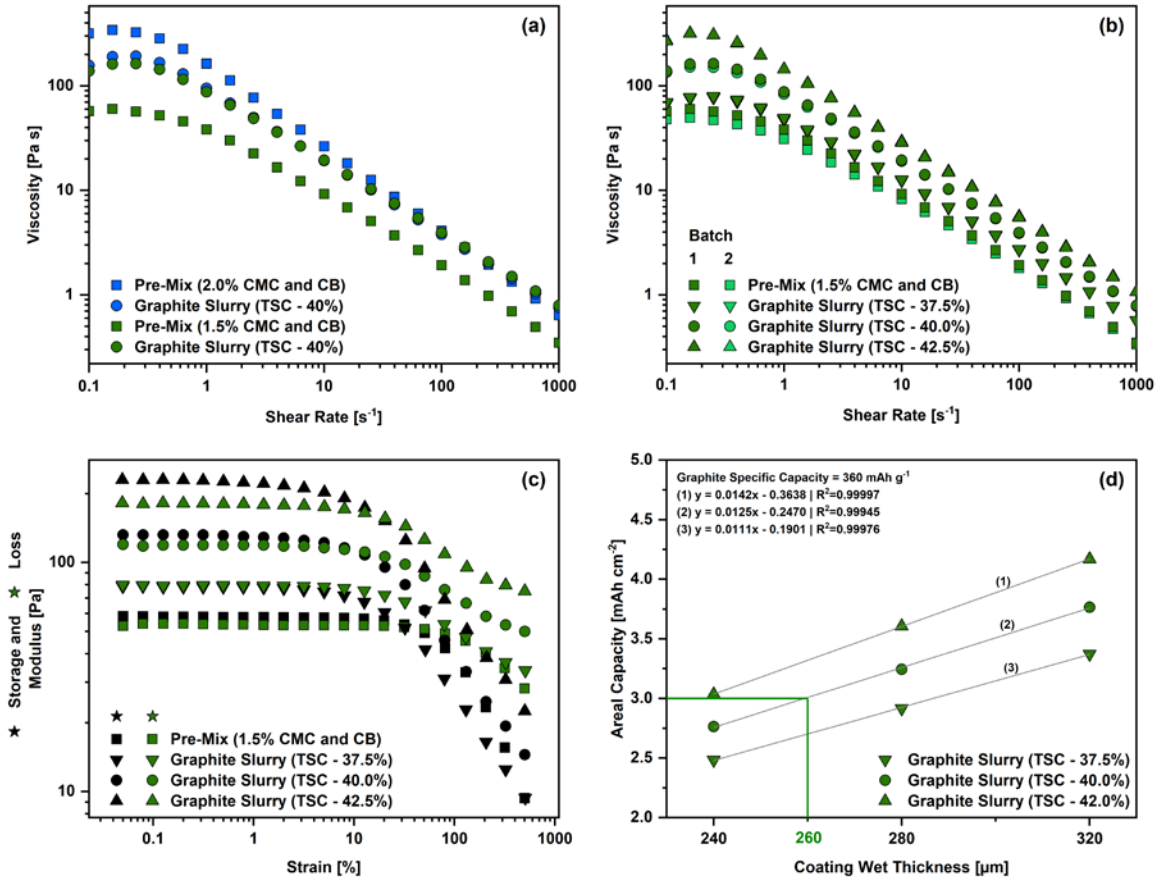

Figure 6.17 Graphite slurry and electrode properties: a, b) Rheological flow curves and c) amplitude sweep of different pre-mix and graphite slurries. d) Linear relationship between coating wet thickness and areal capacity for all slurries.

Figure 6.18 shows, that graphite electrodes with a homogeneous and uniform-looking coating were obtained. Areal capacities of 3.0 mAh cm^{-2} were obtained for coatings on standard current collectors. In contrast, coatings on perforated current collectors exhibited more variable values (2.8 – 3.2 mAh cm^{-2}). Notably, in the calendered state, the segmentation between the hole and land regions on the electrode surface is less pronounced compared to the initial coatings shown in **Figure 6.15** (page 54).

The as-prepared graphite electrodes were deemed sufficient for initial testing in demonstrator pouch cells (see **Chapter 6.4** on page 62).

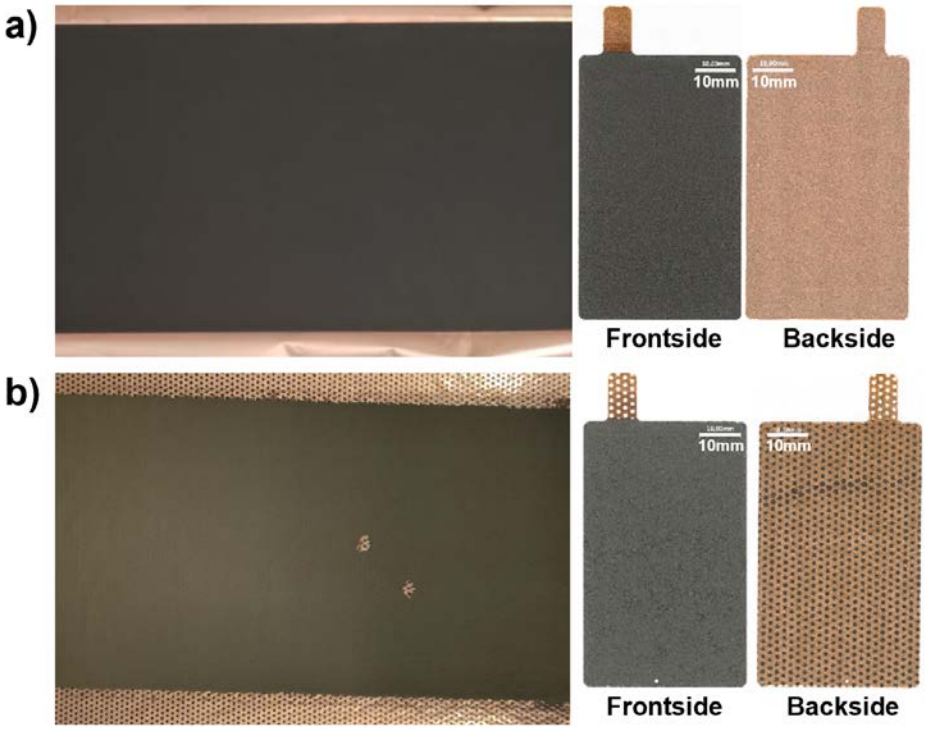

Figure 6.18 Photographs and microscopic images of a graphite coating and cut pouch electrodes with a) standard and b) perforated current collector foils.

6.3.2 Initial LFP electrode development

A LFP electrode formulation of AM:CB:Graphite:PVDF - 92:2:2:4 was chosen. **Figure 6.19** provides a schematic overview of the processing steps and instruments.

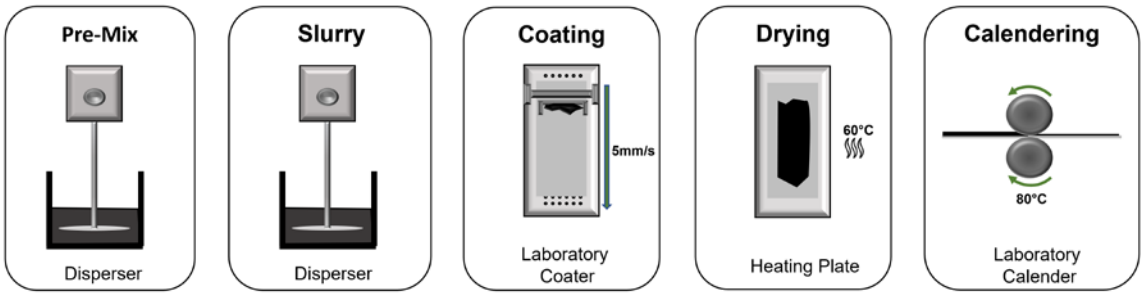

Figure 6.19 Schematic overview of the processing steps and instruments used to manufacture LFP electrodes.

Similar to the previously described graphite anode slurry development, two pre-mix solutions with different binder concentrations (4 wt.% PVDF and 5 wt.% PVDF) were tested to ensure that the final slurry viscosity depends only on its formulation and materials, and not on the pre-mix preparation process. The ratio of PVDF:CB:Graphite – 2:1:1 was kept constant in both pre-mix solutions, and each pre-mix was used to prepare one batch of LFP slurry with a TSC of 45%. Recorded flow curves in **Figure 6.20a** show that the more concentrated pre-mix has a higher viscosity (13.4 Pa s at 1 s^{-1}) than the less concentrated one (5.4 Pa s at 1 s^{-1}). Moreover, the data confirm that the final LFP slurry viscosity (53 Pa s at 1 s^{-1}) is independent of the initial pre-mix binder concentration. Overall, data of **Figure 6.20a – c** demonstrate the high reproducibility of both the pre-mix and LFP slurry preparation procedure.

One LFP slurry was coated at three different coating gaps (300 µm, 350 µm, and 400 µm) *via* doctor blade coating technique onto standard aluminum current collectors. The linear relationship between coating gap and areal capacity was quantified, as shown in **Figure 6.20d**.

Finally, the LFP slurry was coated onto both standard and perforated aluminum current collectors at the specified wet thickness of 385 µm to produce LFP coatings with an areal capacity of 2.6 mAh g^{-1} (18.1 mg cm^{-2}). The electrodes were calendered to a coating density of 2.0 g cm^{-3} and cut into pouch cell format.

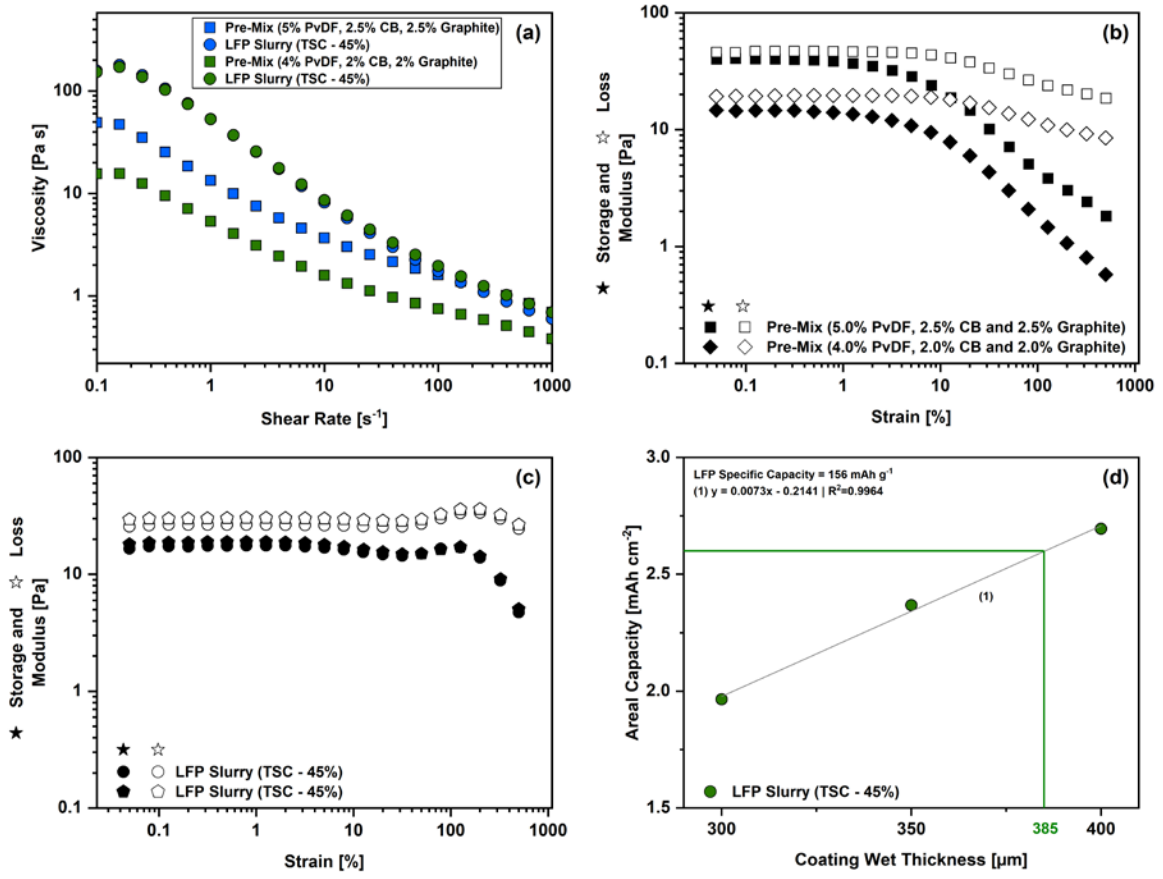

Figure 6.20 LFP slurry and electrode properties: a, b) Rheological flow curves and c) amplitude sweep of different pre-mix and LFP slurries. d) Linear relationship between coating wet thickness and areal capacity for all slurries.

Photographs and microscopic images of LFP coatings on standard and perforated current collectors are shown in **Figure 6.21**. While coatings on standard foils exhibited the target areal capacity of 2.6 mAh cm^{-2}, coatings on perforated foils showed significant higher values (2.9 – 3.0 mAh cm^{-2}). Also, a visible segmentation between hole and land regions on the electrode surface is pronounced again in microscopic images. Moreover, large parts of the electrode's backside are covered by an inhomogeneous coating layer. This coating defect indicates loading and density inhomogeneities across the electrode. Furthermore, the electrochemical activity of the AM in this layer is expected to negatively impact the performance of the electrode, as it is directly connected to increased lithium-ion diffusion pathways.

In summary, the initial LFP electrode development presented here suggests that NMP-based slurries are more challenging to handle when coating perforated current collectors. In addition to slurry viscosity, and substrate surface quality, drying time is identified as another key factor influencing the coating quality on the novel current collector design. Consequently, the LFP slurry needed to be further optimized, by switching to an alternative water-based formulation, to prevent coating defects on the electrode's backside (see **Chapter 7.2** on page 91).

Nevertheless, the as-prepared, non-optimized, NMP-based LFP electrodes presented here, were deemed sufficient for initial electrochemical testing in demonstrator pouch cells, as discussed in the following chapter.

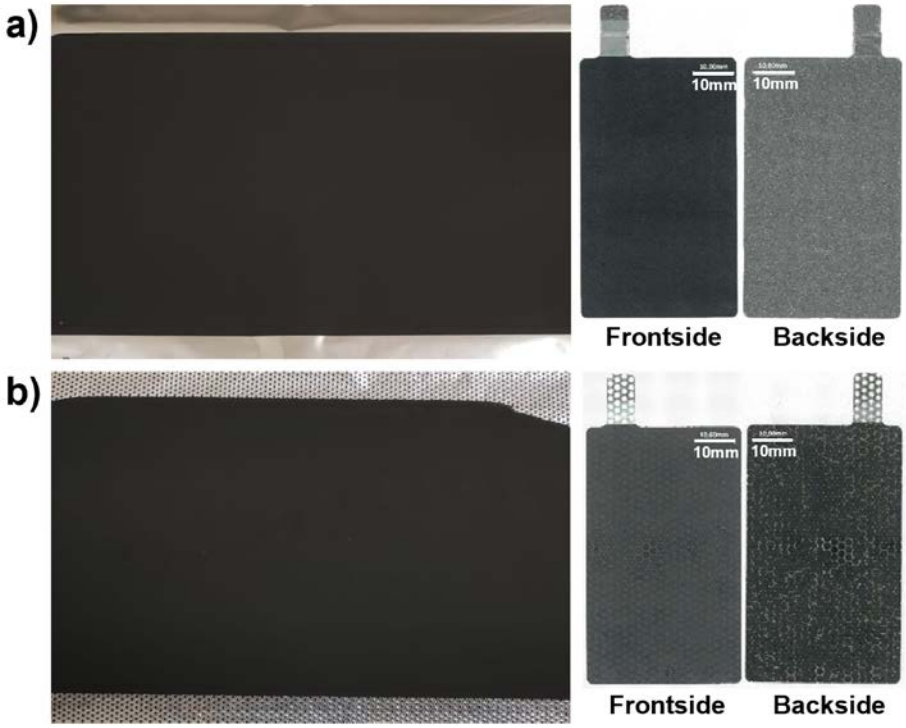

Figure 6.21 Photographs and microscopic images of a LFP coating and stamped pouch electrodes with a) standard and b) perforated current collector foils.

6.4 Single-Layer Demonstrator Pouch Cells

Graphite‖LFP single-layer electrode stacks were prepared, using various combinations of electrodes and current collectors, as illustrated in **Figure 6.22**.

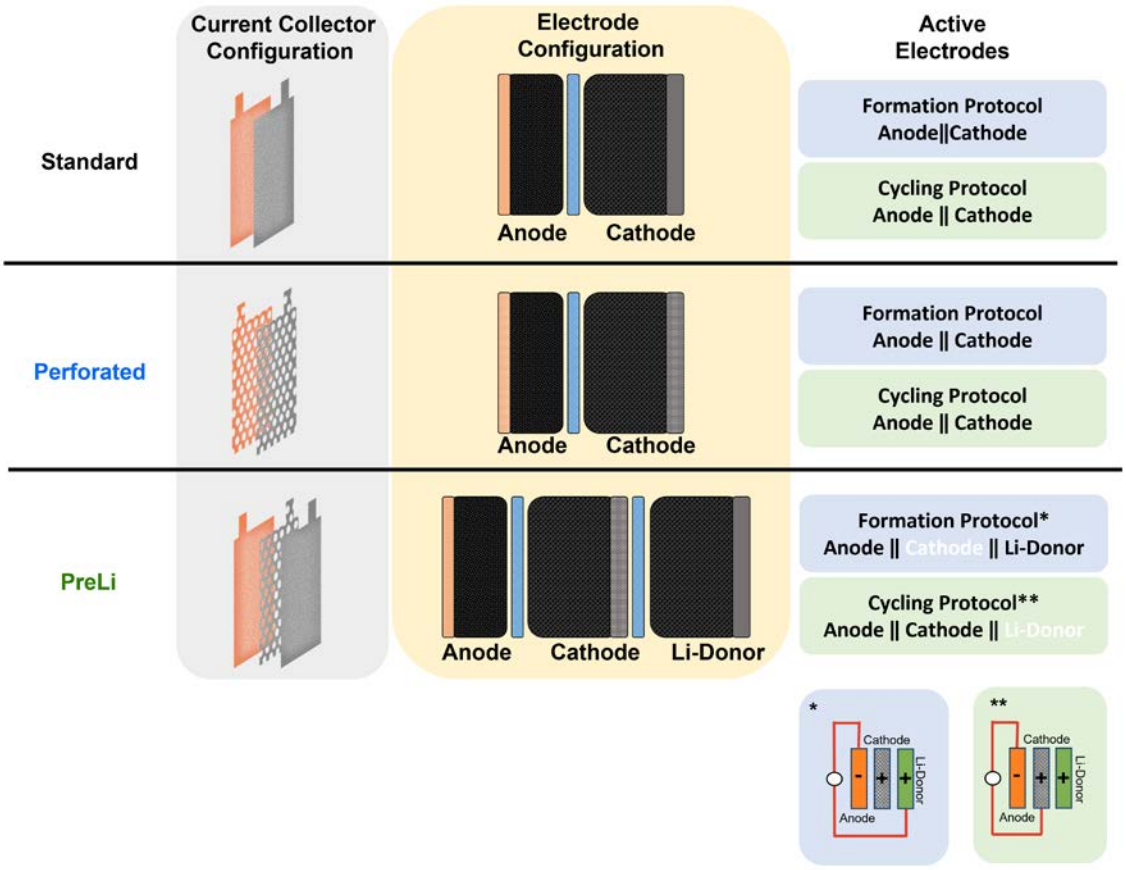

Figure 6.22 Graphite‖LFP single-layer pouch cell setups, along with the electrode connections during their formation and cycling protocols. Black-marked electrodes are active in the respective protocol, while white-marked electrodes remain inactive.

The two upper setups displayed in **Figure 6.22** are basic single-layer pouch cells, with the key distinction of having electrodes made of standard or perforated current collectors for the anode and the cathode. These two setups assess the direct impact of current collector design on cell electrochemistry. For simplicity, this chapter will refer to single-layer pouch cells with standard current collectors as the "Standard" setup and to those with perforated current collectors as the "Perforated" setup.

In the "PreLi" setup, an LFP electrode with a perforated aluminum current collector is sandwiched between standard graphite and LFP electrodes. The outer LFP electrode serves as a lithium donor electrode for prelithiation. Its lithium ions can migrate through the permeable cathode and reach the graphite anode. This facilitates anodic SEI formation without consuming active lithium from the sandwiched cathode itself. After prelithiation, the anode and cathode are connected as usual.

Meanwhile, the outer LFP electrode remains inactive in the cell. Therefore, the PreLi cells allow for the proof-of-concept of the prelithiation strategy examined in this study, featuring perforated current collector design for the first time to the best of the author's knowledge.

Two single-layer pouch cells (approx. 60 mAh) were assembled for each configuration (Standard, Perforated, and PreLi). Celgard 2325 was used as the separator and 1.2 mL of 1 M $LiPF_6$ in EC:EMC (3:7) + 2 wt.% VC was used as the electrolyte. The N/P-ratio was set to 1.15 for all cells. After assembly, the cells were clamped between two plexiglas plates at a pressure of approx. 4 N cm^{-2} and left to rest for 10 hours to allow sufficient time for the electrolyte to soak into the electrodes and separator.

Five formation cycles were performed within the voltage window of 2.5 to 3.7 V. The active electrodes for each setup are marked in **Figure 6.22**. A CCCV-charge (I = C/10 until V_{cell} > 3.7 V; V = 3.7 V until I < C/20) and CC-discharge (I = C/10 until V_{cell} < 2.5 V) protocol was used. The initial CCCV-charge voltage profile for one cell of each configuration is shown in **Figure 6.23**.

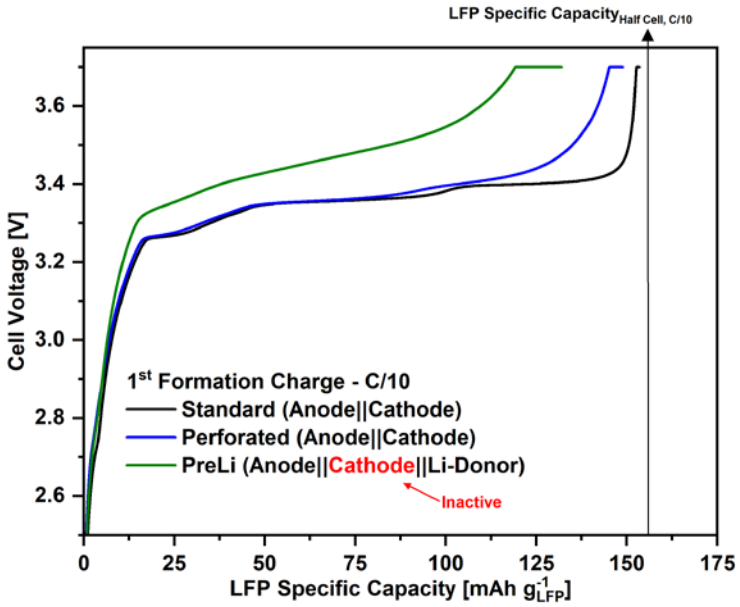

Figure 6.23 Initial charge voltage profiles of Graphite‖LFP single-layer pouch cells. In the PreLi setup, the Li-donor electrode is connected to the anode, while the sandwiched lithium-ion permeable cathode remained inactive.

The characteristic Graphite‖LFP voltage profile is observable during the initial charge of the Standard setup, as shown in **Figure 6.23**. Three distinct voltage plateaus mirror those of the negative electrode due to the flat voltage profile of LFP and correspond to the formation of lithium-graphite intercalation compounds.[112,228] The initial charge capacity of the Standard setup cells is consistent with the practical LFP specific capacity obtained from half-cell measurements (see **Appendix**: **Figure 15.1** on page 186). In contrast, cells of the Perforated setup exhibit increased polarization at states of charge above 50%. While the first voltage plateau is the same for cells of both, the Standard and Perforated setups, the second plateau is shorter for the Perforated setup

and gradually transitions into a sloping voltage profile. Consequently, the cut-off voltage is reached before complete delithiation of the cathode AM in its CC-charging step. In cells of the PreLi setup, polarization effects are even more pronounced. The first voltage plateau is barely observable, and a sloping voltage profile dominates. Kinetic constraints impede the full delithiation of the cathode within the applied measurement protocol.

This unwanted polarization in Perforated and PreLi setups must be carefully interpreted. The used LFP electrodes with perforated current collectors have an inhomogeneous coating layer on their backside (see **Figure 6.21** on page 61). In addition to a significant amount of AM on the wrong side of the electrode, regions of varying coating densification are also expected in the land and hole areas, as discussed in **Chapter 6.3** (page 53). Both coating defects are expected to alter the lithium-ion diffusion pathways within the coating layer, which directly affects electrode's kinetics. Consequently, it is difficult to determine whether or in which extend the observed polarization originates from the design of the current collector or from the described coating defects of the cathode.

Furthermore, in the PreLi setup, the diffusion pathway of lithium ions from the Li-donor electrode to the anode involves traversing the inactive, sandwiched cathode. Therefore, this cell setup is expected to exhibit kinetic constraints during the prelithiation treatment, as also reported in related literature. Watanabe et al., using laser-structured electrodes, and Zensen, using expanded metal current collectors, observed varying anode lithiation degrees after prelithiation treatment depending on the anode's distance from the Li-donor electrode and the applied measurement protocol.[214,215] However, the extent of polarization observed in the PreLi configuration shown here was surprising and underscores the significant influence that lithium-ion migration pathway lengths can have on a cell's electrochemical performance. With certainty, it can be stated that the electrochemical activity between anode and Li-donor in the PreLi configuration (**Figure 6.23**) includes the formation of an anodic SEI. Thus, the goal of anodic prelithiation appears to have been achieved.

As discussed in the theoretical background of this work, accurately assessing the degree of prelithiation and the controllability of the process remains challenging. Insufficient active lithium supply results in incomplete anodic SEI formation. Consequently, it compensates for ICLs to a lesser extent. Excessive active lithium supply, on the other hand, can introduce safety risks within the cell due to undesirable lithium plating.[48] This work will compare the maximum reversible specific capacity of the cathode AM, as measured in half-cells, with its usable specific capacity obtained in full-cells. In addition to analyzing the AM capacity utilization and initial cycle CE, the voltage profiles of prelithiated and non-prelithiated cells will be examined in detail.

To this end, the PreLi cells underwent an additional cycling protocol after the prelithiation treatment (formation protocol) was completed. This time the Li-donor electrode remained inactive while the sandwiched cathode was connected as the active working electrode as shown in **Figure**

6.22. Five charge/discharge cycles were performed again within the same measurement protocol applied during cell formation, at a C-rate of C/10.

Figure 6.24 shows the voltage profiles of the first and fifth anode‖cathode cycle of each cell configuration, as well as the practical, reversible, specific capacity of the LFP AM, as measured in a half-cell at the same current density and voltage window.

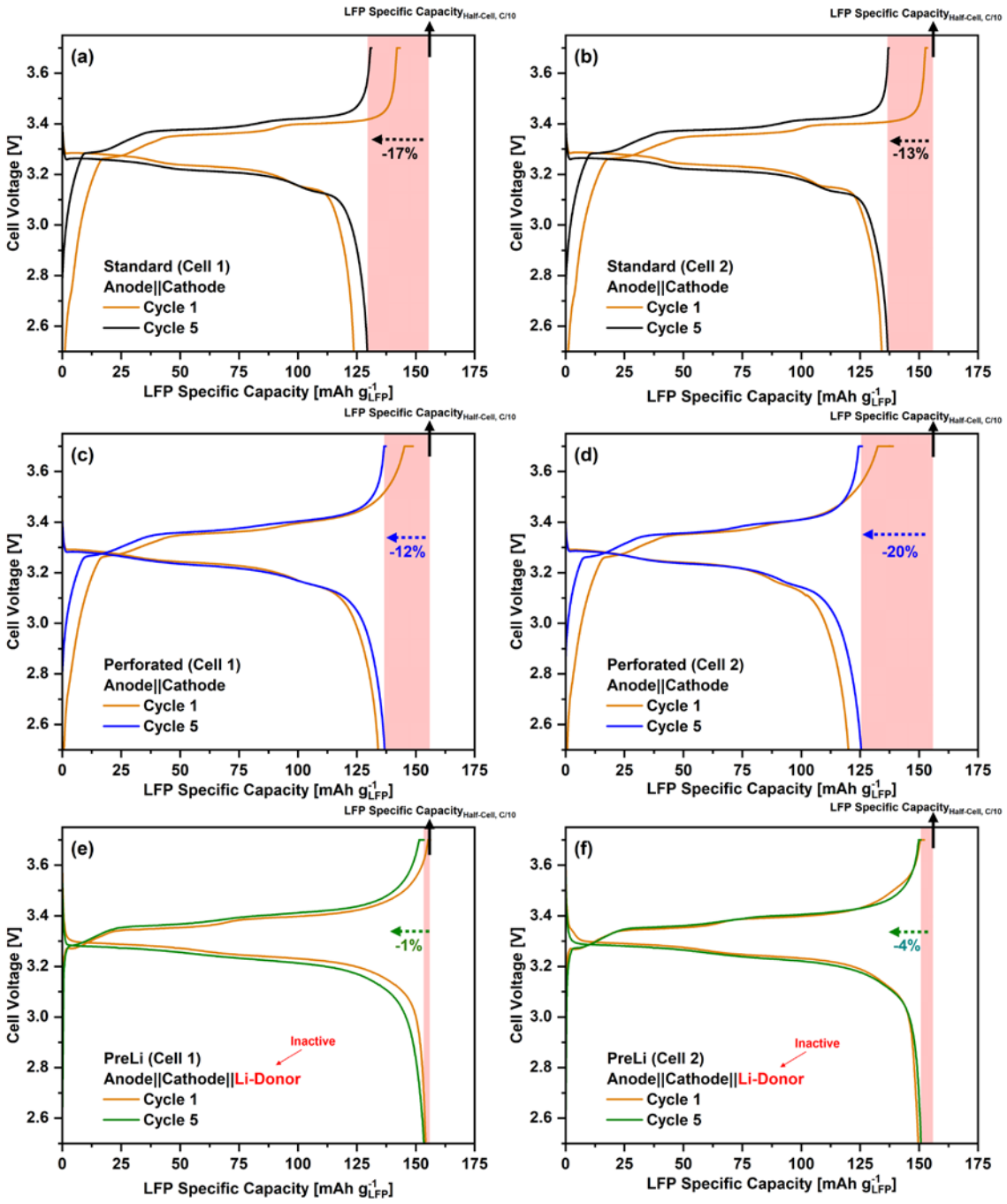

Figure 6.24 First and fifth anode‖cathode cycle voltage profiles of different Graphite‖LFP single-layer pouch cell setup. Two cells of each setup are shown: a, b) Standard, c, d) Perforated, and e, f) PreLi. In the PreLi setup, the sandwiched cathode is connected to the anode, while the Li-donor electrode remained inactive.

In cells of the Standard and Perforated setup, the first anode‖cathode cycle involves the formation of an anodic SEI. In the fifth cycle, 80% to 88% of the cathode's specific capacity remains accessible. In cells of the PreLi setup, the anodic SEI was formed in advance using the Li-donor electrode, as described above. In both cells, 96% – 99% of the cathode's specific capacity is accesible in the first and fifth anode‖cathode cycle, reflecting the completion of anodic SEI formation during prelithiation treatment.

Huge variations from cell to cell of each setup are notable in the data presented in **Figure 6.24**. This lack of reproducibility indicates inhomogeneities in the material or coating within the cell's electrodes, independent of the current collector system used. It is worth clarifying that these initial LFP electrodes were fabricated with an old batch of LFP AM as preliminary trial. Given the state of the used AM, variations in its quality and electrochemical performance cannot be ruled out.

Nevertheless, clear trends can be identified from **Figure 6.24**:

1) Cells of the Standard and Perforated setup exhibit similar cell formation behavior in terms of cathode AM capacity utilization, but differ in their degree of polarization at higher states of charge.
2) Cells of the PreLi setup demonstrate that nearly the full specific capacity of the cathode AM can be utilized following prelithiation treatment.

Figure 6.25a provides a closer look at the voltage profiles of cells from the Perforated and PreLi setup, which contain at least one perforated current collector electrode. The voltage profile of the prelithiated PreLi setup in direct comparison to the non-prelithiated Perforated setup is significantly shifted. Its electrochemical activity begins and ends at the midpoint of the graphite's first voltage plateau.

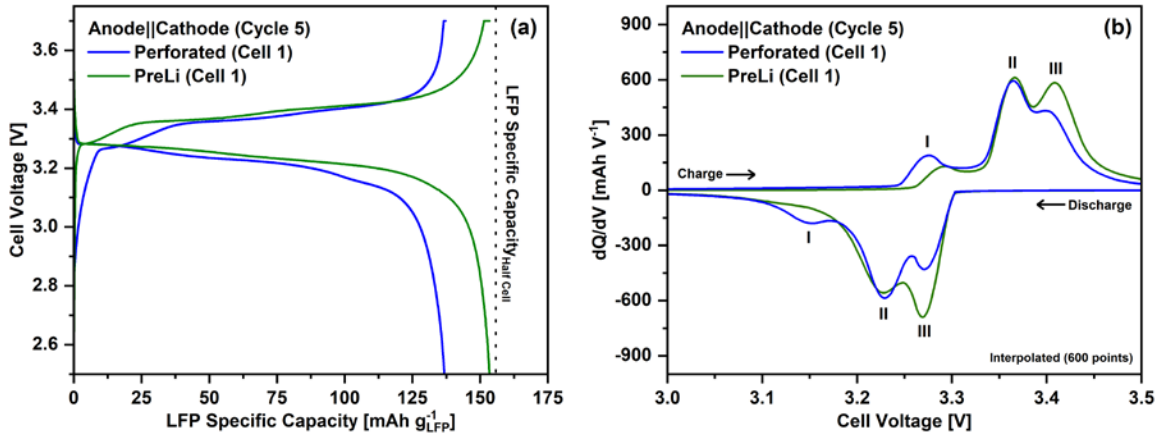

Figure 6.25 a) Voltage profiles and b) derivative analysis of Graphite‖LFP single-layer pouch cells, which contain at least one perforated current collector electrode.

As previously mentioned, the voltage plateaus in Graphite‖LFP cells can be directly attributed to the formation of lithium-graphite intercalation/deintercalation compounds due to the flat voltage

profile of LFP.[112,228] This feature of Graphite‖LFP cells can be used to gain in-depth insights into the graphite lithiation/delithiation activity of prelithiated and non-prelithiated cells by comparing the intensity of these plateaus in their derivative analysis (dQdV-plots). For this purpose, the corresponding peaks in the dQdV-plots have been labeled I, II, and III. Peak III activity relates to the last voltage plateau associated with the formation or decomposition of the fully lithiated graphite structure, LiC_6.[112]

As shown in **Figure 6.25b**, the derivative analysis clearly reveals decreased electrochemical activity of peak I, similar activity of peak II, and increased activity of peak III in prelithiated cells compared to the non-prelithiated one. Activity of peak II mostly overlap in cells of both setups, which indicates equivalent cell properties in terms of electrode activity, balancing, and cell kinetics. Decreased peak I activity reveals a partially lithiated anode in the discharged state of the prelithiated cell. This means that the prelithiation treatment not only offset ICLs due to anodic SEI formation but also established an active lithium reservoir in the anode. As a result of prelithiation and anodic Li-reservoir, the active lithium inventory of the cell is increased. Therefore, more active lithium is available for electrochemical activity of peak III in the cells of the PreLi setup.

In summary, the data presented in **Figure 6.24** demonstrate that ICLs in the PreLi setup were effectively offset by the prelithiation treatment at the cell level. However, a detailed analysis of the voltage profiles shown in **Figure 6.25** reveals that, additionally, an anodic lithium reservoir has formed. In general, a controlled anodic lithium reservoir can compensate for ALL during cell operation, thus enhancing the cells' cycle life. Prelithiation studies by Chevrier et al. at the electrode level and by Zensen at the cell level demonstrated this concept by using anodes with a high silicon content.[215,229] Nevertheless, an excessive amount of active lithium in a LIB can result in safety issues during operation due to the risk of metallic lithium plating if the resulting capacity of the two electrodes, i.e., the N/P-ratio, is not adequately balanced.[48] This highlights that knowing exactly the active lithium level after prelithiation treatment is key for safe cell operation. However, the results presented above confirm prelithiation and indicate an anodic lithium reservoir, but still are not able to quantify its exact size.

Figure 6.26 shows the LFP specific charge and discharge capacities as a function of cycle number throughout the entire formation protocol. It also shows the accumulated capacity of each cell after its formation protocol. The accumulated capacity is calculated as the sum of the differences between charge and discharge capacities over all cycles.

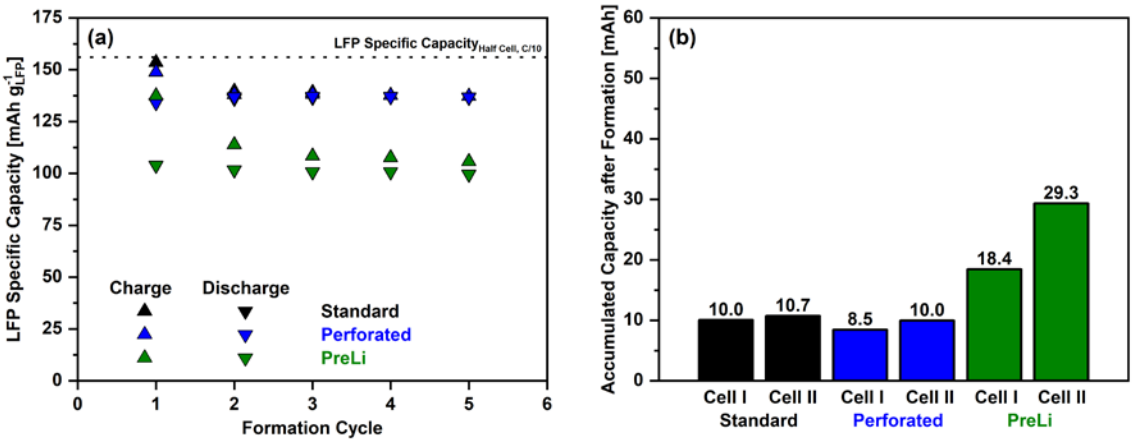

Figure 6.26 Formation data of Graphite‖LFP single-layer pouch cells: a) LFP specific capacity as a function of cycle number, and b) accumulated capacity after formation. In the PreLi cell, the Li-donor electrode is connected to the anode, while the sandwiched lithium-ion permeable cathode remained inactive.

As clearly visible in **Figure 7.26a** cells of the Standard and Perforated setup almost utilize the full cathode's capacity during their initial CCCV-charge. The following CC-discharge capacity is reduced due to ICLs associated with the formation of the anodic SEI. The subsequent charge and discharge capacities align with each other, which indicates that a stable SEI has formed. In the final formation cycle, both cell setups demonstrate comparable usable LFP specific capacity (136 mAh g^{-1}) together with high CE (> 99.6%). Cells of the PreLi setup exhibit a different formation performance. Low CEs are observed not only for the first formation cycle, but for all formation cycles. Namely, 75.6%, 89.2%, 92.9%, 93.6%, and 94.1% from cycle 1 to 5, respectively. In other words, significant more active lithium leaves the cathode compared to the anode in each cycle.

Figure 6.26b clearly confirms, that there is an enhanced accumulated capacity gap between the Standard or Perforated and PreLi cell setups after their formation protocol. Cells of Standard and Perforated setups show an accumulated capacity of approx. 10 mAh (15% of the cell capacity), whereas cells of the PreLi setup exhibit an accumulated capacity of 18 – 29 mAh. Assuming that no additional irreversible reactions occurred in the PreLi setup, and that the total accumulated capacity of approximately 10 mAh measured in the Standard and Perforated setups represents the full amount of ICLs due to anodic SEI formation in the PreLi setup too, the size of the anodic lithium reservoir would be 8 – 19 mAh (equivalent to 13 – 33% of the cell capacity). Considering an anodic lithium reservoir equivalent to 13% of the cell's capacity and a N/P-ratio of 1.15, the anode can theoretically still accommodate all of the cathode's active lithium in the fully charged state. However, for an anodic lithium reservoir equivalent to 33% of the cell's capacity, the anode would lack the necessary intercalation sites to host all of the available active lithium during cycling. This would result in lithium plating at high states of charge. Due to these safety concerns, cells of the PreLi setup were not investigated further. Therefore, it remained unclear to what extend the quantified accumulated capacity was probably kinetically trapped in the anode or lost in irreversible

reactions within the cell. All these matters will be thoroughly explained in the **Chapter 7** (page 71) using optimized electrodes and cells.

Cells of the Standard and Perforated setup exhibited similar cycling behavior over 25 cycles as shown in **Figure 6.27**.

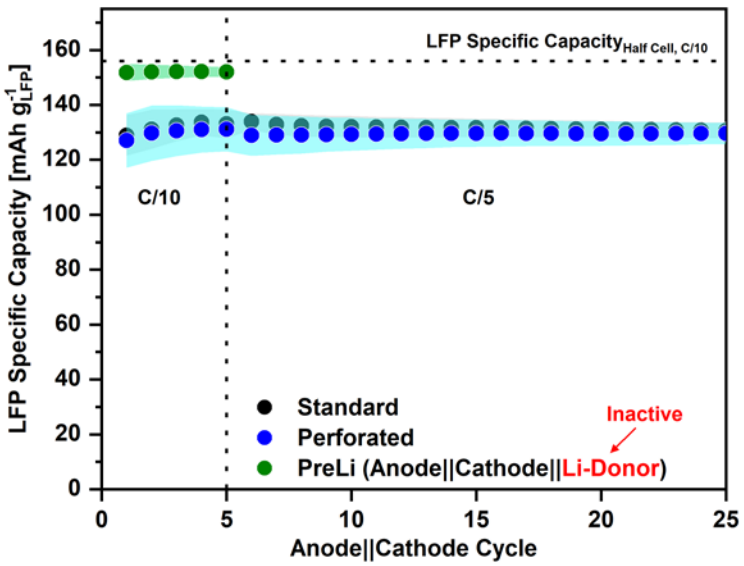

Figure 6.27 Cycling data of Graphite‖LFP single-layer pouch cells. The cycling protocol involves a CCCV-charge and CC-discharge in the potential window 2.5 – 3.7V

6.5 From Prediction to Demonstration

Figure 6.28 plots the specific capacity at the electrode level (anode and cathode) as the function of the cathode's areal capacity using both theoretical and experimental data. This plot validates the calculation method used to make the predictions presented in **Chapter 6.2** (page 46) with data from real cells. As shown in **Figure 6.28**, the data from real cells (dots) aligns closely with the calculated ones (lines). Minor deviations are likely due to small variations in the N/P balancing of the real cells. As predicted for single-layer pouch cells, perforated current collectors and prelithiation result in approx. 12% and 22% higher specific capacities, respectively, compared to the reference.

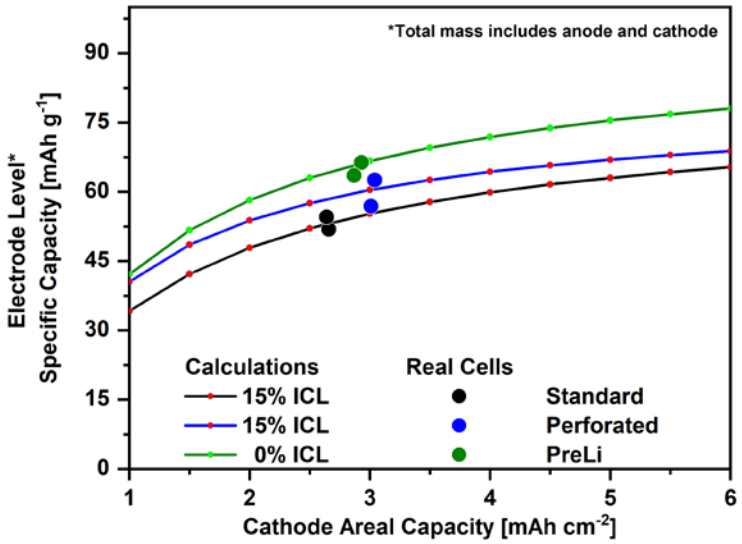

Figure 6.28 Specific capacity at the electrode level* as a function of the cathode's areal capacity of all single-layer pouch cell setups under investigation (*total mass includes the anode and cathode). Comparison of theoretical calculated values (lines) and real cell data (dots).

The theoretical and practical findings demonstrate that the here introduced perforated current collector design can significantly increase the energy density of LIBs. In addition to reducing the mass and volume contribution of the current collector within the cell, they enable the implementation of a prelithiation strategy at the cell level.

7. Prelithiation and Beyond

In this chapter, I aim to provide a fundamental electrochemical understanding of active lithium inventory control and its impact on cell performance. Three distinct Graphite‖LFP cell systems that differ only in the size of their initial active lithium inventory will be prepared and investigated for this purpose, as shown in **Figure 7.1**.

i) Standard, where ICL are not compensated
ii) PreLi, where ICL are compensated
iii) Li-Reservoir, where ICL are compensated and an additional anodic Li-reservoir equivalent to 10% of the cell's capacity is provided.

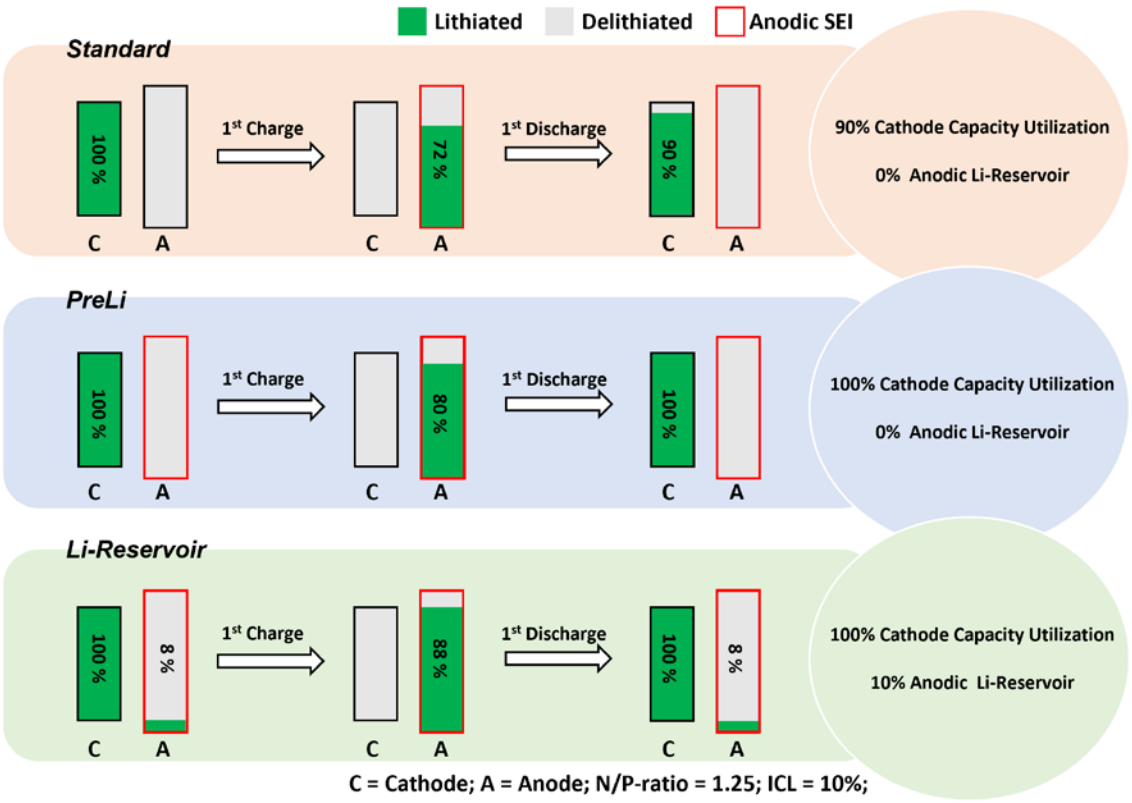

Figure 7.1 Illustration of three distinct Graphite‖LFP LIB systems that differ only in the size of their initial active lithium inventory: Standard (top), where ICL are not compensated; PreLi (center), where ICL are compensated; Li-Reservoir (bottom), where ICL are compensated and an additional anodic lithium reservoir equivalent to 10% of the cell's capacity is provided.

7.1 Predicted Impact on LIB Performance

Figure 7.2, **Figure 7.3**, and **Figure 7.4** show the expected electrode behavior of a Standard, PreLi, and Li-Reservoir Graphite‖LFP cell system during initial charge and discharge, as well as consecutive cycles from a purely theoretical point of view. The plots are made with potential profiles from graphite and LFP half-cell measurements at C/50. For all systems, a N/P-ratio of 1.25 is considered based solely on the reversible capacity of the electrodes. Furthermore, for the Standard system an ICL of 10% of the cell's capacity is assumed, while for the Li-Reservoir system an anodic Li-reservoir of 10% of the cell's capacity is assumed.

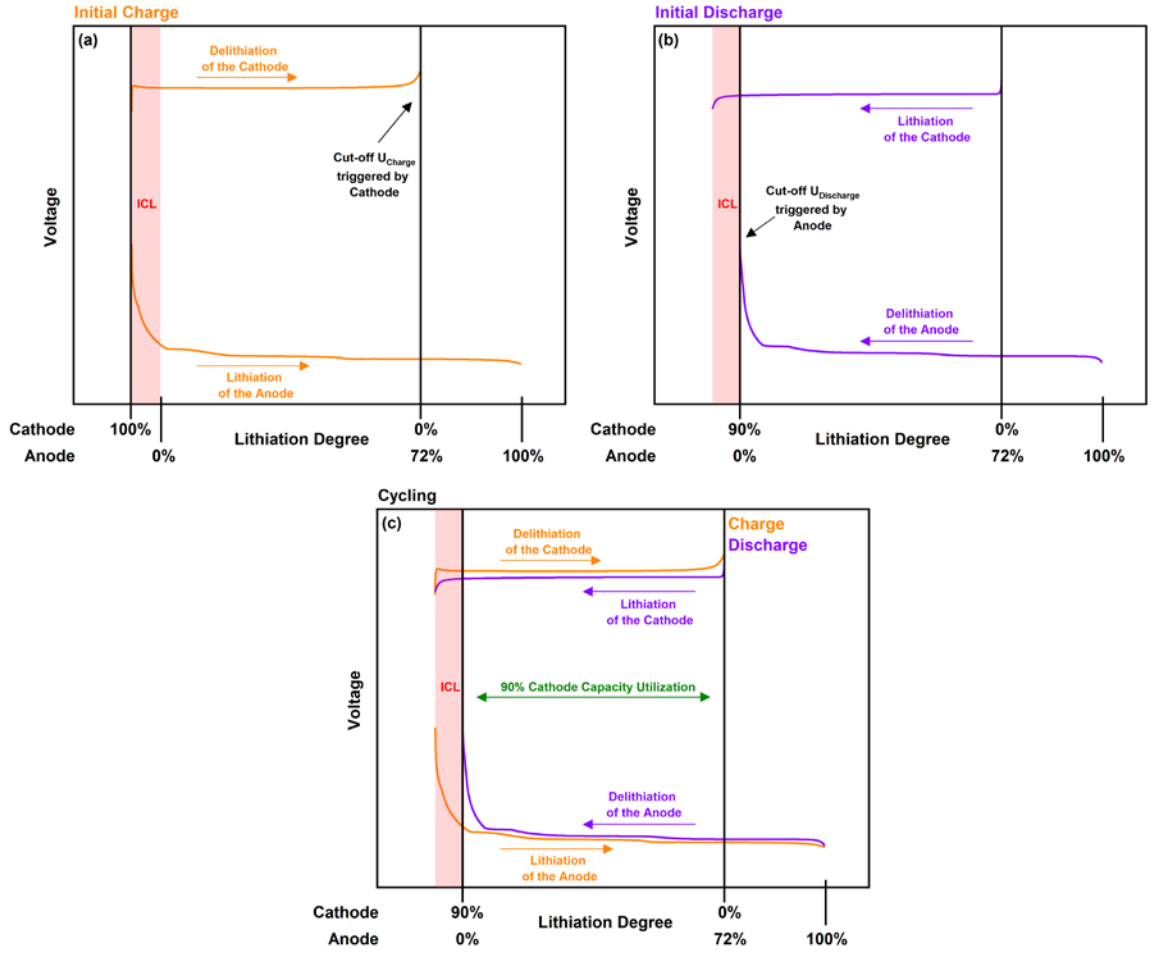

Figure 7.2 Illustration of electrode lithiation/delithiation behavior of Standard Graphite‖LFP cell system during a) initial charge, b) initial discharge, and c) subsequent cycling. A N/P-ratio of 1.25 and a ICL of 10% is considered.

In the initial state of Standard Graphite‖LFP cell systems, the cathode contains all of the active lithium. During the initial charge, some of the active lithium becomes irreversibly bound within the anodic SEI while the rest intercalates into the graphite structure (**Figure 7.2a**). The charge cutoff voltage is triggered by a steep voltage increase of the cathode due to complete delithiation. In the

charged state, the anode stores all of the cell's active lithium. It is lithiated up to 72% of its total storage capacity. During the subsequent discharge, active lithium migrates back from the anode to the cathode. This results in a cathode lithiation degree of 90% in the fully discharged state (**Figure 7.2b**). The discharge cutoff voltage is triggered by a steep voltage increase of the anode due to complete delithiation. Thus, for the Standard Graphite‖LFP system under consideration, 90% of the initial cathode capacity is theoretically available for reversible energy storage, as illustrated in **Figure 7.2c**.

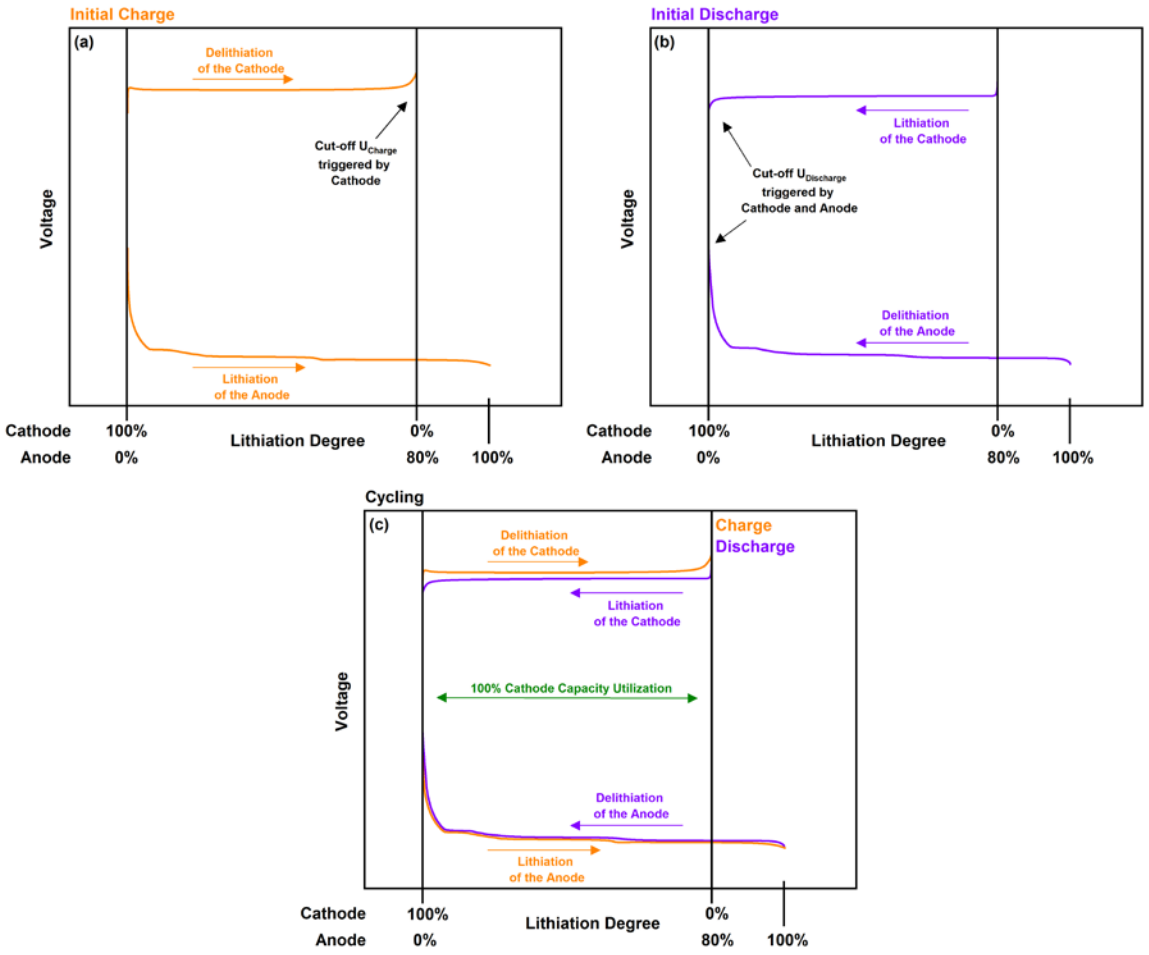

Figure 7.3 Illustration of electrode lithiation/delithiation behavior of PreLi Graphite‖LFP cell system during a) initial charge, b) initial discharge, and c) subsequent cycling. A N/P-ratio of 1.25 is considered.

The key difference of the PreLi to the Standard Graphite‖LFP cell is that the anodic SEI has been pre-formed with an additional active lithium source. Consequently, all the active lithium in the cathode intercalates into the graphite structure during the initial cell charge (**Figure 7.3a**). The charge cutoff voltage is triggered again when the cathode becomes fully delithiated. In the charged state, the anode is lithiated up to 80% of its total storage capacity. During the subsequent discharge, the cathode is lithiated again, reaching a lithiation degree of 100% in the fully discharged state (**Figure 7.3b**). The discharge cutoff voltage is triggered by both complete anode delithiation, causing

a steep increase of the anode voltage, and full cathode lithiation, resulting in a steep drop of the cathode voltage. For the PreLi Graphite‖LFP system under consideration, 100% of the initial cathode capacity is theoretically available for reversible energy storage in the operating cell, as illustrated in (**Figure 7.3c**).

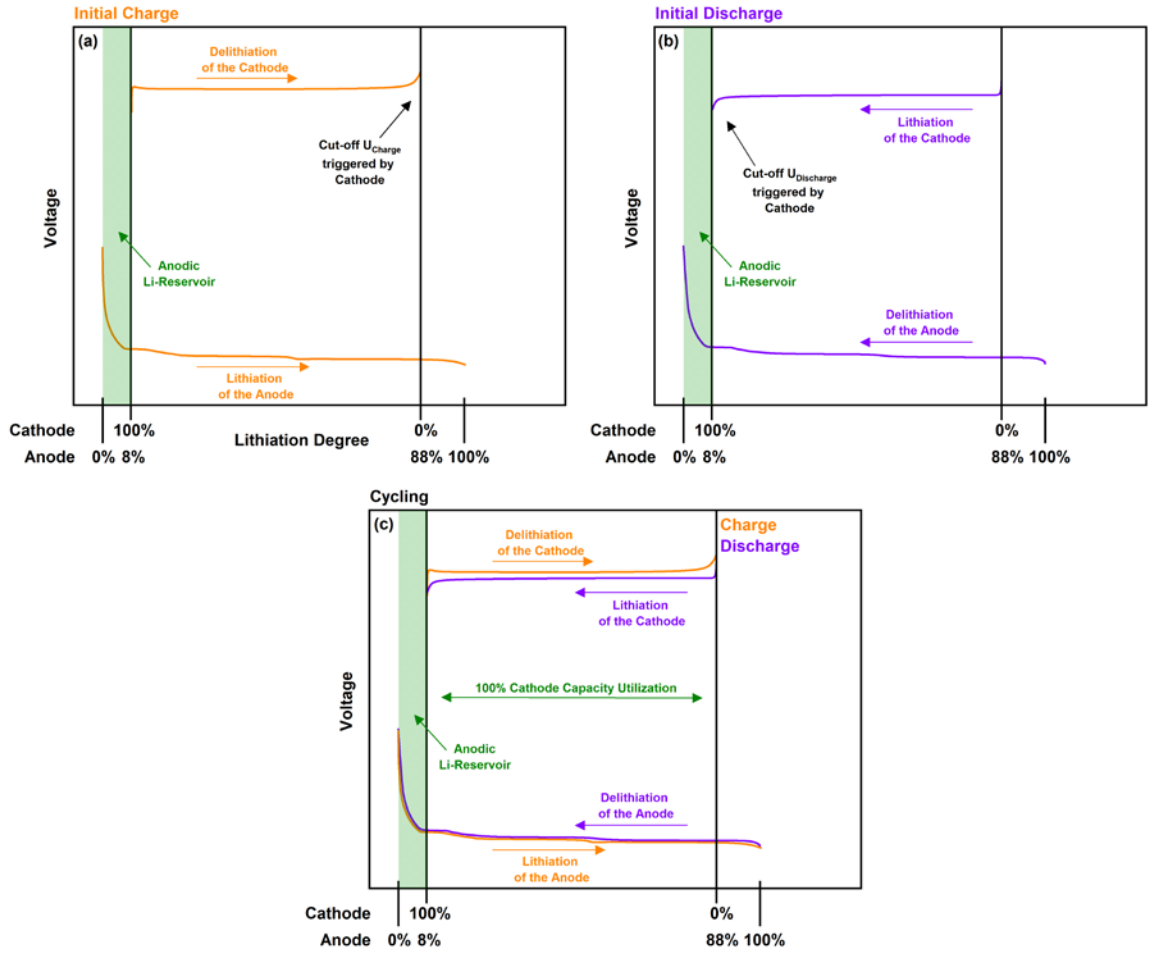

Figure 7.4 Illustration of electrode lithiation/delithiation behavior of Li-Reservoir Graphite‖LFP cell system during a) initial charge, b) initial discharge, and c) subsequent cycling. A N/P-ratio of 1.25 and an anodic Li-Reservoir of 10% of the total cell capacity is considered.

The Li-Reservoir Graphite‖LFP cell system's initial state is comparable to that of the PreLi system, with the inclusion of an anodic lithium reservoir equivalent to 10% of the cell's total capacity (the anode is lithiated to 8% of its total storage capacity). This results in a distinctive feature of Li-Reservoir systems: in their initial state, both the cathode and the anode contain active lithium. During the initial charge, all active lithium from the cathode intercalates into the graphite structure. The charge cutoff voltage is triggered again when the cathode becomes fully delithiated. In the charged state, the anode is lithiated to 88% of its total storage capacity (**Figure 5.4a**). During the subsequent discharge, the cathode is again lithiated, reaching a lithiation degree of 100%. Meanwhile, the anode remains partially lithiated at 8% in the fully discharged state (**Figure 7.4b**). The discharge cutoff voltage is triggered by a steep drop of the cathode voltage caused by full

lithiation. In Li-Reservoir Graphite‖LFP cells, the full cathode capacity is again available for reversible energy storage (**Figure 7.4c**). Furthermore, the anodic lithium reservoir compensates for ALL during cycling. E.g., assuming a CE of 99.95%, an anodic lithium reservoir equivalent to 10% of the cell's total capacity would extend the cell's cycle life by over 47% before reaching EOL, compared to a similar cell without an anodic lithium reservoir.

Table 7.1 provides an overview of the predicted effects of different sizes of active lithium inventory (Standard, PreLi, and Li-Reservoir) on the Graphite‖LFP cell characteristics during initial charge and discharge, as well as consecutive cycles.

Table 7.1 Overview of the anticipated effects of different sizes of active lithium inventory (Standard, PreLi, and Li-Reservoir) on Graphite‖LFP cell performance characteristics. *Considering only reversible capacity of anode and cathode **Considering also ICL, prelithiation, and anodic lithium reservoir ***EOL.

		Standard	**PreLi**	**Li-Reservoir**
Initial State	N/P-Ratio (Electrode Level*)	1.25	1.25	1.25
	N/P-Ratio (Cell Level**)	1.39	1.25	1.14
	Cathode Lithiation Degree	100%	100%	100%
	Anode Lithiation Degree	0%	0%	8%
	Anodic SEI preformed	No	Yes	Yes
1st Charge	ICL	10%	0%	0%
	Cathode Lithiation Degree	0%	0%	0%
	Anode Lithiation Degree	72%	80%	88%
	Anodic SEI formed	Yes	Yes	Yes
1st Discharge	Cathode Lithiation Degree	90%	100%	100%
	Anode Lithiation Degree	0%	0%	8%
Cycling	Cathode Capacity Utilization	90%	100%	100%
	Cycle Life*** CE: 99.95%	446 Cycle	446 Cycle	656 Cycle

Table 7.1 shows a distinction between the N/P-ratio at the electrode and at the cell level. In this work, electrode balancing is employed considering the N/P-ratio at the electrode level. This approach relies solely on the reversible areal capacities of the electrodes ($Q_{rev,areal,anode,half\text{-}cell}$ and $Q_{rev,areal,cathode,half\text{-}cell}$), which are measured in half-cells, according to **Equation 7.1**.

$$\frac{N}{P} - ratio_{\ Electrode\ Level} = \frac{Q_{\ rev,areal,anode,half-cell}}{Q_{rev,areal,cathode,half-cell}} \qquad \textbf{7.1}$$

Values greater than 1.0 ensure that the anode can accommodate the entire reversible capacity of the cathode in the assembled cell. This is important, as otherwise, a surplus of lithium would plate on the anode's surface.

However, the N/P-ratio at the electrode level considers only the reversible capacities of the electrodes in isolation (half-cell measurements are used to determine the values). It neglects changes to the active lithium inventory of the cell due to ICLs or prelithiation treatments in a full-cell application of these electrodes. For this, the N/P-ratio at the cell level provides more comprehensive information about the total active lithium inventory ($Q_{Li\text{-}inventory}$) in relation to the anodic lithium storage sites (Q_{anode}) in the operating full-cell. It can be calculated according to **Equation 7.2**.

$$\frac{N}{P} - ratio_{\ Cell\ Level} = \frac{Q_{anode}}{Q_{Li-inventory}} \qquad \textbf{7.2}$$

Values greater than 1.0 guarantee that the number of lithium storage sites on the anode exceeds the cell's total active lithium inventory in its operating state.

While the N/P-ratio at the electrode level is a fixed value that considers only the electrodes in their isolated states, the N/P-ratio at the cell level is dynamic and varies during cell operation. E.g., cell aging may reduce the number of anodic lithium storage sites (or Q_{anode}) due to detachment of AM or decrease the cell's active lithium inventory through ALL. Due to the complexity of ICLs, prelithiation and cell aging, accurate control of the N/P-ratio at the cell level can be challenging in practice. Therefore, in this study, this value is used solely as a theoretical guideline to ensure safe cell operation. The N/P-ratio at the electrode level is applied for real cell electrode balancing.

According to the theoretical understanding provided here, demonstrator pouch cells will be balanced using an N/P-ratio of 1.25 at the electrode level. The predicted N/P-ratio at the cell level (1.39 for Standard, 1.25 for PreLi, and 1.14 for Li-Reservoir system; **Table 7.1**), suggests that there are no safety concerns due to lithium plating under moderate operating conditions, regardless of the size of the active lithium inventory in the respective cells. Moreover, maintaining a constant N/P-ratio at the electrode level allows the use of electrodes from the same coating batch across all cell systems. This ensures reliable comparison, as only the size of the active lithium inventory differs in the final cells.

First, the graphite and LFP slurry and coatings must be tailored to assemble these cells. Single-sided coated graphite electrodes (standard current collector) with an areal capacity of 3.0 mAh cm^{-2} and single-sided coated LFP electrodes (standard and perforated current collector) with an areal capacity of 2.4 mAh cm^{-2} are required to achieve the targeted N/P-ratio at the electrode level equal to 1.25.

7.2 Lab Scale Electrode Development

7.2.1 Upscaled graphite electrode development

In **Chapter 6.3.1** (page 53), graphite electrodes with standard and perforated copper current collectors were developed using a water-based slurry. The graphite coatings on perforated current collectors obtained were of good quality, with the backside of the electrode remaining free of coating (see **Figure 6.18** on page 58). No further adjustments to the slurry formulation are required for the scope of this work. However, the initial slurry batches were limited to 35 g, so scaling up the slurry mixing process while maintaining its properties is essential for next steps. For this, the AM had to be changed from Graphite-1 to Graphite-2 for availability reasons.

The graphite electrode formulation of AM:CB:CMC:SBR – 94:2:2:2 remained consistent with the initial graphite electrode development presented in **Chapter 6.3.1** (page 53). The TSC was adjusted to 43.0% to ensure the slurry had sufficient viscosity. **Figure 7.5** provides a schematic overview of the processing steps and instruments used to coat the graphite electrodes.

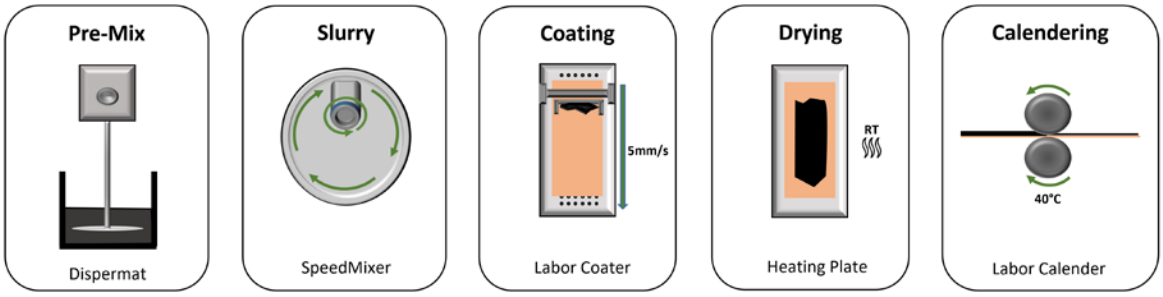

Figure 7.5 Schematic overview of the processing steps and instruments used to manufacture graphite electrodes.

The pre-mix (Water:CB:CMC – 97:1.5:1.5) was prepared using a disperser with a cowles blade. Rheological measurements presented in **Figure 7.6a** and **b** demonstrate the consistency of the pre-mix properties when scaling up from a 120 g batch to a 1,500 g batch. Regardless of the batch size, the external shear of the dispersing disc was limited to a maximum of 420 cm s^{-1}. With these mixing conditions, the rheological properties of the suspension seem to depend only on its formulation, TSC, and the materials used rather than on batch size or mixing time. This ensures that the suspension can be reproduced and scaled up. Furthermore, the suspension can be stored for over a week while maintaining its rheological properties (see **Appendix**: **Figure 16.1** on page 187).

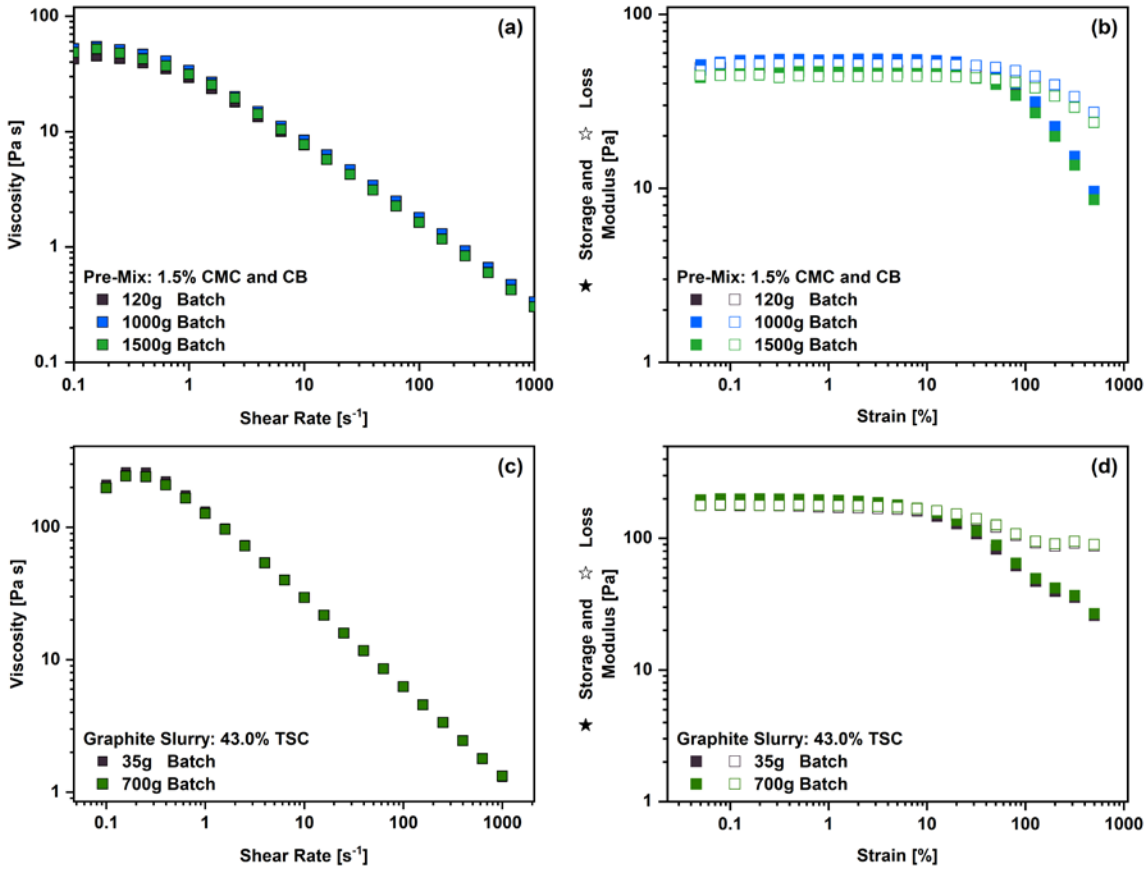

Figure 7.6 Rheological data (flow curve and amplitude sweep) of a, b) pre-mixes and c, d) graphite slurries from different batch sizes.

The graphite slurry was prepared using a centrifugal mixer. Rheological measurements presented in **Figure 7.6c** and **d** demonstrate the consistency of the slurry properties when scaling up from a 35 g batch to a 700 g batch. The rheological properties could only be maintained by scaling up the process with a gentler mixing sequence. For the 35 g batch, the AM was added in two steps and mixed at 1,500 rpm for three minutes each. For the 700 g batch, the AM was added in five steps and the mixing intensity was reduced to 1,000 rpm for three minutes each. The graphite slurry can be stored over several days by maintaining its rheological properties (see **Appendix Figure 16.1** on page 187).

The graphite slurry was coated onto standard copper current collector foils using the lab-scale doctor blade coating technique at three different wet thicknesses: 200 µm, 230 µm, and 260 µm. A graphite specific capacity of approx. 360 mAh g^{-1} was determined in half-cell measurements (**Figure 7.7a**) and the linear relationship between coating wet thickness and areal capacity was evaluated (**Figure 7.7b**). Finally, the graphite slurry was coated onto standard copper current collectors at the specified wet thickness of 230 µm to produce graphite coatings with an areal capacity of 3.0 mAh g^{-1}. The coatings were calendered to a coating density of 1.4 g cm^{-3} and cut into pouch cell format.

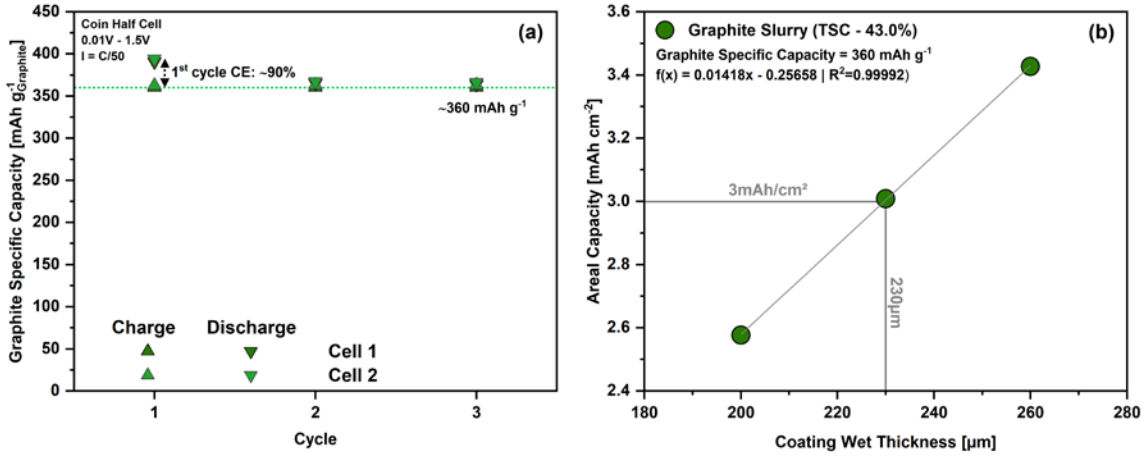

Figure 7.7 a) 2032-coin half-cell (Li‖Graphite) formation data of graphite electrodes. The protocol involves three CCCV-lithiation and CC-delithiation cycles of the electrode AM at a current density of C/50 in the potential window 0.05 – 1.50 V. b) Linear relationship between coating wet thickness and areal capacity.

Figure 7.8 shows SEM images of the graphite coating from the top and cross-section views. A homogeneous coating layer without defects is clearly visible. As-prepared graphite electrodes with a standard copper current collector foil were used in the single-layer demonstrator pouch cells discussed in **Chapter 7.3** (page 78).

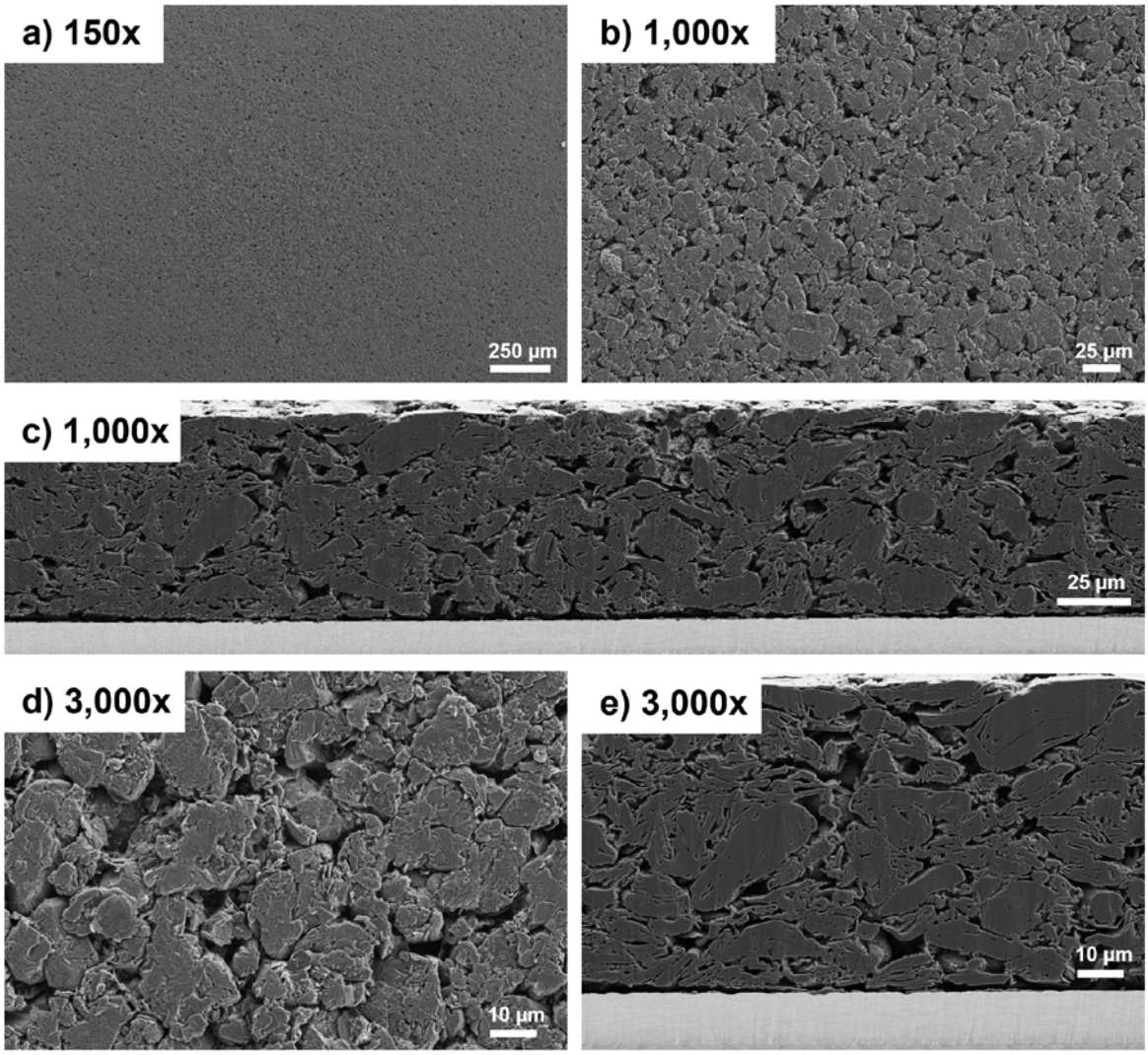

Figure 7.8 SEM micrographs of graphite coating deposited on a standard copper current collector foil: a) top-view image at 150× magnification, b) top-view image at 1,000× magnification, c) cross-sectional image at 1,000× magnification, d) top-view image at 3,000x magnification, and e) cross-sectional image at 3,000x magnification.

7.2.2 Upscaled LFP electrode development

In **Chapter 6.3.2** (page 59), LFP electrodes were developed with both standard and perforated aluminum current collectors using an NMP-based slurry. Coatings on perforated current collectors exhibited an inhomogeneous coating layer on the electrode backside (see **Figure 6.21** on page 61). This unwanted backside layer appears to negatively impact electrochemical performance by increasing the diffusion path of lithium ions to the AMs (see **Chapter 6.4** on page 62). Further optimization of the LFP slurry and electrode processing is required to eliminate these coating defects on the electrode backside.

Water-based processed graphite coatings on perforated current collectors exhibited a coating-free electrode backside (see **Figure 6.18** on page 58). Water has a lower boiling point than NMP, resulting in shorter drying times. When combined with sufficient slurry viscosity, this seems to prevent the slurry from flowing through the perforations onto the backside of the electrode during the lab-scale doctor blade coating process. As outlined in **Chapter 2.3.2** (page 20, Theoretical Background), environmental, safety, and cost concerns also motivate the switch from an NMP-based to a water-based LFP slurry.

An LFP electrode formulation of AM:SFG6L:CB:CMC:SBR – 92:1:3:1:3 was developed. The old batch of LFP AM (LFP-1) was replaced with a state-of-the-art LFP (LFP-2), and the TSC was set to 55.0% to ensure that the slurry had sufficient viscosity for coating perforated current collector foil. **Figure 7.9** provides a schematic overview of the processing steps and instruments used to coat the LFP electrodes.

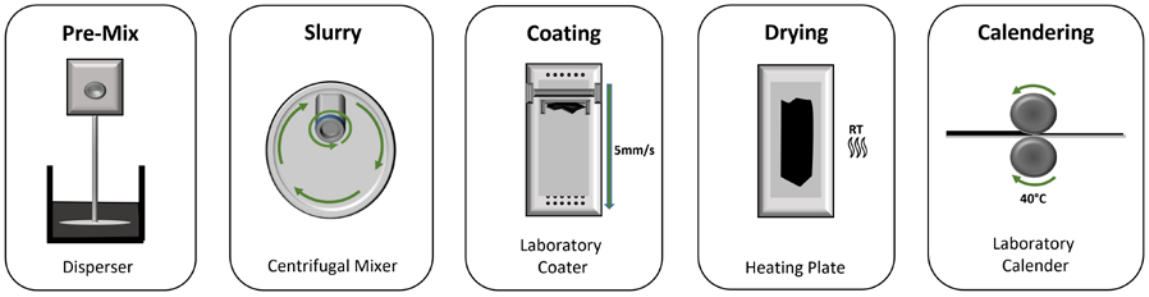

Figure 7.9 Schematic overview of processing steps and instruments used to manufacture LFP electrodes.

The pre-mix (Water:graphite:CB:CMC – 92.5:1.5:4.5:1.5) was prepared using a disperser with a cowles blade. Rheological measurements in **Figure 7.10a** and **b** show good consistency of pre-mix properties by scaling up from a 150 g batch to a 1,500 g batch. The final suspension can be stored over several days by maintaining its rheological properties (see **Appendix**: **Figure 16.2** on page 187),

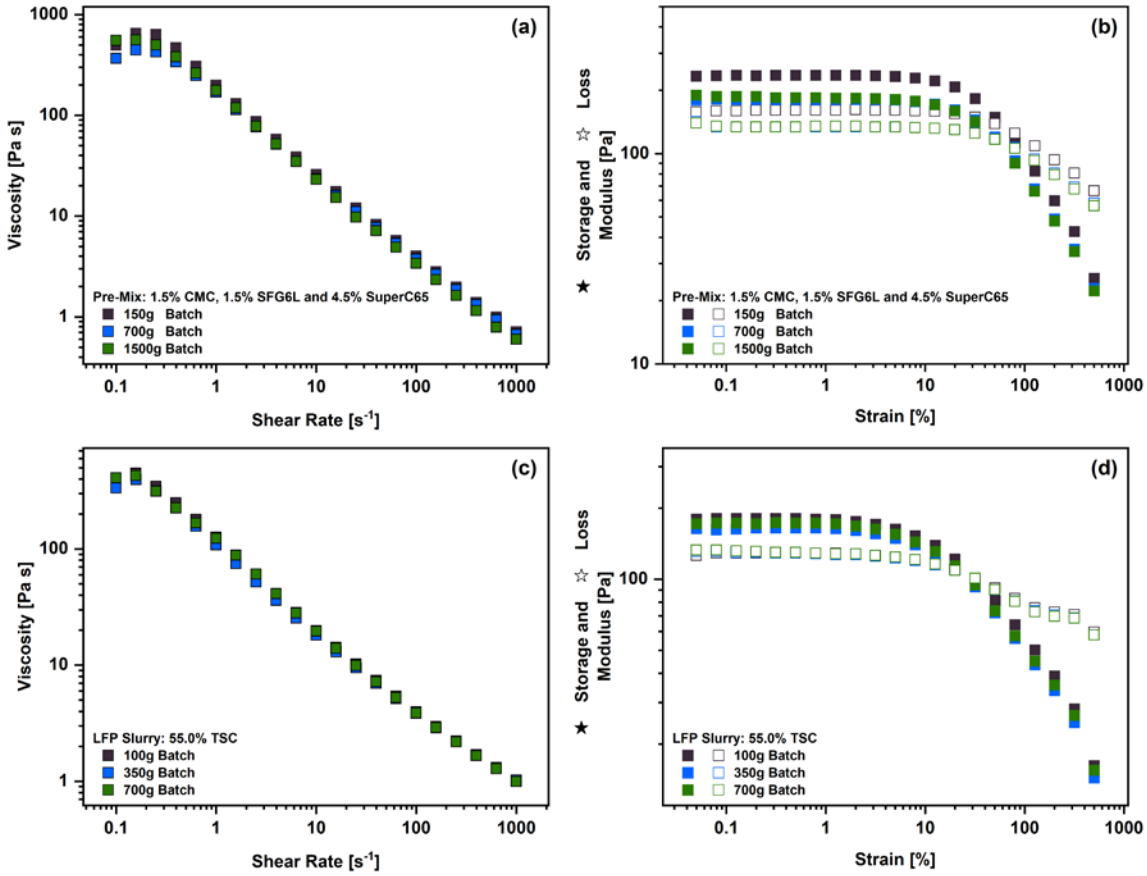

Figure 7.10 Rheological data of a, b) pre-mix and c, d) LFP slurry from different batch sizes.

The LFP slurry (AM:graphite:CB:CMC:SBR – 92:1:3:1:3) was prepared using a centrifugal mixer. Rheological measurements in **Figure 7.10c and d** show again good consistency of slurry properties by scaling up from a 100 g batch to a 700 g batch.

The LFP slurry was coated onto standard aluminum current collector foils using the lab-scale doctor blade coating technique at three different wet thicknesses: 280 µm, 300 µm, and 320 µm. A LFP specific capacity of approx. 149 mAh g^{-1} was determined in half-cell measurements (**Figure 7.11a**) and the linear relationship between coating wet thickness and areal capacity was evaluated (**Figure 7.11b**). Finally, the LFP slurry was coated onto both standard and perforated aluminum current collectors at the specified wet thickness of 290 µm to produce LFP coatings with an areal capacity of 2.4 mAh g^{-1}. The coatings were calendered to a coating density of 2.0 g cm^{-3} and cut into pouch cell format.

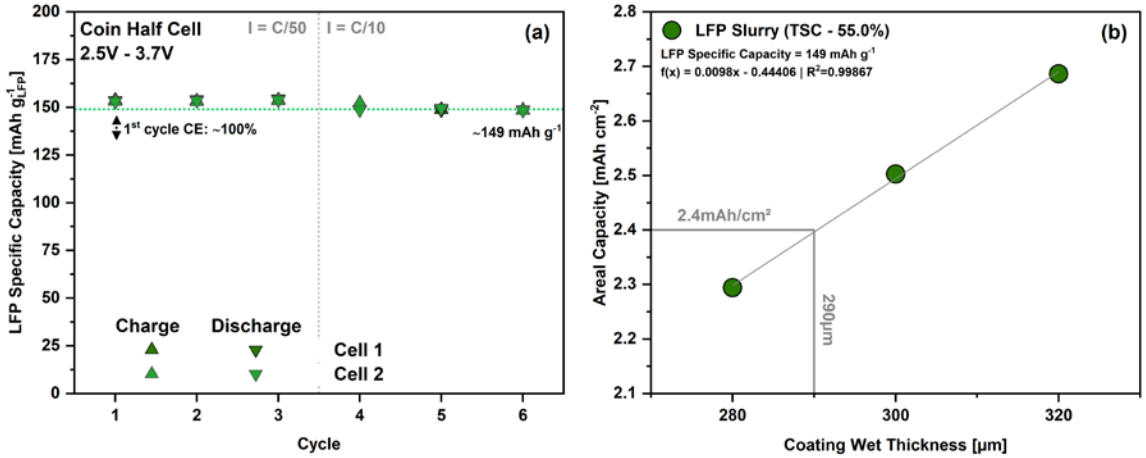

Figure 7.11 a) 2032-coin half-cell (Li‖LFP) data of LFP electrodes. The protocol involves three CCCV-lithiation and CC-delithiation cycles of the electrode AM at a current density of C/50 and C/10 in the potential window 2.5 – 3.7 V. b) Linear relationship between coating wet thickness and areal capacity.

Figure 7.12 and **Figure 7.13** show SEM images of the water-based processed LFP electrodes with standard and perforated current collectors, respectively. Electrodes with the standard current collector system exhibit a uniform distribution of components and surface texture throughout the coating. In contrast, electrodes with the perforated current collector system exhibit distinct outlines of the holes. Three regions can be distinguished on the coating surface with the naked eye: the "land" region, the "transition" region, and the "hole" region (**Figure 7.13a**).

Higher-magnification SEM images of the hole, transition, and land regions reveal visible differences in surface texture. The hole region surface texture (**Figure 7.13c**) appears to be similar to the LFP coating surface texture on the standard current collector (**Figure 7.12b**). The land region (**Figure 7.13b**) shows a less compact surface texture, while the transition area (**Figure 7.13c**) shows a more compact surface texture. This optical distinction indicates the previously discussed possibility of regions with different levels of densification across the electrode surface when perforated current collectors are used as substrates (discussed in ***Chapter 6.3*** on page 53).

Lastly, **Figure 7.13e** shows a cross-sectional SEM image revealing a well-adhered interface between the coating and the current collector without cracks. Moreover, the electrode's backside remained free of coating, except for a slight overlap at the transition area. As-prepared LFP electrodes with standard and perforated current collectors were used in the single-layer demonstrator pouch cells discussed in the next chapter (**Chapter 7.3** on page 78).

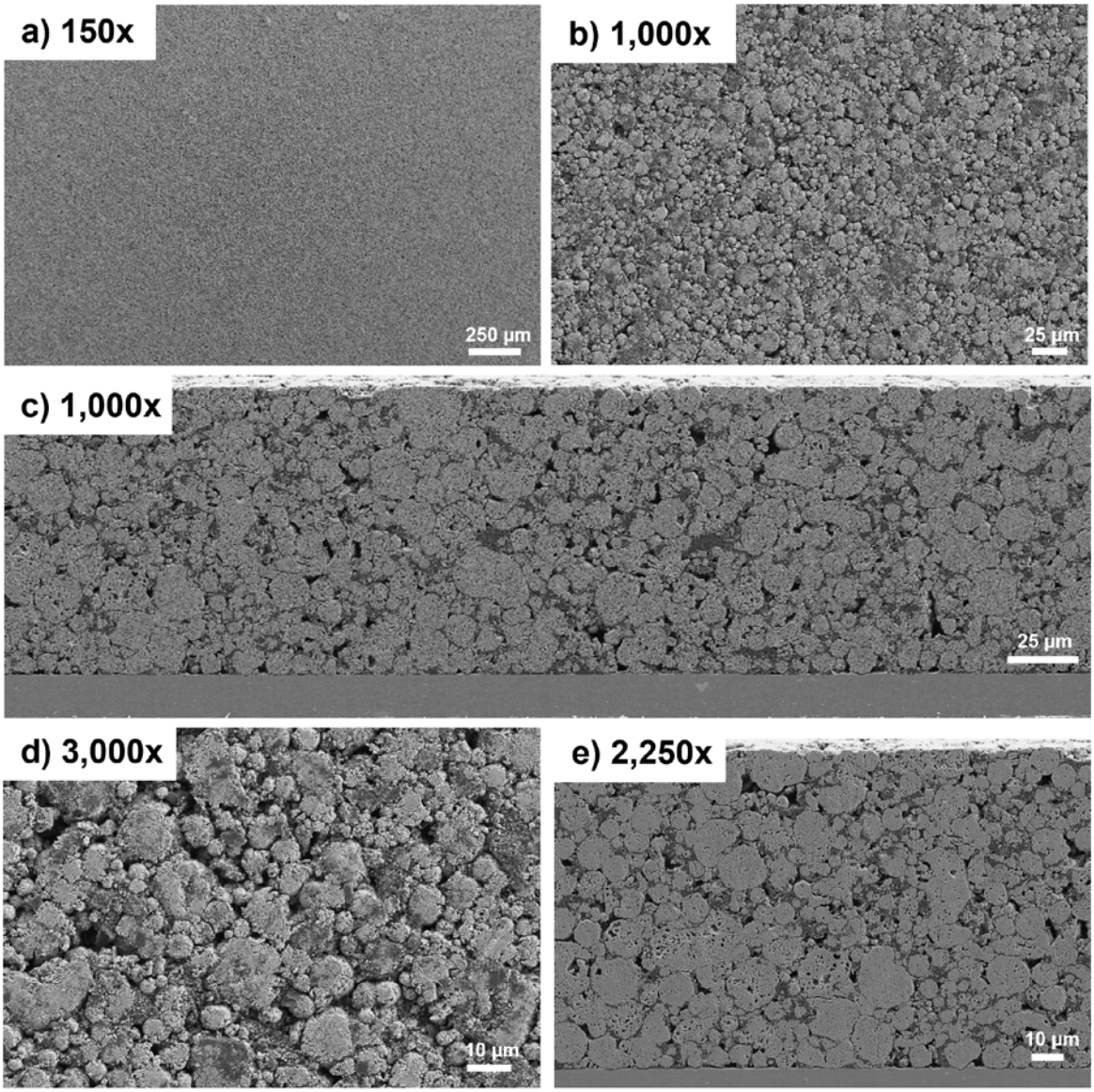

Figure 7.12 SEM micrographs of LFP coating deposited on a standard aluminum current collector foil: a) top-view image at 150× magnification, b) top-view image at 1,000× magnification, c) cross-sectional image at 1,000× magnification, d) top-view image at 3,000x magnification, and e) cross-sectional image at 2,250x magnification.

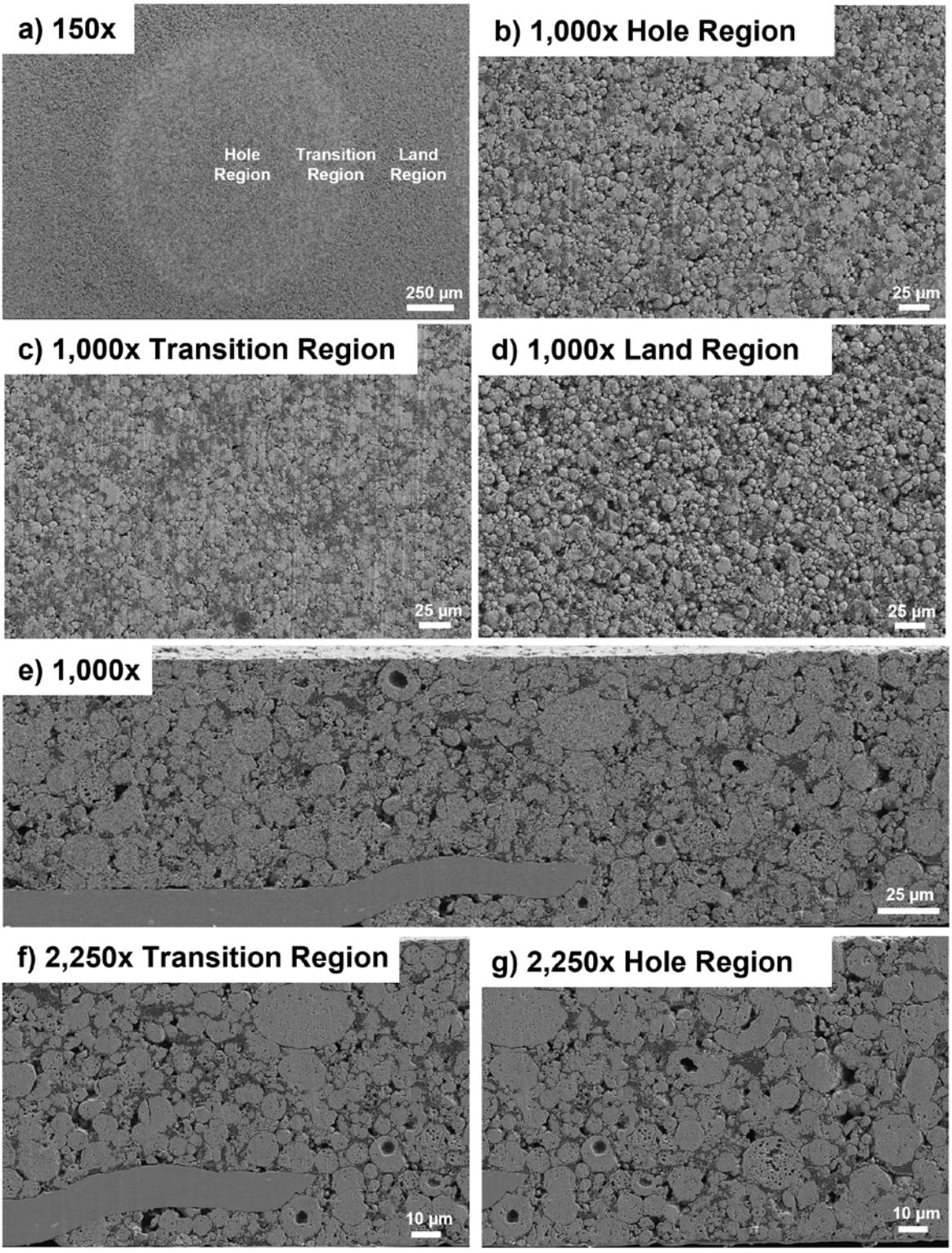

Figure 7.13 SEM micrographs of LFP coating deposited on a perforated aluminum current collector foil: a) top-view image at 150× magnification, b) top-view image of hole region at 1,000× magnification, c) top-view image of transition region at 1,000× magnification, d) top-view image of land region at 1,000× magnification, e) cross-sectional image at 1,000× magnification, f) cross-sectional image of transition region at 2,250x magnification, and g) cross-sectional image of hole region at 2,250x magnification.

7.3 Single-Layer Demonstrator Pouch Cells

In **Chapter 6.4** (page 62), the permeability of electrodes with perforated current collectors was demonstrated in a modified Graphite‖LFP‖Li-Donor single-layer pouch cell setup. ICLs of the cell were successfully compensated by prelithiation at the cell level using the Li-donor electrode during cell formation. However, next to ICL compensation the formation of an unintended anodic Li-reservoir was observed in the cycling data of the prelithiated cells. These cells' uncontrolled elevated active lithium inventory poses safety concerns due to lithium plating and restricted further performance testing. Furthermore, initial produced LFP electrodes with perforated current collectors exhibited coating defects on their backsides, which negatively impacted their kinetics compared to cells with standard current collectors.

In this chapter, optimized LFP electrodes (see **Chapter 7.2.2** on page 82) will be used and the formation protocol will be fine-tuned to enable accurate control of the cell's initial active lithium inventory. In agreement with the theoretical discussion in **Chapter 7.1** (page 72), three distinct Graphite‖LFP single-layer pouch cell systems that differ only in the size of their initial active lithium inventory will be assembled and investigated.

i) ***Standard***, where ICL are not compensated
ii) ***PreLi***, where ICL are compensated
iii) ***Li-Reservoir***, where ICL are compensated and an additional anodic lithium reservoir equivalent to 10% of the cell's capacity is provided.

7.3.1 Single-Layer Pouch Cell Setups

Two single-layer pouch cells (58 mAh) from each setup illustrated in **Figure 7.14** (Standard, PreLi, and Li-Reservoir) were assembled. Celgard 2325 was used as separators and 1.2 mL of 1 M LiPF6 in EC:EMC (3:7) + 2 wt.% VC was used as the electrolyte. The N/P-ratio at the electrode level was set to 1.25 for all cells. After assembly, the cells were clamped between two plexiglas plates under a pressure of approx. 4 N cm^{-2} and left to rest for 10 hours to allow sufficient time for the electrolyte to soak into the electrodes and separator.

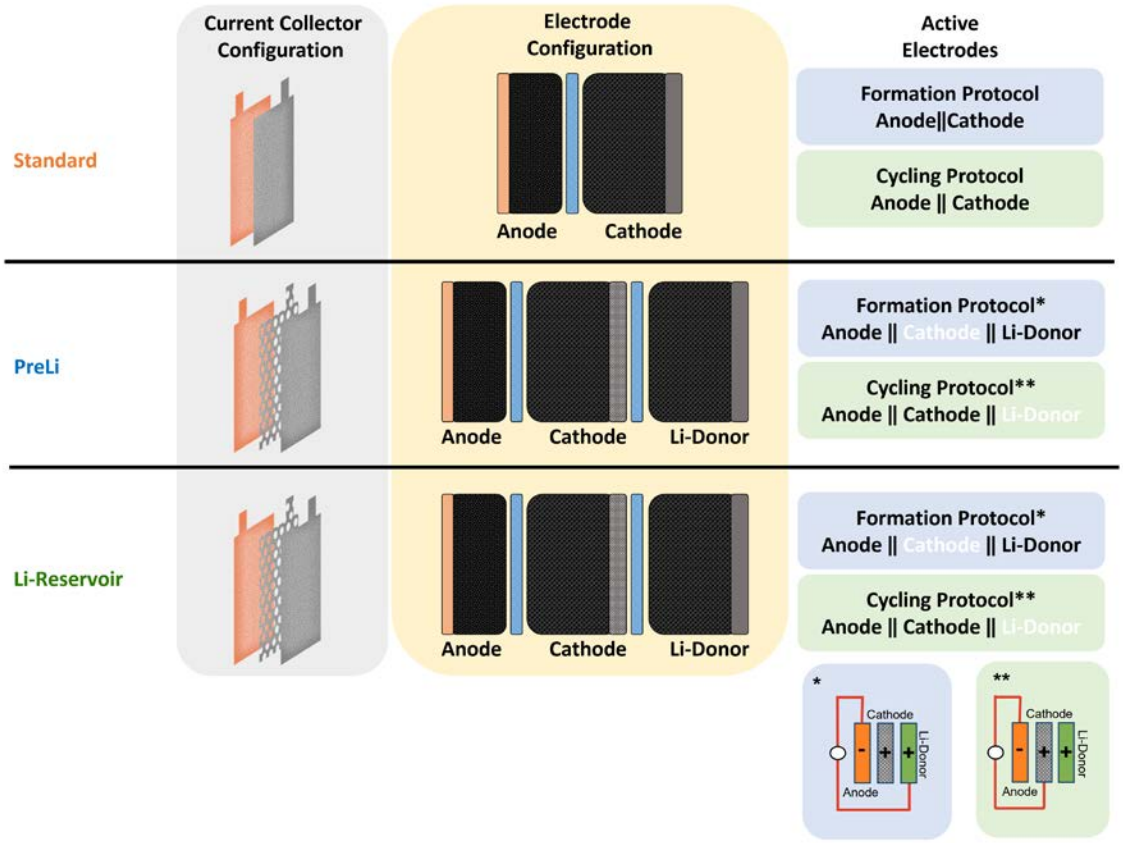

Figure 7.14 Illustration of various Graphite‖LFP single-layer pouch cell setups, along with the electrode connections during the formation/prelithiation and cycling protocols. Black-marked electrodes are active in the respective protocol, while white-marked electrodes remain inactive.

All cells contained graphite and LFP electrodes prepared as described in **Chapter 7.2** (page 78).

7.3.2 Formation, Prelithiation and Establishing the Li-Reservoir

Five formation cycles were performed within the voltage window 2.5 – 3.7 V, using a CCCV-charge (I until V_{cell} > 3.7 V; V = 3.7 V until I < C/20) and a CC-discharge (I until V_{cell} < 2.5 V) protocol at a C-rate of C/10. The active electrodes during cell formation for each pouch cell setup are indicated in **Figure 7.14**.

Figure 7.15a summarizes all formation protocol steps, **Figure 7.15b** shows the initial charge and discharge voltage profiles, **Figure 7.15c** shows the charge and discharge capacities, and **Figure 7.15d** shows the accumulated capacity after each protocol step.

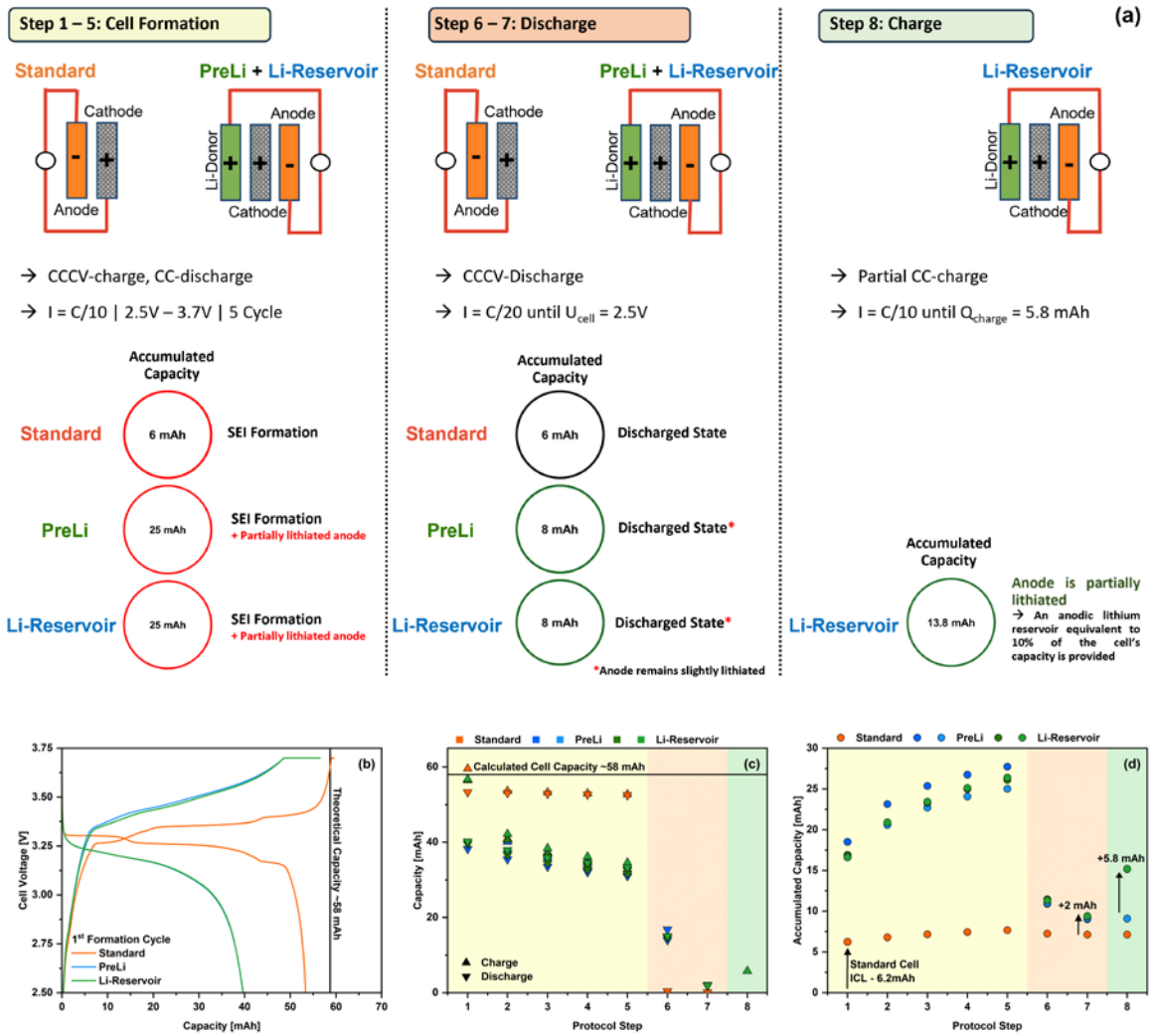

Figure 7.15 Formation data of Standard, PreLi and Li-Reservoir Graphite‖LFP single-layer pouch cell setups. a) Measurement protocol overview, b) voltage profiles of the initial charge and discharge, c) capacity as a function of protocol step, and d) accumulated capacity as a function of protocol step. All cells contain a postive electrode with an areal capacity of ~2.40 mAh cm^{-2}, a N/P-ratio of 1.25, and LP10VC02 as electrolyte. In the PreLi and Li-Reservoir cells, the Li-donor electrode is connected to the anode, while the sandwiched lithium-ion permeable cathode remains inactive.

The characteristic Graphite‖LFP voltage profile is observable during the initial charge and discharge of the Standard cell (**Figure 7.15b)**. Three distinct voltage plateaus mirror those of the negative electrode due to the flat voltage profile of LFP and correspond to the formation of lithium-graphite intercalation compounds.[112,228] The initial charge capacity corresponds to the theoretical calculated cell capacity. A 1st cycle CE of approx. 90% is obtained, followed by stable high CE values (> 99%) in subsequent cycles (**Figure 7.15c**). Thus, anodic SEI formation resulted in an ICL of approx. 10% (~6 mAh) in the Standard cells.

PreLi and Li-Reservoir cell setups, which feature an inactive LFP electrode that must be traversed by lithium ions to reach the anode, show significantly pronounced overpotentials in their initial charge and discharge voltage profiles (**Figure 7.15b**). Polarization effects within the cell limit the CC-charge and CC-discharge capacities. Even the additional CV-charge step is insufficient to achieve full delithiation of the Li-donor electrode in the applied formation protocol. A poor 1st cycle CE of approx. 70% is observed, followed by persistently low CE values (< 96%) in the subsequent formation cycles (**Figure 7.15c**). After formation protocol, PreLi and Li-Reservoir cells show an enhanced accumulated capacity of approx. 25 mAh, which is a plus of 19 mAh (~33% of the cell's capacity) compared to the Standard cells (**Figure 7.15d**).

A similar electrochemical behavior has been observed and discussed in initial demonstrator cells of this study, which employed similar single-layer pouch cell setups and formation protocols, as described in **Chapter 6.4** (page 62). The modified cells' accumulated capacity during formation protocol exceeded that of the reference cells also by up to 33 mAh. Thus, the obtained formation data from initial and here presented modified cell setups at a C-rate of C/10 are reproducible and reflect configuration or protocol specific limitations. The cycling data from prelithiated cells presented in **Chapter 6.4** indicated the presence of an unintended anodic Li-reservoir. It was proposed that the cell's kinetics hinder the anode's complete delithiation during discharge in the applied formation protocol. Therefore, the formation of an anodic Li-reservoir, rather than higher ICLs, would account for the differences in accumulated capacity. However, the differentiation between irreversible ICLs and unintended anodic Li-reservoir formation could no longer be quantified in these initial demonstrator cells of **Chapter 6.4**.

The cells of the current chapter can now be used to verify this hypothesis. Two CCCV-discharges (I until V_{cell} < 2.5 V; V = 2.5 V until I < C/40) at a C-rate of C/20 were applied to all cell systems (protocol step 6 – 7 in **Figure 7.15a**).

As expected, Standard cells cannot be discharged further as shown in **Figure 7.15** (protocol step 6 – 7). After cell formation (protocol step 1 – 5) they are in a fully discharged state. The accumulated capacity corresponds to its ICLs. In contrast, the PreLi and Li-Reservoir cells show a significant discharge activity in protocol step 6 and minor discharge activity in step 7. This data demonstrates that the anode in these modified pouch cell setups remained partially lithiated after the formation protocol is completed. The accumulated capacity of the PreLi and Li-Reservoir cells

after protocol step 7 remains 2 mAh higher than that of the Standard cells (**Figure 7.15d**). Either a small Li-reservoir equivalent to ~3% of the cell's capacity or a slightly higher irreversible ICL can explains these differences. However, no further discharge was performed, as the already low applied current was insufficient to fully extract any remaining active lithium from the anode, if present. It can be concluded, that an accurate compensation of the cell's ICLs is achieved in PreLi and Li-Reservoir cells after protocol step 7.

Lastly, an additional relithiation treatment was performed to the Li-Reservoir cells to create a well-controlled anodic Li-reservoir equivalent to 10% of the cell's capacity. A CC-Charge at a C-rate of C/10 was applied until active lithium equivalent to a capacity of 5.8 mAh were transferred from the Li-donor to the graphite electrode as shown in **Figure 7.15** (protocol step 8).

It can be concluded that the prelithiation approach demonstrated here offers high control over the degree of prelithiation. **Figure 7.15** shows the data obtained during the prelithiation treatment, which indicates the successful preparation of three distinct Graphite‖LFP single-layer pouch cell systems that differ only in the size of their initial active lithium inventory. Namely, Standard cells with an active lithium inventory equivalent to 90% of $Q_{cathode}$, PreLi cells with an active lithium inventory equivalent to 100% of $Q_{cathode}$, and Li-Reservoir cells with an active lithium inventory equivalent to 110% of $Q_{cathode}$.

Up to this point in this study, the prelithiation treatment included a full formation protocol of five cycles at C/10, using the anode and Li-donor electrode as the active electrodes, as described in **Chapter 6.4** and in the present chapter. In this formation protocol, polarization effects within the cell limited the charge and discharge capacities, leaving the anode partially lithiated afterwards. Adjusting the protocol prevents the unintentional formation of an anodic Li-reservoir and enables a well-controlled degree of cell prelithiation, as demonstrated in the present chapter (***Figure* 7.15**). However, these adjustments go hand in hand with lower C-rates and, consequently, longer cell formation times, which may pose economic challenges for the implementation of this concept in the LIB industry.

From this point of view, the prelithiation approach at the cell level should be rather regarded as a relithiation treatment at the cell level. The formation protocol should be performed as usual using the anode and cathode as active electrodes. ICLs during cell formation can be exactly quantified and subsequently compensated by a single, short, and well-controlled relithiation step of equivalent capacity using the Li-donor electrode. Thus, rather than being prelithiated during formation, the cell would undergo relithiation after formation. This would enable accurate management and control of the cell's active lithium inventory. This forward-thinking approach will be applied to and discussed in stacked Graphite‖LFP pouch cells in **Chapter 8.2** (page 126) and in single-layer SiC‖LFP pouch cells in **Chapter 9.1** (page 147).

7.3.3 Rate Capability and Electrochemical Characterization

Next, a discharge rate capability protocol was performed within the voltage window 2.5 – 3.7 V, using a CCCV-charge (I_{Charge} until V_{cell} > 3.7 V; V = 3.7 V until I < C/20) and CC-discharge ($I_{Discharge}$ until V_{cell} < 2.5 V) protocol with I_{Charge} = C/10 and $I_{Discharge}$ = C/10, C/20, C/5, C/2 and 1C. The active electrodes during cycling protocols for each pouch cell setup are indicated in **Figure 7.14**.

Figure 7.16 shows the rate capability test data for all cell systems under investigation. PreLi and Li-Reservoir cells exhibit significantly higher LFP specific capacities at discharge C-rates below 1C compared to Standard cells. At very low C-rates (C/20, cycles 11 - 13), almost the full LFP specific capacity can be utilized for reversible energy storage in these prelithiated cells. This corresponds to a 10% improvement in LFP specific capacity utilization relative to Standard cells and demonstrates the successful compensation of ICLs in both cell systems.

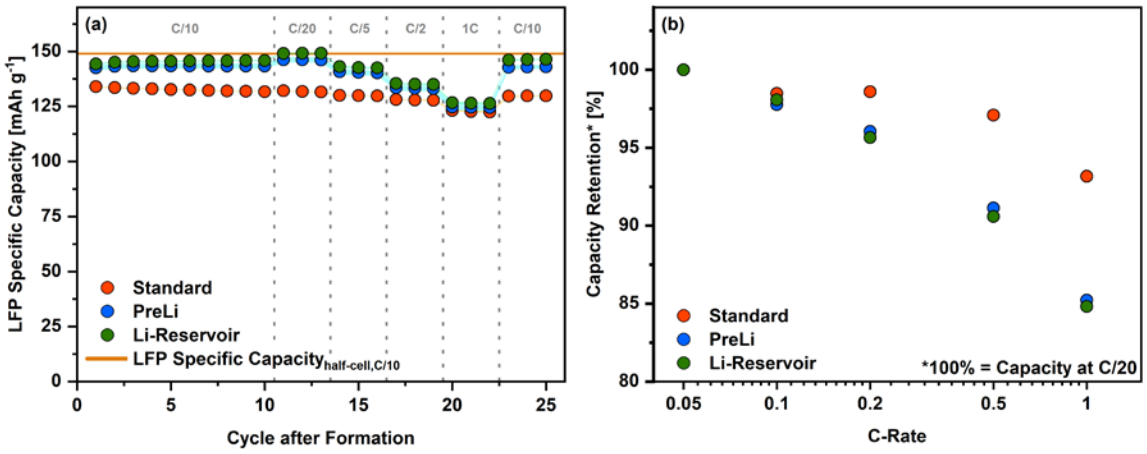

Figure 7.16 Discharge rate capability data of Standard, PreLi and Li-Reservoir Graphite‖LFP single-layer pouch cell setups: a) LFP specific capacity as a function of cycle number, and b) capacity retention as a function of C-rate. The measurement is performed in the voltage window 2.5 – 3.7 V. All cells contain a positive electrode with an areal capacity of ~2.40 mAh cm^{-2}, a N/P-ratio of 1.25 and LP10VC02 as electrolyte.

The main difference of all cell systems is the size of their active lithium inventory. In Standard cells, the active lithium inventory is equivalent to 90% of the cathode's capacity. ICLs during cell formation led to an active lithium deficiency within the cell and, consequently, only 90% of the cathode's maximum capacity can be used for reversible energy storage. In PreLi cells, the active lithium inventory is eqivalent to 100% of the cathode's capacity. As a result, the full cathode capacity can be utilized for reversible energy storage. In Li-Reservoir cells, the active lithium inventory is equivalent to 110% of the cathode's capacity. However, still only 100% of the cathode's capacity can be utilized for reversible energy storage, as the cathode remains the capacity-limiting electrode in the full-cell configuration.

At C/20, the cell's active lithium inventory relative to the cathode's capacity (deficit, balanced or surplus) together with the maximum capacity of the cathode limit the cells utlizable capacity (**Figure**

7.16). Kinetic limitations are additional factors that come into play at higher C-rates. In fact, the capacity retention of PreLi and Li-Reservoir cells clearly decreases with increased C-rates, while the one of Standard cells exhibit a plateau up to C/2. This result suggests that the capacity retention of PreLi and Li-Reservoir cells is limited by ionic or electronic conductivity of the electrodes at C-rates above C/20. In contrast, the capacity retention of Standard cells up to C/2 appears to be primarily limited by their active lithium deficiency and not its electrode's kinetics. At a discharge rate of 1C, all cell systems exhibit similar LFP specific capacity utilzation. This implies that, beyond this point, ionic and electronic conductivity of the electrodes, rather than the size of the active lithium inventory of the cell, become the dominant limiting factor for all cell systems.

The next key question is whether the active lithium inventory in the cells can be examined or even quantified.

As highlighted previously, the voltage plateaus in Graphite‖LFP cells can be directly attributed to the formation of lithium-graphite intercalation/deintercalation compounds due to the flat voltage profile of LFP.[112,228] This feature of Graphite‖LFP cells can be used to gain in-depth insights into the graphite lithiation/delithiation activity of prelithiated and non-prelithiated cells by comparing the intensity of these plateaus using their derivative analysis (dQ/dV-plots). For this purpose, the voltage plateau peaks are labeled I, II, and III in the dQ/dV-plot. Peak III activity relates to the last voltage plateau associated with the formation or decomposition of the fully lithiated graphite structure, LiC_6.[112]

Figure 7.17 shows the voltage profile and dQ/dV-plot of the 12th cycle of the rate capability test at C/20 for all cell systems. Peak II activity highly overlaps with no observable shift in voltage or intensity across all cells and systems. This indicates equivalent cell properties with respect to electrode design, N/P-ratio, and cell kinetics. Overall, this electrochemical consistency indicates a substantial enhancement in the quality of the electrodes compared to those in the initial demonstrator cells (**Chapter 6.4** on page 62). In those, the perforated current collector electrodes exhibited pronounced overpotentials compared to the unmodified ones. However, it was not possible to determine whether the overpotentials originated from the current collector design or from coating defects on the back of the respective LFP electrodes. The optimized LFP electrodes with perforated current collectors used in the present chapter do not have any coating defects on their backsides, and the kinetic drawbacks within full-cell measurements seem to have disappeared, as clearly shown in **Figure 7.17a**. This suggests that the perforated current collector design introduced in this work does not significantly affect the electrode's kinetics. Further investigations of current collector substitution and its impact on cell performance are presented in **Chapter 8.2** (page 126) using bi-layer pouch cells.

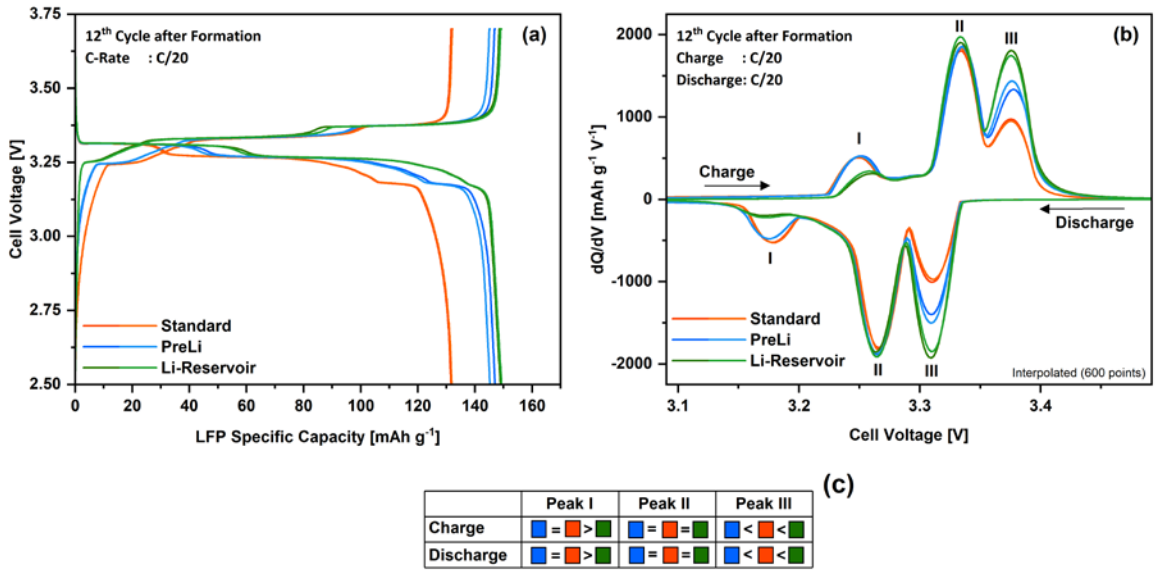

Figure 7.17 Voltage profile (a), derivative analysis (dQ/dV-plot) (b), and comparison of the corresponding dQ/dV-plot peak activities (c) of the 12th rate capability test cycle at C/20 for Standard, PreLi and Li-Reservoir Graphite‖LFP single-layer pouch cells.

Furthermore, the dQ/dV-plot in **Figure 7.17b** clearly reveals differences in the activity of peak I and III in the systems. Peak I activity in the derivative analysis mirrors the first voltage plateau activity of the graphite electrode at low states of lithiation. In both the Standard and PreLi cells, the graphite electrode is mostly delithiated in the cells discharged state, and the two cell systems exhibit similar peak I activity during cycling. In contrast, Li-Reservoir cells show significantly reduced peak I activity. This strongly supports the concept that the graphite electrode remains partially lithiated in the discharged state of these cells. Peak III activity in the derivative analysis mirrors the last voltage plateau activity of the graphite electrode at high states of lithiation. Li-reservoir cells exhibit the highest peak III activity, followed by PreLi cells and, finally, Standard cells.

It can be concluded that the size of the active lithium inventory in Graphite‖LFP cells can be estimated from their voltage profiles if a reference is available. In the dQ/dV-plots (**Figure 7.17**) Standard cells are the reference system. A prelithiated cell can be identified by similar peak I and II activity and enhanced peak III activity. An anodic Li-reservoir can be identified by a reduction in peak I activity accompanied by a simultaneous increase in peak III activity. On the other hand, similar peak I and II activity combined with a reduced peak III activity would correspond to a reduction of the active lithium inventory e.g., ALL during cycling.

However, the voltage profiles and corresponding dQ/dV-plots presented still cannot quantify the exact size of the cell's active lithium inventory. As discussed, the cell's active lithium inventory size can exceed the equivalent cathode's capacity but should never exceed the equivalent anode's capacity. Next to $Q_{cathode}$, Q_{anode}, and, Q_{cell} a Li-inventory capacity ($Q_{Li\text{-}inventory}$) should be defined. To ensure safe cell operation, $Q_{Li\text{-}inventory}$ must be between 0 and Q_{anode}. Consequently, the $Q_{Li\text{-}inventory}$ can be quantified by the cell's maximum degree of anode lithiation according to **Equation 7.3**. The

active lithium inventory size can afterwards be expressed relative to the cell's maximum reversible capacity ($Q_{rev,cathode}$), according to **Equation 7.4**.

$$Q_{Li-inventory} = Anode\ Lithiation\ Degree\ (Charged\ State) \cdot Q_{rev,anode} \quad \textbf{7.3}$$

$$Li - inventory\ size = Q_{Li-inventory} \div Q_{rev,cathode} \quad \textbf{7.4}$$

Figure 7.18 shows the voltage profiles of the 12th cycle of the rate capability test at C/20, as a function of the graphite lithiation degree, for all cell systems. The overlapping activity of the second voltage plateau was used to determine the exact size of the anodic Li-reservoir of each system. For this purpose, the Standard cells served as a fixed reference (graphite lithiation degree of 0% in the fully discharged state). The voltage profiles of the PreLi and Li-reservoir cells were then shifted along the x-axis until their second voltage plateau fully overlapped with that of the Standard cells.

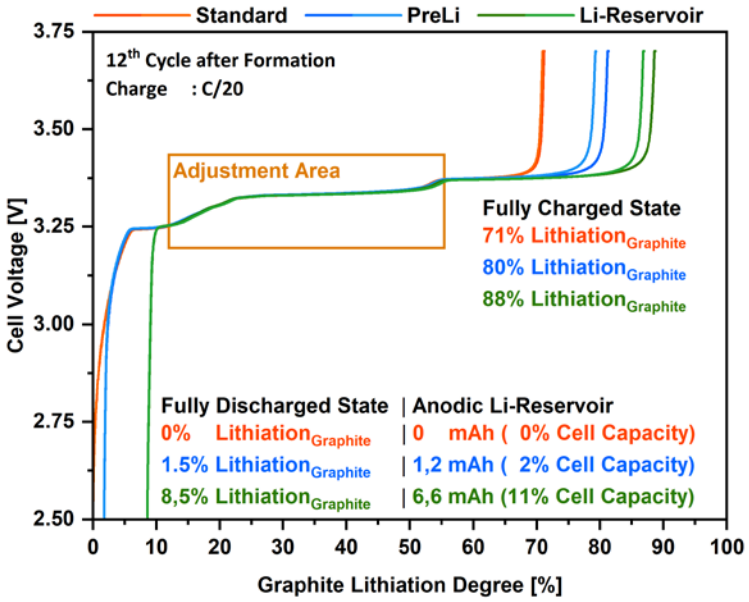

Figure 7.18 Voltage profiles as a function of the graphite lithiation degree of the 12th rate capability charge at C/20 for Standard, PreLi and Li-Reservoir Graphite‖LFP single-layer pouch cells.

Figure 7.18 reveals in depth insights into the anodic lithiation states of all cell systems at a low C-rate. Anodic Li-reservoirs of approx. 2% and 11% of the cell's capacity can be quantified for the PreLi and Li-reservoir cells, respectively. The presence of small anodic Li-reservoir in PreLi cells is in agreement with the formation data discussed in **Chapter 7.3.2** (page 89), where PreLi cells showed a 2 mAh higher ICL compared to Standard cells. It can be concluded that the majority of this difference in ICL was reversibly trapped in the anode and not irreversibly consumed in parasitic reactions. In the fully charged states, anodes of Standard, PreLi and Li-Reservoir cells are lithiated to 71%, 80%, and 88%, respectively. It can be noted that all experimentally measured graphite lithiation degrees in the charged and discharged states fully align with the theoretically predicted values presented in **Chapter 7.1** (page 72). Specifically, lithiation degrees of 0%, 0%, and 8% were

predicted in the discharged state, and 72%, 80%, and 88% in the charged state for the Standard, PreLi, and Li-reservoir Graphite‖LFP cells, respectively.

According to **Equation 7.3** and **7.4**, the Standard, PreLi, and Li-Reservoir cells manufactured and investigated in the present chapter possess the targeted active lithium inventory size corresponding to 89%, 100%, and 110% of the cell's maximum reversible capacity ($Q_{rev,cathode} = Q_{rev,cell}$), respectively.

It can be finally stated that three distinct Graphite‖LFP single-layer pouch cell systems that differ only in their initial active lithium inventory size were successfully fabricated with high accuracy. Moreover, it is demonstratet that in-depth voltage profile analysis is a powerful tool for verifying the size of the active lithium inventory of Graphite‖LFP LIB cells when a reference is available.

7.3.4 Long-Term Cycling and Cell Aging

Following the discharge rate performance test, a long-term cycling protocol was applied within the same voltage window (2.5 – 3.7 V), using a CCCV-charge (I_{Charge} until V_{cell}> 3.7 V; V = 3.7 V until I < C/20) and CC-discharge ($I_{Discharge}$ until V_{cell} < 2.5 V) protocol. One check-up cycle was performed at C/10, followed by 49 cycles at C/2, for a total of 1,701 cycles.

Figure 7.19 shows the long-term cycling data for all cell systems under investigation. For PreLi cell system, one outlier cell was removed; Standard and Li-Reservoir cell systems show two-cell averages with error bars.

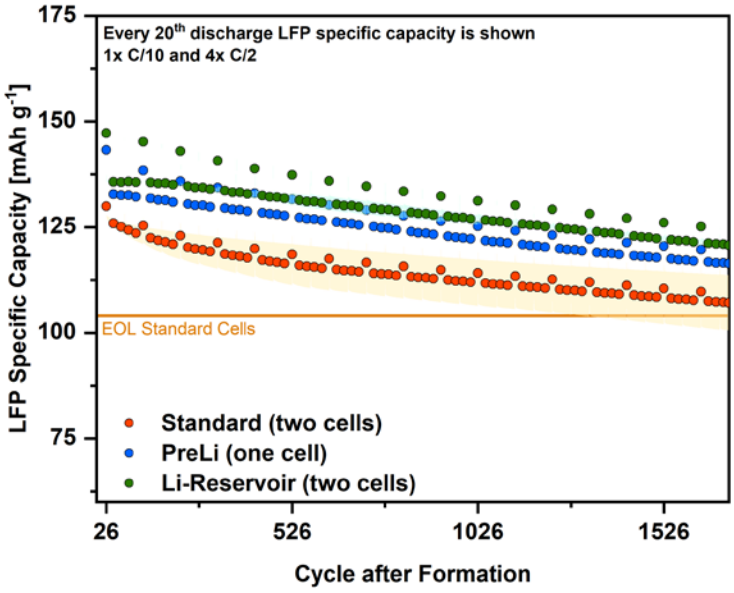

Figure 7.19 Long-term cycling data – LFP specific capacity as a function of cycle number – of Standard, PreLi and Li-Reservoir Graphite‖LFP single-layer pouch cell setups. The measurement is performed in the voltage window 2.5 – 3.7 V. All cells contain a positive electrode with an areal capacity of ~2.40 mAh cm^{-2}, a N/P-ratio of 1.25 and LP10VC02 as electrolyte.

Figure 7.19 demonstrates clearly stable long-term cycling performance of all cell systems under investigation. Standard cells show the lowest initial LFP specific capacity of 130 mAh g^{-1}, which decreases by a total of 20 mAh g^{-1} (~15% of its initial capacity) over the subsequent 1,500 cycles. The cell's initial stages of life come with significantly accelerated loss of LFP specific capacity. Specifically, 11, 5 and 4 mAh g^{-1} are lost at successive 500-cycle intervals. PreLi and Li-Reservoir cells, exhibit higher initial LFP specific capacities of 143 mAh g^{-1} and 147 mAh g^{-1}, respectively, compared to Standard cells. Both advanced cell systems seem to exhibit an aging behavior similar to that of the Standard cells, with LFP specific capacity losses of 12, 6, and 4 mAh g^{-1} over successive 500-cycle intervals, resulting in a total LFP specific capacity loss of 22 mAh g^{-1} in the first 1,500 long-term cycles.

Figure 7.20 shows the evolution of the voltage profiles during the C/10 check-up cycles. ALL can be clearly identified as the primary aging mechanism for all cell systems. In Standard cells, the charge

voltage profiles over all cycles overlap completely, with only the final plateau shrinking over the cell's cycle life due to a decrease in the cell's active lithium inventory. PreLi and Li-Reservoir cells exhibit similar voltage profile evolution over cycle life with the important difference being the presence of an anodic Li-reservoir in their initial state. As clearly visible in **Figure 7.20**, next to a shrinking last plateau activity, an increased first plateau activity can be observed over the cell's cycle life. Once the anodic Li-reservoir has been depleted, only the final plateau activity continues to shrink throughout the cell's cycle life similar to the aging behavior of Standard cells.

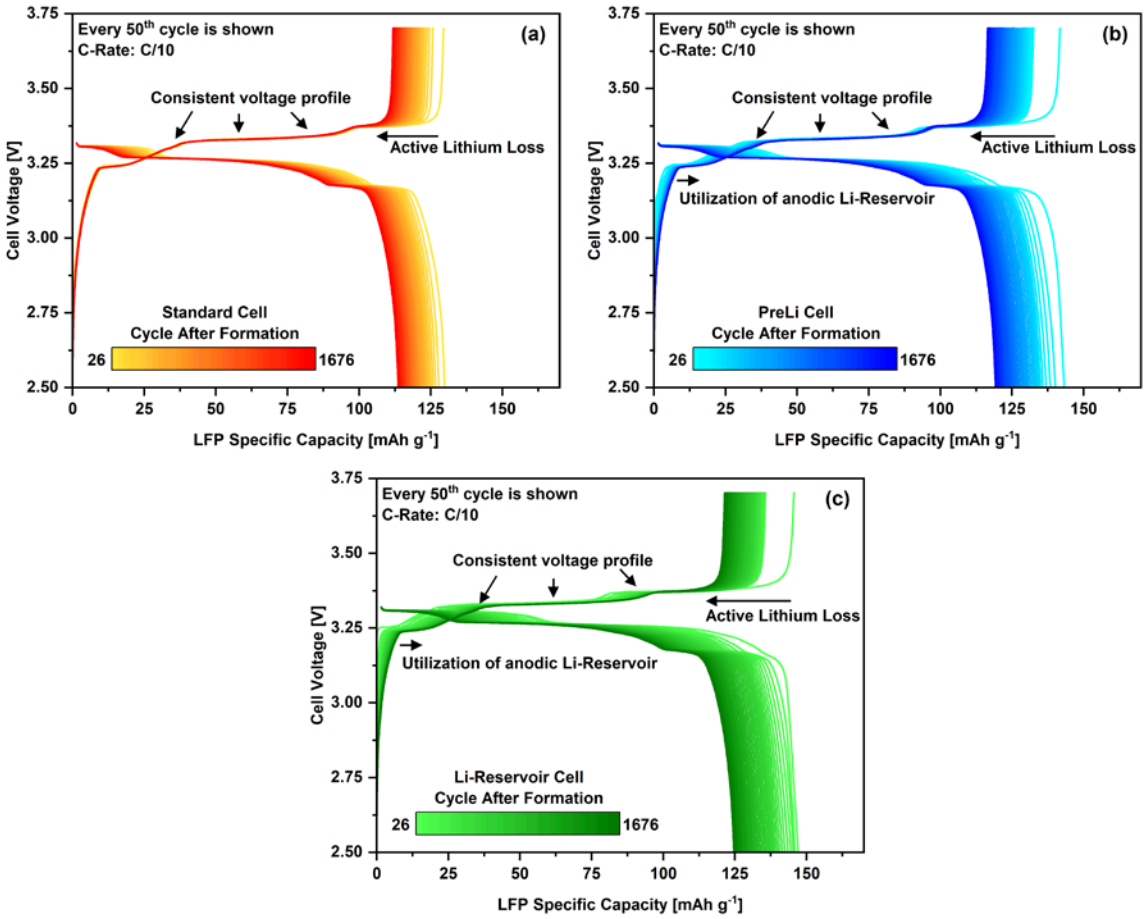

Figure 7.20 Evolution of the C/10 check-up cycle voltage profiles in long-term cycling protocol of a) Standard, b) PreLi, and c) Li-Reservoir Graphite‖LFP single-layer pouch cells.

Notably, discharge capacities appear to exceed charge capacities in the check-up cycle voltage profiles (**Figure 7.20**). This is due to the long-term cycling protocol applied: each check-up cycle is preceded by a C/2 discharge, which can leave the anode partially lithiated because electrode overpotentials trigger the discharge cut-off early. The only exception is the first check-up cycle (cycle 26 after cell formation), which followed a slow C/10 cycle from the preceding rate capability cycling protocol.

Figure 7.21 shows the evolution of the voltage profiles of the C/2 charge following the check-up cycle for all cell systems. These data allow for a more accurate assessment of the Li-reservoir depletion over cycle life, since all cells are fully discharged at the beginning of this C/2 charge step.

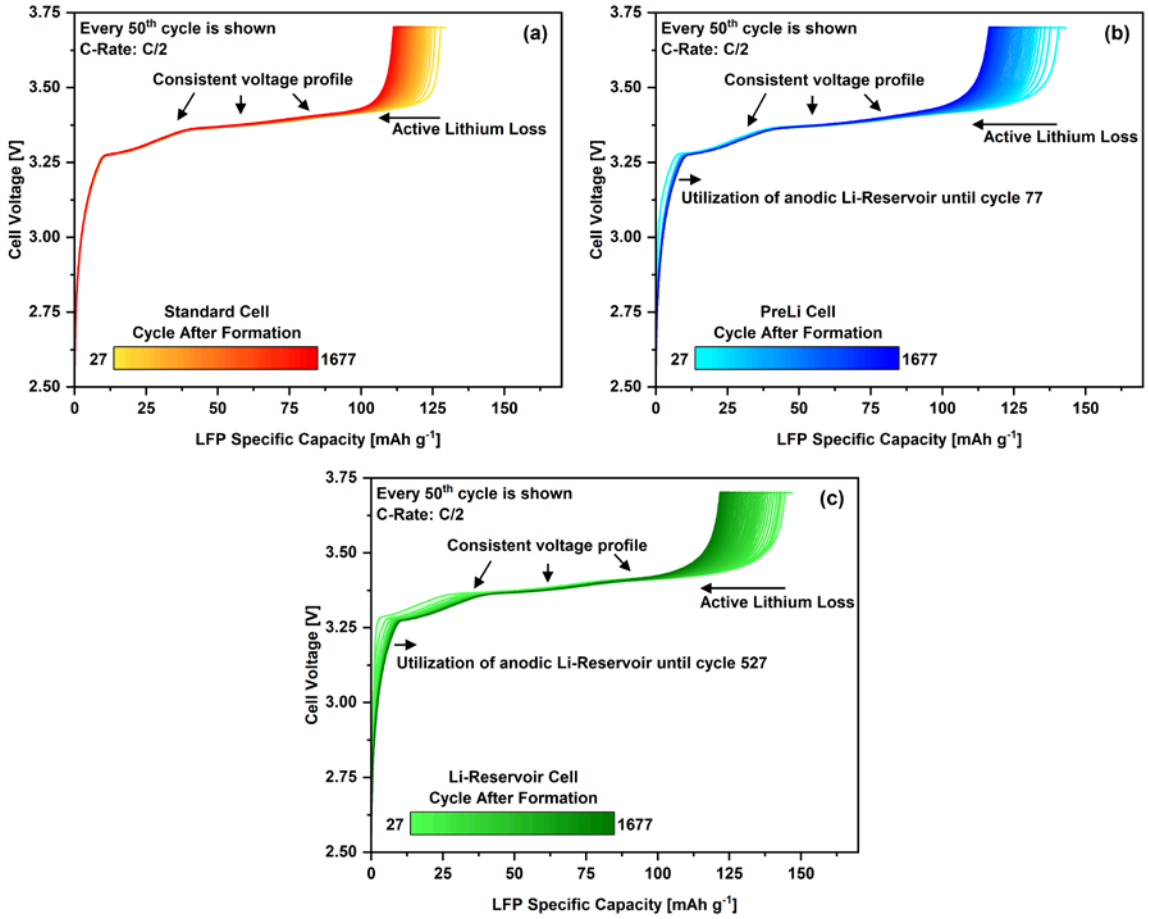

Figure 7.21 Evolution of the C/2 charge voltage profiles following the check-up cycle in long-term cycling protocol of a) Standard, b) PreLi, and c) Li-Reservoir Graphite‖LFP single-layer pouch cells.

Standard cells again display clear ALL aging behavior. In PreLi cells, the small anodic Li-reservoir (~2% of the cell's capacity) is fully consumed within the first 77 long-term cycles. Afterwards, PreLi cells follow a pure ALL aging behavior voltage profile evolution similar to that of Standard cells. In Li-Reservoir cells, the anodic lithium reservoir (~11% of the cell's capacity) is fully depleted by cycle 527. This quantification aligns well with the aging rate obtained in Standard cells, which also exhibit a total ALL of approximately ~10% of the cell's capacity by the same number of long-term cycles.

In theory, depleting the anodic lithium reservoir should maintain a stable LFP specific capacity utilization or cell's SOH. However, **Figure 7.19** and **Figure 7.23** show that there is a continuous fade in LFP specific capacity and SOH also in the first 527 cycles in Li-reservoir cells.

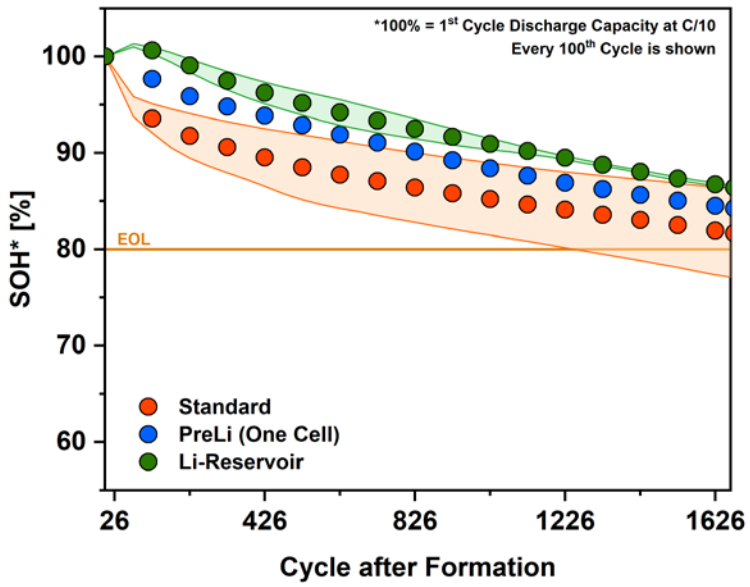

Figure 7.22 Long-term cycling data – SOH as a function of cycle number – of Standard, PreLi and Li-Reservoir Graphite‖LFP single-layer pouch cell setups. The measurement is performed in the voltage window 2.5 – 3.7 V. All cells contain a positive electrode with an areal capacity of ~2.40 mAh cm^{-2}, a N/P-ratio of 1.25 and LP10VC02 as electrolyte.

To quantitatively assess the cell's aging rate, the capacity loss for each cycle and cell system was calculated according to **Equation 7.5**.

$$Capacity\ Loss_{Cycle\ X,C/10} = Capacity_{Cycle\ 1,C/10} - Capacity_{Cycle\ X,C/10} \qquad \textbf{7.5}$$

Figure 7.23a shows the calculated capacity loss as a function of cycle number for all cell systems. Standard cells exhibit a total capacity loss of 9.6 ± 2.4 mAh after 1,676 charge/discharge cycles, followed by PreLi cells with 8.7 mAh and Li-reservoir cells with 7.6 ± 0.0 mAh. PreLi and Li-reservoir cells appear to age more slowly than Standard cells. However, Li-Reservoir cells also appear to show no capacity loss until cycle 176 in **Figure 7.23a**. Since ALL is expected to occur during the first 176 cycles in Li-Reservoir cells, the data plot in **Figure 7.23a** seems not to accurately reflect aging behavior of cells featuring an anodic Li-reservoir. ALL which is compensated by anodic Li-reservoir depletion is not visible in the calculated capacity losses according to **Equation 7.5**. As a consequence, the presented data in **Figure 7.23a** neglects the presence of an anodic Li-reservoir in PreLi (1.2 mAh) and Li-Reservoir (6.6 mAh) cells and underestimates their real aging rate.

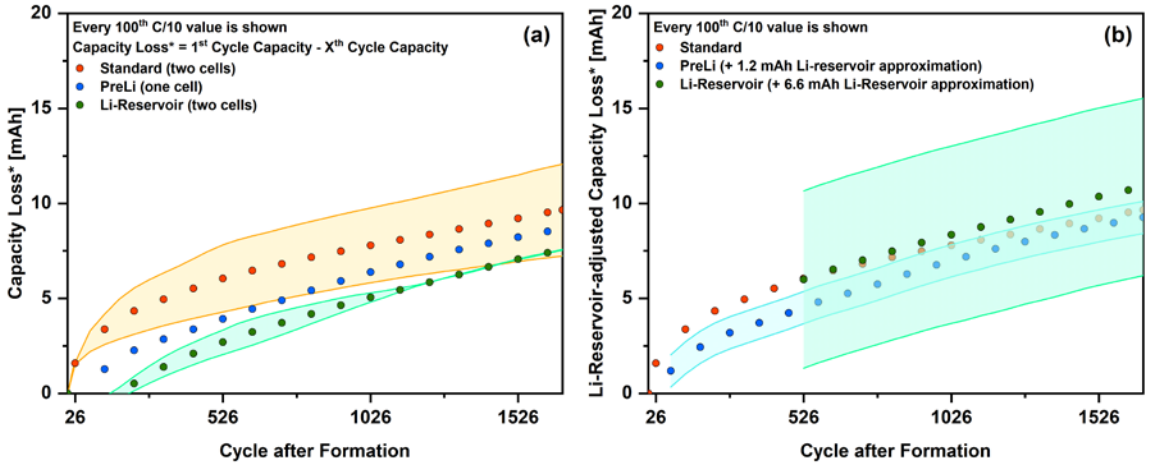

Figure 7.23 Long-term cycling data – a) capacity loss as a function of cycle number and b) Li-reservoir-adjusted capacity loss as a function of cycle number – of Standard, PreLi and Li-Reservoir Graphite‖LFP single-layer pouch cell setups

To approximate the true capacity loss and aging rate of cells with anodic lithium reservoir, the calculated capacity losses according to **Equation 7.5** are considered as the lower limit (no anodic lithium reservoir consumption) and the same values plus the anodic lithium reservoir size represent the upper limit (full anodic lithium reservoir consumption). The real capacity loss of the PreLi and Li-Reservoir cells will lie between these two extremes, as presented in **Figure 7.23b**. Since full anodic lithium reservoir consumption was identified by cycle 76 in PreLi cells and by cycle 526 in Li-Reservoir cells, the Li-reservoir–adjusted capacity loss for each system begins from these respective cycles. From the author's point of view more accurate total capacity loss values are now presented for each cell system. Standard cells still exhibit a capacity loss of 9.6 ± 2.4 mAh after 1,676 charge/discharge cycles, while the Li-reservoir-adjusted capacity losses are 9.3 ± 0.8 mAh for PreLi cells and 10.8 ± 4.7 mAh for Li-reservoir cells.

It can be concluded that Standard and PreLi cells exhibit similar aging behavior, whereas Li-Reservoir cells indicate a slightly higher aging rate. Since the cells differ only in their initial active lithium inventory, the higher aging rate of Li-reservoir cells can be attributed to increased anode stress at high states of charge. While the graphite electrode in Standard and PreLi cells is lithiated to 72% and 80%, respectively, the anode of the Li-Reservoir cell reaches a degree of lithiation of up to 88%. This suggests that a critical threshold exists between the PreLi and Li-Reservoir active lithium inventory sizes for the anode AM used, beyond which the aging rate accelerates slightly.

Lastly, **Figure 7.24** shows voltage profiles and dQ/dV-plots of all cell systems at different cycles with similar levels of active lithium inventory.

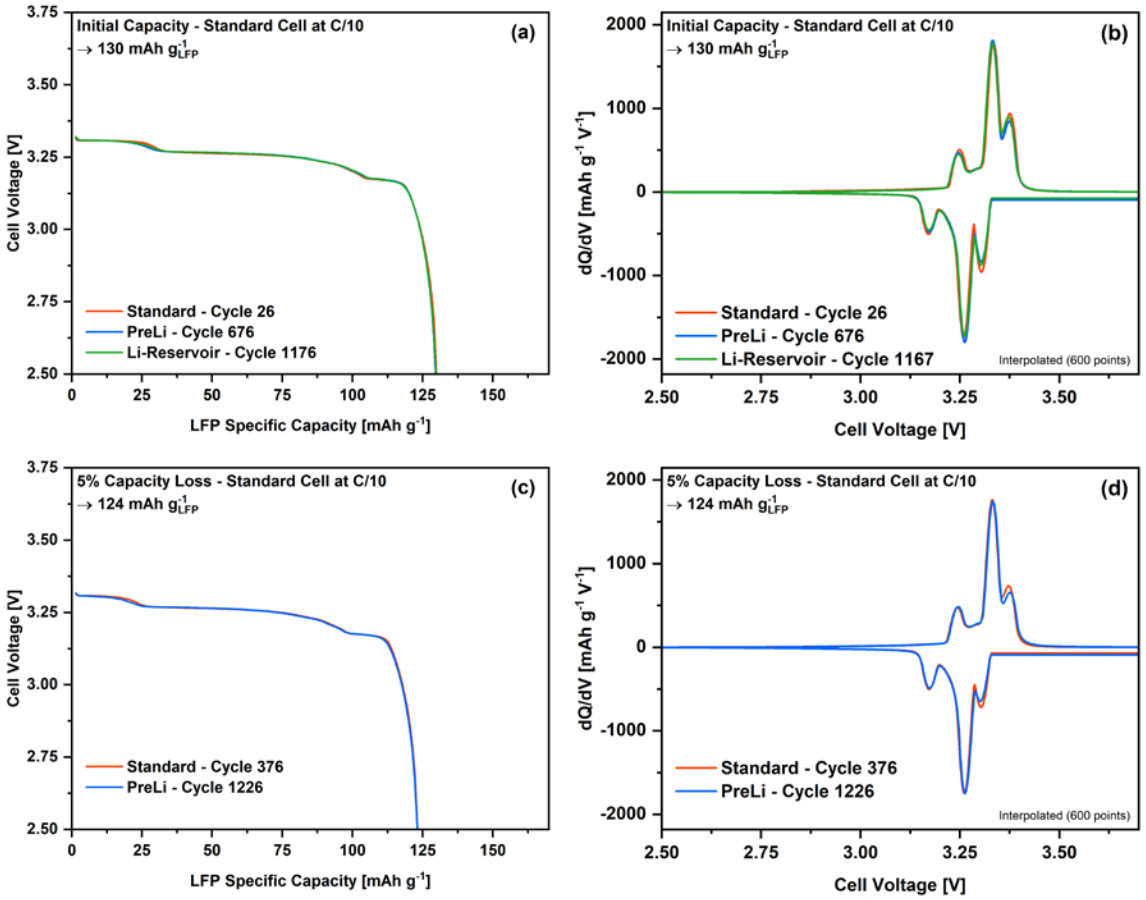

Figure 7.24 Voltage profiles and dQ/dV plots of Standard, PreLi, and Li-Reservoir Graphite‖LFP single-layer pouch cells at different cycle lives, corresponding to similar active lithium inventory levels: a, b) active lithium inventory size equivalent to ~90% of maximum reversible cell capacity and c, d) active lithium inventory size equivalent to ~85% of maximum reversible cell capacity.

PreLi and Li-Reservoir cells reach the initial active lithium inventory size of the Standard cells after 676 and 1,176 cycles, respectively. At these cycles, the voltage profiles and dQ/dV-plots of all cell systems completely overlap (**Figure 7.24a** and **b**), indicating that all cells are in comparable SOH. Apart from ALL, no additional degradation mechanisms are evident in the voltage profiles of PreLi or Li-Reservoir cells compared to the one of the almost uncycled Standard cells. The same analysis is valid for the aged Standard cell at 95% SOH (cycle 376). The PreLi cell reaches an equivalent active lithium inventory size at cycle 1,226. Li-Reservoir cells, have not reached this low level of active lithium inventory even after 1,700 cycles, therefore, the corresponding voltage profile of this system is not available.

7.4 Relithiation of Aged Cells

ALL was identified as the main aging mechanism in all investigated Graphite‖LFP cell systems. No additional degradation mechanisms could be detected as demonstrated in **Figure 7.24**. From a broader perspective, if the active lithium inventory is the sole capacity-limiting factor in aged cells and the AMs, electrodes, and electrolyte remain intact, the cell's initial capacity could be restored several times over the course of its cycle life through a relithiation approach at the cell level that compensates for the cell's active lithium deficiency.

PreLi and Li-Reservoir cell long-term cycling measurements were stopped and the cells were fully discharged at a low C-rate. The Li-donor electrode was connected to the anode again. A CC-charge at C/10 was then applied until an amount of active lithium equivalent to the cell's total active lithium deficiency was transferred from the Li-donor to the graphite electrode. After relithiation at the cell level, the anode and cathode were reconnected, while keeping the Li-donor electrode inactive within the cell. Then, the long-term cycling protocol was started again for the relithiated PreLi and Li-Reservoir cells. This time, the relithiation of Li-Reservoir cells only compensated for the cells' active lithium deficiency and did not establish an additional anodic Li-reservoir.

Figure 7.25a shows the initial (cycle 26 after formation), aged (cycle 1,676 after formation), and relithiated (cycle 1,807 after formation) states of a PreLi cell. It is clearly visible that the cell's full initial capacity could be restored by relithiation of the cell. Furthermore, the first 600 long-term cycles demonstrate enhanced cycling stability for the relithiated compared to their initial cycle life (**Figure 7.25b**). This improvement is likely due to a stabilized anodic SEI at this advanced stage of the cell's life. **Figure 7.25c** and **d** show the voltage profiles at C/10 and C/2 cycles of the PreLi cells in their initial and relithiated states. The voltage profiles largely overlap, indicating that the cell's electrochemistry within the same active lithium inventory remain remarkably similar, even when separated by over 1,800 cycles. To the best of my knowledge, such post-mortem data is not reported in literature, as lack in technology limited the possibility of directly recovering active lithium deficiencies in an aged cell. Here, it is clearly shown that aging in Graphite‖LFP cells does not lead to permanent changes in the electrode's voltage profiles; only the active lithium inventory is reduced, while the electrodes and cell retain their full functionality. Therefore, relithiation of Graphite‖LFP cells appears to be a promising strategy to extend their cycle life, potentially maintaining high energy across a second, third, or even fourth usage phase.

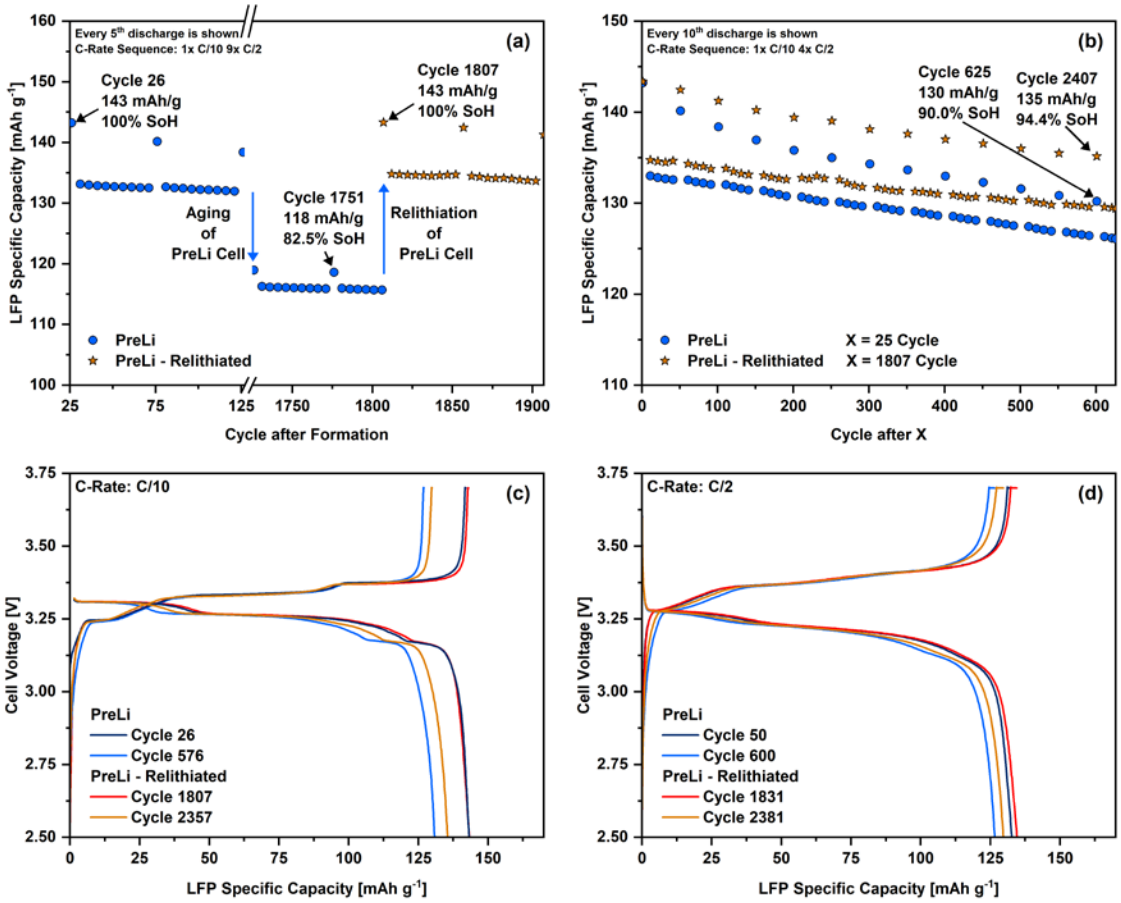

Figure 7.25 Long-term cycling data of a PreLi single-layer pouch cell setup in its initial and relithiated state. a) LFP specific capacity as a function of cycle number, b) comparison of initial and relithiated long-term cycling stability, c) voltage profiles at C/10, and d) voltage profiles at C/2.

The LIB performance results of the relithiation approach presented here is highly reproducible for Graphite‖LFP cells, as demonstrated by similar data for a relithiated Li-reservoir cell, as presented in **Figure 7.26**. The Li-reservoir cell's long-term cycling in the initial (cycle 26 after formation), aged (cycle 1,726 after formation), and relithiated (cycle 1,731 after formation) state is shown. Once again, the cell's full initial capacity is restored through relithiation, accompanied by a reduced aging rate (even this time no anodic lithium reservoir was provided during the relithiation treatment) and voltage profile characteristics similar to those observed during the cell's initial cycle life.

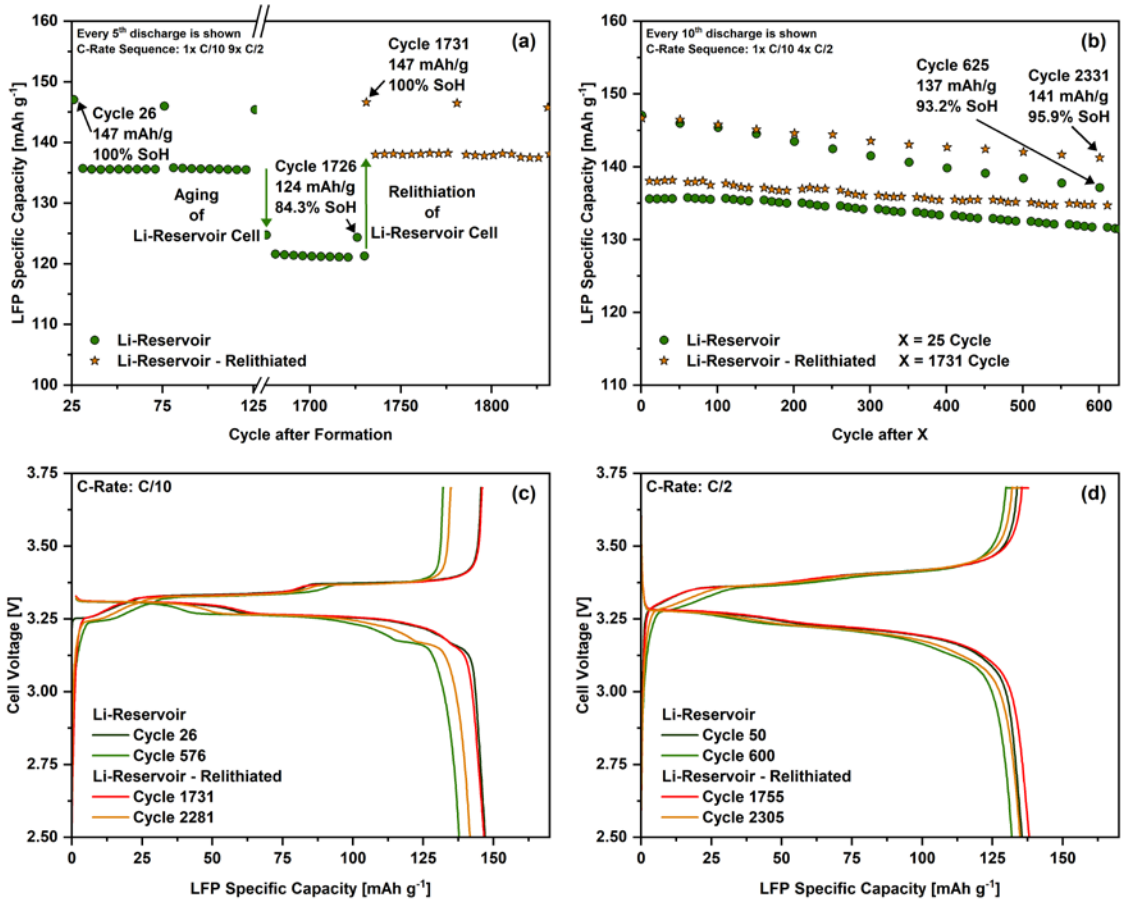

Figure 7.26 Long-term cycling data of a Li-Reservoir single-layer pouch cell setup in its initial and relithiated state. a) LFP specific capacity as a function of cycle number, b) comparison of initial and relithiated long-term cycling stability, c) voltage profiles at C/10, and d) voltage profiles at C/2.

8. Scale Up

8.1 Upscaled Roll-to-Roll Electrode Development

In the context of scaling up electrode production to roll-to-roll processing using perforated current collector systems, simultaneous coating of both sides of the current collector is expected to significantly improve the overall coating quality. **Figure 8.1** illustrates the principle of a simultaneous roll-to-roll coating configuration, which differs from conventional roll-to-roll coating processes.

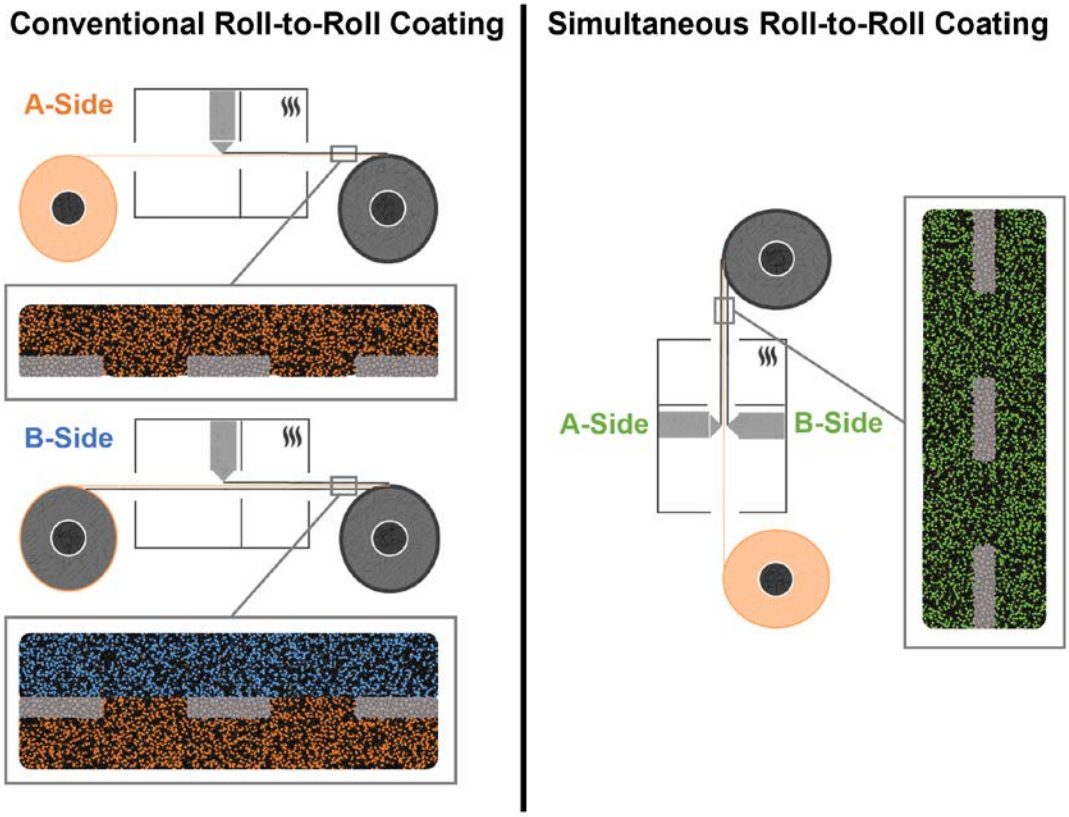

Figure 8.1 Schematic comparison of the conventional roll-to-roll coating process and the modified simultaneous roll-to-roll coating approach.

In a conventional roll-to-roll coating process, the A- and B-Sides of the current collector are coated and dried sequentially (**Figure 8.1** left). For perforated current collectors, however, this sequential approach is expected to introduce several challenges. During A-side coating, the permeability of the current collector allows slurry to pass through. This necessitates protecting the coating device with a nonpermeable, nonadhesive second foil layer to prevent possible contamination. During the B-side coating process, the holes are covered with the dried electrode material from the A-side

coating, which may have surface irregularities, such as overhangs or voids. Thus, the wet-coating layer on the B-side must adhere evenly to two distinct surfaces: the current collector in the land areas and the dried coating layer within the hole areas, all while maintaining homogeneity of the electrode microstructure.

In the modified coating approach, the A- and B-sides are coated simultaneously, allowing the coating layers within the perforations to establish wet-to-wet contact (**Figure 8.1** right). This results in a unified wet coating that encapsulates the perforated current collector from both sides. During drying, the coating solidifies uniformly around the current collector in a fabric-like manner, forming a homogeneous electrode microstructure and potentially improving its mechanical stability. Consequently, the simultaneous coating approach is expected to overcome the limitations of conventional roll-to-roll methods when coating perforated substrates. Not to repeat, in this case, is the fact that realizing this simultaneous coating process was one of the objectives of this work.

Unfortunately, the machine manufacturer of the simulataneous roll-to-roll coater faced economic challenges that markedly delayed the delivery and installation of the device. Consequently, transitioning from lab-scale studies to the simultaneous roll-to-roll coating configuration on a pilot scale coater was not feasible within this study's timeline. Thus, scaling up was done using the conventional roll-to-roll coating equipment available.

The in-house roll-to-roll coater typically processes slurries with viscosities of 10 – 30 Pa s at a shear rate of 1 s^{-1}. However, the slurry viscosity range targeted for coating on perforated current collectors is significantly higher, at 100 – 150 Pa s at a shear rate of 1 s^{-1}. Thus, initial roll-to-roll coatings evaluated the suitability of the available pilot line equipment for the higher-viscosity slurries developed in this study.

Graphite slurries were prepared according to the procedure described in **Chapter 7.2.1** (page 78), with one modification: disperser with a cowles blade was used instead of a centrifugal mixer for mixing the slurry. Two batches of 700 g of graphite slurry with identical formulations and TSC (45%) were prepared; the only difference between the batches was the mixing intensity applied. The first batch (intense mixing) was stirred at an outer rotational dispersing disc speed of 420 cm s^{-1} for three hours, while the second batch (gentle mixing) was stirred at 200 cm s^{-1} for the same duration.

Figure 8.2b shows the flow curves of both batches. The more intense mixed slurry had a final viscosity of 13 Pa s at a shear rate of 1 s^{-1}, whereas the gentler mixed one had a final viscosity of 117 Pa s at a shear rate of 1 s^{-1}. When compared directly to a smaller centrifugal mixer batch (35 g) of the same formulation and TSC, both disperser-prepared slurries exhibited lower viscosity. This indicates that even gentle mixing with the disperser is more intense than the centrifugal mixing process. Grindometer tests confirmed that sufficient mixing was achieved for all batches, as no agglomerates were observed in any of the slurries.

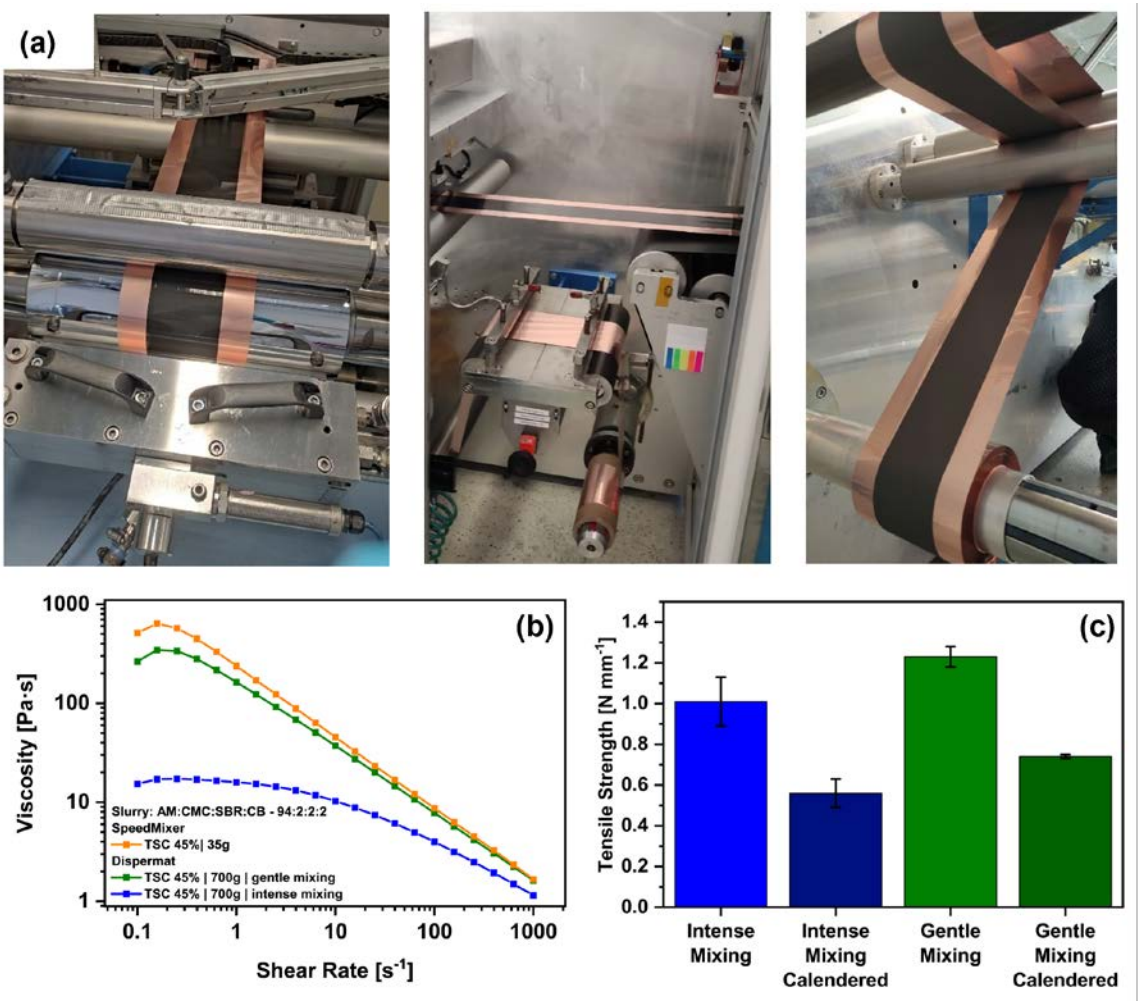

Figure 8.2 Roll-to-roll coating of low and high viscosity graphite slurries onto standard copper foil: a) photographs of the coating process, b) flow curves of graphite slurry batches prepared under different mixing conditions, and c) adhesion test results of roll-to-roll manufactured graphite electrodes.

The lack of reproducibility in slurry rheological properties using the disperser compared to scaling up with the centrifugal mixer (see **Chapter 7.2** on page 78) led to the decision not to further use the disperser for slurry mixing in this study. However, two 700 g graphite slurry batches with similar formulations and TSCs were obtained. Both batches had a slurry density of 1.395 g cm^{-3} and differed only in their viscosity. Thus, these slurry batches were ideal for preliminary testing of the available roll-to-roll coating equipment.

Both 700 g slurry batches were coated onto standard 10-µm-thick copper foil using the available roll-to-roll coater with slot-die coating technique. A constant slurry flow was maintained for both slurry batches throughout the entire coating process. An applied wet thickness of 150 µm resulted in a coating loading of 8.5 mg cm^{-2}, regardless of the slurry's viscosity. Representative images of the coating process are shown in **Figure 8.2a**. The adhesion of both coating layers was evaluated using a Zwick-Roll tensile strength measurement (z-direction test set-up). The gentler mixed slurry coating had higher adhesion in both its initial and calendered states (**Figure 8.2c**). These results

indicate that a gentle yet sufficient mixing process is not only essential for maintaining reproducible slurry properties during scale up, but also influences the final coating properties in terms of mechanical stability.

These preliminary coating trials demonstrate that the roll-to-roll coating equipment available is suitable for the higher-viscosity slurries developed in this study, with no operational difficulties encountered.

8.1.1 Initial roll-to-roll graphite electrode development

In **Chapter 6.1** (page 42), the process of flattening several meter-long perforated copper current collector foils is detailed. As shown in **Figure 8.3**, the flattened perforated foil (about 15 m) was inserted between two standard copper current collector foils (about 25 m) with adhesive strips to get a current collector coil with an appropriate foil length for processing at the pilot line. Additionally, a 20 cm wide silicone-coated paper was included within the foil coil as a protective, non-adhesive second layer. This layer prevents contamination of the coater from potential slurry migration through the perforations during the coating process while ensuring coating adhesion is maintained exclusively to the current collector foil.

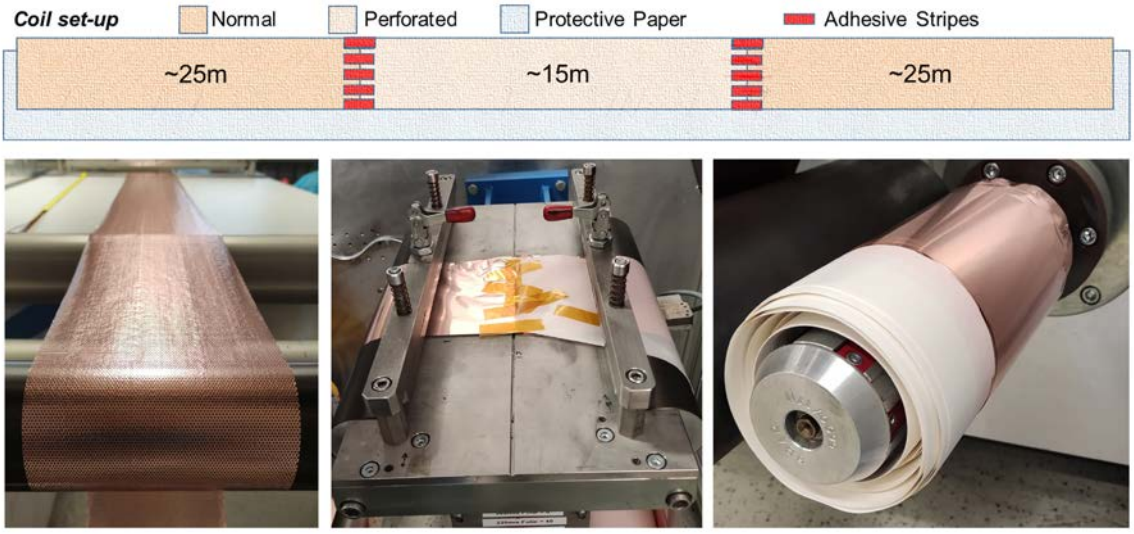

Figure 8.3 Schematic of the modified copper current collector coil and representative photographs of the coil preparation process.

Preliminary lab-scale coatings via the doctor blade technique revealed that a slurry's wet film remains stable on a perforated current collector foil only if the foil's surface is flat, taut, and free of waves or creases. However, it is difficult to achieve this high-quality in foil coils when manually joining sections using foil unwinding and rewinding systems without edge control. Additionally, using multiple adhesive strips to stabilize the foil segments, as well as adding a protective layer, creates irregularities and localized pressure points in the final coil. These defects in the coil are expected to negatively affect the process and quality of the coating. However, due to limited material availability, the prepared foil coil had to be used, even though it may not be perfectly suitable from theoretical point of view.

In **Chapter 7.2.1** (page 78), graphite slurries were scaled up from 35 g to 700 g batches while maintaining consistent slurry properties. Considering the coating length (~45 m), width (8 cm), loading per side (target: 8.8 mg cm^{-2}), and slurry TSC (43%), at least 1.5 kg of graphite slurry is required for the pilot line coating. Therefore, three batches of 700 g of graphite slurry were

prepared. The formulation (AM:CB:CMC:SBR – 94:2:2:2), slurry TSC, electrode materials and processing parameters were kept consistent with those described in **Chapter 7.2.1**.

Figure 8.4 shows photographs of the A-side coating process. The modified coil setup was adequate for this initial coating trial, and sections with a uniform, high-quality coating layer were achieved. Notably, no coating residues were observed on the silicon-coated paper after the drying process, and no significant slurry migration through the perforations occurred. More images of the process can be found in the **Appendix** (**Figure 17.1** one page 188).

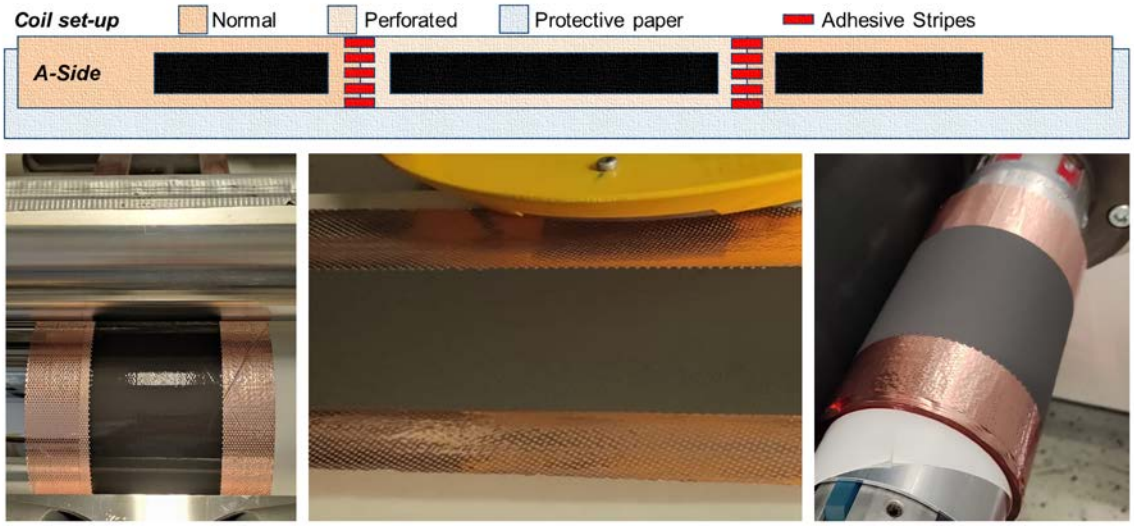

Figure 8.4 Schematic of the A-side coated coil and representative photographs of the coating process.

After coating the A-side, the single-sided coated coil was remounted in the coating device to process the B-side. The silicon-coated protective paper was not used again. Its protective function during the A-side coating process was mistakenly underestimated. Unfortunately, some holes within the A-side coating layer were left uncovered. These coating defects were primarily found in perforated foil parts with surface imperfections from the coil assembly, such as creases or waves (see **Figure 17.1** in the **Appendix** on page 188). During the B-side coating process, slurry began to migrate through the free-standing holes of the single-sided coated foil after a few meters, contaminating the roller. Subsequently, the foil tore due to dried slurry between the current collector foil and the roller surface. The coating process was stopped immediately to prevent further contamination of the machine. Representative images are shown in **Figure 8.5**.

Nonetheless, double-sided, coated graphite electrodes were successfully produced on both standard and perforated current collectors. Regardless of the type of current collector, a coating loading of 8.8 mg cm^{-2} per side (~3.0 mAh cm^{-2} per side) was achieved. Sections with a coating length of approximately 30 cm were cut and calendered to a final electrode density of 1.4 g cm^{-3}. Then, single- and double-sided coated graphite electrodes were cut into pouch cell electrode formats for both current collector systems.

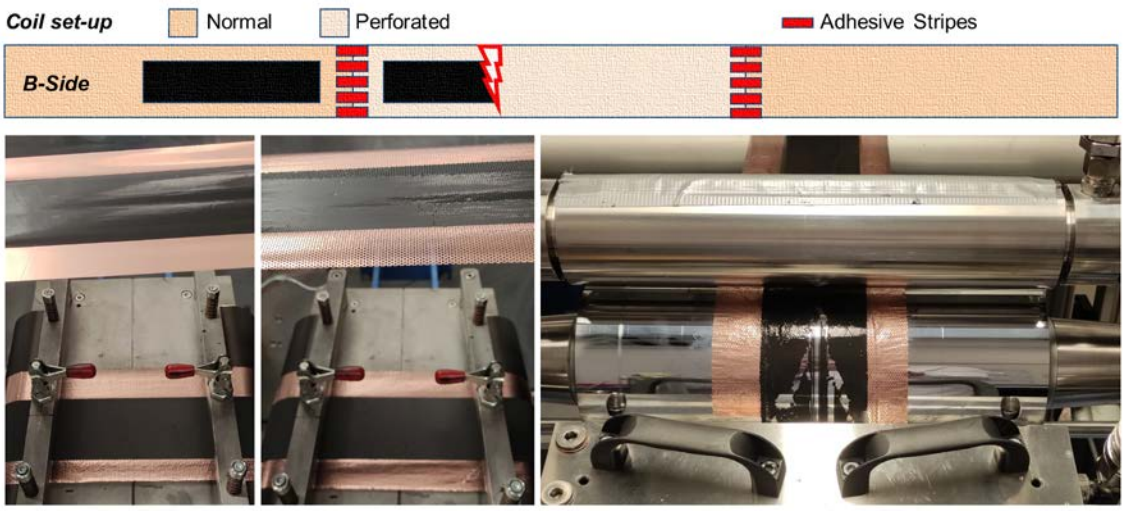

Figure 8.5 Schematic of the B-side coated coil and representative photographs of the coating process.

Figure 8.6 shows SEM microscopic images of the calendered graphite electrode surfaces of the two current collector systems. Interestingly, the hole, transition, and land areas are difficult to differentiate with the naked eye – a hole is present at the center of **Figure 8.6b**. Magnifying this area reveals that the electrode surfaces of both coated current collector systems are nearly indistinguishable from these optical measurements. This indicates similar coating and surface properties of pilot line coatings on both current collector systems. The optical evaluation of the slot-die-coated electrodes presented here, as well as the doctor-blade coated electrodes presented in **Chapter 7.2.2** (page 82), is consistent with the theoretical discussion of how different coating techniques affect the electrode's microstructure of coatings on standard and perforated current collectors, as discussed in **Chapter 6.3** (page 53).

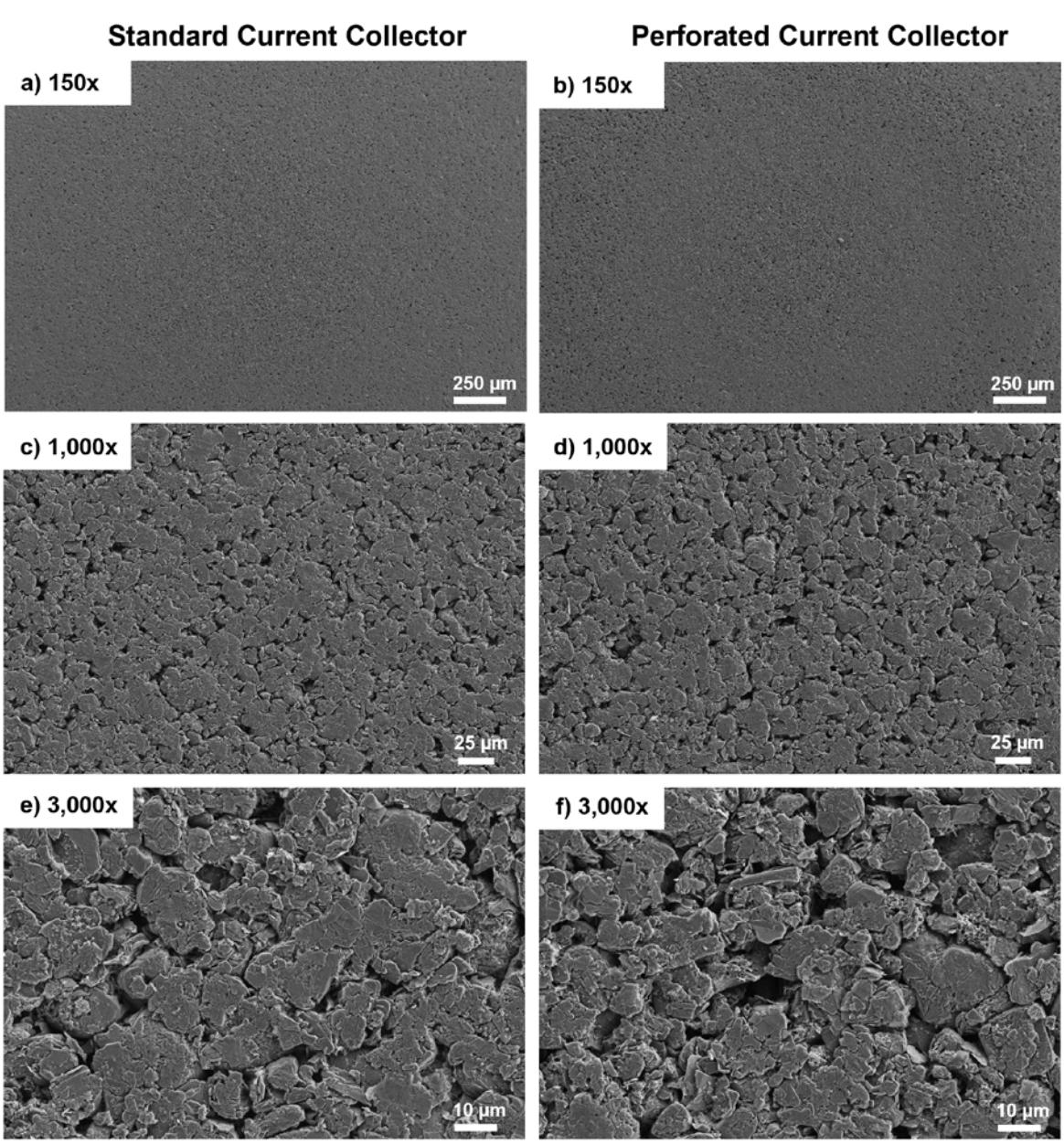

Figure 8.6 SEM micrographs of pilot line graphite coating deposited on standard and perforated copper current collector foil: a,b) top-view image at 150× magnification, c,d) top-view image at 1,000× magnification, and e,f) top-view image at 3,000x magnification.

Figure 8.7a shows a slightly magnified SEM image with subtle visible segmentation of land and transition area. The region referred as the "transition" area (**Figure 8.7b and d**) appears slightly more compressed than the land (**Figure 8.7c and e**) or hole areas (**Figure 8.6d and f**) at the same magnification.

In summary, no critical defects are observable in the recorded SEM top-view images. The overall quality of roll-to-roll coated electrodes with perforated current collectors seems to be similar to that of roll-to-roll coated electrodes with standard current collectors.

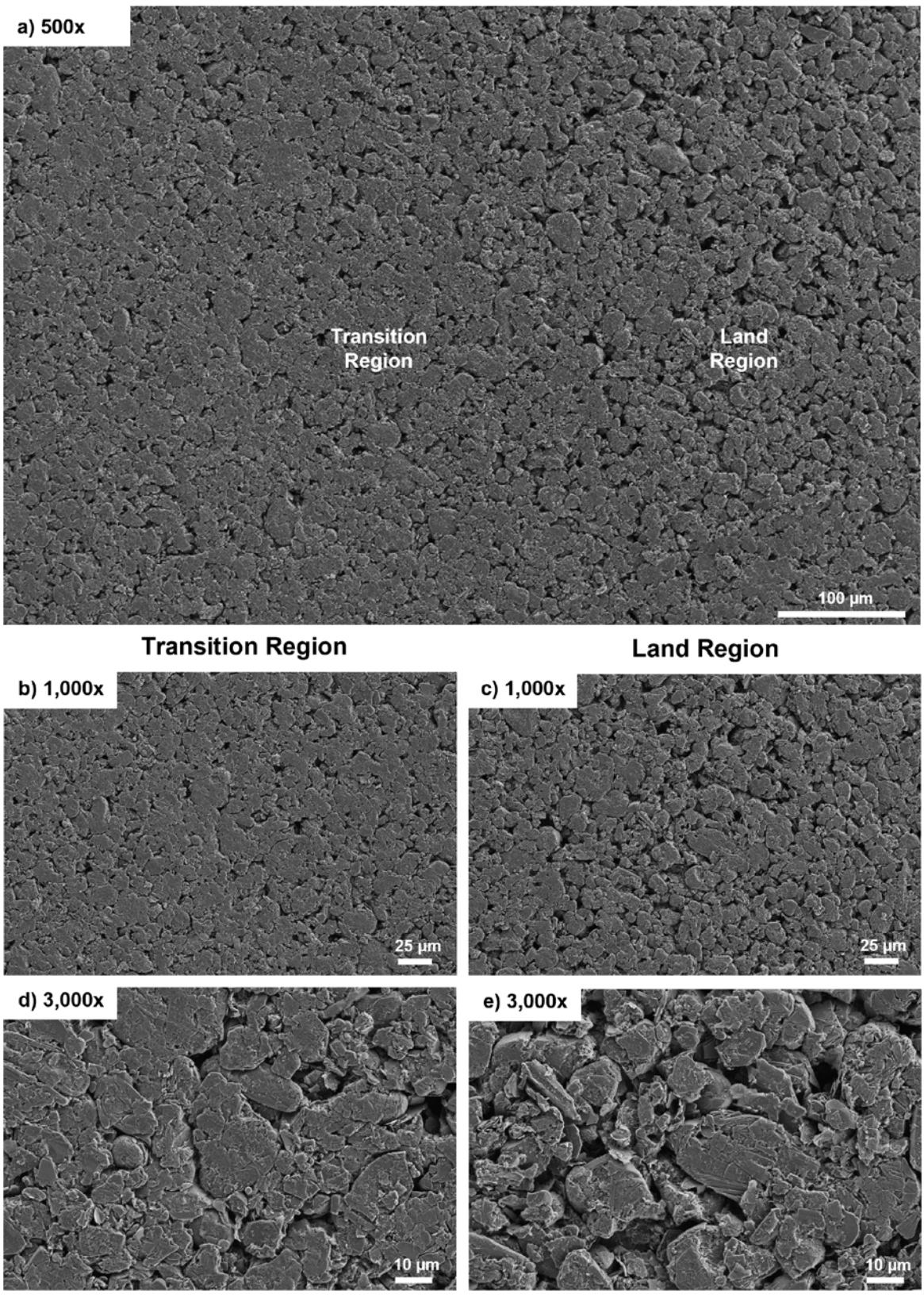

Figure 8.7 SEM micrographs of pilot line graphite coating deposited on perforated copper current collector foil: a) top-view image at 500× magnification, b,c) top-view image at 1,000× magnification, and d,e) top-view image at 3,000x magnification.

Finally, **Figure 8.8** shows SEM images of the electrode cross-section. A highly uniform distribution of electrode material is revealed on both sides of the current collector for both types. It can be seen that the foil edge is slightly shifted at the transition area of the perforated current collector coating, indicating slight bending of the current collector hole edges due to the weight of the coating during the sequential coating process. However, aside from this slight variation, there are no critical visible defects or differences in the electrode microstructure in the cross sections. Additionally, there are no visible cracks at the transition area or holes of the perforated current collector coating. The A- and B-side coatings appear to fit together seamlessly.

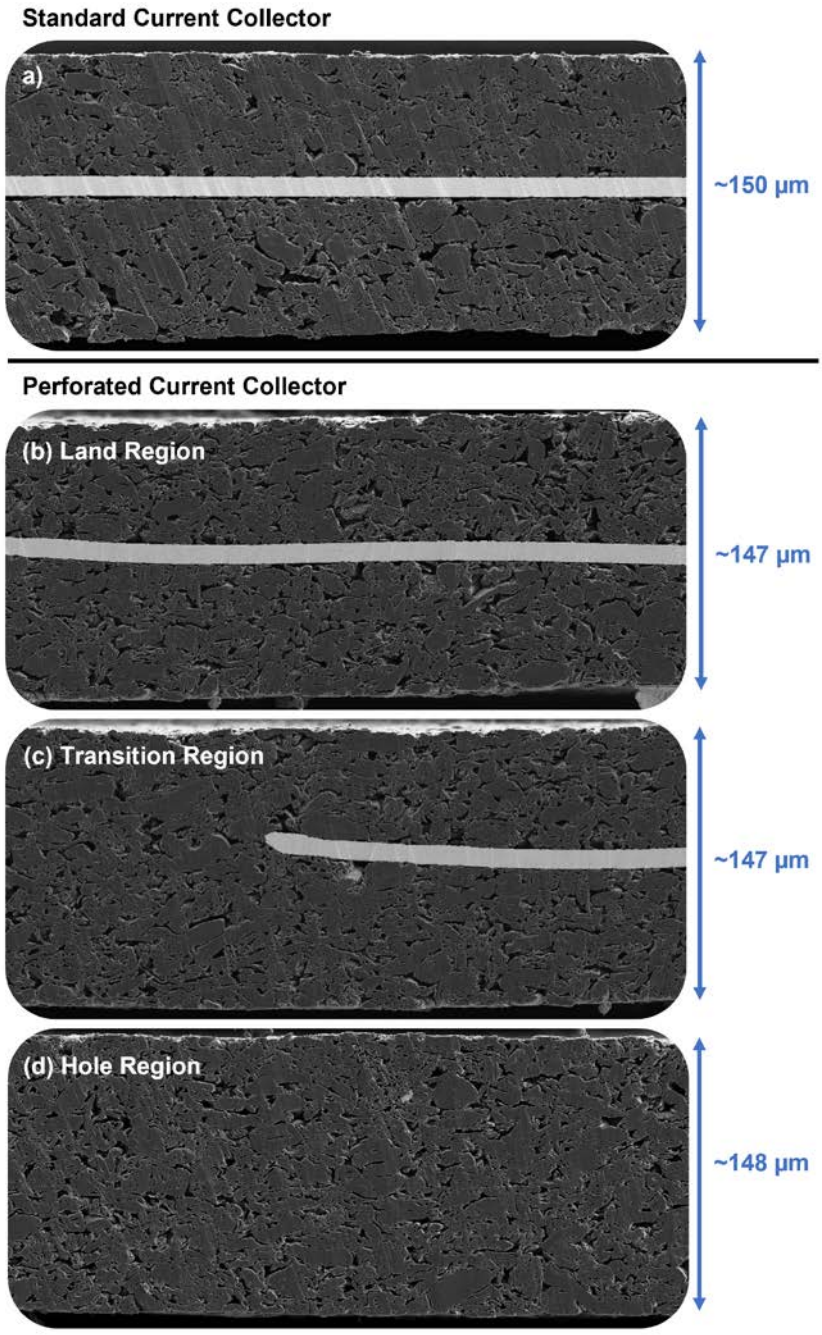

Figure 8.8 SEM micrographs of pilot line graphite coating deposited on standard and perforated copper current collector foil: a-d) cross-section at 1,000× magnification.

The initial roll-to-roll coating trial clearly shows that the perforated copper current collector design can be processed with conventional pilot-line coating equipment. SEM analysis revealed highly comparable coating microstructures and quality on both standard and perforated current collector foils.

The obtained single- and double-sided roll-to-roll coated graphite electrodes are electrochemical investigated in bi-layer and stacked demonstrator pouch cells, as presented in **Chapter 8.2** (page 126).

8.1.2 Initial roll-to-roll LFP electrode development

After completing the initial roll-to-roll coating trial with a high-viscosity graphite slurry on perforated copper current collector foil, the same process was repeated with a high-viscosity LFP slurry on perforated aluminum current collector foil.

In **Chapter 6.1** (page 42), the process of flattening several meter-long perforated aluminum current collector foils is detailed. The flattened perforated foil (about 15 m) was inserted between two standard aluminum current collector foils (about 25 m) with adhesive strips, as shown in **Figure 8.9**. Additionally, a 12 cm width silicone-coated paper was included within the foil coil as a protective, non-adhesive second layer.

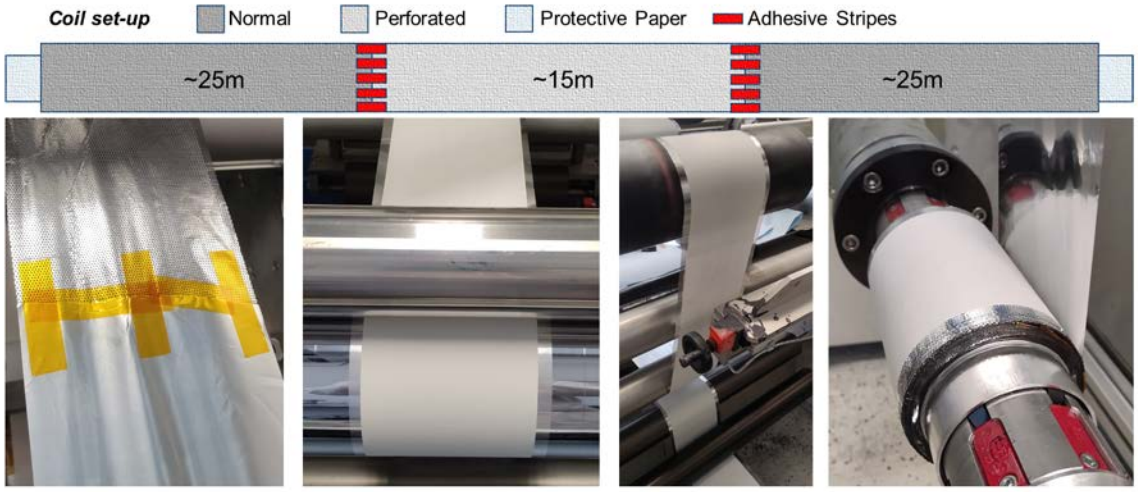

Figure 8.9 Schematic of the modified aluminum current collector coil and representative photographs of the coil preparation process.

Based on the preparation of the modified copper current collector foil coil described in **Chapter 8.1.1** (page 110), the width of the protective paper was adjusted to align more closely with the center of the foil (12 cm width instead of 20 cm). This was done to improve the alignment and winding of the foil in the coil during the addition of the second layer. However, difficulties with tight winding, accurate alignment, and surface irregularities were still encountered in the preparation of the modified aluminum current collector foil coil. The manual coil preparation steps cannot achieve optimal coil quality because the available laboratory equipment does not allow for the necessary level of accuracy. Consequently, manual pretreatment steps, as conducted here, should be avoided in the future. However, due to limited material availability, the prepared foil coil had to be used, even though it may not be perfectly suitable from theoretical point of view again.

In **Chapter 7.2.2** (page 82), LFP slurries were scaled up from 100 g to 700 g batches while maintaining consistent slurry properties. Considering the coating length (~45 m), width (8 cm), loading per side (target: 18.2 mg cm^{-2}), and slurry TSC (55%), at least 2.4 kg of LFP slurry is required for the pilot line coating. Therefore, four batches of 700 g of LFP slurry were prepared. The

formulation (AM:SFG6L:CB:CMC:SBR – 92:1:3:1:3), slurry TSC, electrode materials and processing parameters were kept consistent with those described in **Chapter 7.2.2**.

Figure 8.10 shows photographs of the A-side coating process. Once again, the non-optimal modified coil setup was sufficient for the coating attempt, and sections with a uniform, high-quality coating layer were achieved. No coating residues were observed on the silicon-coated paper after drying, and there was no significant slurry migration through the perforations.

However, as shown in the schematic representation of the single-sided coated coil (**Figure 8.10**), the A-side coating process encountered several challenges this time. These challenges were primarily due to foil cracks caused by suboptimal alignment and surface irregularities within the coil. Adhesive strips were used to join the cracked sections, allowing for a complete A-side coating. Additional images documenting the challenges of the A-side coating process can be found in the **Appendix** (**Figure 17.2** one page 188).

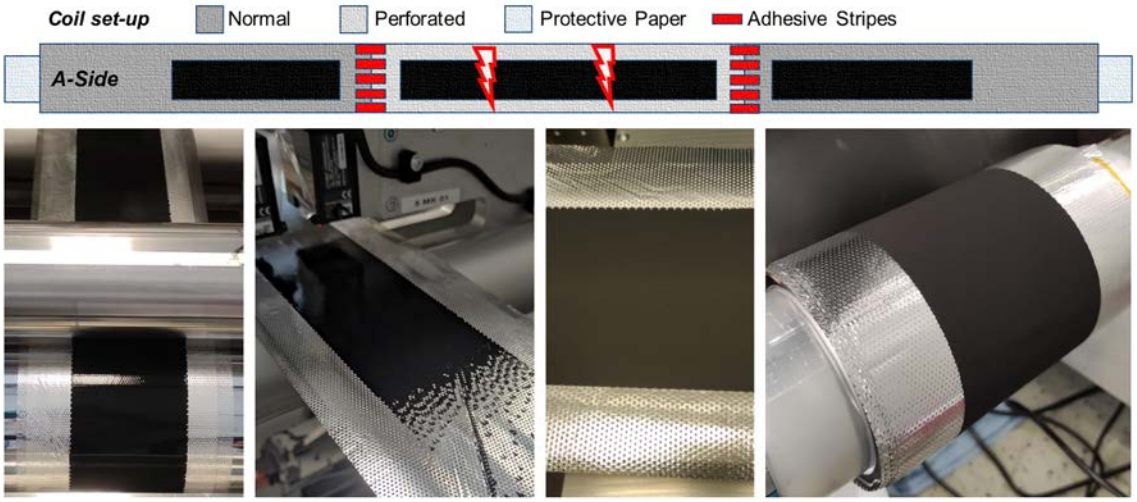

Figure 8.10 Schematic of the A-side coated coil and representative photographs of the coating process.

After the A-side was coated, the single-sided coated coil was remounted in the coating device to process the B-side. The silicone-coated protective paper was reintroduced into the B-Side coating process. This time, it was used only during the coating and drying stages and was not part of the foil coil in its initial state. During the B-side coating process, the adhesive strips that were used to repair cracks in the A-side coating stuck to the underlying foil layers through the perforations. This caused the foil to crack completely, forcing an immediate stop to the process. Representative images are shown in **Figure 8.11**.

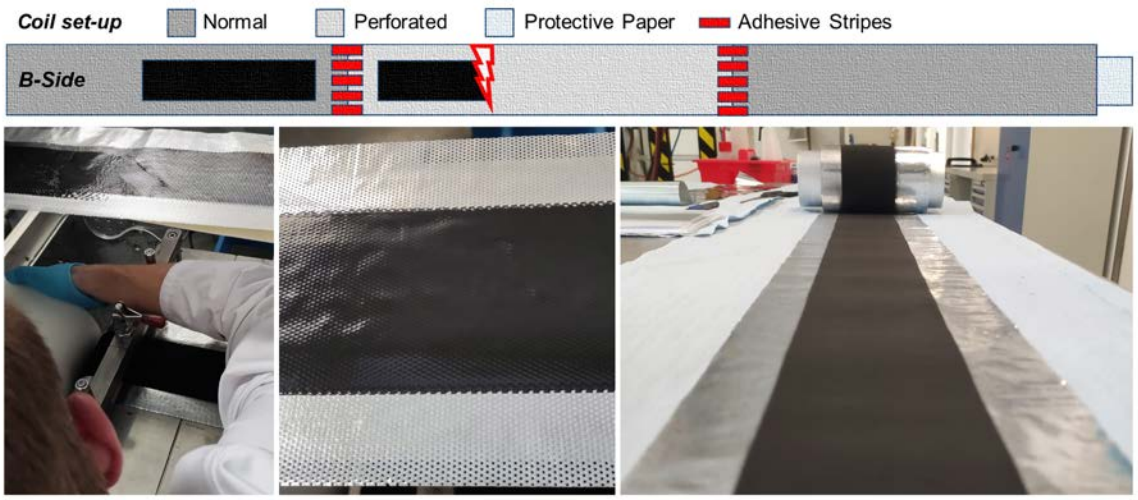

Figure 8.11 Schematic of the B-side coated coil and representative photographs of the coating process.

However, double-sided, coated LFP electrodes were successfully produced on both standard and perforated current collectors. Regardless of the type of current collector, a coating loading of 18.6 mg cm^{-2} per side (~2.55 mAh cm^{-2} per side) was achieved. Sections with a coating length of approximately 30 cm were cut and calendered to a final electrode density of 1.9 g cm^{-3}. Then, single- and double-sided coated graphite electrodes were punched into pouch cell electrode formats for both current collector systems.

Figure 8.12 shows SEM microscopic images of the graphite electrode surfaces of both current collector systems. Also, for LFP coatings the hole, transition, and land areas are difficult to differentiate with the naked eye – a hole is present at the center of **Figure 8.12b**. This optical evaluation indicates similar coating and surface properties of LFP pilot line coatings independent of the current collector system used.

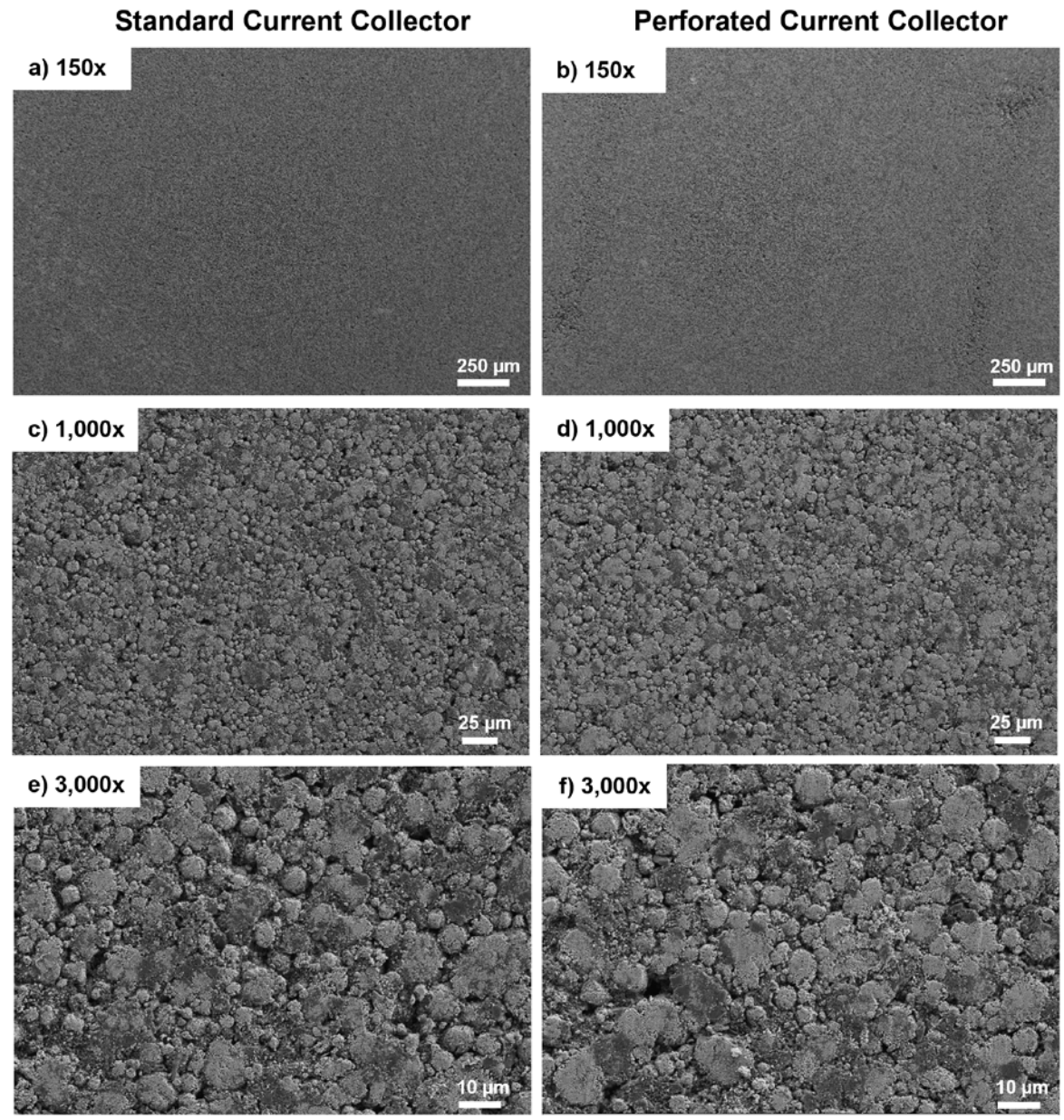

Figure 8.12 SEM micrographs of pilot line LFP coating deposited on standard and perforated aluminum current collector foil: a,b) top-view image at 150× magnification, c,d) top-view image at 1,000× magnification, and e,f) top-view image at 3,000x magnification.

Figure 8.13a shows a slightly magnified SEM image with subtle visible segmentation of land and transition area. The region referred here as the "transition" area (**Figure 8.13b** and **d**) appears slightly more compressed compared to the land (**Figure 8.13c** and **e**) or hole areas (**Figure 8.12d** and **f**) at the same magnification. Despite these subtle variations, which indicate areas of differing densification across the electrode bulk – as also discussed in the preliminary electrode development sections of this work – no critical defects are visible from the recorded SEM top-view electrode images. Overall, the coating quality appears comparable regardless of the current collector used.

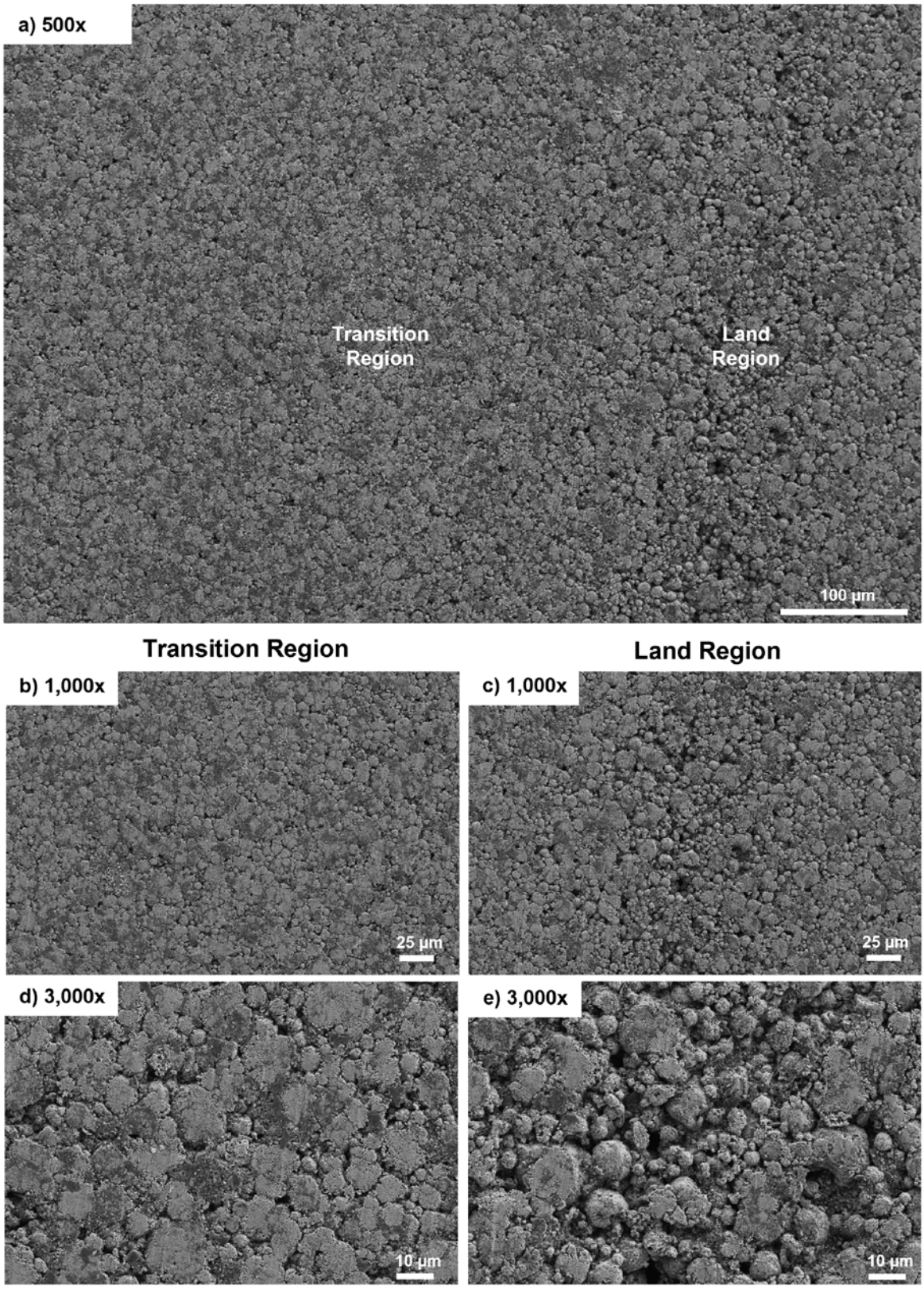

Figure 8.13 SEM micrographs of pilot line LFP coating deposited on perforated copper current collector foil: a) top-view image at 500× magnification, b,c) top-view image at 1,000× magnification, and d,e) top-view image at 3,000x magnification.

Finally, **Figure 8.14** shows SEM images of the electrode cross-section. A highly uniform distribution of electrode material is revealed again on both sides of the current collector for both types. The foil edge is again slightly bendet at the transition region of the perforated current collector coating, suggesting minor deformation of the current collector hole edges caused by the coating weight during the sequential coating process. Apart from this small variation, no critical defects or notable differences in the electrode microstructure are observed in the cross-sections. Moreover, no visible cracks are present at the transition regions or within the holes of the perforated current collector coating. The A- and B-side coatings appear again to align seamlessly.

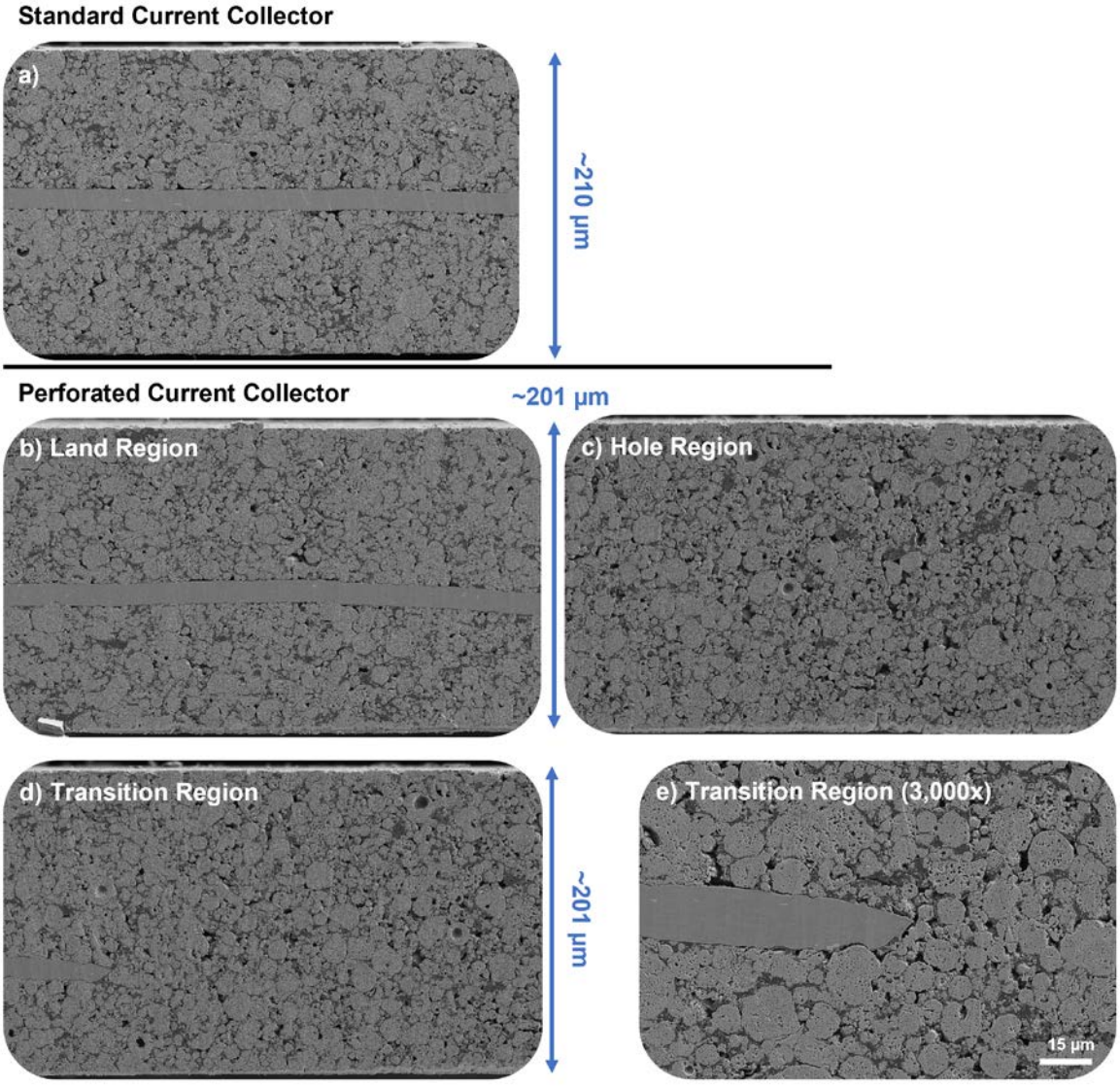

Figure 8.14 SEM micrographs of pilot line LFP coating deposited on standard and perforated copper current collector foil: a-d) cross-section at 1,000× magnification and e) cross-section at 3,000× magnification

Also, the initial LFP roll-to-roll coating trial clearly shows that the perforated current collector design can be processed with conventional pilot-line coating equipment. SEM analysis revealed highly

comparable coating microstructures and quality on both standard and perforated aluminum current collector foils.

The obtained single- and double-sided roll-to-roll coated LFP electrodes are electrochemical investigated in bi-layer and stacked demonstrator pouch cells, as presented in **Chapter 8.2** (page 126)

8.1.3 Roll-to-roll graphite electrode development

In a last pilot line coating attempt, the overall process was significantly optimized. A pre-assembled full coil of perforated current-collector foil, 40 m in length, was used (provided by Bender GmbH-Siegen). This advanced, perforated current collector foil coil required no flattening or other pretreatment anymore. It exhibited coil quality comparable to that of conventional battery current collector foil coils while incorporating the perforation feature. Consequently, thanks to the high-quality initial state of the coil, all manual processing steps and the related defects observed in the perforated current collector foil coils from previous roll-to-roll coating trials were fully avoided. Furthermore, the silicone-coated paper was added only as a protective layer during the coating and drying stages of the A-side and B-side processing. It was not part of the initial or final coil, as illustrated in **Figure 8.15**.

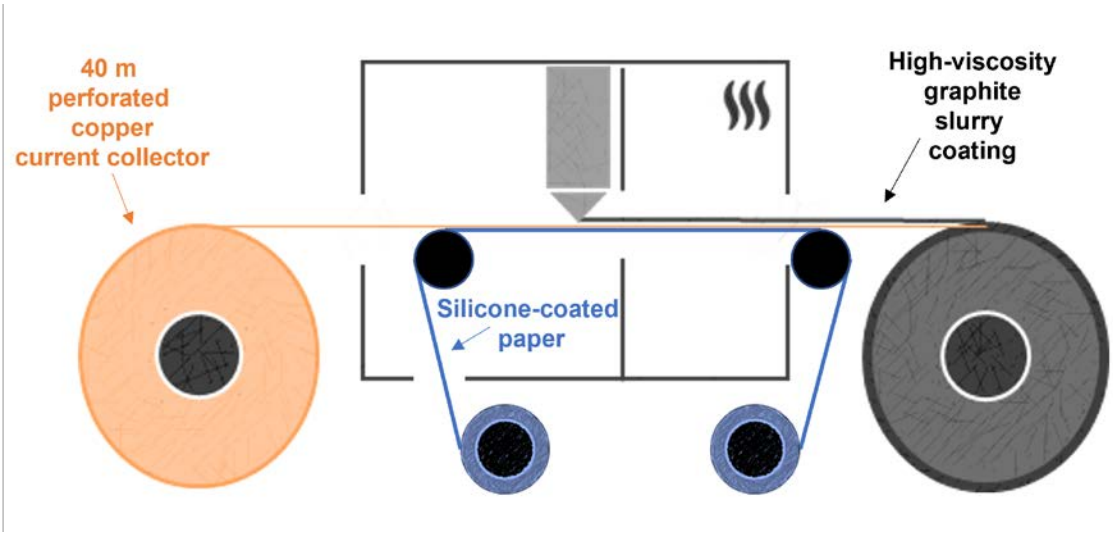

Figure 8.15 Illustration of the final roll-to-roll coating setup for processing perforated current collector foils using state-of-the-art equipment.

Three batches of 700 g of graphite slurry were prepared. The formulation (AM:CB:CMC:SBR – 94:2:2:2), slurry TSC, electrode materials and processing parameters were kept consistent with those described in **Chapter 7.2.1** (page 78).

The final roll-to-roll coating process produced more than 10 meters of double-sided coated graphite electrodes on perforated current collector foil, with no complications. Representative images are shown in **Figure 8.16**. The here presented coating demonstrates that the novel perforated current collector design can be effectively coated even with state-of-the-art pilot line coating equipment if the foil coil has a high-quality. The overall coating process is comparable to that of standard foils. Only minor adjustments are necessary (e.g., slurry viscosity and a protective layer), and there are no drawbacks to the quality of the coating.

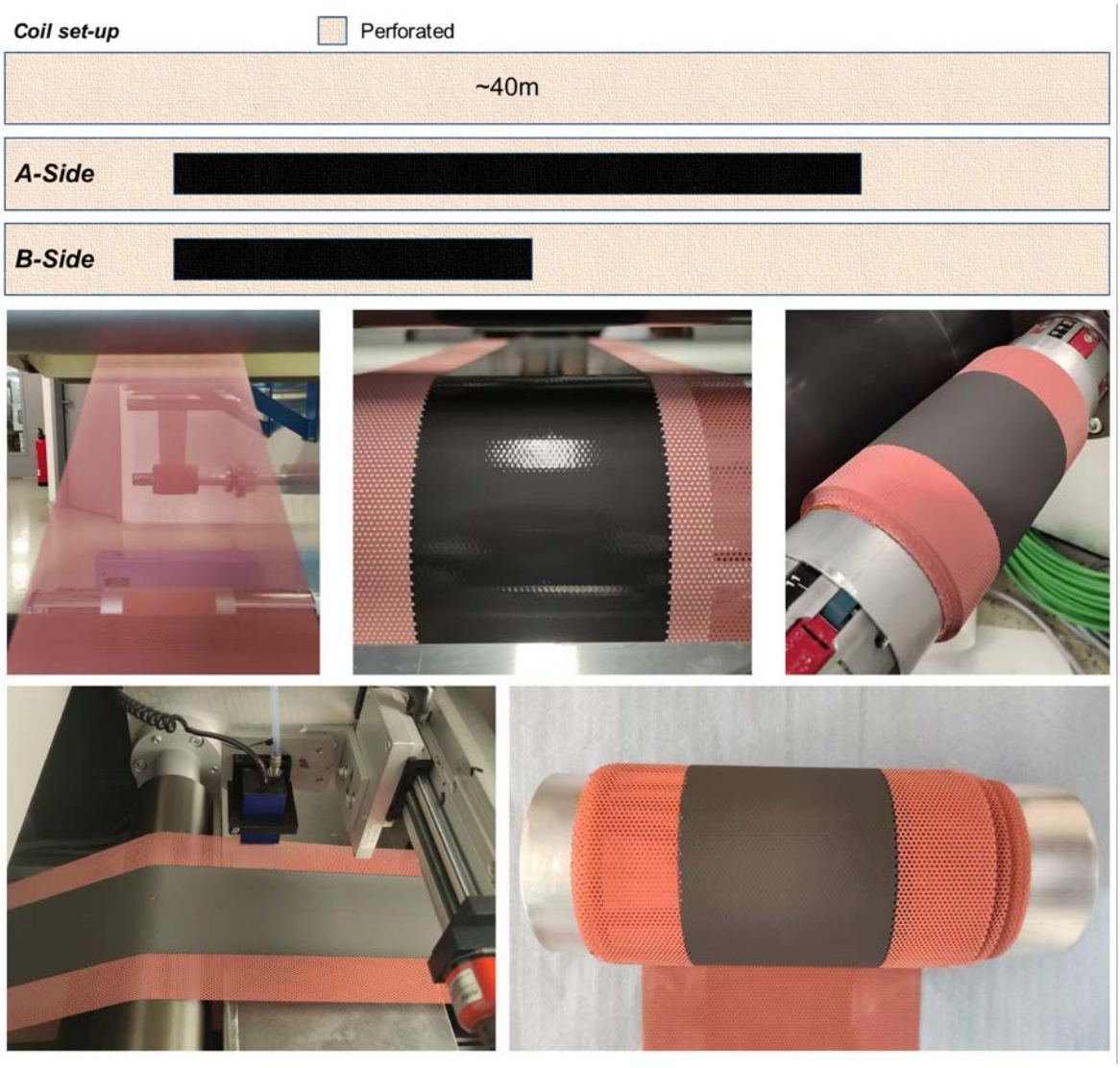

Figure 8.16 Schematic of the copper current collector coil, the A-side coated coil, and the B-side coated coil together with representative photographs of the overall coating process.

In **Chapter 6.1** (page 42), also the preparation of a well-aligned, tightly wound, 40-meter-long perforated aluminum current collector foil coil with a flattened surface was demonstrated using a roll-to-roll calender equipped with foil-edge control. This high-quality aluminum current collector coil is also expected to be suitable for direct use in roll-to-roll coating processes. However, due to the limited availability of the pilot line coating technicum, this could not be verified experimentally within the time-line of this study.

In summary, high-quality foil coils combined with well-designed slurry properties enable smooth and defect-free processing of perforated current collector systems with state-of-the-art pilot line coating equipment.

8.2 Bi-Layer and Stacked Demonstrator Pouch Cells

8.2.1 Initial 2032-Coin Cell Tests

Initial electrochemical tests of the roll-to-roll coated electrodes were performed in 2032-coin cells. Each cell consisted of calendered, single-sided, coated electrodes with standard or perforated current collectors. The graphite and LFP electrodes were obtained from pilot line coatings described in **Chapter 8.1.1** (page 110) and **Chapter 8.1.2** (page 117), respectively. The electrodes with perforated current collector system had no coating residues on their backsides. This information is important, as in the 2032-coin cell setup, the electrode's backside comes into direct contact with the cell's lid or spacer. These initial tests are performed to confirm whether coin cell studies are also a reliable way of evaluating electrodes with perforated current collectors.

2032-coin cells with either fully standard or fully perforated current collectors on both anode and cathode sides were assembled. The N/P-ratio of all cells was approx. 1.15, based on the electrode's reversible areal capacity measured in the half cells (~2.55 mAh cm^{-2} for LFP electrodes). Each cell included two layers of GFA as the separator and 150 µL of 1 M $LiPF_6$ in EC:EMC (3:7) with 2 wt.% VC as the electrolyte. To ensure reproducibility, at least three cells were assembled for each current collector system.

Five formation cycles were performed within the voltage window 2.5 – 3.7 V, using a CCCV-charge (I until V_{cell} > 3.7 V; V = 3.7 V until I < C/20) and a CC-discharge (I until V_{cell} < 2.5 V) protocol at a C-rate of C/10.

Figure 8.17 clearly shows that all cells exhibit similar formation behavior, regardless of the current collector system within their electrodes. One outlier was observed in the perforated current collector cell configuration. Therefore, the results presented are the averages of three cells for the standard configuration and two cells for the perforated configuration. The initial charge capacity is equivalent to the LFP specific capacity measured in half-cells (149 mAh g^{-1}). In the final formation cycle, a usable LFP specific capacity of 136 mAh g^{-1} is obtained for all cells, corresponding to an ICL of 9.3%.

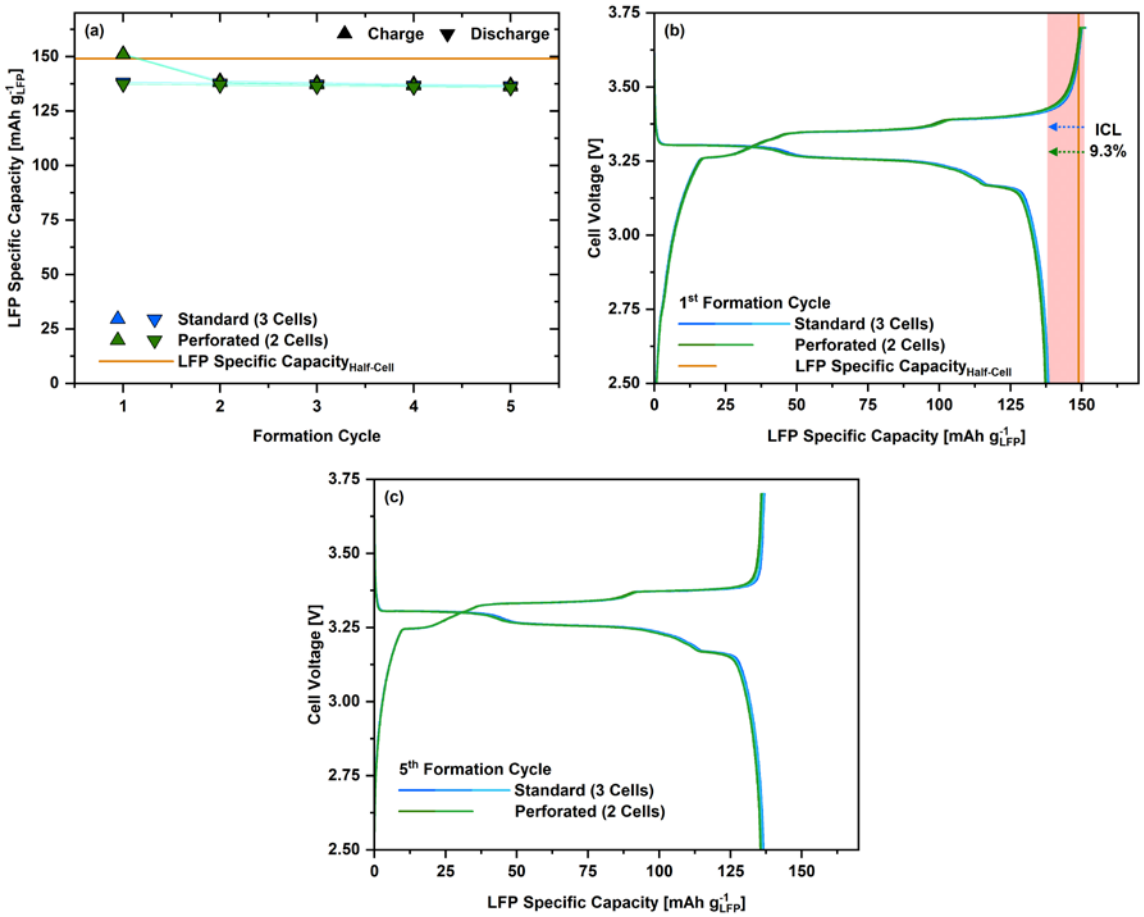

Figure 8.17 Formation data of Graphite‖LFP 2032-coin cells with standard or perforated current collector systems within the electrodes: a) LFP specific capacity as a function of cycle number, b) initial cycle voltage profile, and c) final cycle voltage profile.

Following the formation protocol, discharge (I = C/10, C/20, C/5, C/2, 1C) and charge (I = C/5, C/2, 1C) rate capability measurements were conducted.

Figure 8.18 shows the rate capability data of all Graphite‖LFP 2032-coin cells. All cells, independent of current collector type, show comparable and reproducible rate performance and capacity retention. Furthermore, the usable discharge LFP specific capacities at C/2 and 1C are consistent with those of Graphite‖LFP pouch cells discussed in **Chapters 7.3** (**Figure 7.16** on page 92) and **Chapter 8.2** (**Figure 8.25** on page 137). The LFP specific capacities are 129 mAh g^{-1} (C/2) and 123 mAh g^{-1} (1C) in coin cells, compared to 128 mAh g^{-1} (C/2) and 122 mAh g^{-1} (1C) in pouch cells. These results demonstrate that coin cells provide a reliable initial assessment of rate performance for both standard and perforated current collector electrode systems.

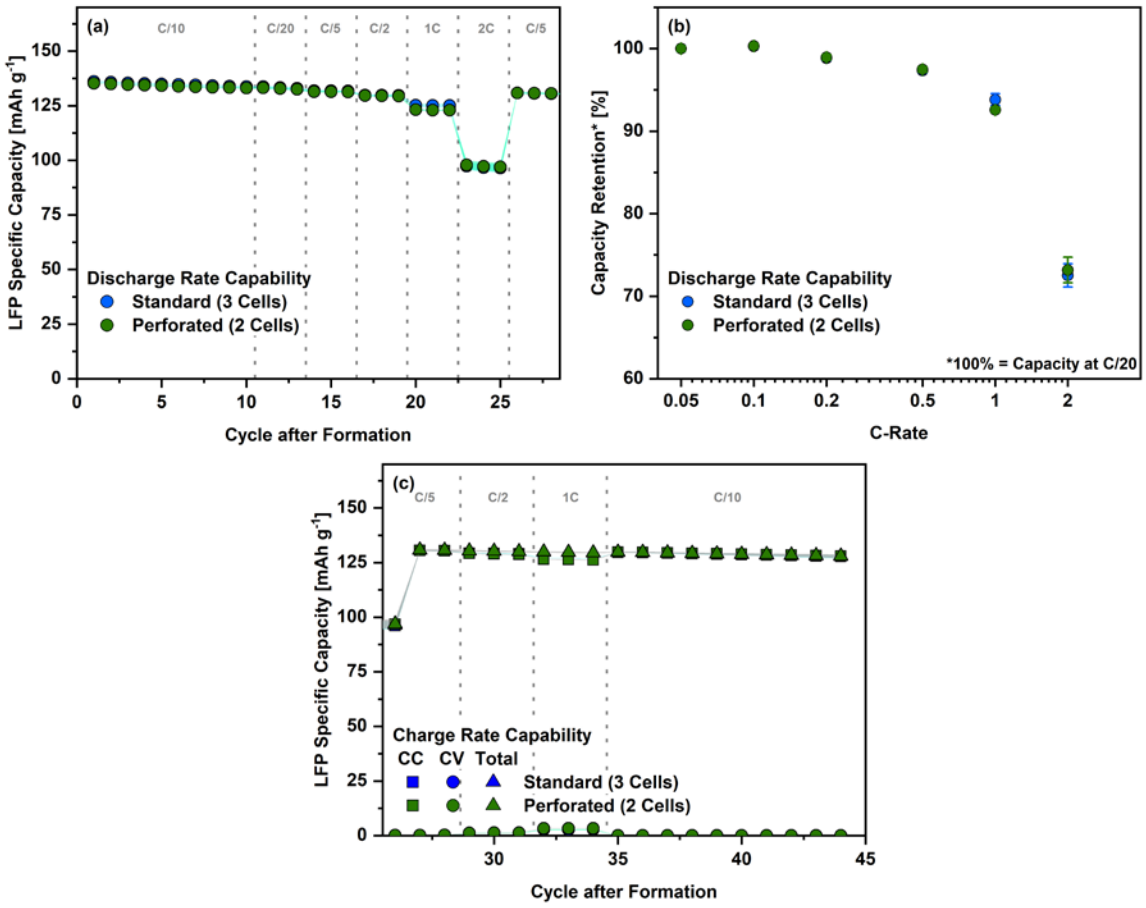

Figure 8.18 Rate capability data of Graphite‖LFP 2032-coin cells with standard or perforated current collector systems within the electrodes: a) discharge LFP specific capacity as a function of cycle number, b) discharge capacity retention as a function of C-rate, and c) charge LFP specific capacity as a function of cycle number.

Finally, a long-term cycling protocol was performed at C/2 with a C/10 check-up every 50th cycle.

Figure 8.19 shows the long-term cycling data of all cells. Even after more than 150 cycles, again all cells exhibit consistent and comparable performance. The aging rate of the coin cells is slightly faster, but still comparable, to that of the pouch cells investigated in **Chapter 7.2** (**Figure 7.23** on page 101) and **Chapter 8.2** (**Figure 8.30** on page 142). The SOH is ~89% after 145 cycles in the coin cells, versus ~94% SOH after 126 cycles in the single-layer and ~91% SOH after 142 cycles in the bi-layer pouch cells.

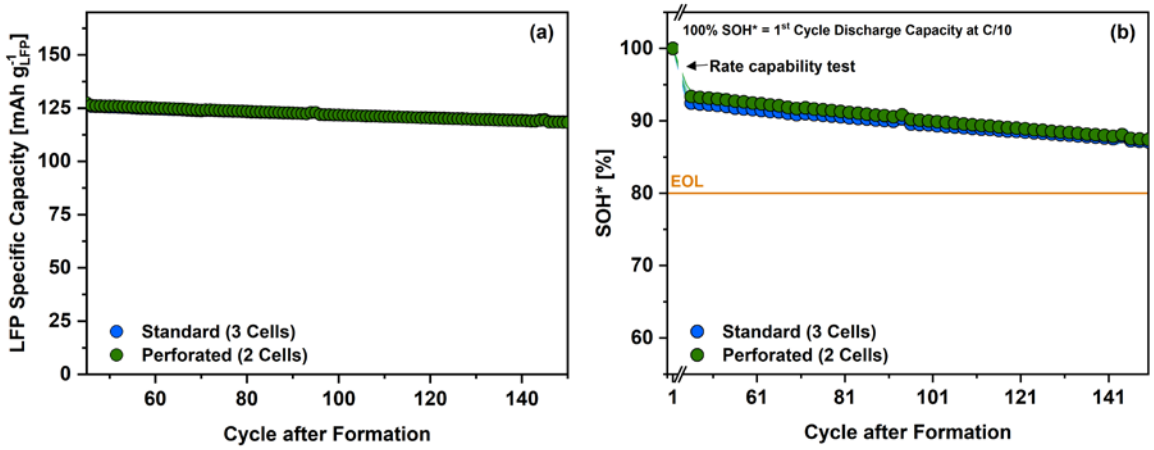

Figure 8.19 Long-term cycling data of Graphite‖LFP 2032-coin cells with standard or perforated current collector systems within the electrodes a) LFP specific capacity as a function of cycle number and b) SOH as a function of cycle number.

It can be concluded that replacing standard current collectors with perforated ones does not compromise the performance of coin cells as long as there are no defects on the electrode's backside. The measurement results obtained from coin cells closely align with those from single- and bi-layer pouch cells with the same electrode chemistry (see **Chapter 6.4** and **Chapter 8.2** of this work).

8.2.2 Bi-Layer and Stacked Pouch Cell Setups

Advanced electrochemical tests were performed using bi-layer (~120 mAh) and stack (~180 mAh) pouch cell setups, as illustrated in **Figure 8.20**.

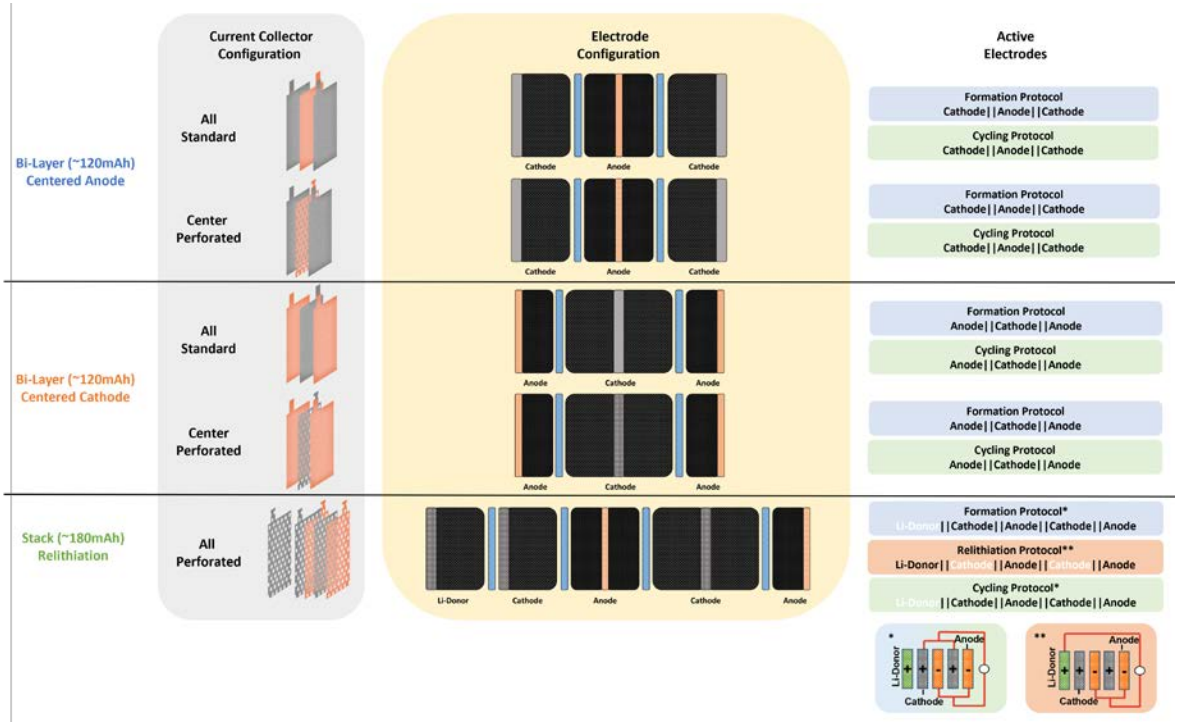

Figure 8.20 Illustration of various bi-layer and stacked pouch cell setups, along with the electrode connections during the formation, relithiation and cycling protocols. Black-marked electrodes are active in the respective protocol, while white-marked electrodes remain inactive.

The bi-layer setup incorporated a sandwiched double-sided coated anode or cathode – using either standard or perforated current collectors – paired with standard single-sided coated electrodes of the opposite type. These cells assess the impact of collector substitution on the cell's electrochemical performance.

The stack pouch cell setup employed both single-sided and double-sided coated anodes and cathodes, exclusively using electrodes with perforated current collectors, and included an additional single-sided coated cathode as an extra Li-donor electrode. This cell setup allows compensation for ICLs, as described and demonstrated in previous chapters, and assess the scalability of the prelithiation strategy studied in this work.

In **Figure 8.20**, it is noticeable that the term "relithiation" is used instead of "prelithiation". In the preliminary, prelithiated, single-layer pouch cells discussed in **Chapter 6.4** (page 62) and **Chapter 7.2** (page 78), the prelithiation treatment was performed during the cell's formation by connecting the anode to a sacrificial Li-donor electrode. This procedure showed unfavorable formation behavior, as lithium ions had to pass through one inactive permeable electrode during

all five formation cycles. Prelithiated cells performed well once the prelithiation protocol was better understood and managed. However, interaction between the Li-donor electrode and the anode should be minimized to avoid kinetic limitations, which are expected to become more pronounced in stacked pouch cells due to the increasing number of inactive cathode layers that lithium ions must traverse. To this end, the prelithiation approach was reconceptualized as a relithiation approach. First, a standard cell formation protocol (anode vs. cathode) is conducted to ensure proper SEI formation. Subsequently, a controlled relithiation step (anode vs. Li-donor) is applied to compensate for the active lithium deficiency in a single, well-controlled charging step. From a theoretical point of view, "prelithiation" is no longer the correct term in this context because the procedure used here will actually be a relithiation, similar to that discussed in **Chapter 7.4**, except it is performed directly after cell formation.

A total of ten pouch cells were assembled (two per setup), as shown in **Figure 8.21**. All of the graphite and LFP electrodes were obtained from the pilot line coatings described in **Chapter 8.1.1** (page 110) and **Chapter 8.1.2** (page 117), respectively. The N/P-ratio at the electrode level was set to 1.15 for all cells. Cellgard 2325 was used as the separator and 1.5 mL of 1 M $LiPF_6$ in EC:EMC (3:7) with 2 wt.% VC was used as the electrolyte. After assembly, the cells were clamped between two Plexiglas plates under a pressure of approx. 4 N cm^{-2} and left to rest for 10 hours to allow sufficient time for the electrolyte to soak into the electrodes and separator.

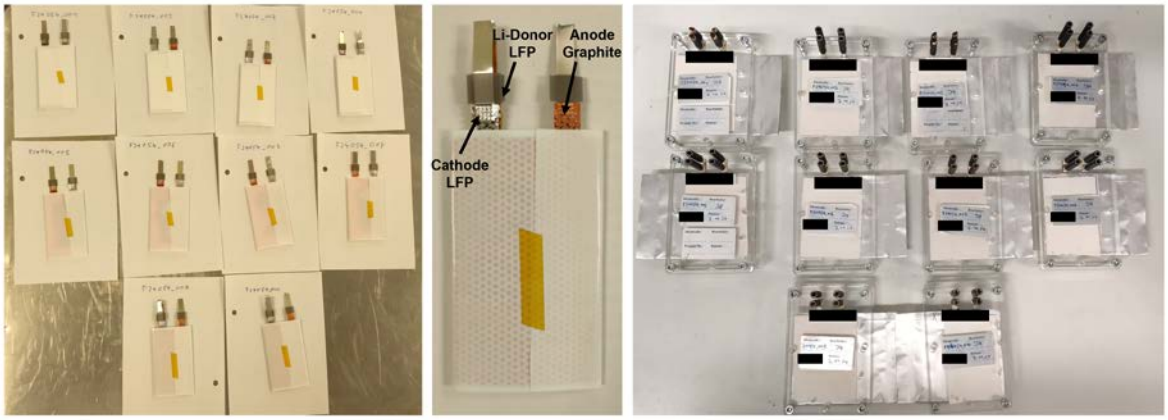

Figure 8.21 Photographs of bi-layer and stack pouch cell assemblies.

8.2.3 Formation

Five formation cycles were performed within the voltage window 2.5 – 3.7 V, using a CCCV-charge (I until V_{cell} > 3.7 V; V = 3.7 V until I < C/20) and a CC-discharge (I until V_{cell} < 2.5 V) protocol at a C-rate of C/10. The active electrodes during cell formation for each pouch cell setup are indicated in **Figure 8.20**.

Figure 8.22a shows the cell capacity as a function of the cycle number, while **Figure 8.22c** and **e** present the voltage profiles of the initial and final cycles as a function of cell capacity, respectively. The stacked pouch cells show significantly higher capacities, as they contain a greater number of electrode pairs. The electrochemical performance of cells with different capacities can be more meaningfully compared by normalizing cell capacity to the cathode AM mass (i.e., LFP specific capacity), as shown in in **Figure 8.22 b, d,** and **f**. This representation of the formation data demonstrates that all cells exhibited highly consistent formation behavior, independent of the pouch cell setup or current collector system used.

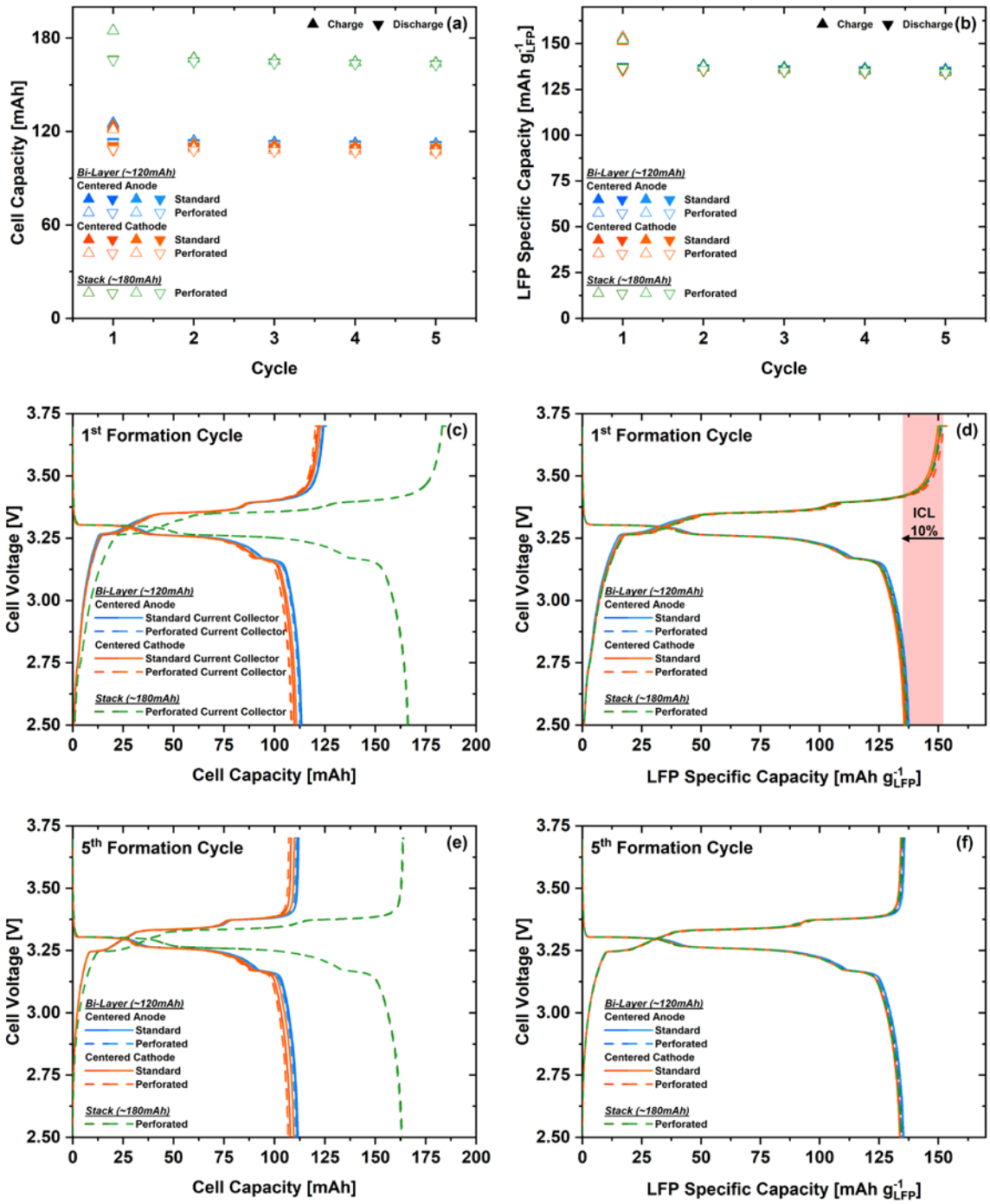

Figure 8.22 Formation data of Graphite‖LFP bi-layer and stacked pouch cells with standard or perforated current collector systems within the electrodes: a) cell capacity as a function of cycle number, b) LFP specific capacity as a function of cycle number c) initial cycle voltage profile (cell capacity), d) initial cycle voltage profile (LFP specific capacity), e) final cycle voltage profile (cell capacity) and f) final cycle voltage profile (LFP specific capacity).

In summary, the initial charge LFP specific capacities (~151 mAh g^{-1}) of the pouch cells closely match those measured in half-cells (~149 mAh g^{-1}), followed by an ICL of ~10%, resulting in a usable LFP specific capacity of ~135 mAh g^{-1} in the final formation discharge. No overpotentials or artifacts are observed in the voltage profiles of any of the pouch cell setups.

8.2.4 Relithiation

As illustrated in **Figure 8.23**, the stacked pouch cells underwent an additional electrochemical step following cell formation, referred to as relithiation. The ICLs of the cell formation were quantified (~20 mAh) and compensated by conducting a well-controlled charging step. This was done by connecting the Li-donor electrode to the anodes while keeping the cathodes inactive. A partial CC-charge protocol at a low current of 1 mA was applied until Q_{charge} reached Q_{ICL}.

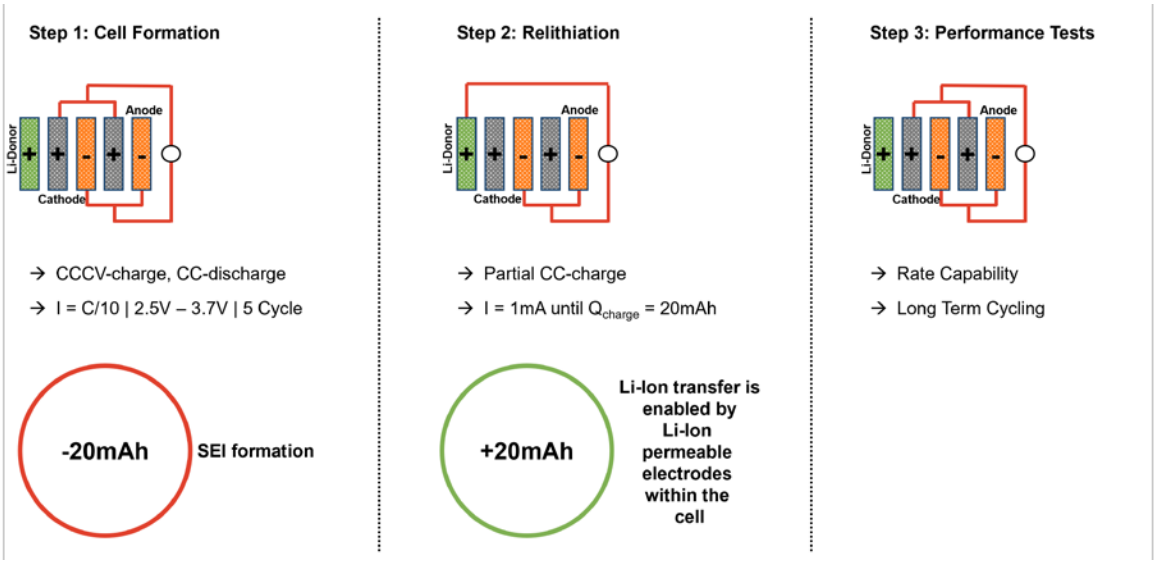

Figure 8.23 Illustration of the relithiation procedure applied to stacked pouch cells.

Figure 8.24 shows the CC-charge voltage profile of the final formation cycle (anode‖cathode, I = 18 mA until U > 3.7 V) in direct comparison with the CC-charge voltage profile of the relithiation step (anode‖Li-donor, I = 1 mA until Q_{charge} = 20 mAh) of both stacked pouch cells. As clearly demonstrated, the number of lithium ions transferred can be accurately controlled by the charge capacity and only minor polarization effects are observed during the cell's relithiation treatment. Furthermore, the pre-formed SEI is expected to be of the same quality as the one of standard cells as the formation conditions are identical. In conclusion, I recommend applying the relithiation at the cell level procedure presented here in future works instead of the prelithiation approach discussed in **Chapter 6.4** (page 62) and **Chapter 7.2** (page 78), as it provides significantly better control.

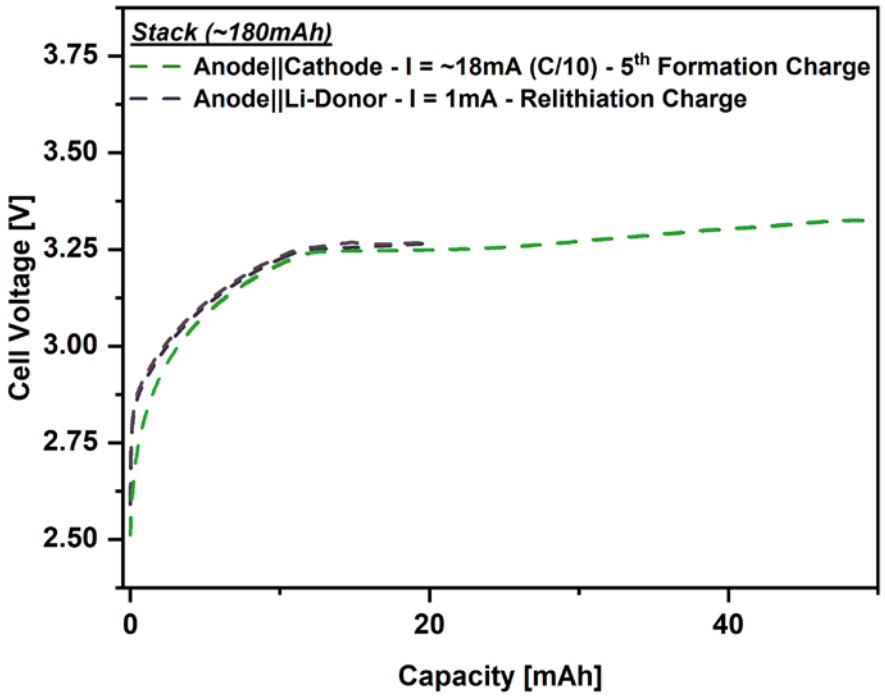

Figure 8.24 Comparison of voltage profiles of the final formation cycle charge and the relithiation charge in stacked Graphite‖LFP pouch cells.

8.2.5 Rate Capability and Electrochemical Characterization

Following the formation protocol (all cell setups) and the relithiation protocol (stack pouch cell setup only), discharge (I = C/10, C/20, C/5, C/2, 1C) and charge (I = C/5, C/2, 1C) rate capability measurements were conducted under standard active electrode conditions (anodes‖cathodes), as highlighted in **Figure 8.20**.

Figure 8.25 presents the rate performance data for all cells. All bi-layer pouch cells exhibited similar rate characteristics. The high consistency of the recorded data indicates homogeneous electrode quality and cell kinetics that is independent of current collector or electrode type in the cell's sandwiched layers. Even at the highest applied charge and discharge C-rates of 1C, the voltage profiles mostly overlap in all bi-layer pouch cells under investigation. Based on the presented rate capability measurements up to 1C, it can be concluded that substituting the current collector has no significant effect on the cell's rate performance. However, as stated in **Chapter 6.2** (page 46), using perforated current collectors in LIBs results in cells with enhanced specific energy due to the reduction of the inactive component of the current collector within its electrodes.

As can be seen clearly in **Figure 8.25**, relithiated pouch cells – incorporating only perforated current collector design within their electrodes – demonstrate an even greater enhancement. The full reversible cathode capacity can be utilized when cycled at a low current of C/20 in these advanced cells. The novel relithiation treatment introduced here seems to have replenished the cell's active lithium deficiency, caused by ICLs during cell formation, successfully.

The overall cell performance data of Graphite‖LFP cells from this chapter is consistent with the data of the prelithiated and non-prelithiated Graphite‖LFP single-layer pouch cells discussed in **Chapter 7.2** (page 78).

Relithiated cells, show enhanced LFP specific capacity utilization at discharge C-rates below 1C due to their relithiation treatment. At a discharge C-rate of 1C, all cells demonstrate similar LFP specific capacity utilization, regardless of the size of the respective cell's active lithium inventory. Once again, the rate performance of standard Graphite‖LFP cells appears to be primarily limited by the size of their active lithium inventory up to currents of C/2. Prelithiated or relithiated Graphite‖LFP cells, on the other hand, are mainly limited by kinetic factors related to the electrode and electrolyte properties (e.g., ionic and electronic conductivity), as they have access to sufficient active lithium within the cell. As mentioned before, for cell setups, the LFP specific capacity utilization converges at a discharge current of 1C. At this point, cell performance is limited by the electrode kinetics rather than the size of the cell's active lithium inventory. This finding is supported by the 1C charge and discharge voltage profiles shown in **Figure 8.25c** and **d**, in which all cells display mostly similar voltage profile features.

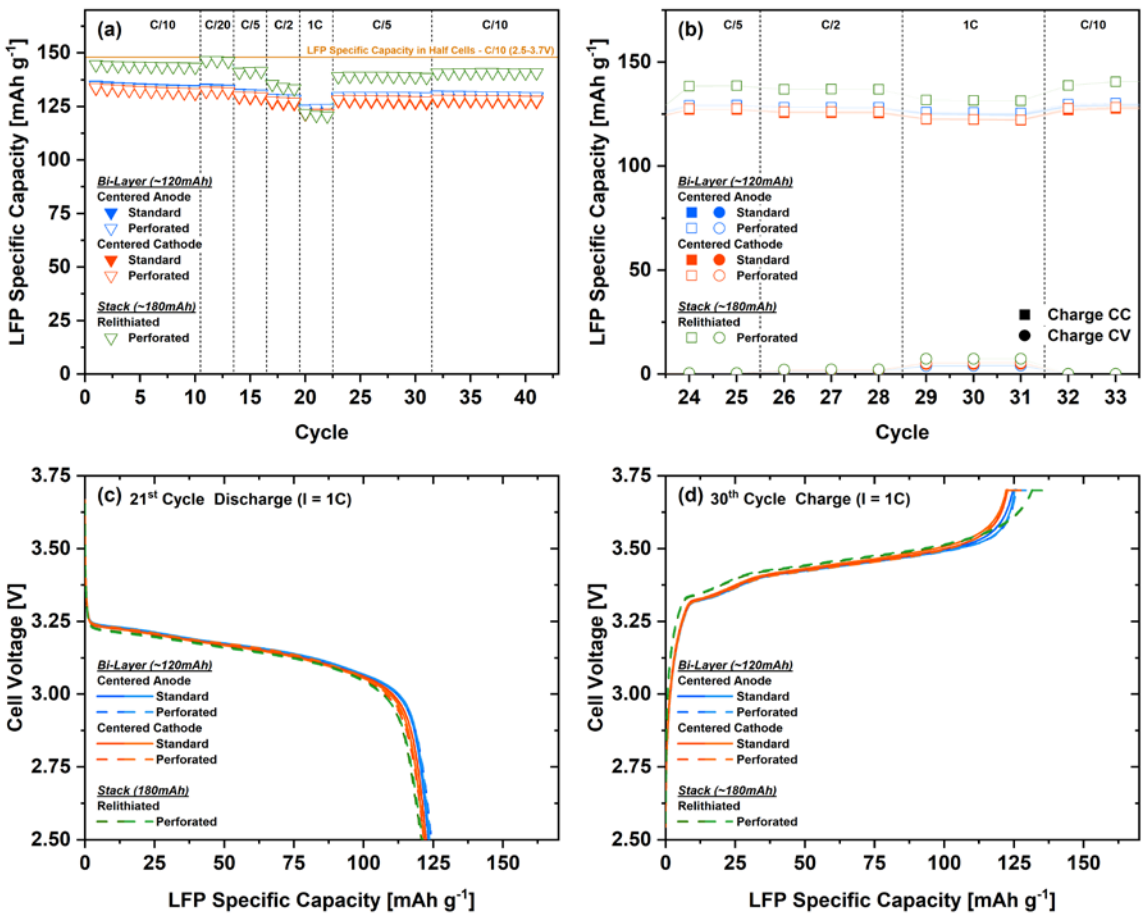

Figure 8.25 Rate capability of Graphite‖LFP bi-layer and stack pouch cells: a) discharge performance, b) charge performance, c) discharge voltage profile at 1C, and d) charge voltage profile at 1C.

Figure 8.26 compares the discharge capacity retention of the current chapter's C-rate capability data directly with the corresponding single-layer pouch cell data discussed in **Chapter 7.2** (page 78). All standard Graphite‖LFP cells investigated in this work (coin cell, single-layer pouch cell, and bi-layer pouch cell) exhibit highly overlapping rate performance, as clearly shown in **Figure 8.26b**. These data indicate that the quality of the electrodes remains consistent when scaling up from a laboratory-scale coating process to a pilot-line electrode manufacturing process. Furthermore, as the data in **Figure 8.26a** shows, relithiated stacked pouch cells demonstrate also similar rate performance to prelithiated and Li-reservoir single-layer pouch cells discussed in **Chapter 7.2**. This demonstrates that the overall concept of managing the size of the cell's active lithium inventory by using a sacrificial lithium donor source and permeable electrodes can be scaled to larger cell systems with a high degree of reproducibility, provided that appropriate relithiation/prelithiation protocols are used.

In summary, the perforated current collector design concept and the relithiation concept investigated here could both be implemented as drop-in technologies in the LIB industry. While the former can be realized directly with standard LIB manufacturing equipment, the latter would require developing a novel cell design that incorporates a fixed or removable lithium donor source.

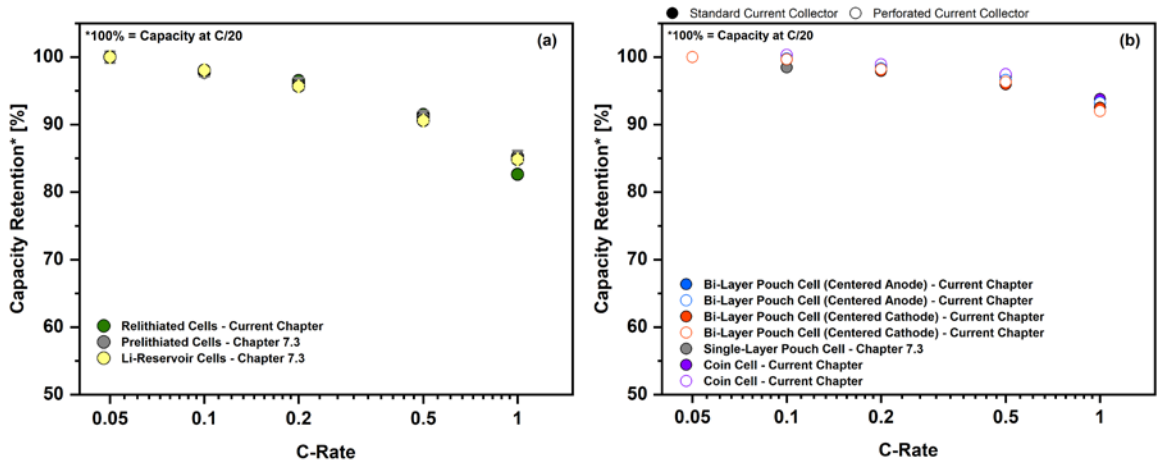

Figure 8.26 Comparison of the discharge rate capability performance of different Graphite‖LFP cell formats in a) prelithiated and b) standard state. The cell's capacity retention is shown as a function of the C-rate.

One step back: Before claiming the success and scalability of relithiation in Graphite‖LFP cells, as indicated by the rate capability data presented above, the exact size of the active lithium inventory in the relithiated cells must be first determined to verify the accuracy of the relithiation concept. **Figure 8.27** presents the voltage profile of the 12th cycle after formation at C/20, along with the corresponding derivative analysis for all bi-layer and stacked pouch cell setups. As mentioned in previous chapters, the voltage plateaus in Graphite‖LFP cells can be directly attributed to the formation of lithium-graphite intercalation/deintercalation compounds due to the flat voltage profile of LFP.[112,228] The corresponding peaks in the derivative voltage analysis are labeled I, II, and III, with peak III corresponding to the final voltage plateau associated with the formation or decomposition of the fully lithiated graphite structure, LiC_6.[112] As discussed in **Chapter 7.2** (page 78), the replenishment of the active lithium deficiency in a Graphite‖LFP cell relative to a reference cell is confirmed when the cell's peak I and II activity overlaps with that of the reference cell and peak III activity is enhanced simultaneously. As clearly visible in the zoomed-in dQ/dV-plot in **Figure 8.27b**, there is enhanced peak III activity, as well as overlapping peak I and II activity, for the relithiated pouch cells compared to the references.

This analysis qualitatively verifies that the relithiation treatment introduced here successfully compensated for the cell's ICLs without forming an anodic lithium reservoir. The remaining question is, to what extent the ICLs were compensated?

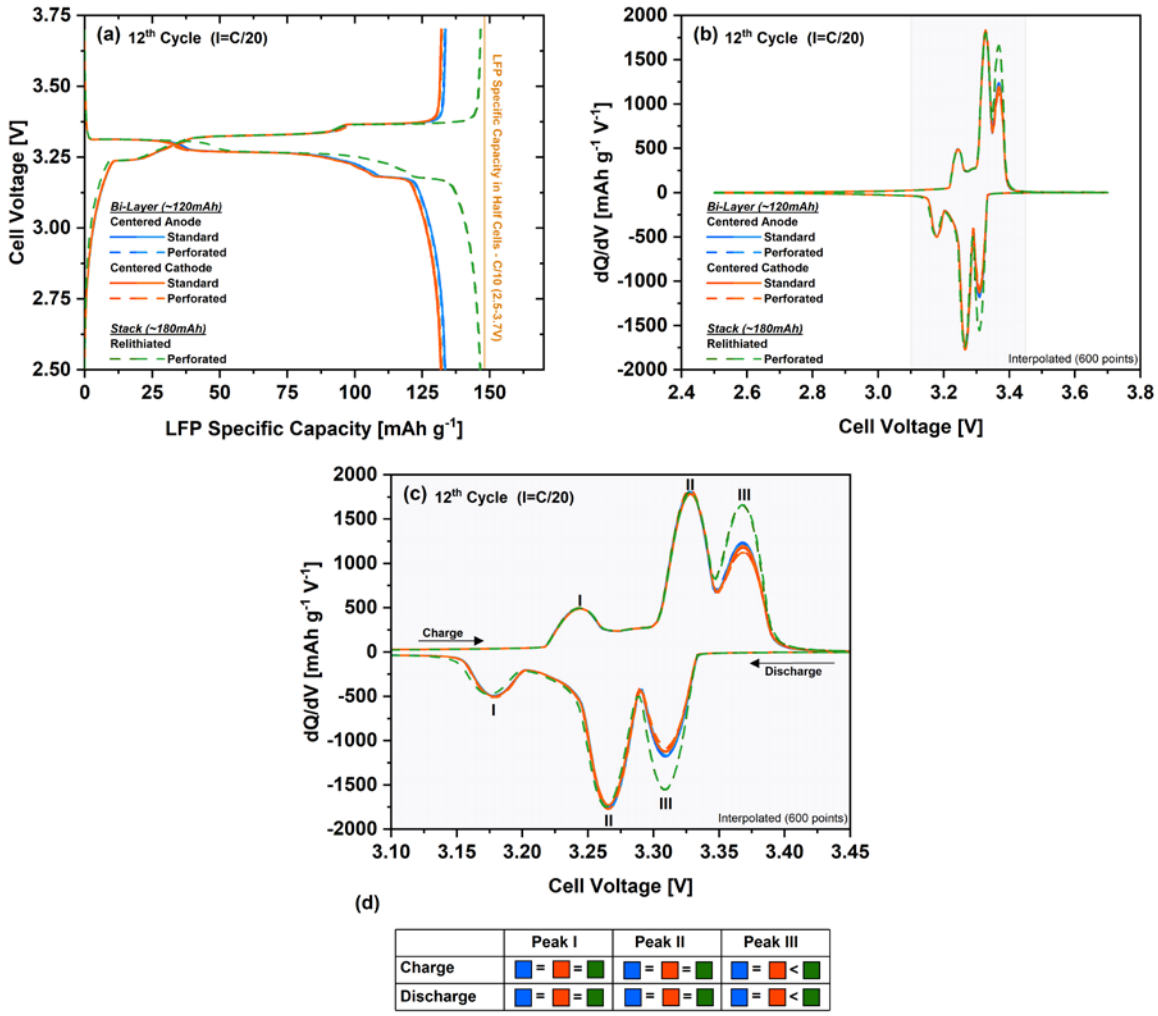

Figure 8.27 12th Cycle at C/20 of Graphite‖LFP bi-layer and stack pouch cells: a) voltage profile, b) derivative analysis, c) zoomed derivative analysis, and d) comparison of the corresponding dQ/dV-plot peak activities.

For this, the quantitative analysis approach described in **Chapter 7.3** (page 87) was employed to determine the exact size of the cell's active lithium inventory in relation to the cell's maximum reversible capacity. As shown in **Figure 8.28**, the maximum anodic lithiation degree for the relithiated stacked pouch cells is 78%, corresponding to an active lithium inventory size of 99% of the cell's maximum reversible capacity ($Q_{rev,cathode} = Q_{rev,cell}$). In contrast, the maximum anodic lithiation degree for standard bi-layer cells (ICLs are not compensated) is ~70%, corresponding to an active lithium inventory size of 89% of the cell's maximum reversible capacity. This value is in agreement with the Graphite‖LFP cells ICL of ~10%.

The quantitative analysis confirms that the relithiation treatment accurately compensated for the cell's ICLs, resulting in nearly 100% utilization of the maximum reversible cathode AM capacity in the operating cell. In conclusion, it can be stated that the relithiation procedure presented here offers a very high accuracy in managing a cell's active lithium inventory size, even in scaled cell setups.

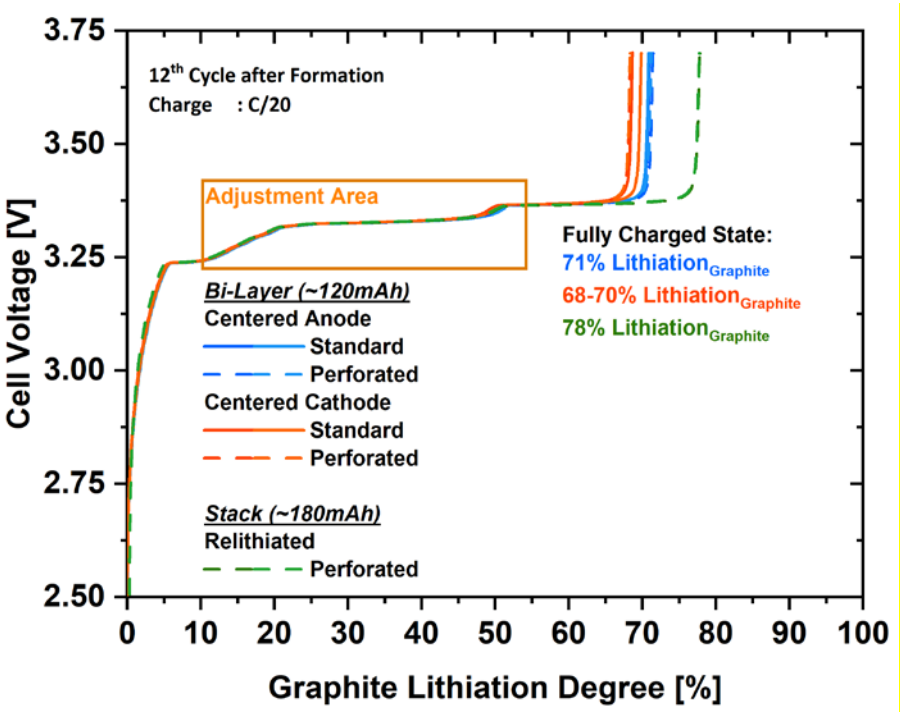

Figure 8.28 Voltage profiles as a function of the graphite lithiation degree of the 12th rate capability charge at C/20 for Graphite‖LFP bi-layer and stacked pouch cells.

8.2.6 Long-Term Cycling and Cell Aging

Following the rate capability protocol (cycle 1 – 41), a long-term cycling protocol was performed within the same potential range of 2.5 to 3.7 V. Two check-up cycles were performed at $I_{Charge/Discharge}$ = C/10, followed by 98 cycles at $I_{Charge/Discharge}$ = C/2 for a total of 2,000 cycles.

All Graphite‖LFP bi-layer and stack pouch cell setups exhibit good cycling performance, as demonstrated in **Figure 8.29**. Notably, cells with the perforated current collector system exhibit reduced capacity fade, indicating a slower aging mechanism compared to cells with only standard current collectors. As a result of its relithiation treatment, the relithiated stack pouch cells exhibit increased utilization of the LFP specific capacity throughout all cycles.

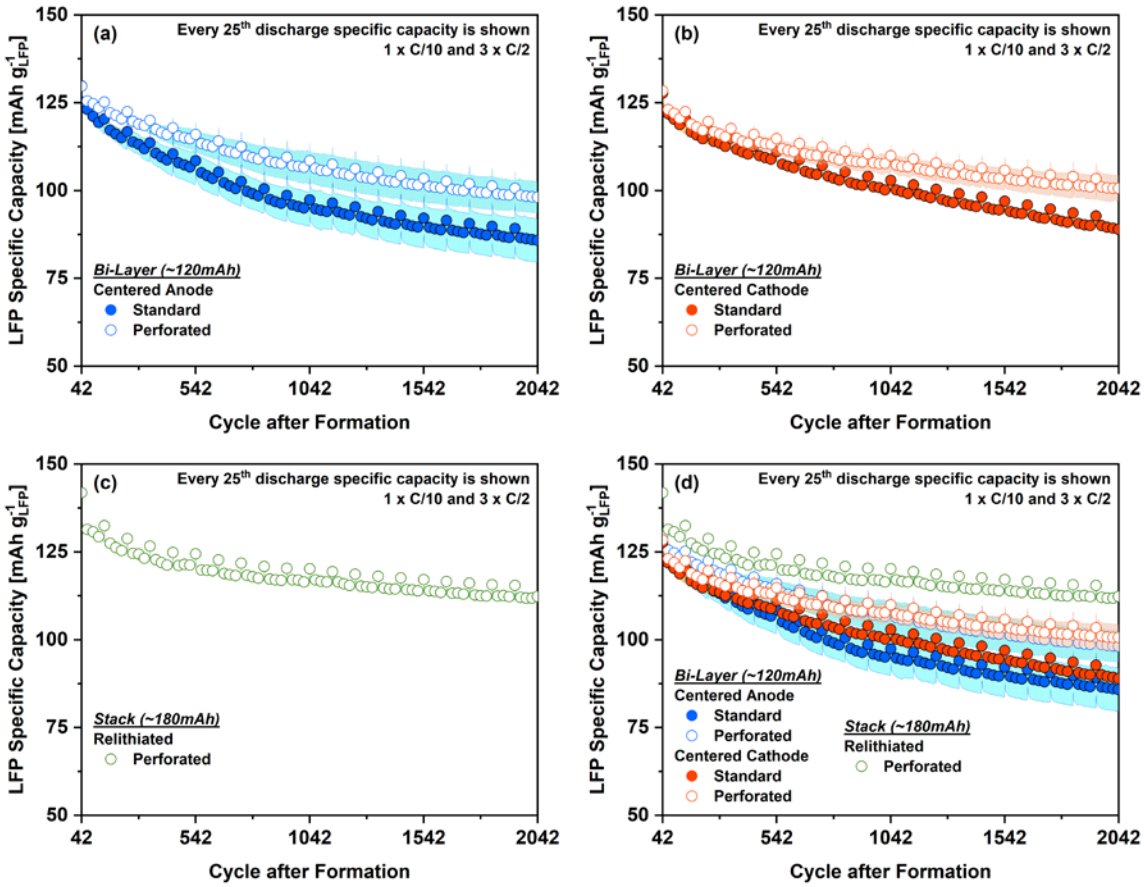

Figure 8.29 Long-term cycling of Graphite‖LFP pouch cells: a) bi-layer cells with centered anode, b) bi-layer cells with centered cathode, c) relithiated stack pouch cells, and d) all pouch cells in one plot.

Figure 8.30 presents the SOH and the accumulated LFP specific capacity loss as a function of cycle number, which is determined from the C/10 check-up cycles. This data provides a better comparison of cell aging across all cell setups. Both plots clearly show that using perforated current collectors in at least one electrode enhances the cell's cycling stability significantly. The advantage of permeable electrodes on the cell's cycle life may stem from beneficial lithium-ion mobility throughout the cell. The underlying process could be described as an inherent self-protection

mechanism mediated by the "communication" of electrode layers via lithium-ion diffusion pathways across the entire cell. Redistribution of lithium ions to the most stable electrochemical regions likely mitigates their activity in more critical areas, which provides a plausible explanation for the reduced aging rate observed in **Figure 8.30**. Nevertheless, the measurements presented here only indicate benefits to cycling stability from permeable electrodes and cannot identify their exact origin. A lower aging rate of LIB cells containing permeable electrodes was also reported in a related study by Zou et al.[227] Thus, the measurements presented here support Zou et al.'s finding that permeable electrodes can improve the long-term cycling performance of LIBs. Further investigation is needed, however, to confirm and understand the underlying difference in the cell's aging mechanism.

Moreover, **Figure 8.30** clearly demonstrates that the cell's aging rate appears to be independent of electrode arrangement or pouch cell size. Relithiated stack pouch cells exhibit a similar aging rate to non-relithiated, bi-layer cells with centered, perforated anodes or cathodes. The enhanced active lithium inventory size of the relithiated cells does not appear to negatively impact their long-term cycling stability.

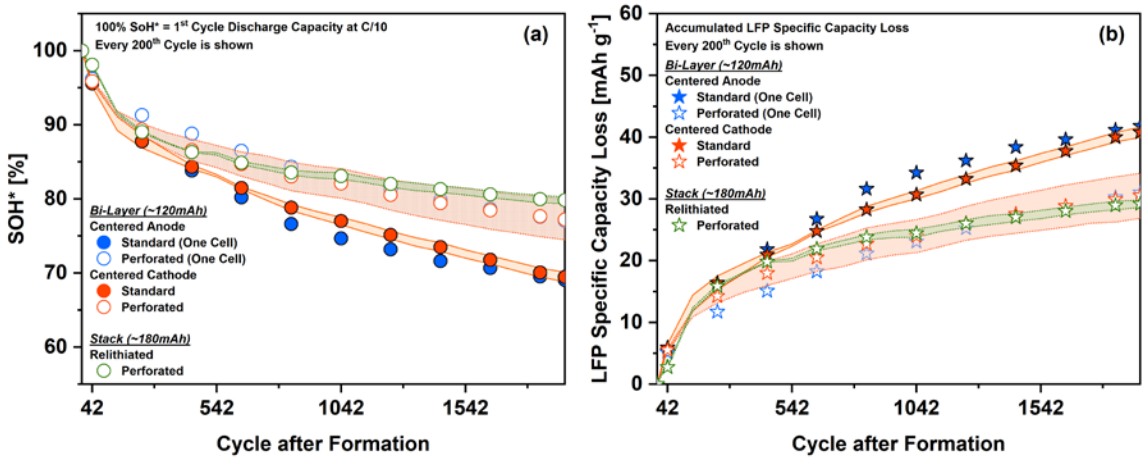

Figure 8.30 Long-term cycling of Graphite‖LFP pouch cells: a) SOH as a function of cycle number and b) LFP specific capacity loss as a function of cycle number.

Once again, it has been found that all of the Graphite‖LFP pouch cells investigated here were predominantly impacted by ALL aging. Consequently, relithiated cells reach an active lithium inventory comparable to that of the reference cells, albeit at a different stage of their cycle life. This hypothesis is supported by the observation of overlapping voltage profiles of the bilayer and stacked pouch cells at different set-up specific cycle numbers, as shown in the **Figure 8.31**.

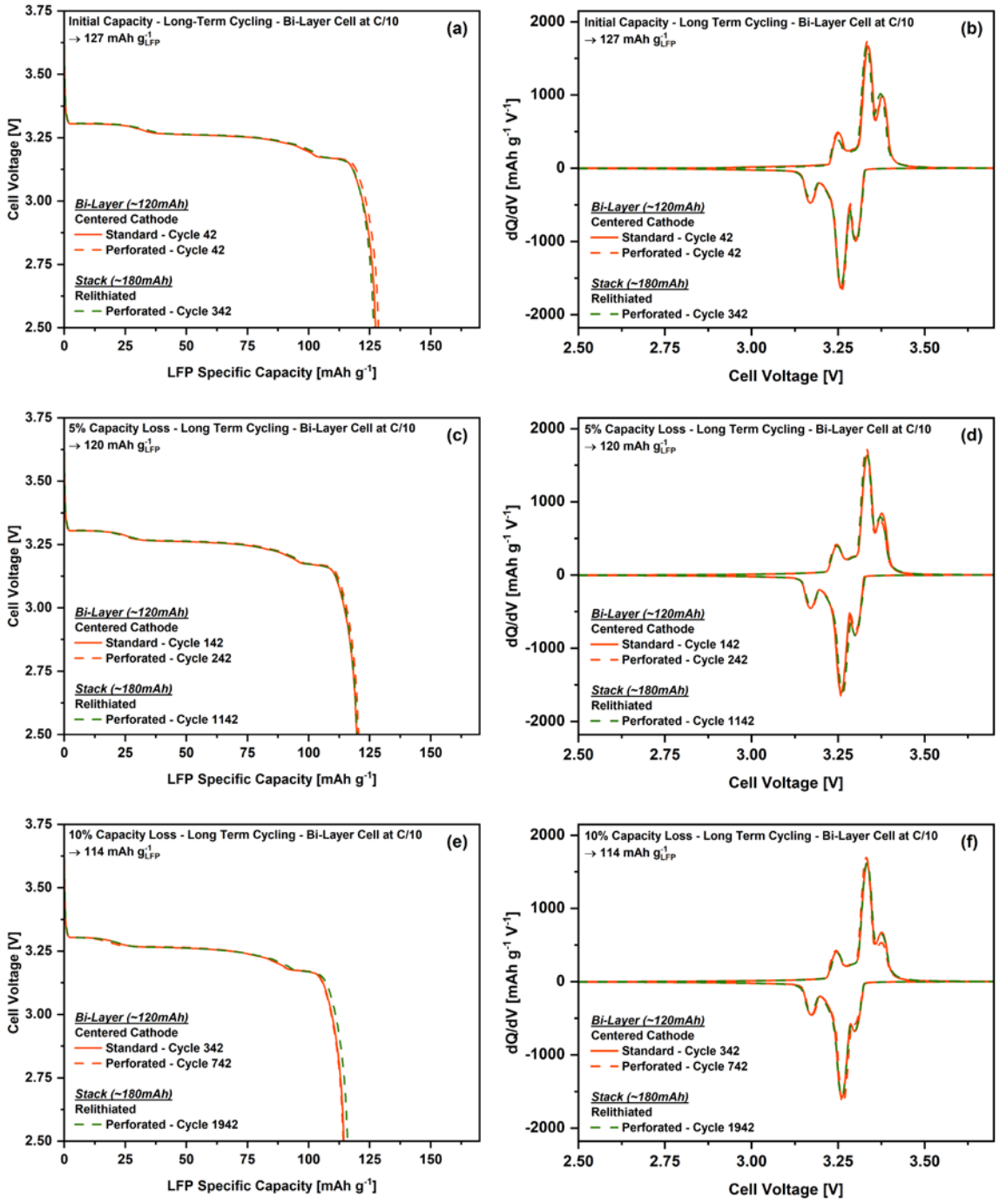

Figure 8.31 Voltage profile and derivative analysis of Graphite‖LFP cells at different SOHs: a,b) Initial capacity of non-relithiated pouch cells, c,d) 5% capacity loss of non-relithiated pouch cells, and e,f) 10% capacity loss of non-relithiated pouch cells.

The initial SOH of standard bi-layer pouch cells in their long-term cycling, corresponding to an LFP specific capacity of 127 mAh g^{-1} (cycle 42), is reached by the relithiated stacked pouch cells after 342 cycles. An additional capacity loss of 5% and 10% is observed at cycles 142 and 342 for bi-layer cells with a standard current collector system, at cycles 242 and 742 for bi-layer cells with a perforated current collector system, and at cycles 1,142 and 1,942 for relithiated stacked pouch

cells. As demonstrated in **Figure 8.31**, the voltage profiles and derivative analysis of all cell setups exhibit almost complete overlap at corresponding cycles.

In summary, cells that feature perforated current collectors in their electrodes demonstrate comparable rate performance and enhanced cycle life when compared to reference cells equipped with conventional current collectors. In addition, a successful application of the relithiation treatment to stacked pouch cells composed exclusively of electrodes with perforated current collectors has been demonstrated. The compensation of the cells' ICLs via relithiation was achieved with high accuracy and reliability, and most importantly, without negatively impacting the cells' rate or cycling performance. In contrast, both exhibited substantial enhancements in direct comparison to reference cells, which contained electrodes from the same pilot line coating batch.

9. Transfer to High Capacity SiC Anode Active Material

The prelithiation and relithiation of Graphite‖LFP LIB cells using perforated current collectors within the electrodes and a sacrificial Li-donor electrode within the cell were demonstrated and discussed in previous chapters. In brief, the size of the cell's active lithium inventory could be accurately controlled and adjusted. Graphite‖LFP cells with an increased inventory of active lithium exhibited improved LFP specific capacity utilization and rate performance while maintaining cycling stability.

This final chapter will transfer the Graphite‖LFP single-layer pouch cell investigation from **Chapter 7** (page 71) to a high capacity SiC anode AM. **Figure 2.4** (page 17) shows half-cell measurements of the SiC AM in direct comparison to the graphite AM. Furthermore, full-cell measurements of both anode AMs using an LFP cathode are provided in **Figure 2.7** (page 25). The SiC electrodes have a coating specific capacity of ~1,280 mAh g^{-1}, that is 370% higher than that of the graphite electrodes used in the previous chapters (343 mAh g^{-1}). However, they have a higher mass contribution of the current collector within the electrode (see **Figure 6.8** on page 48) and higher ICLs. Specifically, the ICL of the SiC‖LFP cells investigated in this study is 24%, compared to 10% for the Graphite‖LFP cells. As discussed in **Chapter 6.2** (page 46), compensating for ICLs allows SiC anode AM chemistry to surpass the well-established graphite anode AM chemistry in LIBs in terms of significant capacity advantages. This chapter aims to provide an initial understanding of active lithium inventory control and its impact on the electrochemical performance of SiC‖LFP cells. To this end, three distinct SiC‖LFP cell systems that differ only in the size of their initial active lithium inventory will be prepared and examined.

i) ***Standard***, where ICL are not compensated
ii) ***ReLi***, where ICL are compensated
iii) ***Li-Reservoir***, where ICL are compensated and an additional anodic Li-reservoir equivalent to 10% of the cell's capacity is provided.

The target N/P-ratio at the electrode level is 1.20 for all cell systems. However, the N/P-ratio at the cell level and the anode and cathode state of lithiation will differ depending on the cell's active lithium inventory size, as illustrated in **Figure 9.1**.

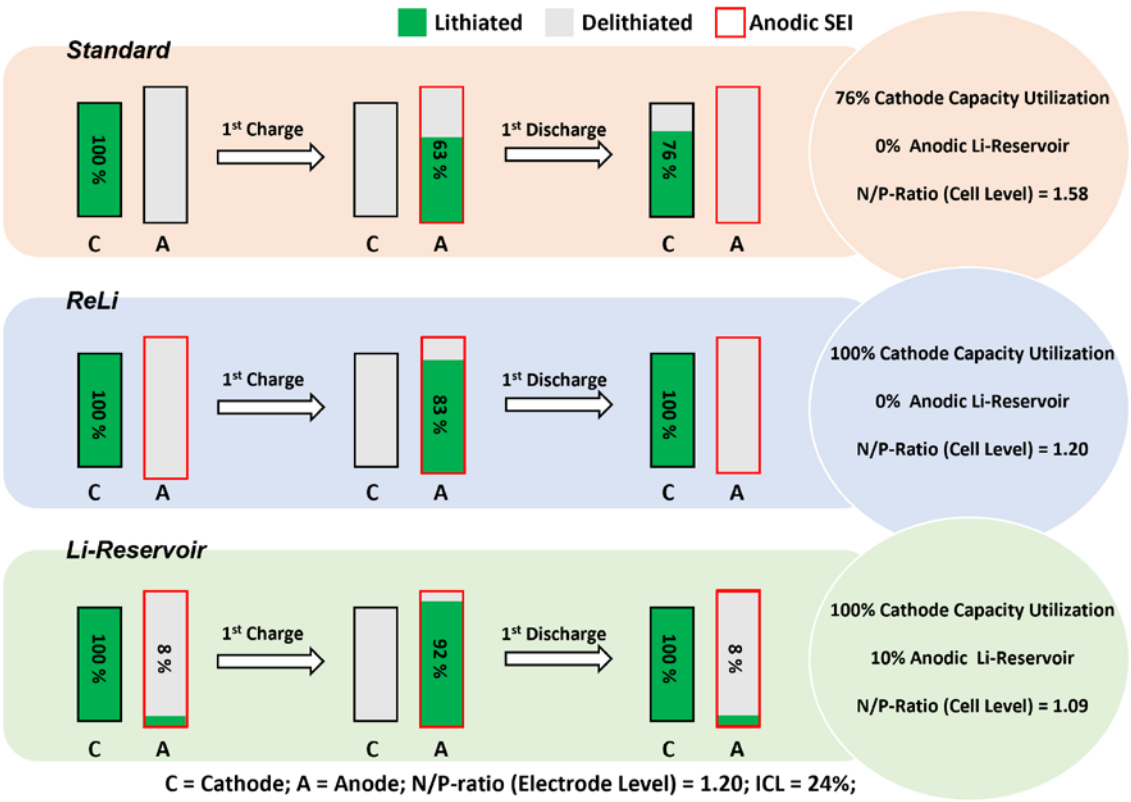

Figure 9.1 Illustration of three distinct LIB SiC‖LFP systems that differ only in the size of their initial active lithium inventory: Standard (top), where ICL are not compensated; ReLi (center), where ICL are compensated; Li-Reservoir (bottom), where ICL are compensated and an additional anodic lithium reservoir equivalent to 10% of the cell's capacity is provided.

9.1 Single-Layer Pouch Cells

9.1.1 Single Layer Pouch Cell Setups

For each of the three active lithium inventory systems presented in **Figure 9.1** (Standard, ReLi, and Li-Reservoir), two SiC‖LFP single-layer pouch cells (~60 mAh) were assembled as illustrated in **Figure 9.2**. The ReLi and Li-Reservoir setups allow compensation for ICLs, as described and demonstrated in previous chapters. Celgard 2325 were used as the separators and 1.2 mL of 1 M LiPF6 in EC:EMC (3:7) + 2 wt.% VC + 10% FEC (LP10VC02FEC10) was used as the electrolyte. All cells contained LFP electrodes prepared as described in **Chapter 7.2** (page 78) and SiC anodes with an areal capacity of 3.0 mAh cm^{-2} provided by Wacker Chemie AG. The N/P-ratio at the electrode level was adjusted between 1.20 and 1.25 for all cells.

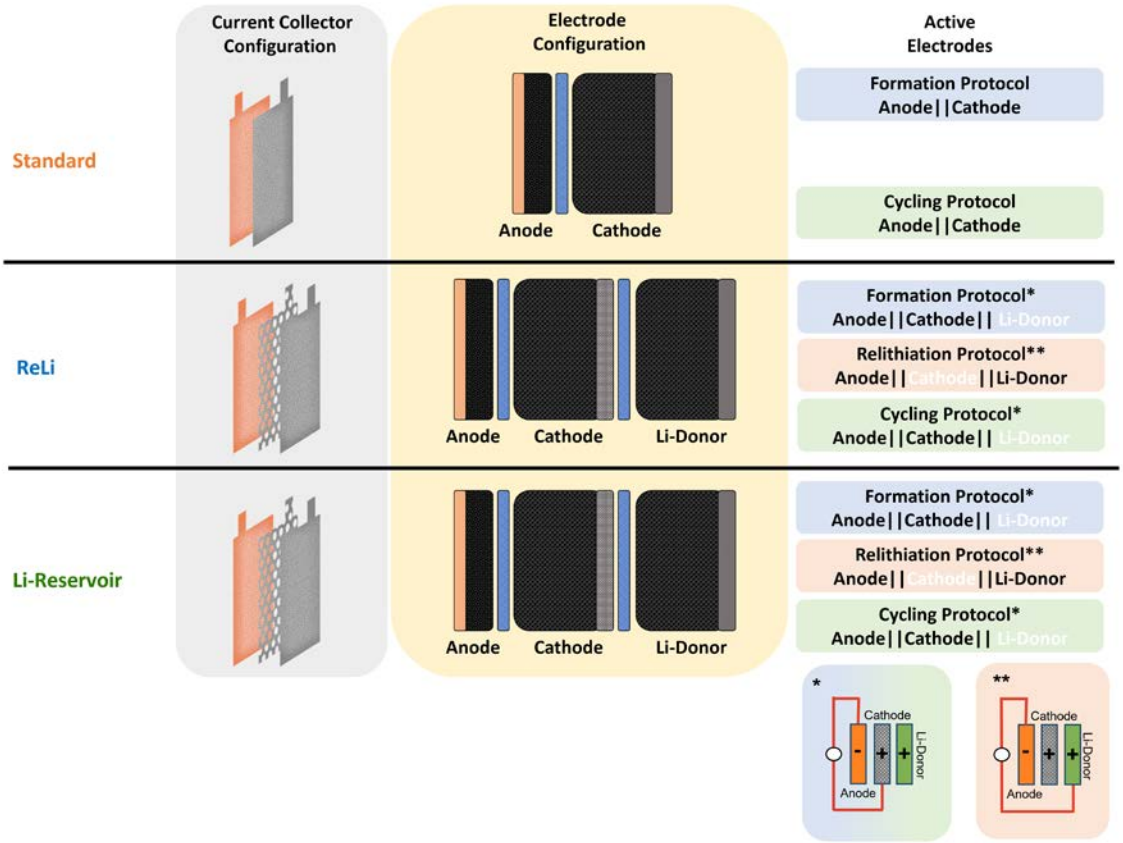

Figure 9.2 Illustration of various SiC‖LFP single-layer pouch cell setups, along with the electrode connections during the formation, relithiation and cycling protocols. Black-marked electrodes are active in the respective protocol, while white-marked electrodes remain inactive.

9.1.2 Formation

Five formation cycles were performed within the voltage window 2.5 – 3.7 V, using a CCCV-charge (I until V_{cell} > 3.7 V; V = 3.7 V until I < C/20) and a CC-discharge (I until V_{cell} < 2.5 V) protocol at a C-rate of C/10. The active electrodes during cell formation for each pouch cell setup are indicated in **Figure 9.2**.

Figure 9.3 shows the formation data of all cell systems. All cells exhibit comparable cell capacities with an initial charge LFP specific capacity utilization of ~151 mAh g^{-1} closely to those measured in half-cells (~149 mAh g^{-1}), followed by an ICL of ~24%, resulting in an usable LFP specific capacity of ~114 mAh g^{-1} in the final formation discharge. Interestingly, Standard cell systems with standard current collector cathode's show slight overpotentials in their initial charge. Beside this, no severe overpotentials or other electrochemical drawbacks are observed in the formation data of all cell systems under investigations.

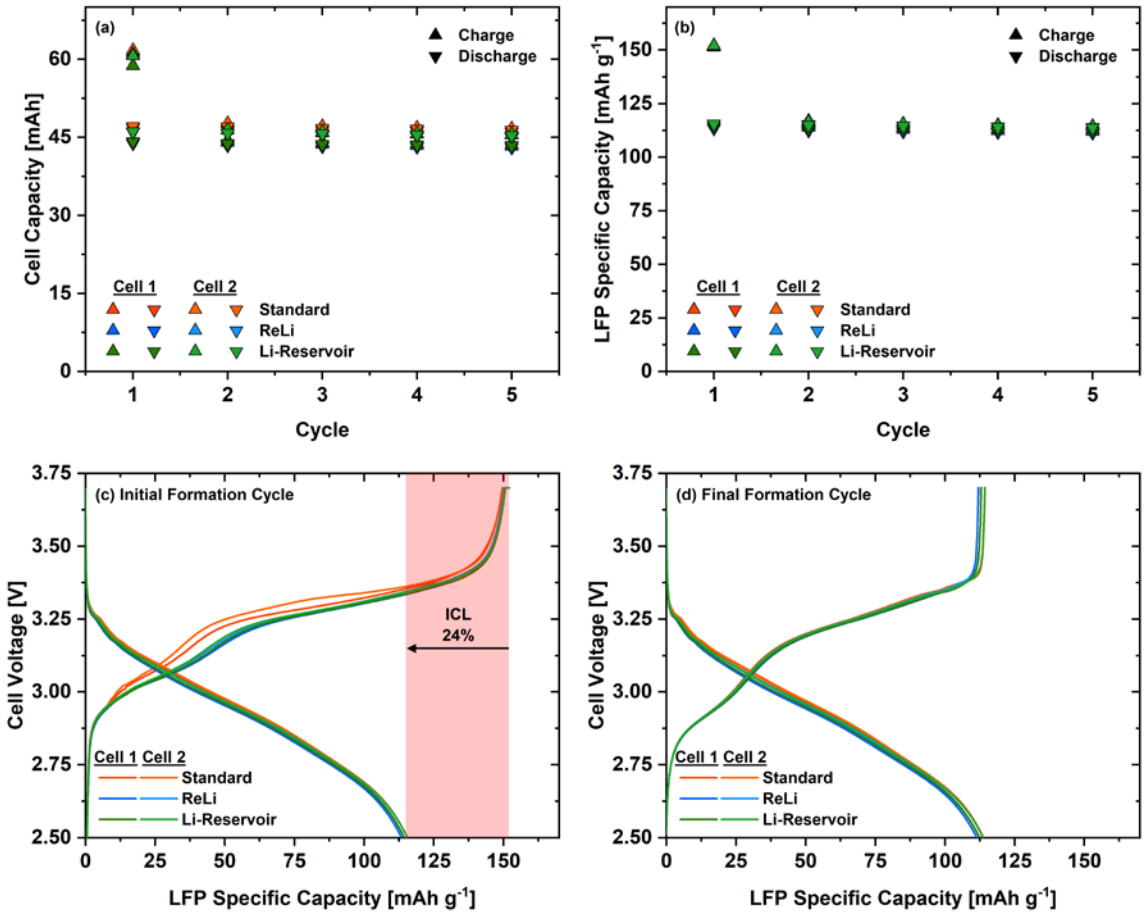

Figure 9.3 Formation data of SiC‖LFP single-layer pouch cell systems: a) cell capacity as a function of cycle number, b) LFP specific capacity as a function of cycle number, c) initial cycle voltage profile, and d) final cycle voltage profile. All cells contain a positive electrode with an areal capacity of ~2.45 mAh cm^{-2}, a N/P-ratio of 1.20 – 1.25, and LP10VC02FEC10 as electrolyte.

9.1.3 Relithiation

Following the cell formation protocol, the ReLi and Li-Reservoir cells underwent an additional relithiation protocol. The ICLs of the cells were quantified at ~15 mAh and compensated by connecting the Li-donor electrode to the anodes while keeping the cathodes inactive during a well-controlled charging step. A partial CC-charge protocol at a low current density of 1 mA was applied until $Q_{charge} = Q_{ICL}$ for ReLi cells and $Q_{charge} = Q_{ICL+Li\text{-}Reservoir}$ for Li-Reservoir cells, as illustrated in **Figure 9.4**.

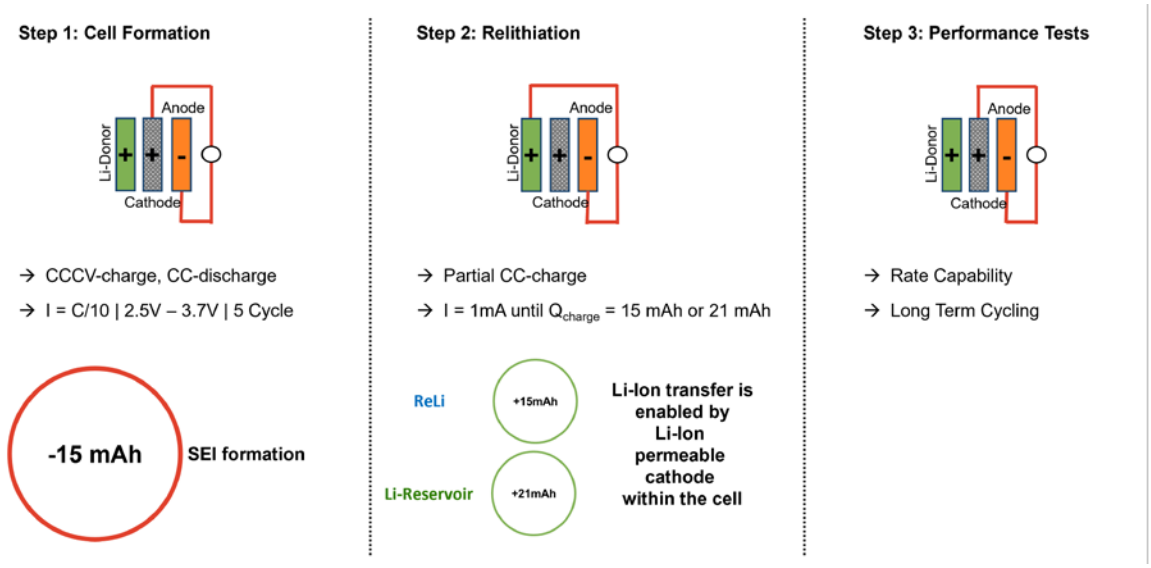

Figure 9.4 Illustration of the relithiation procedure applied to SiC‖LFP single-layer pouch cells.

Figure 9.5 shows the CC-charge voltage profile of the final formation cycle (anode‖cathode, I = 6 mA) in direct comparison with the CC-charge voltage profile of the relithiation step (anode‖Li-donor, I = 1 mA until Q_{charge} = 15 mAh or 21 mAh) of ReLi and Li-Reservoir cells. As clearly demonstrated, the amount of lithium ions transferred can be again accurately controlled by the charge capacity and only minor polarization effects are observed during the cell's relithiation treatment. The pre-formed SEI on the anode surface of ReLi and Li-Reservoir cells is expected to be of the same quality as that of Standard cells because they were formed under the same conditions. It can be concluded that the relithiation approach presented in this study can be transferred directly to other cell chemistries.

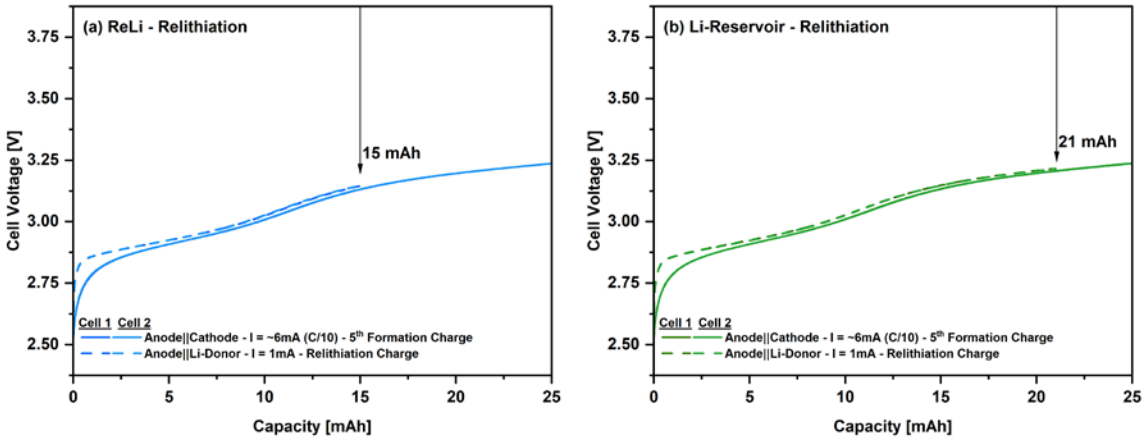

Figure 9.5 Comparison of voltage profiles of the final formation cycle charge and the relithiation charge of a) ReLi and b) Li-Reservoir SiC‖LFP single-layer pouch cells.

9.1.4 Rate Capability and Electrochemical Characterization

Following the formation protocol (all cell setups) and the relithiation protocol (ReLi and Li-Reservoir cells), discharge (I = C/10, C/20, C/5, C/2, 1C) and charge (I = C/5, C/2, 1C) rate capability measurements were conducted under standard active electrode conditions (anode‖cathode), as highlighted in **Figure 9.2**.

Figure 9.6 presents the data for the discharge and charge rate performance tests. Throughout the entire rate capability test, ReLi and Li-Reservoir cells demonstrate increased utilization of LFP specific capacity compared to Standard cells. Relithiation treatment successfully replenished the lithium deficiency caused by ICLs during cell formation. This is evident from the nearly full utilization of LFP's reversible specific capacity at low C-rate cycles (C/20), which corresponds to a capacity improvement of over 20% at C/20 compared to non-relithiated Standard cells.

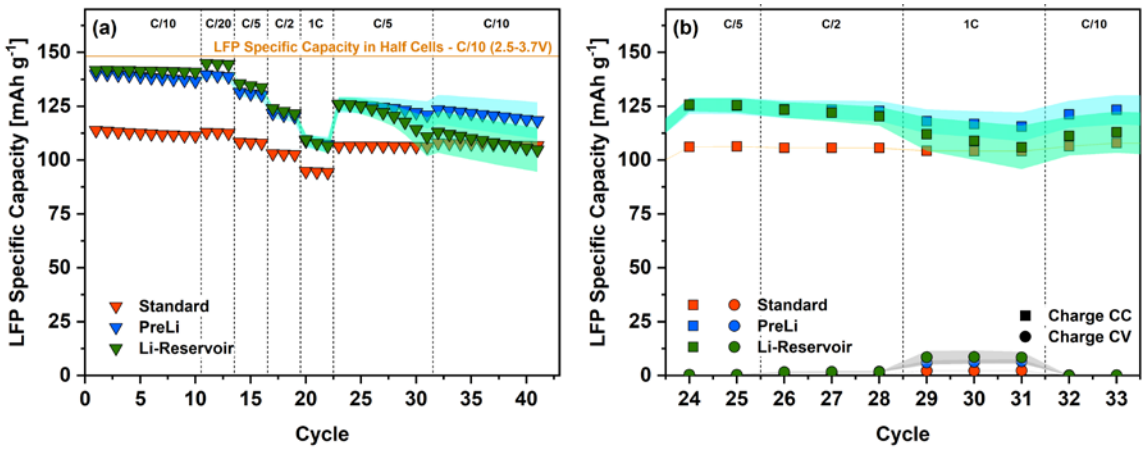

Figure 9.6 Rate capability of SiC‖LFP single-layer pouch cells: a) discharge performance, b) charge performance. All cells contain a positive electrode with an areal capacity of ~2.45 mAh cm^{-2}, a N/P-ratio of 1.20 – 1.25, and LP10VC02FEC10 as electrolyte.

However, unlike prelithiated/relithiated Graphite‖LFP cells discussed in previous chapters, relithiated SiC‖LFP cells exhibit a severe capacity fade during their rate performance testing as clearly observable in **Figure 9.6a**. Meanwhile, the capacity fade of the non-relithiated Standard cells is far less pronounced, without showing significant aging throughout the entire measurement protocol. As **Figure 9.1** shows, a higher level of active lithium inventory within the cells is directly related to a higher degree of anodic lithiation during charging. For the SiC anode chemistry, greater volume expansion is associated with higher anodic lithiation levels.[133,134] This can result in electrode and AM degradation during cycling.[136,140,141] In **Figure 9.6a**, especially at higher charging C-rate cycles of C/2 and 1C, pronounced capacity fade is evident for Reli and Li-Reservoir cells. It should be noted that, in addition to more severe volume expansion, the risk of undesired anodic lithium plating also increases with higher anodic lithiation levels, as electrode polarization at higher charging rates can cause the anode potential to drop below 0 V vs. Li^+/Li more easily.[47,48] For this, higher anodic lithiation levels and charging rates can negatively impact the cycling stability of SiC electrode chemistry, as shown in the here presented rate performance data.

Figure 9.7a shows the cell's SOH as a function of cycle number at low C-rate (C/10), before and after rate performance testing, confirming that ReLi and Li-Reservoir SiC‖LFP cells age more quickly following rate testing than the non-relithiated Standard cells. Unlike the Graphite‖LFP cell chemistry examined in previous chapters, adding active lithium to the SiC‖LFP cells with a similar N/P-ratio at the electrode level doesn't maintain their cycling stability – especially at higher charging rates – and actually makes them age faster. The critical degree of anodic lithiation level necessary for the stable cycling of the here investigated SiC AM appears to have already been exceeded for the respective ReLi cells. This sensitivity to high anodic lithiation states was not observed for respective cells with graphite anodes, as shown in **Figure 9.7b** and **c**. Graphite‖LFP cells with an enhanced active lithium inventory in **Figure 9.7b** slightly exceed 100% SOH in their initial C/10 cycles. This unusual cycling trend can be explained by the activation of active sites and the presence of an anodic active lithium inventory over their initial cycles in both, PreLi and Li-Reservoir cells, as figured out in **Chapter 7.3.3** (page 92).

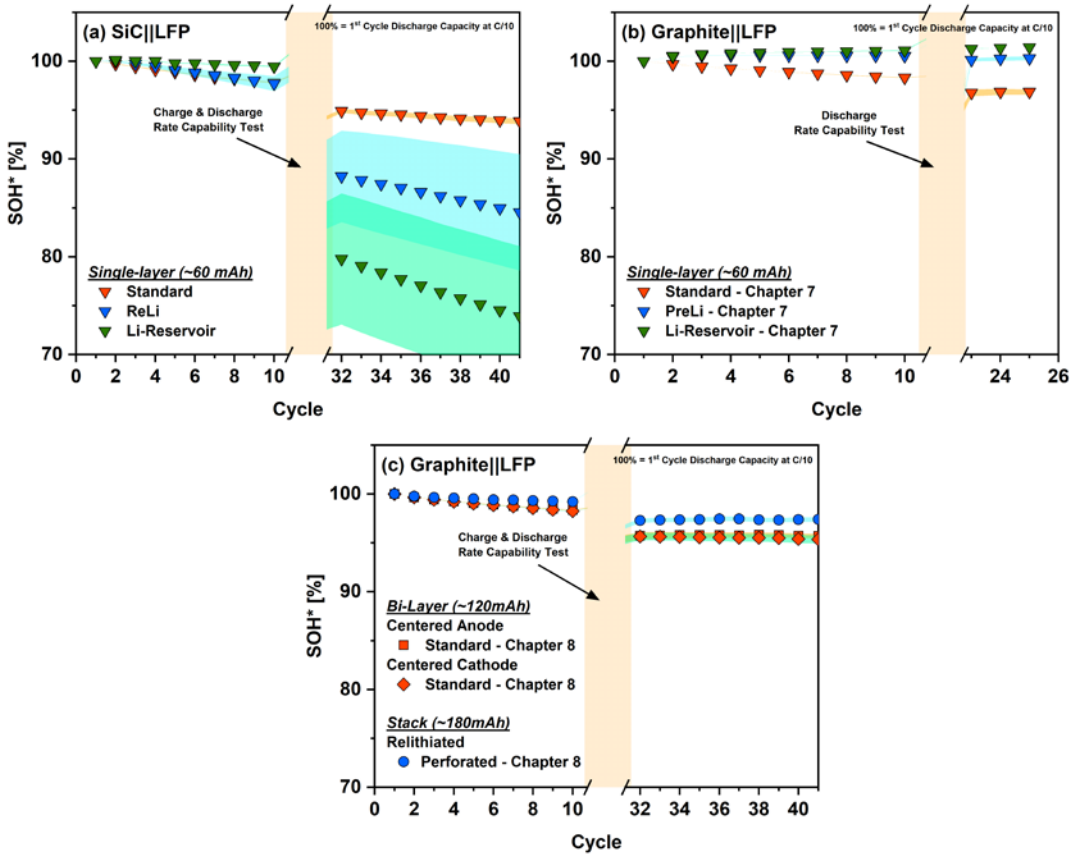

Figure 9.7 SOH as a function of cycle number of C/10 cycles before and after rate performance testing: a) SiC‖LFP cells from the current chapter, b) Graphite‖LFP cells from chapter 7, and Graphite‖LFP cells from chapter 8.

Voltage profiles and dQ/dV-plots at 1C charge and discharge for all SiC‖LFP systems are provided in **Figure 18.1** on page 189 in the appendix. In short, regardless of their active lithium inventory size, all cells exhibit similar polarization effects at increased C-rates since their dQ/dV peak positions are aligned.

The next key question is whether the active lithium inventory in SiC‖LFP cells can be examined and quantified in a manner similar to Graphite‖LFP cells. The accelerated aging mechanism at higher lithiation states is not the only difference between both cell chemistries. The voltage profile shape of the SiC anode chemistry is also more complex than those of the graphite anode chemistry, as shown in the half-cell measurements presented in **Figure 2.4** (page 17). Nonetheless, similar to Graphite‖LFP full-cells, the voltage profile shape in SiC‖LFP full-cells mirror those of the cell's anode due to the flat voltage profile of LFP. This feature can be used again to gain in-depth insights into the cell's anodic lithiation/delithiation activity at low C-rates.

Figure 9.8 shows the voltage profile and the corresponding derivative analysis for all SiC‖LFP cell systems at a C/20 rate. In the dQ/dV-plot, three "zones" of anodic activity are distinguished to provide sufficient analysis. Namely, zone I, zone II, and zone III, with zone III activity relating to a high degree of lithiation of the SiC electrode.

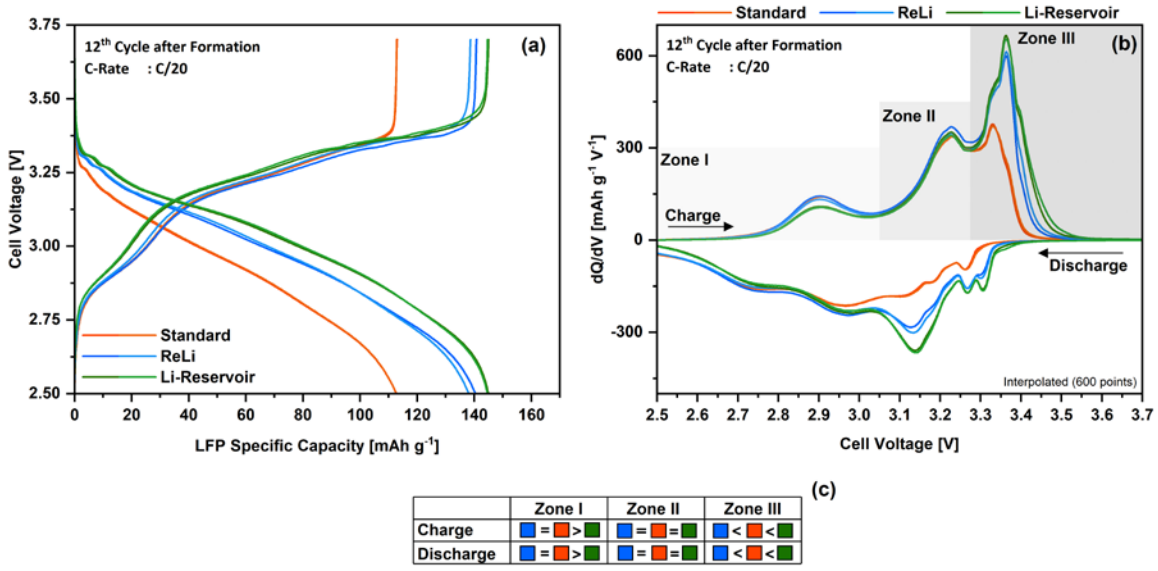

Figure 9.8 12th Cycle at C/20 of SiC‖LFP single-layer pouch cells: a) voltage profile, b) derivative analysis, and c) comparison of the different dQ/dV-plot zone activities.

As shown in the derivative analysis in **Figure 9.8**, the activity of all SiC‖LFP cell systems in Zone II overlaps to a high degree. ReLi cells, in which only ICLs were compensated, show additional overlapping Zone I activity, as well as enhanced Zone III activity, compared to the Standard cells. And Li-Reservoir cells, in which ICLs were compensated and an anodic lithium reservoir equivalent to 10% of the cell's capacity was established, Zone I activity is decreased, while Zone III activity is enhanced, compared to the Standard and ReLi cells.

A pattern similar to that of respective Graphite‖LFP cells with different active lithium inventory sizes from ***Chapter 7.3*** (page 87) can be clearly identified. Namely, compared to a reference, similar activity at the beginning of charging (Zone I for SiC‖LFP or Peak I for Graphite‖LFP), overlapping activity in the middle (Zone II for SiC‖LFP or Peak II for Graphite‖LFP), and increased activity at the

end (Zone III for SiC‖LFP or Peak III for Graphite‖LFP) directly indicates an increased active lithium inventory without an anodic lithium reservoir. Lower activity at the beginning of charging, together with overlapping activity in the middle and enhanced activity at the end, corresponds to a cell with an anodic lithium reservoir. Lastly, similar beginning and center activity and decreased end activity identify a decreased active lithium inventory, or an ALL aged cell.

Figure 9.9 summarizes the overall qualitative analysis method to indicate the size of a cell's active lithium inventory. An arbitrary dQ/dV-plot shape is used to emphasize that the analysis is expected to be valid regardless of the anode and cathode chemistry of the studied cell. Two requirements must be fulfilled to apply this qualitative analysis: i) data from a low C-rate charge of the studied cell, as well as from a suitable reference cell (ideally immediately after the reference cell's formation), is necessary, and ii) the voltage profile shapes of the electrodes must be stable (no severe degradation next to ALL should be present). A suitable reference cell is one that has similar electrode design and balancing (N/P-ratio at the electrode level) to that of the studied cell. Overall, if both requirements are met, this analysis is expected to be valid for post-lithium systems as well. In this case, of course, lithium would no longer be the charge carrier. Proving this would go beyond the scope of this work. However, future studies should investigate this, ideally starting with sodium-ion battery cells using perforated current collectors and a sacrificial sodium donor electrode.

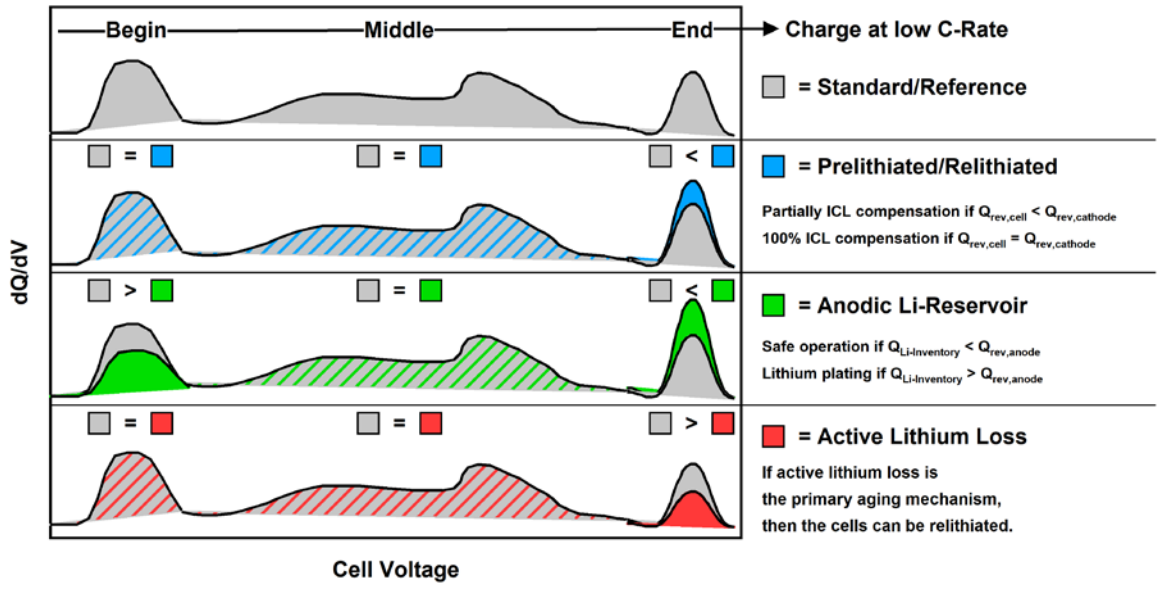

Figure 9.9 Schematic summary of the qualitative analysis method used to estimate the size of a cell's active lithium inventory by means of derivative analysis during low C-rate charging of the studied cell compared to a suitable reference cell. A suitable reference cell is one that has similar electrode design and balancing (N/P-ratio at the electrode level) to that of the studied cell. An arbitrary dQ/dV-plot shape is used to emphasize that the analysis is expected to be valid regardless of the anode and cathode chemistry of the studied cell.

Finally, the overlapping Zone II activity of all three cell systems in their derivative analysis (**Figure 9.8**) was used to quantify the active lithium inventory, in a manner similar to that used for Graphite‖LFP cells, as presented in **Chapter 7.3.3** (page 92). To this end, the degree of anode

lithiation in the discharged and charged states was determined by adjusting the cell's voltage profiles in the Zone II region by shifting them along the x-axis until they overlapped with the standard cell's voltage profile, as plotted in **Figure 9.10**. This analysis quantifies that the size of the anodic lithium reservoir in the Li-Reservoir cells under investigation was equivalent to 6% rather than 10% of the cell's capacity. It appears that not all the donated active lithium remained active after the relithiation treatment. It seems that capacity losses above 4% of the cell's capacity occurred during the preceding ten C/10 cycles. Moreover, anodic lithiation states of 60%, ~72% and ~78% are observed in the fully charged state in the Standard, ReLi and Li-Reservoir cells, respectively. These values correspond to active lithium inventory sizes of 75.8%, 95.7% and 104.1% relative to the cell's maximum reversible capacity (calculated using **Equation 7.3** from **Chapter 7.3.3** on page 95). The active lithium inventory size of 75.8%$Q_{rev,cell}$ for the Standard cells matches the predicted value of 76%$Q_{rev,cell}$ (ICL of 24% → 76% of the cell's maximum reversible capacity remain). Interestingly, ReLi and Li-Reservoir cells show significant inconsistencies, as their intrinsic active lithium inventory size is much lower than their expected one. Specifically, 95.7%$Q_{rev,cell}$ instead of 100%$Q_{rev,cell}$ for the ReLi cells and 104.1%$Q_{rev,cell}$ instead of 110%$Q_{rev,cell}$ for the Li-Reservoir cells. It again seems that not all of the donated active lithium remained active during the initial C/10 cycles following the cell's relithiation treatment in the ReLi and Li-Reservoir systems.

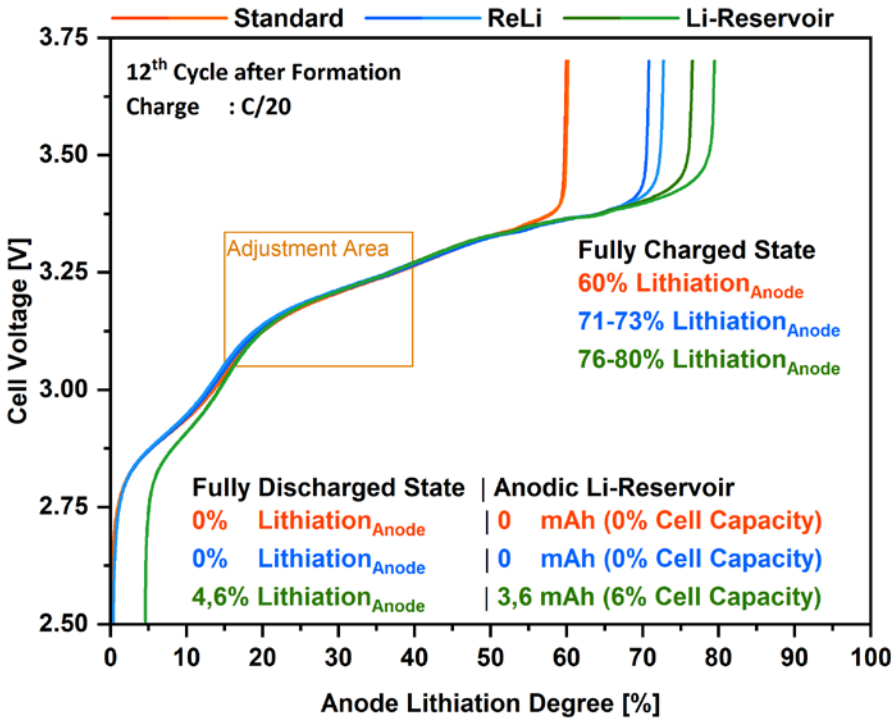

Figure 9.10 Voltage profiles as a function of the anodic lithiation degree of the 12th rate capability charge at C/20 for Standard, ReLi and Li-Reservoir SiC‖LFP single-layer pouch cells.

Figure 9.5 clearly demonstrates that during the cell's relithiation the right amount of capacity was transferred from the donor to the anode in ReLi and Li-Reservoir cells. In conclusion, the accurate

adjustment of the active lithium inventory size in SiC‖LFP cells is much more complex, as severe aging mechanisms seem to be present from the beginning when anodic lithiation levels reach a critical point. This was not the case in the context of Graphite‖LFP cells, which appear to be less sensitive to high anodic lithiation states. However, the quantitative analysis method presented here to determine a cell's exact active lithium inventory size appears to be highly accurate and should be employed in the context of prelithiation/relithiation studies.

Figure 9.11 summarizes the overall quantitative analysis method used to determine the size of a cell's active lithium inventory, as well as the size of the anodic lithium reservoir, if present. Again, an arbitrary voltage profile shape is used to emphasize that the analysis is expected to be valid regardless of the anode and cathode chemistry of the studied cell. Two requirements must be fulfilled to apply this quantitative analysis: i) data from a low C-rate charge of the studied cell, as well as from a suitable reference cell (ideally immediately after the reference cell's formation), is necessary, and ii) the voltage profiles of both cells must be stable and overlap significantly in the middle of their anodic lithiation in order to find a sufficient adjustment area (there should be no severe degradation next to ALL present).

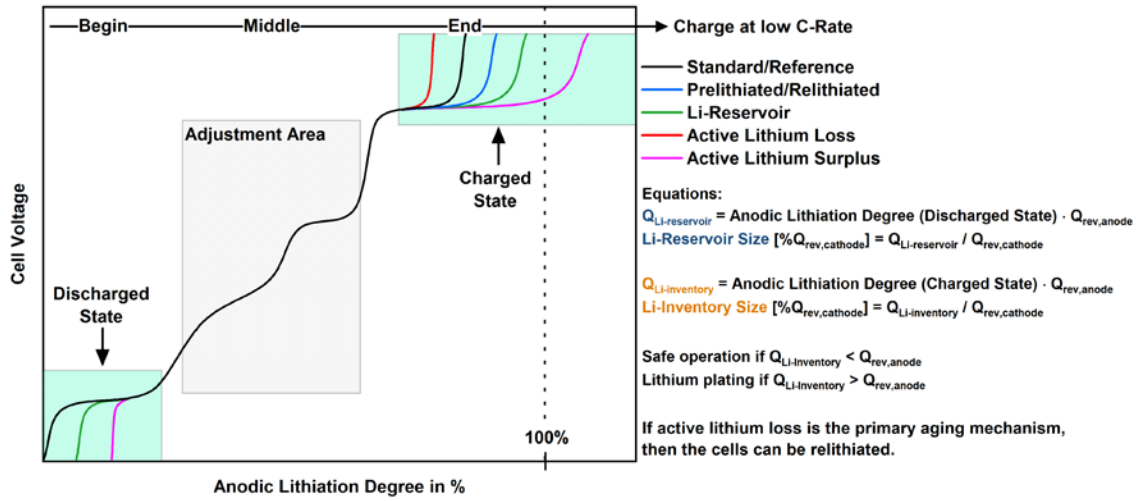

Figure 9.11 Schematic summary of the quantitative analysis method used to quantify the size of a cell's active lithium inventory, as well as the size of the anodic lithium reservoir, if present, by means of the cell's voltage profile as a function of anodic lithiation degree during low C-rate charging of the studied cell compared to a suitable reference cell. A suitable reference cell is one that has similar electrode design and balancing (N/P-ratio at the electrode level) to that of the studied cell. An arbitrary voltage profile shape is used to emphasize that the analysis is expected to be valid regardless of the anode and cathode chemistry of the studied cell.

9.1.5 Cell Aging

Following the rate capability protocol, a long-term cycling protocol was performed within the same voltage range of 2.5 to 3.7 V. One check-up cycle was performed at C/10, followed by 49 cycles at C/2, for a total of 200 cycles.

Figure 9.12 shows the long-term cycling data for all of the cell systems that were investigated. While standard cells exhibit an almost constant aging rate, ReLi and Li-Reservoir cells demonstrate pronounced, non-constant aging behavior. Overall, SiC‖LFP cells with a higher initial active lithium inventory age more severely. Long term cycling data confirms that surpassing a critical degree of anodic lithiation during charging of SiC‖LFP cells results in an accumulated, irreversible degradation mechanism within the respective cell.

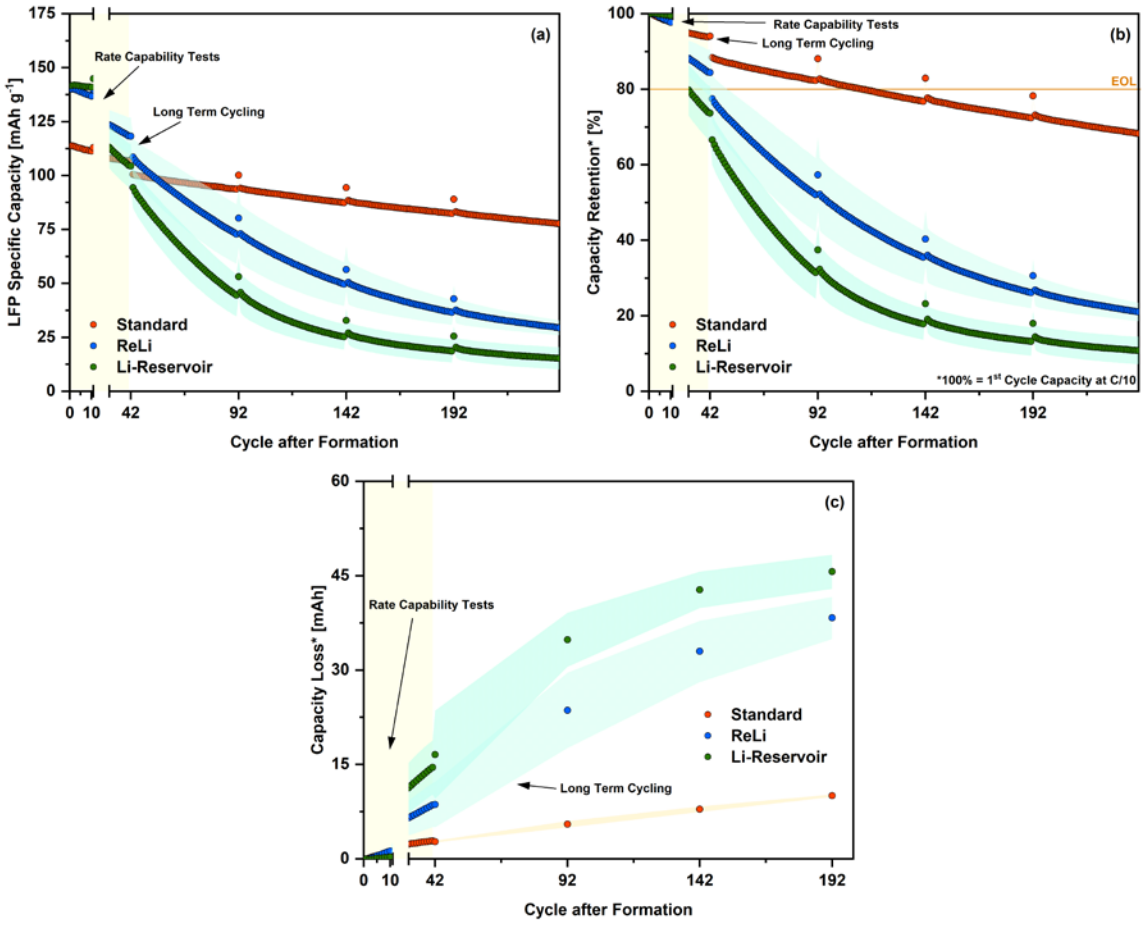

Figure 9.12 Cycling data of SiC‖LFP cells: a) LFP specific capacity as a function of cycle number, b) capacity retention as a function of cycle number, and c) capacity loss as a function of cycle number. All cells contain a positive electrode with an areal capacity of ~2.45 mAh cm^{-2}, a N/P-ratio of 1.20 – 1.25, and LP10VC02FEC10 as electrolyte.

Figure 9.13 shows the evolution of the voltage profiles during C/10 cycles. Unlike the previously discussed Graphite‖LFP cells, the SiC‖LFP cells discussed here exhibit significant changes in their voltage profile shape throughout their cycle life. The severity of the SiC‖LFP degradation mechanism

appears to correlate with the cell's maximum anodic lithiation degree. A higher initial active lithium inventory size seems to result in faster capacity fade and a more rapid change in the respective cell's voltage profile shape.

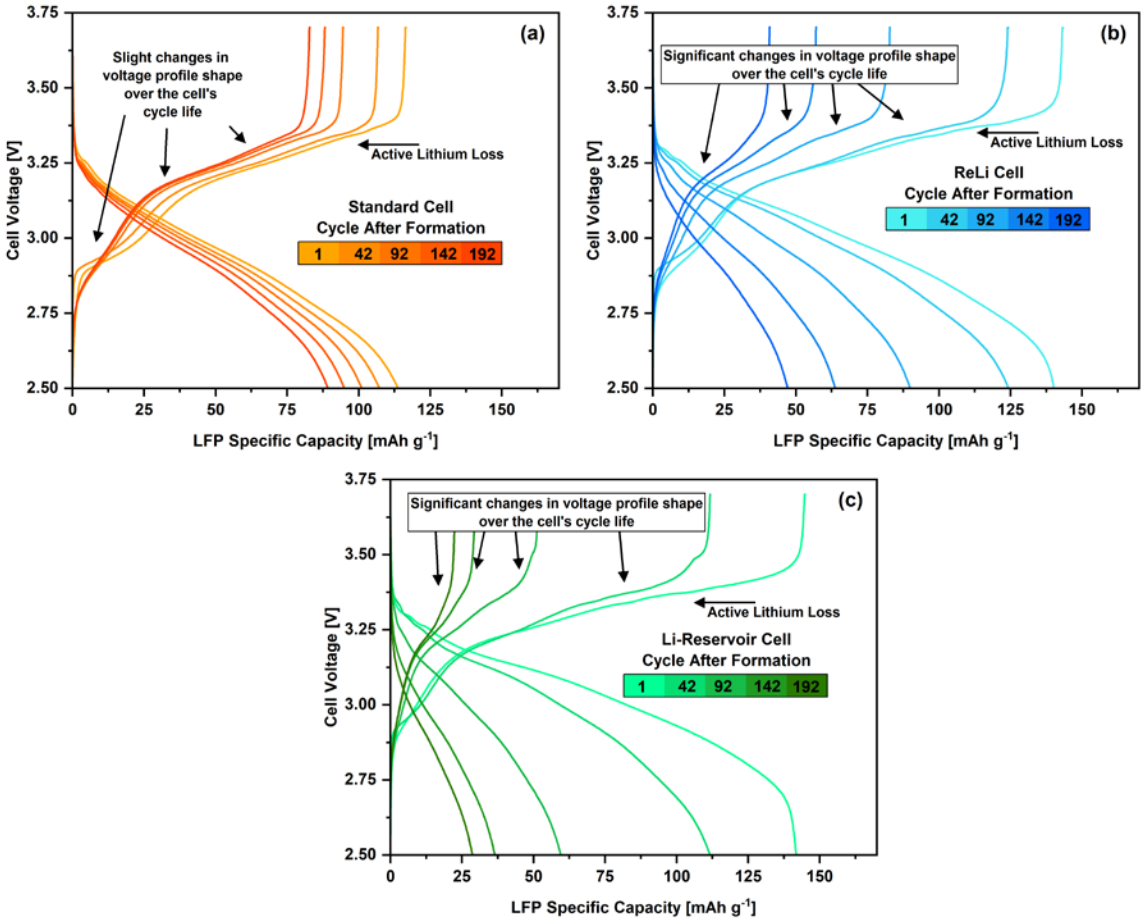

Figure 9.13 Evolution of the C/10 cycle voltage profiles in the cycling protocol of a) Standard, b) ReLi, and c) Li-Reservoir SiC‖LFP single-layer pouch cells.

The initial SiC‖LFP cell chemistry data presented here demonstrates the transferability of the overall relithiation concept to other cell chemistries. However, the poor cycling stability of the relithiated SiC‖LFP cells also shows that still more research and development are needed to realize the full potential of high-capacity SiC anode AMs for commercial application. Next to ICL compensation a stable cycling performance is of utmost importance for the SiC‖cathode cell chemistry. It seems that, for Si or SiC anodes, a critical degree of lithiation should not be exceeded, especially in the case of prelithiation or relithiation of the respective cells. Consequently, electrode balancing should be carried out with respect to the cell's maximum anodic lithiation degree under operation (N/P-ratio at the cell level). This adaption is expected to ensure more comparable and stable cycling performance of relithiated and non-relithiated cells in future studies. Note that this adjustment to the electrode balancing has to be done at the cost of the cell's total specific and volumetric energy.

Conclusion and Outlook

10. Conclusion

This thesis explored the role of perforated current collectors in lithium-ion batteries (LIBs), with a focus on their integration into manufacturing processes and their impact on electrochemical cell performance. Beyond addressing fundamental scientific questions, a key aspect of the work was to demonstrate the scalability of the overall concept and its applicability across different LIB electrode chemistries.

It has been identified and demonstrated that the innovation potential of a perforated current collector design for LIB technology relies, on the one hand, on reducing the mass and volume of the inactive current collector component within the electrode and, on the other hand, on the resulting lithium-ion permeability of the electrodes that can be used in multiple aspects to allow beneficial cell operation but especially a longer cycle-life.

The perforated current collector design studied was provided by Bender GmbH-Siegen and consists of round holes with a diameter of 1.0 mm that are arranged in a hexagonal, staggered pattern along the entire length and width of the foil, as illustrated in **Figure 10.1**. The perforation pattern reduces the mass and volume of the current collector's metal by 27.5%, compared to the pristine foil.

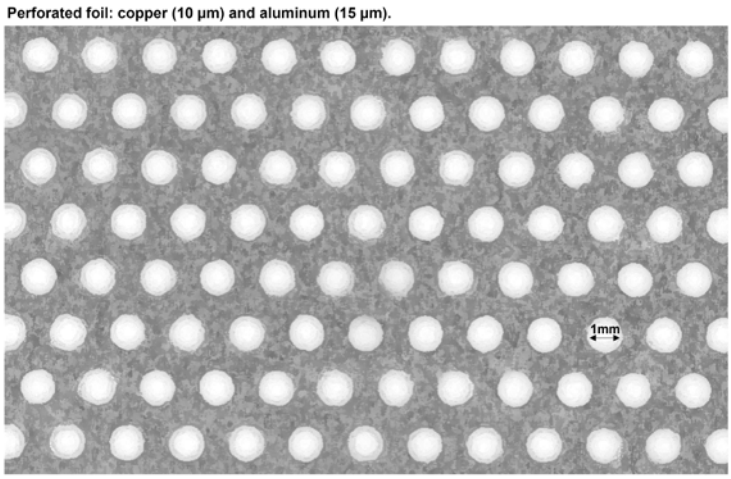

Figure 10.1 Illustration of the perforated current collector design investigated in this thesis.

In the initial part of this study, the advantages and limitations of this novel current collector design, in direct comparison with the pristine foil across various LIB electrode and cell chemistries, have been quantified (**Chapter 6.2** on page 46).

At the electrode level, an increase of 3 – 4% in specific capacity can be anticipated for LFP and NMC811 cathodes with an areal capacity of 2.5 mAh cm^{-2} per side. A more significant increase of 11% and 21% in specific capacity can be anticipated for graphite and SiC anodes, respectively,

considering an areal capacity of 2.9 mAh cm^{-2} per side. Advancements in electrode volumetric capacity are less significant, with expected gains from 2% to 4%.

At the cell level, substituting pristine current collector foils with perforated ones is anticipated to increase the specific energy by 4.5 – 6.5% across all anode‖cathode combinations of the electrode chemistries considered above, assuming a cathode areal capacity of 2.5 mAh cm^{-2} per side and an N/P-ratio of 1.15.

Moreover, the use of a perforated current collector design enables a prelithiation strategy at the cell level, as illustrated in **Figure 10.2**. This prelithiation method relies on two fundamental prerequisites: (i) the lithium-ion permeability of the electrodes, i.e., the use of perforated current collectors, and (ii) the presence of a Li-donor electrode or other Li-source in the battery cell. Initial capacity losses (ICLs) can then be compensated by lithium ions from such Li-donor source within the fully assembled and hermetically sealed cell. Only limited research on this concept is available so far and therefore a well-structured and detailed approach had to be pursued in this thesis.[214,215]

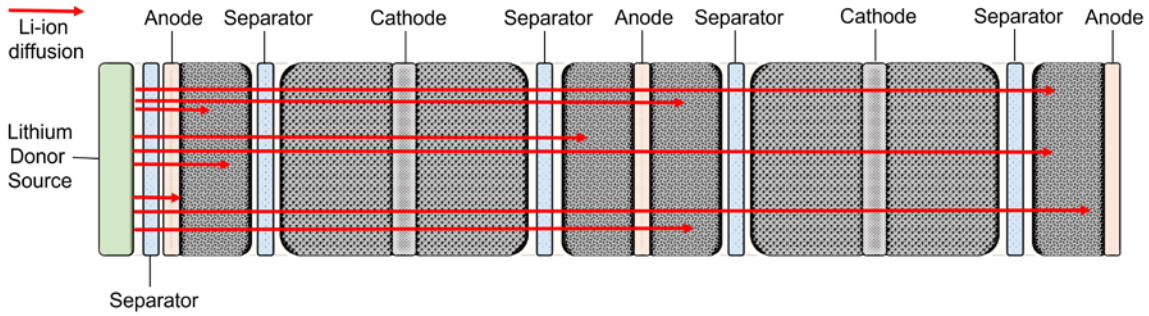

Figure 10.2 Illustration of the prelithiation approach at the cell level investigated in this thesis.

At the cell level, substituting pristine current collector foils with perforated ones together with compensation of the cell's ICLs via prelithiation is anticipated to result in a breakthrough increase in specific energy of Graphite‖cathode and SiC‖cathode cell chemistries by 16% – 17% and 32% – 33%, respectively, assuming again a cathode areal capacity of 2.5 mAh cm^{-2} per side and an N/P-ratio of 1.15.

Key Takeaway 1

The calculated improvements in overall LIB performance indicators by substituting pristine current collector foils with perforated ones are promising.

In **Chapter 6.5** (page 70), initial demonstrator Graphite‖LFP single-layer pouch cells with electrodes made of pristine and perforated foil were assembled. Theoretical calculated parameters, considering the ZSW specific single-layer pouch cell format, closely aligned with the measured

values from the real cells. This verified good accuracy of the calculated performance improvement in **Chapter 6.2** (page 46).

In the practical work of this study, the advantages and limitations of the perforated current collector design, in direct comparison with the pristine foil across various LIB electrode and cell chemistries, have been investigated and discussed.

It has been shown that the perforated foil can be coated and processed using standard laboratory (doctor blade coating; **Chapter 6.3** on page 53 and **Chapter 7.2** on page 78) and pilot-line (slot-die-coating; **Chapter 8.1** on page 106) electrode fabrication procedures. The only adaptation required was the addition of a non-adhesive protective foil as a second layer during the coating process, as illustrated in **Figure 10.3**. This protected the equipment from the possibility of slurry flowing through the perforations and contaminating the devices. The straightforward integration of the novel current collector design into standard electrode manufacturing processes highlights its potential as an innovative, drop-in technology for the LIB industry.

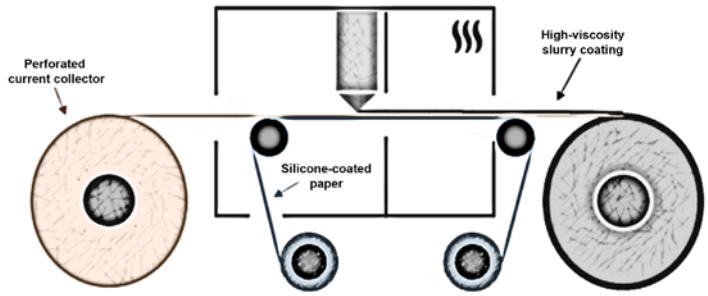

Figure 10.3 Illustration of the adaptions in pilot-line electrode fabrication procedure.

However, compared to coating pristine foil, the coating process of perforated foil is more sensitive to variations in slurry characteristics. Slurry rheology and drying time were identified as the most critical parameters for forming a homogeneous, closed coating that covers the perforations without passing through them. While the quality of the water-based graphite slurry coating was sufficient by only adjusting the slurry's viscosity, good-quality LFP slurry coatings could only be obtained by adjusting the slurry rheology and switching from an NMP-based to a water-based formulation. Faster drying times of the slurry solvent seem to prevent the slurry from flowing through perforations after its application to the foil. Optimization of the slurry formulation led to single-sided coatings in which only the holes were filled, with no undesired coating defects on the electrode backside. Single- and double-sided coated graphite electrodes (~3 mAh cm^{-2} per side; ~1.4 g cm^{-3}) and LFP electrodes (~2.5 mAh cm^{-2} per side; ~2.0 g cm^{-3}), using pristine and perforated current collectors, were successfully manufactured.

In addition to slurry characteristics, the quality of the substrate is of utmost importance for obtaining a good-quality coating. The coating process of perforated foils is more sensitive to substrate defects compared to that of pristine foils.

Key Takeaway 2

Standard laboratory and pilot-line LIB electrode manufacturing equipment can be used to process perforated current collector foil.

In **Chapter 8.2** (page 126), the direct substitution of the electrode current collector was investigated electrochemically in Graphite‖LFP bi-layer pouch cells with a capacity of 120 mAh. Independent of the current collector design, all cells exhibited similar formation and rate performance behavior. Moreover, cells with perforated current collectors showed enhanced long-term cycling performance. The reduced aging rate is expected to be an inherent positive side effect of the lithium-ion permeability of electrodes with perforated current collector design. Lithium-ion transport in cells of these advanced electrode architectures is no longer limited to the region between opposing anodic and cathodic coating layers. Instead, redistribution of lithium ions toward more stable regions throughout the cell likely mitigates their activity in more critical areas. However, these initial results only indicate benefits to cycling stability from lithium-ion permeable electrodes and do not conclusively verify their exact origin. It can be concluded that substitution of pristine current collector foil with a perforated one does not introduce any drawbacks to the electrochemical performance of a LIB cell; on the contrary, it reduces the fraction of inactive components within the electrodes and appears to improve overall cycling stability.

Key Takeaway 3

Replacing the pristine foil in the electrode with a perforated one does not negatively affect the electrochemical performance of the resulting LIB cell. In contrast, it appears to reduce the cell's aging rate.

In **Chapter 7** (page 71), the prelithiation method illustrated in **Figure 10.2** was applied to Graphite‖LFP single-layer pouch cells with a capacity of 60 mAh. Three cell systems were prepared and investigated:

i) ***Standard***, where ICL are not compensated: $Q_{Li\text{-}Inventory}$ is equivalent to 90% of $Q_{rev,cathode}$
ii) ***PreLi***, where ICL are compensated: $Q_{Li\text{-}Inventory}$ is equivalent to 100% of $Q_{rev,cathode}$
iii) ***Li-Reservoir***, where ICL are compensated and an anodic lithium reservoir equivalent to 10% of $Q_{rev,cathode}$ is provided: $Q_{Li\text{-}Inventory}$ is equivalent to 110% of $Q_{rev,cathode}$

All cell systems contained electrodes with similar loading; only the size of the active lithium inventory was varied. It has been demonstrated that the size of the active lithium inventory in a Graphite‖LFP cell can be accurately managed by applying an appropriate prelithiation protocol.

Prelithiated cells exhibit full utilization of the reversible cathode capacity at low C-rates and, consequently, a ~10% higher capacity compared to standard cells in which ICLs were not compensated. Moreover, they show higher LFP specific capacity utilization during rate capability tests and similar aging behavior in long-term cycling tests. Introducing an anodic lithium reservoir in addition to ICL compensation leads to a further enhancement in the cell's cycle life. The initial active lithium inventory of non-prelithiated standard cells, corresponding to an LFP specific capacity utilization of 130 mAh g^{-1}, was reached after 676 cycles for the PreLi system and after 1,176 cycles for the Li-reservoir system.

Key Takeaway 4

Prelithiation at the cell level for Graphite‖LFP cell chemistry has been shown to maintain the cell's cycling stability and significantly enhance the cell's specific energy, volumetric energy, and rate performance.

Active lithium loss (ALL) was found to be the main aging mechanism in the Graphite‖LFP single-layer pouch cells under investigation. Thus, a novel relithiation treatment at the cell level was applied to the aged PreLi and Li-Reservoir cells. The Li-donor source within the cell was used to replenish the cells active lithium deficit. The initial capacity of aged cells (>1,700 cycles) could be completely recovered. A comparison of the first 600 cycles after prelithiation with the first 600 cycles after relithiation demonstrated that the relithiated cells again utilized the full reversible cathode capacity and, moreover, exhibited a slower aging rate during its second-life application.

Key Takeaway 5

Active lithium deficiencies in LIBs can be compensated by a relithiation procedure at the cell level even after a cell has reached its end of life. This allows full utilization of the cell's capacity in second-life applications, without the need for recycling, as long as active lithium loss is the cell's main aging mechanism.

In **Chapter 8.2** (page 126), the concept of relithiation at the cell level was applied to stacked Graphite‖LFP pouch cells with a capacity of 180 mAh to compensate for their ICLs. As illustrated in **Figure 10.4**, a basic cell formation was performed to form the anodic solid electrolyte interphase (SEI). The ICLs were quantified, and the cell's active lithium deficit was accurately replenished during a subsequent relithiation procedure. In contrast to conventional prelithiation procedures, the resulting SEI is expected to be of similar quality to that of non-prelithiated reference cells, as its formation conditions can be kept identical. An active lithium inventory equivalent to 99% of $Q_{rev,cathode}$ was achieved in relithiated stacked pouch cells, demonstrating high accuracy and control of the relithiation process. The relithiated cells exhibited good rate capability and cycling performance. It has been shown that the overall concept can be scaled to larger cell formats.

Key Takeaway 6

Relithiation at the cell level can be used to accurately manage the size of a LIBs active lithium inventory in every stage of its operational life.

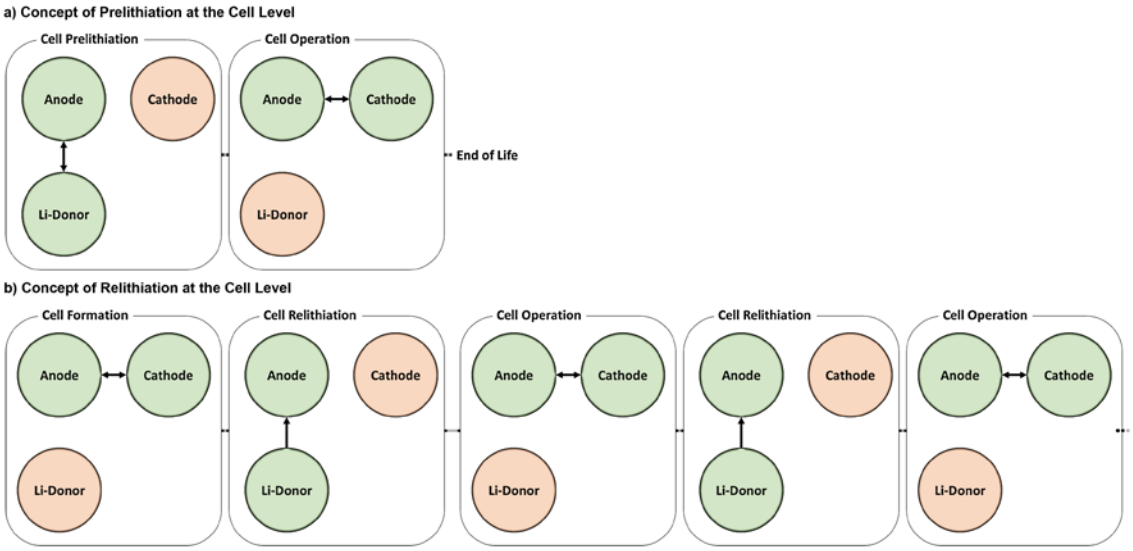

Figure 10.4 Illustration and differentiation of the concepts of a) prelithiation and b) relithiation at the cell level.

Lastly, in **Chapter 9** (page 145), the relithiation procedure was applied to SiC‖LFP single-layer pouch cells with a capacity of 60 mAh. Again, ICLs could be compensated. However, for the SiC‖LFP chemistry, more severe capacity fade was observed for ReLi and Li-reservoir cells in comparison to non-relithiated reference cells. Higher active lithium inventories in the here investigated cells are directly linked to higher anodic lithiation degrees in the cell's charged state, as all cell systems contain electrodes with similar loadings. While the initial discussed graphite anode chemistry does not appear to be significantly affected by higher lithiation degrees in the applied measurement protocols (72% in Standard and 88% in Li-reservoir cells), SiC anode chemistry exhibit strongly increased capacity fade when the anodic lithiation degree is increased from 63% in the Standard system to 92% in the Li-reservoir system. It is well known for Si- and SiC-based anode chemistries that higher lithiation degrees are directly associated with more severe volume expansion, which can negatively affect cell performance. As a conclusion, cell chemistries which contain high-capacity Si- or SiC-based anodes should be, especially in the context of prelithiation and relithiation approaches, be carefully balanced with respect to the maximum anodic lithiation degree at which a stable cycling performance can be maintained in future.

Key Takeaway 7

Compensation of ICLs for SiC‖LFP cell chemistry has resulted in poor cycling stability in direct comparison to a reference as a critical lithiation degree of the anode was exceeded during cell operation at increased active lithium inventory levels.

In addition, this study provides a qualitative and quantitative analysis approach to determine a cell's active lithium inventory in relation to the cathode's maximum reversible capacity. The quantification of the cell's active lithium inventory after prelithiation or relithiation treatment is important, as an uncontrolled surplus of active lithium within the cell can lead to performance or even safety problems during cell operation.

Key Takeaway 8

A quantitative and qualitative analysis approach to determine a cell's active lithium inventory size is provided.

In conclusion, this thesis offers a comprehensive examination of the role of perforated current collector design in LIBs, spanning from theoretical concepts to experimental validation. Two key innovations are highlighted, and their practical feasibility is demonstrated: the general concept of introducing a perforated current collector design at the electrode level and a novel relithiation approach at the cell level. While the former can be readily implemented using standard LIB manufacturing equipment if high-quality perforated current collector materials are available, the latter requires the development of an advanced cell design incorporating a fixed or removable sacrificial lithium donor source.

11. Outlook

This work established a solid foundation and provided a proof-of-concept. However, several key aspects require further investigation and optimization in future work.

First, this work investigated only one design-type of perforated current collectors. The perforation was hole-type with a hole diameter of 1 mm that is relatively large in respect to other electrode characteristics such as the coating thickness, which is generally below 200 µm. Consequently, the electrode manufacturing is expected to be even less critical if perforated current collector designs with micrometer-scale perforations would be available. Advanced perforation designs should be developed and tested in future work.

Second, this work investigated prelithiation and relithiation procedures at the cell level using only prototype cells, as the focus was on evaluating the general concept rather than its implementation in industry-like cell formats. Advanced engineering of cell design and lithium donor sources will be important in future work.

Third, in addition to performance targets, production costs and time are also critical factors in LIB manufacturing. These economic factors should also be quantified and evaluated to assess whether concepts such as perforated current collectors or relithiation can be profitably implemented in commercial cells.

The author recommends applying simulations to identify the optimal perforation design, cell design and relithiation protocol parameters. This would facilitate transfer to larger cell formats while minimizing the risk of failure caused by uneven distribution of lithium ions within the cell's electrodes due to suboptimal relithiation conditions.

Fourth, this work focused solely on lithium-ion battery technology. However, the overall concepts should also be transferred to post-lithium systems, such as sodium-ion batteries, in future work.

Lastly, the author suggests that the current collector design introduced here may also be beneficial for fundamental research. Current collector perforations with a diameter of 1 mm can be beneficial in the context of in-situ measurements, as no obstructing metal is present in these areas, allowing the coating materials to be in-situ investigated more realistically under cell-relevant conditions. Future work should also consider this analytical opportunity regarding the role of perforated current collectors in battery electrodes.

Materials and Methods

12. Materials

12.1 Electrode Materials

Electrode materials used in this work are summarized in **Table 12.1**.

Table 12.1 Electrode material overview.

Material	Name	Manufacturer	Function
Graphite	Commercial Graphite-1	Confidential	Anode Active Material
	Commercial Graphite-2	Confidential	
	C-NERGY SFG6L	Imerys S.A.	Conductive Additive
Silicion Carbon Composite (SiC)	Confidential	Wacker Chemie AG	Anode Active Material
Lithium Iron Phosphate (LFP)	Commercial LFP-1	Confidential	Cathode Active Material
	Commercial LFP-2	Confidential	
Carbon Black	C-NERGY Super P	Imerys S.A.	Conductive Additive
	C-NERGY SuperC65	Imerys S.A.	
Carboxymethylcellulose (CMC)	Sunrose MAC500	Nippon Paper Industries Co., Ltd.	Binder
Styrene-Butadiene Rubber (SBR)	-	Zeon Europe	Binder
	-	ENEOS Materials Corporation	
Polyvinylidene Difluoride (PVDF)	Solef 5130	Solvay S.A.	Binder
Copper Foil	-	JX-Nippon	Current Collector
	-	Bender GmbH	
Aluminum Foil	-	Speria	Current Collector
N-Methyl-2-pyrrolidone (NMP)	-	Sigma-Aldrich	Solvent

Copper and aluminum current collector foil coils were mechanically perforated by Bender GmBH (57078 Siegen).

12.2 Cell Materials

Cell materials used in this work are summarized in **Table 12.2**.

Table 12.2 Cell material overview.

Material	Name	Manufacturer	Function
NMC811 Electrode	Confidential	ZSW	Cathode
SiC Electrode	Confidential	Wacker Chemie AG	Anode
Lithium discs	-	Alfa Aeasar	Counter Electrode
Glas Fiber Layer	Whatman GF/A	Cytiva	Separator
Trilayer Microporous Membrane (PP/PE/PP)	Celgard2325	Celgard	Separator
Nickel Tab	-	Sumitomo Electric Industries, Ltd.	Electrode Tab
Aluminum Tab	-	Sumitomo Electric Industries, Ltd.	Electrode Tab
Capton Tape	-	CMC Klebetechnik GmbH	Insulator
Laminated Pouch Material	-	Targray	Housing
Epoxid	-	R&G Faserverbundwerkstoffe GmbH,	Sealing
1 M LiPF6 in EC:EMC (3:7) + 2 wt.% VC	-	Gotion	Electrolyte
1 M LiPF6 in EC:EMC (3:7) + 2 wt.% VC +10wt.% FEC	-	Gotion & BASF Chemicals were used	Electrolyte

13. Instrumentals

Mixer

Magnetic Stirrer

Pre-Mix (60 g) were prepared using magnetic stirrer RCT standard (IKA-Werke GmbH & Co. KG).

Disperser

Pre-Mix (100 g – 2000 g) were prepared using Dispermat CN10 (VMA-GETZMANN GMBH).

Centrifugal Mixer

Electrode slurries (10 g – 700 g) were prepared using SpeedMixer DAC800.2. VAC-P (Hauschild SpeedMixer Inc).

Rheometer

Rheological measurements were conducted using modular compact rheometer MCR102 with a parallel plate PP25 measurement head geometry (Anton Paar GmbH).

Grindometer

Slurry quality was evaluated using high precision gap gauge with a range from 0 – 250 µm (Elcometer Limited).

Density meter

Slurry density was measured using density meter DMA 4100M (Anton Paar GmbH).

Coater

Table Coater

Lab scale coatings were prepared using table coater (ERICHSEN GmbH & Co. KG) with a coating gap adjustable doctor blade (Elcometer Limited).

Pilot-Scale Roll-to-Roll Coater

Pilot scale coatings were prepared using slot-die coating system (Lacom GmbH; nowadays Aumann AG) with a coating width of 8 cm on a pilot coating-line (Lacom GmbH; nowadays Aumann AG) featuring four distinct drying zones over a total length of 8 metres. A 1000D SyriXius pump system (Axel Semrau GmbH) was used to regulate the slurry flow.

Calender

Table Calender

Small sheets of electrode coatings (30 – 40 cm) were densified using a tabletop calender (CA5, Sumet-Messtechnik).

Pilot-Scale Roll-to-Roll Calender

Foil coils were flattened using Kal 2523 pilot calender-line (Mathis AG).

Cutting

Round electrodes of different diameter (12 µm and 16 µm) were cut using hydraulic press (Bosch Rexroth AG) or a high precision electrode cutter EL-Cut (EL-Cell GmbH). Pouch electrodes were cut into desired dimensions using a roll-based die-punching method with a custom stainless-steel template.

Laser Ablation

Coating residues on the electrode tabs were removed using an Easymark 5 ablation laser (Coherent Corp.).

Tab Welding

Anode (nickel) and cathode (aluminum) electrode tabs were welded to the electrodes using an Ultrasonic Welder L20 (Branson Ultrasonics).

Drying

Cell components were dried in vacuum oven before usage (BINDER GmbH or BÜCHI Labortechnik AG).

Adhesion Tests

The adhesion of the coating layers was evaluated using a tensile strength measurement setup in the Z-direction (ZwickRoell GmbH & Co. KG).

Micrometer

Electrode thickness measurements were done using high accuracy digital micrometer (Mitutoyo Deutschland GmbH).

Microscopy

Digital Microscope

Microscope images were recorded with VHX-7000 Digital Microscope (KEYENCE DEUTSCHLAND GmbH).

Scanning Electron Microscope (SEM)

Electron microscope images were recorded using SEM Leo 1530 VP (Carl Zeiss AG). Cross sections of electrodes were prepared using argon ion beam milling system IM400Plus (Hitachi).

Dry Room

Work in dry atmosphere was done in ZSW dry room (20 °C, dew point: -66 °C).

Glovebox

Work in inert atmosphere was done using glovebox with < 0.1 ppm H_2O and < 0.1 ppm O_2 (M. Braun Inertgas-Systeme GmbH).

Battery Cycler

Electrochemical cells were tested using battery test system BaSyTec (Basytec GmbH).

14. Procedures

14.1 Theoretical Calculations

The material and electrode parameters considered for theoretical calculations are provided in **Table 14.1** and **Table 14.2.** Values were obtained from material suppliers, literature (theoretical specific capacity, average working potential)[34,82,112], and own experience (coating composition, coating porosity). All calculations were performed using Microsoft Excel Spreadsheets (Microsoft Corporation).

Table 14.1 Material parameters considered for theoretical calculations.

Material	Density [g cm^{-3}]	Specific Capacity [mAh g^{-1}]	Average Voltage [V]	Thickness [µm]	Porosity [%]	Function
LFP	3.60	170	3.45	-	-	**AM**
NMC811	4.80	190	3.70	-	-	
Graphite	2.23	372	0.20	-	-	
SiC	2.26	1550	0.40	-	-	
Carbon Black	1.85	-	-	-	-	**Conductive Additive**
PVDF	1.78	-	-	-	-	**Binder**
CMC	1.60	-	-	-	-	
SBR	0.94	-	-	-	-	
PAA	1.40	-	-	-	-	
Al-Foil	2.70	-	-	15	0 / 27.5	**Current Collector**
Cu-Foil	8.96	-	-	10	0 / 27.5	
Celgard 2325	1.42	-	-	25	39	**Separator**
1 M LiPF6 in EC:EMC (3:7) + 2wt.% VC	1.30	-	-	-	-	**Electrolyte**

Table 14.2 Electrode paramaters considered for theoretical calculations.

Electrode	Coating Composition		Coating Porosity [%]	Current Collector
LFP	LFP:PVDF:CB:Graphite	92:4:2:2	40	Al-Foil
NMC811	NMC811:PVDF:CB:Graphite	94:3:2:1	25	Al-Foil
Graphite	Graphite:CMC:SBR:CB	94:2:2:2	37	Cu-Foil
SiC	SiC:Graphite:PAA:CB	70:20:8:2	55	Cu-Foil

Electrode level

Electrode calculations consider double-sided coated current collectors and are representative for all electrode formats excluding the electrode tabs.

Cell level

Cell unit calculations consider a double-sided coated cathode, a double-sided coated anode, two separators, and electrolyte. A cell unit is stackable and can be used to predict the energy characteristics of unknown LIB cell formats by omitting the cell housing, tab design and anode edge overhang (illustrated in **Figure 6.9** on page 49). For simplification, the N/P-ratio was fixed to 1.15 for all anode‖cathode systems, using the reversible areal capacity of anode and cathode before ICLs. An ICL of 0%, 10% and 20% is considered for prelithiated, graphite and SiC cells, respectively. ICLs are directly subtracted from the cell unit's final capacity. The electrolyte volume corresponds to the total free pore volume in the anode, cathode and separators.

ZSW single layer pouch cell format at the electrode level

Single-layer pouch cell at the electrode level calculations consider ZSW pouch cell specifications (cathode area: 23.94 cm^2, anode area: 26 cm^2, and tab size 0.84 cm^2). Active material specific capacities were received from coin half-cell tests. An ICL of 0% and 15% is considered for prelithiated and standard cells in agreement to full cell measurements. The total mass of anode and cathode are taken into account, while the mass of the Li-donor electrode is neglected in the calculations and real cell values.

14.2 Pre-Mix Preparation

Things to note

The Pre-Mix is prepared to ensure complete binder dissolution and a homogeneous dispersion of deagglomerated conductive additives. Only stable binders, such as CMC or PVDF, are used at this initial stage of electrode slurry preparation. SBR, which is not stable under high shear conditions, is therefore added in the final step of slurry preparation under moderate mixing conditions.

Basic Procedure

The total amount of binder is dissolved in the solvent under continuous stirring, using either a magnetic stirrer (Chapter 6) or a dissolver (Chapter 6 – 9). Once no undissolved binder residues remain, the conductive additives are gradually added in multiple steps until a uniform, agglomerate-free dispersion is achieved. In this study, the peripheral speed of the outer dispersion disc of the dissolver was limited to 420 cm s^{-1} to ensure reproducible mixing conditions.

Quality Control

The quality of the Pre-Mix was assessed using a rheometer and a grindometer.

Pre-Mix Formulation

Chapter 6

Anode: Two different pre-mix formulations are used: (1) Water:CMC:CB – 96:2:2, and (2) Water:CMC:CB – 97:1.5:1.5. The components were carbon black SuperP (Imerys S.A.), CMC Sunrose MAC500 (Nippon Paper Industries Co., Ltd.) and Water (with an electrical conductivity of 0.05 µS cm^{-1} at RT).

(Pre-Mix 1) 4% TSC; 163 Pa s at 1 s^{-1}; 4.1 Pa s at 100 s^{-1}; no agglomerates

(Pre-Mix 2) 3% TSC; 38.2 Pa s at 1 s^{-1}; 1.9 Pa s at 100 s^{-1}; no agglomerates

Cathode: Two different pre-mix formulations are used: (1) NMP:PVDF:CB:Graphite – 90:5:2.5:2.5, and (2) NMP:PVDF:CB:Graphite – 92:4:2:2. The components were carbon black SuperC65 (Imerys S.A.), Graphite SFG6L (Imerys S.A.), PVDF 5130 (Solvay Solexis) and NMP (Sigma-Aldrich).

(Pre-Mix 1) 10% TSC; 13.4 Pa s at 1 s^{-1}; 1.6 Pa s at 100 s^{-1}; no agglomerates

(Pre-Mix 2) 8% TSC; 5.4 Pa s at 1 s^{-1}; 0.7 Pa s at 100 s^{-1}; no agglomerates

Chapter 7

Anode: A pre-mix formulation of Water:CMC:CB – 97:1.5:1.5 is used. The components were carbon black SuperC65 (Imerys S.A.), CMC Sunrose MAC500

(Nippon Paper Industries Co., Ltd.) and Water (with an electrical conductivity of 0.05 µS cm^{-1} at RT).

(Pre-Mix) 3% TSC; 29 – 34 Pa s at 1 s^{-1}; 1.6 – 1.9 Pa s at 100 s^{-1}; no agglomerates

Cathode: A pre-mix formulations of Water:graphite:CB:CMC – 92.5:1.5:4.5:1.5 is used. The components were carbon black SuperC65 (Imerys S.A.), Graphite SFG6L (Imerys S.A.), CMC Sunrose MAC500 (Nippon Paper Industries Co., Ltd.) and Water (with an electrical conductivity of 0.05 µS cm^{-1} at RT).

(Pre-Mix) 7.5% TSC; 170 – 200 Pa s at 1 s^{-1}; 3.4 – 4.0 Pa s at 100 s^{-1}; no agglomerates

Chapter 8

Anode: The procedure and materials were kept similar to that described for Chapter 7.

Cathode: The procedure and materials were kept similar to that described for Chapter 7.

Chapter 9

Cathode: The procedure and materials were kept similar to that described for Chapter 7.

14.3 Slurry Preparation

Things to note

The electrode slurry contains all the essential components of the electrode – active material, conductive additives, and binder – dispersed in a solvent. These components physically interact within the slurry, forming a wet-state matrix that ultimately defines the electrode's microstructure. Therefore, the final electrode structure is directly influenced by the quality of particle dispersion in the slurry. The objective is to achieve a homogeneous dispersion of fully deagglomerated active materials and conductive additives. Mixing conditions must be carefully selected to avoid damaging individual components due to excessive shear forces.

Basic Procedure

The total amount of Pre-Mix (as prepared in **Chapter 14.2**) is diluted with the remaining solvent to achieve the target TSC of the slurry in the end. Afterwards, the active material is added in multiple incremental steps, each followed by mixing with a SpeedMixer for 1 – 3 minutes at 800 – 1500 rpm, until a uniform, agglomerate-free dispersion is achieved. If SBR is part of the electrode formulation, it is incorporated in the final slurry preparation step under the lowest SpeedMixer mixing intensity (3 minutes at 800 rpm), to prevent degradation due to shear.

Quality Control

The quality of the slurry was assessed using a rheometer, a density meter and a grindometer.

Slurry Formulation

Chapter 6

Anode: A graphite electrode formulation of AM:CB:CMC:SBR – 94:2:2:2 is used. The electrode materials used were Graphite-1 (commercial graphite), carbon black SuperP (Imerys S.A.), CMC Sunrose MAC500 (Nippon Paper Industries Co., Ltd.), SBR (Zeon Europe GmbH), and copper foil (thickness 10µm, JX-Nippon).

(Slurry 1) 37.5% TSC; 49.3 Pa s at 1 s^{-1}; 2.8 Pa s at 100 s^{-1}; no agglomerates

(Slurry 2) 40.0% TSC; 87.7 Pa s at 1 s^{-1}; 3.9 Pa s at 100 s^{-1}; no agglomerates

(Slurry 3) 42.5% TSC; 145 Pa s at 1 s^{-1}; 5.5 Pa s at 100 s^{-1}; no agglomerates

Cathode: A LFP electrode formulation of AM:CB:Graphite:PVDF – 92:2:2:4 is used. The electrode materials used were LFP-1 (commercial LFP; old batch), carbon black SuperC65 (Imerys S.A.), Graphite SFG6L (Imerys S.A.), PVDF 5130 (Solvay Solexis) and aluminum foil (thickness 15µm, speria).

(Slurry) 45.0% TSC; 53.0 Pa s at 1 s^{-1}; 2.0 Pa s at 100 s^{-1}; no agglomerates

Chapter 7 Anode: A graphite electrode formulation of AM:CB:CMC:SBR – 94:2:2:2 is used. The electrode materials used were Graphite-2 (commercial graphite), carbon black SuperC65 (Imerys S.A.), CMC Sunrose MAC500 (Nippon Paper Industries Co., Ltd.), SBR (Zeon Europe GmbH), and copper foil (thickness 10µm, JX-Nippon).

(Slurry) 43.0% TSC; 127 – 132 Pa s at 1 s^{-1}; 6.2 – 6.3 Pa s at 100 s^{-1}; no agglomerates

Cathode: A LFP electrode formulation of AM:SFG6L:CB:CMC:SBR – 92:1:3:1:3 is used. The electrode materials used were LFP-2 (commercial LFP), carbon black SuperC65 (Imerys S.A.), graphite SFG6L (Imerys S.A.), CMC Sunrose MAC500 (Nippon Paper Industries Co., Ltd.), SBR (ENEOS Materials Corporation) and aluminum foil (thickness 15µm, speria).

(Slurry) 55.0% TSC; 108 – 123 Pa s at 1 s^{-1}; 3.9 – 4.0 Pa s at 100 s^{-1}; no agglomerates

Chapter 8 Anode: The procedure and materials were kept similar to that described for Chapter 7.

Cathode: The procedure and materials were kept similar to that described for Chapter 7.

Chapter 9 Cathode: The procedure and materials were kept similar to that described for Chapter 7.

14.4 Rheological Measurements

Basic Procedure

Approximately 0.5 mL of the premix or slurry dispersion was applied to the measurement plate. The measurement head was lowered slightly below the measurement height, down to a gap of 1.05 mm. Any overhanging dispersion was carefully removed (trimmed) from the measurement head. The gap was then lowered to a measurement position of 1.00 mm, after which a solvent trap was attached. The flow curve and amplitude sweep measurement protocols were then performed sequentially. The measurement temperature was held at 20°C.

Flow Curve Measurement Protocol

Flow curves were performed at shear rates between 0.1 and 1000 s^{-1}. Twenty-one measurement points were recorded at 5 Pt. dec^{-1}. To ensure an equilibrium state of the viscosity during recording of each point without the total measurement time being too long, the measurement time of each measurement point decreased logarithmically from 10 s at low shear rates to 1 s at high shear rates.

Amplitude Sweep Measurement Protocol

Amplitude sweeps were performed at strains between 0.05 and 500% at an angular frequency 10 rad s^{-1} (approx. 1.6 Hz). Twenty-one measurement points were recorded at 5 Pt. dec^{-1}.

14.5 Coating

Things to note

The electrode coating forms the final microstructure of the electrode. The final structure is influenced by all three processes: coating, drying, and calendering. Therefore, all processes must be accurately defined with respect to the electrode materials and performance targets. The following must be achieved: a homogeneous distribution of all coating components; accurate control of the final loading after drying; sufficient mechanical stability and flexibility; and good ionic and electronic conductivity within the bulk coating.

Lab Scale Basic Procedure

Electrode slurries were coated on current collector foils (30 – 40 cm length) using the doctor blade technique on a laboratory coater at a coating speed of 5 mm s^{-1}. Coatings on perforated current collectors require the use of a protective layer beneath the collector to prevent contamination of the laboratory coater caused by slurry migration through the holes. Suitable protective layers include non-adhesive, mechanically stable materials such as silicone-coated paper or rigid plastic foils. NMP-based coatings were dried overnight at 60 °C, while water-based coatings were dried overnight at room temperature.

To establish a linear relationship between wet film thickness and coating mass loading, the slurry was applied to the current collector at a minimum of three different wet thicknesses, using coating gap variations of more than 20 µm. This approach enabled the use of linear regression to accurately determine the coating gap required to achieve target loadings for lab scale electrodes.

Finally, the loading-adjusted coated sheets were calendered using a table calender under controlled line pressure to achieve the target densification.

Pilot Scale Basic Procedure

Electrode slurries were coated onto full current collector coils (min. 40 m foil length) using the slot-die coating technique on a pilot coating-line. When coating perforated current collectors, a protective layer must be used beneath the foil to prevent contamination of the coating equipment. Suitable protective layers include non-adhesive, mechanically stable materials, such as silicone-coated paper. The slurry density was determined in order to set the coating parameters required to achieve the desired electrode loadings. Graphite coatings were produced at a line speed of 1 m min^{-1}, with a slurry flow of 15.56 ml min^{-1} and drying zones of 40|40|40|70 °C. LFP coatings were produced at a line speed of 1 m min^{-1}, with a slurry flow of 17.39 ml min^{-1} and drying zones of 40|40|40|70 °C. Both current collector sides were coated sequentially.

Quality Control

The quality of the coatings was assessed using a balance, a micrometer, a microscope, and adhesion tests.

Final Electrodes

Chapter 6 Anode: Lab scale - A graphite slurry with 40.0% TSC and a coating gap of 260 µm is used.

(Graphite Electrode) 8.8 mg cm^{-2}; 3.0 mAh cm^{-2}; 1.4 g cm^{-3}

Cathode: Lab scale - A LFP slurry with 45.0% TSC and a coating gap of 385 µm is used.

(LFP Electrode) 18.1 mg cm^{-2}; 2.6 mAh cm^{-2}; 2.0 g cm^{-3}

Chapter 7 Anode: Lab scale - A graphite slurry with 43.0% TSC and a coating gap of 230 µm is used.

(Graphite Electrode) 8.8 mg cm^{-2} per side; 3.0 mAh cm^{-2} per side; 1.4 g cm^{-3}

Cathode: Lab scale - A LFP slurry with 55.0% TSC and a coating gap of 290 µm is used.

(LFP Electrode) 17.5 mg cm^{-2}; 2.4 mAh cm^{-2}; 2.0 g cm^{-3}

Chapter 8 Anode: Pilot scale - A graphite slurry with 43.0% TSC and …

(Graphite Electrode) 8.8 mg cm^{-2}; 3.0 mAh cm^{-2}; 1.4 g cm^{-3}

Cathode: Pilot scale - A LFP slurry with 55.0% TSC and …

(LFP Electrode) 18.6 mg cm^{-2} per side; 2.55 mAh cm^{-2} per side; 1.9 g cm^{-3}

Chapter 9 Anode: SiC electrodes were provided by Wacker Chemie AG.

(SiC Electrodes) 3.0 mAh cm^{-2}

Cathode: Lab scale - The procedure and materials were kept similar to that described for Chapter 7.

(LFP Electrodes) 18.2 mg cm^{-2}; 2.5 mAh cm^{-2}; 2.0 g cm^{-3}

14.6 Cell Assembly

Coin Cells

Round electrodes were cut (16 mm diameter) and dried overnight at 120 °C under reduced pressure (10^{-2} mbar).

2032-coin cells were assembled in a two-electrode configuration using a working electrode, a counter electrode, two glass fiber separators, and 150 µl of electrolyte.

All cells were assembled in an argon-filled glovebox. After assembly, the cells were left to rest for 10 hours to allow sufficient time for the electrolyte to soak into the electrodes and separator

Pouch Cells

Pouch format electrodes were cut to size (cathode area: 23.94 cm^2; anode area: 26 cm^2; tab area: 0.84 cm^2). The coating was selectively removed from the tab areas using laser ablation. The electrodes were then dried overnight at 120 °C under reduced pressure.

Pouch cell electrode stacks were assembled in a dry room using single- or double-sided coated electrodes and Celgard 2325 as the separator. The assembled stacks were then transferred into an argon-filled glovebox and dried overnight at 80 °C under reduced pressure. After drying, 1.2 ml of electrolyte was added, and the pouch bag was sealed and welded.

Finally, the pouch cells were removed from the glovebox and clamped between two Plexiglas plates under a pressure of approximately 4 N cm^{-2}.

14.7 Battery Testing

Basic Cell Testing Procedure

After assembly, the cells were rested for 10 hours to ensure sufficient time for the electrode electrolyte soaking. Subsequently, five formation cycles were performed at a current rate of C/10. After the formation procedure, specific protocols for rate capability and long-term cycling tests — using varying C-rates and cycle numbers — were conducted.

Basic Measurement Protocol Setup

The cells were cycled in the selected potential window ($V_{lower\ cut\text{-}off} - V_{upper\ cut\text{-}off}$) with a constant current (until $V_{Cell} > V_{upper\ cut\text{-}off}$) constant voltage (until $I < C/20$) charge and a constant current (until $V_{cell} < V_{lower\ cut\text{-}off}$) discharge protocol. A minimum of 300 measurement points were collected for each half cycle.

Appendix

15. Appendix: Proof of Concept

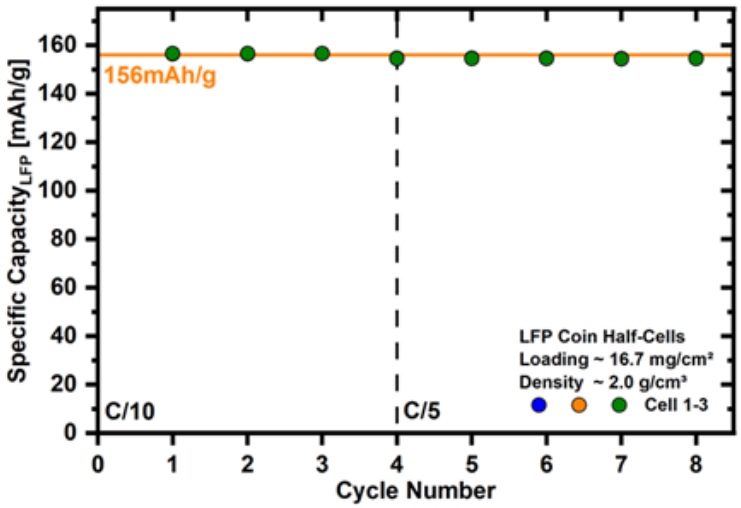

Figure 15.1 2032-coin half-cell (Li‖Electrode) data of LFP electrodes used in **Chapter 6** (page 42). The measurement protocol involves CCCV-delithiation and CC-lithiation cycles in the potential window 2.5 – 3.7 V. All cells contain electrodes with a loading of ~16.7 mg cm^{-2} and LP10VC02 as electrolyte.

16. Appendix: Prelithiation and Beyond

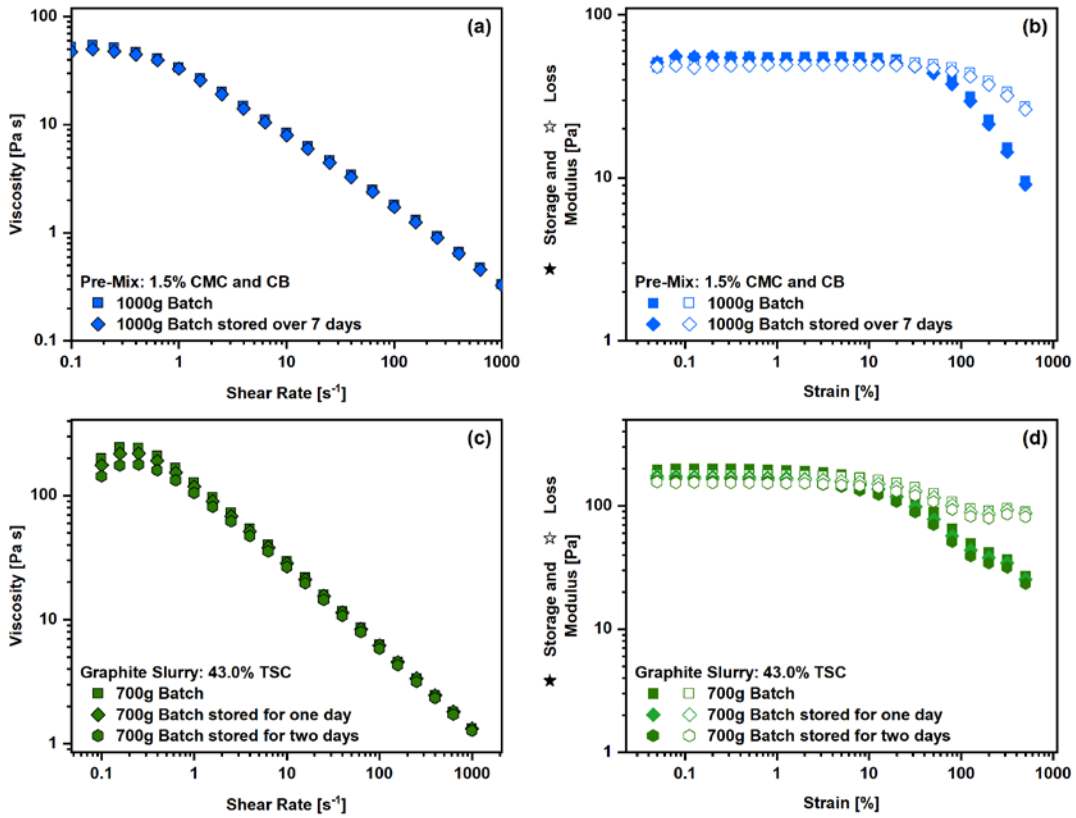

Figure 16.1 Rheological data of a, b) pre-mix and c, d) slurry at different storage times (**Chapter 7.2.1** on page 78).

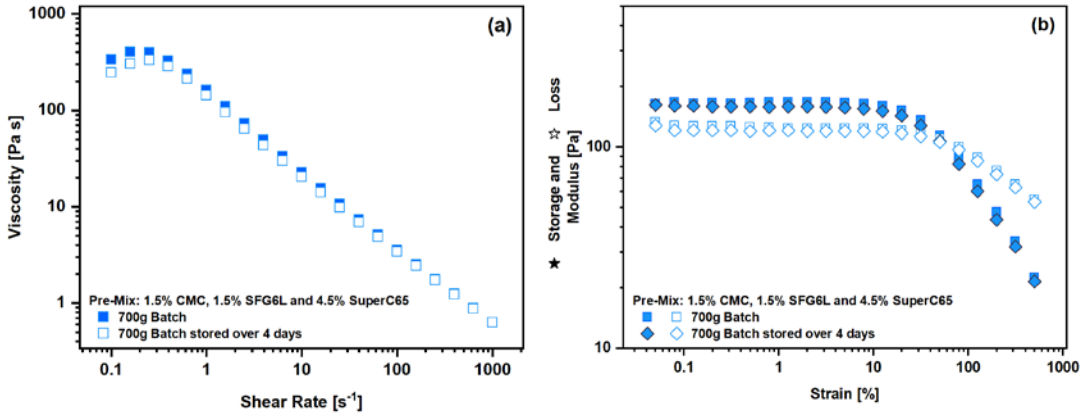

Figure 16.2 Rheological data of pre-mix at different storage times (**Chapter 7.2.2** on page 82).

17. Appendix: Scale Up

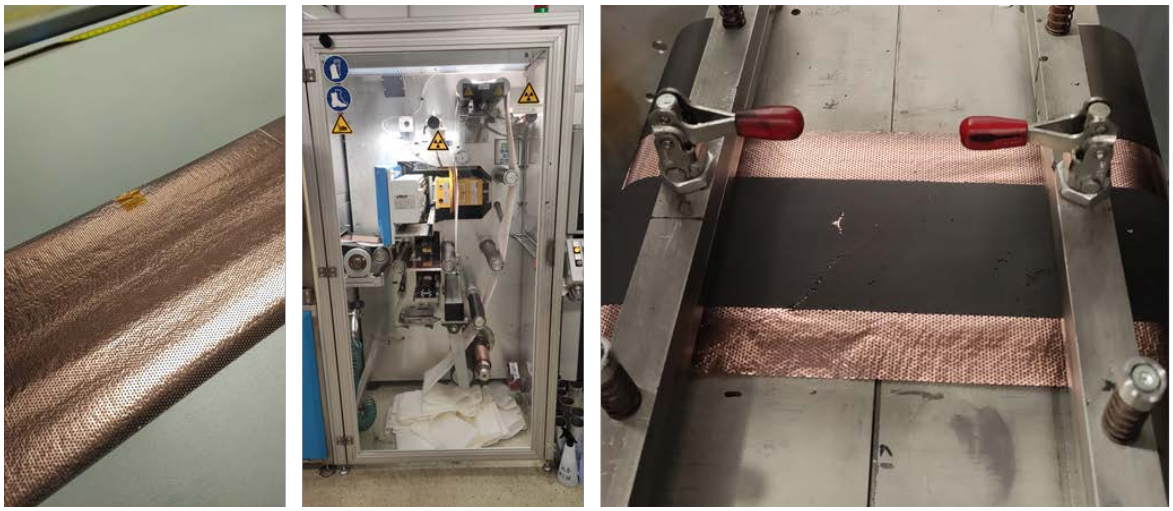

Figure 17.1 Additional photographs of the graphite electrode pilot-line coating process (**Chapter 8.1.1** on page 110).



Figure 17.2 Additional photographs of the LFP electrode pilot-line coating process (**Chapter 8.1.2** on page 117).

18. Appendix: Transfer to High Capacity SiC Anode Active Material

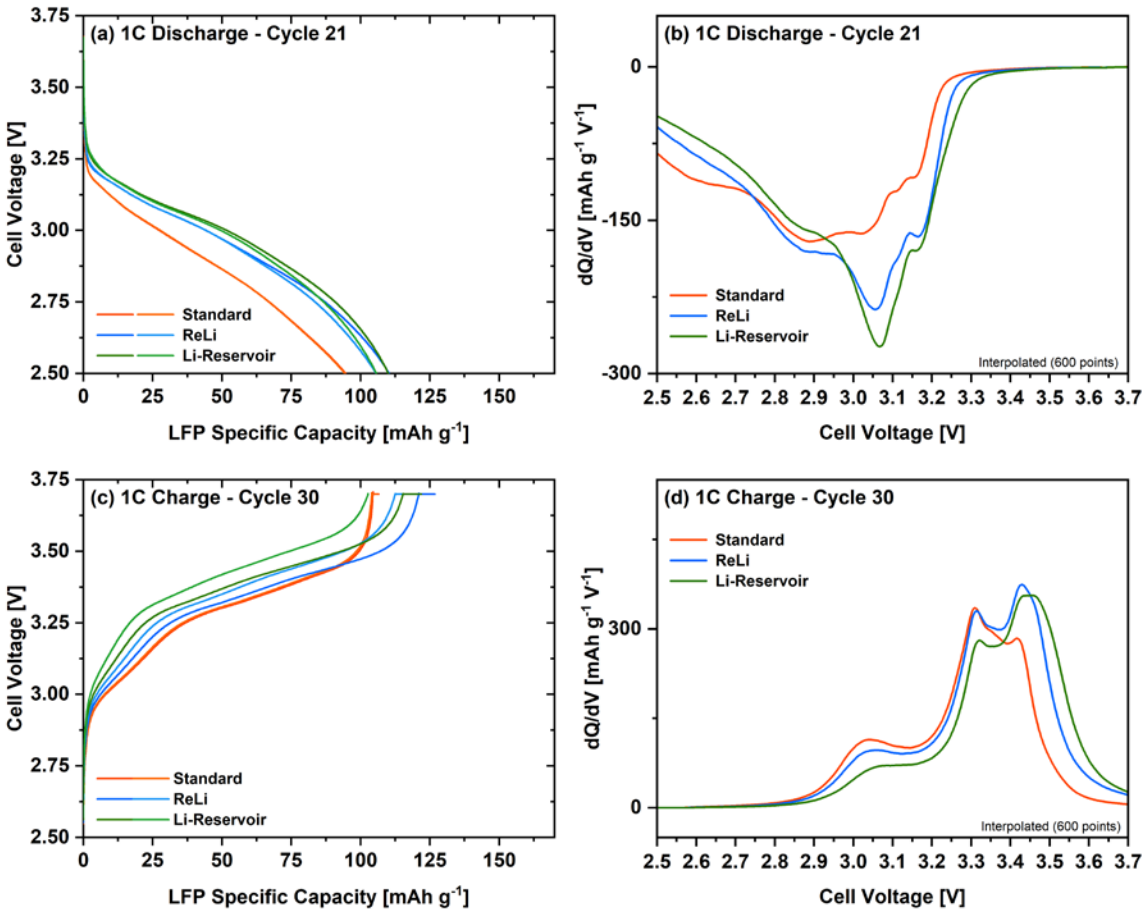

Figure 18.1 Rate capability data of SiC‖LFP single-layer pouch cells: a) voltage profile at 1C discharge, b) dQ/dV-plot at 1C discharge, c) voltage profile at 1C charge, and d) dQ/dV-plot at 1C charge (**Chapter 9.1.4** on page 151).

References

1. Statistical Review of World Energy 2025. Energy Institute, 2025.
2. World Energy Outlook 2025. International Energy Agency, 2025.
3. Hannah Ritchie and Pablo Rosado and Max Roser. Energy. Available at https://ourworldindata.org/energy#all-charts (2026).
4. GHG Emissions of all World Countries. European Commission, 2025.
5. Filonchyk, M., Peterson, M. P., Zhang, L., Hurynovich, V. & He, Y. Greenhouse gases emissions and global climate change: Examining the influence of CO2, CH4, and N2O. *The Science of the total environment* **935,** 173359; 10.1016/j.scitotenv.2024.173359 (2024).
6. Anderson, T. R., Hawkins, E. & Jones, P. D. CO2, the greenhouse effect and global warming: from the pioneering work of Arrhenius and Callendar to today's Earth System Models. *Endeavour* **40,** 178–187; 10.1016/j.endeavour.2016.07.002 (2016).
7. Kweku, D. *et al.* Greenhouse Effect: Greenhouse Gases and Their Impact on Global Warming. *JSRR* **17,** 1–9; 10.9734/JSRR/2017/39630 (2018).
8. P. D. Jones, M. New, D. E. Parker, S. Martin, I. G. Rigor. Surface air temperature and its changes over the past 150 years. *Reviews of Geophysics* **37,** 173–199 (1999).
9. Lee, H. *et al.* Climate Change 2023: Synthesis Report. IPCC, 2023.
10. Scripps CO2 Program. Available at https://scrippsco2.ucsd.edu/graphics_gallery/mauna_loa_and_south_pole/index.html (2026).
11. Global Temperature - Earth Indicator. Available at https://science.nasa.gov/earth/explore/earth-indicators/global-temperature/ (2026).
12. Carbon Dioxide - Earth Indicator. Available at https://science.nasa.gov/earth/explore/earth-indicators/carbon-dioxide/ (2026).
13. Yearly Average Atmospheric CO2. Available at https://climatechangetracker.org/co2/yearly-atmospheric-co2 (2026).
14. Yearly Average Temperature. Available at https://climatechangetracker.org/global-warming/yearly-average-temperature (2026).

15. Hannah Ritchie and Pablo Rosado and Max Roser. CO_2 and Greenhouse Gas Emissions. Available at https://ourworldindata.org/co2-and-greenhouse-gas-emissions#all-charts (2026).

16. Hannah Ritchie and Pablo Rosado and Veronika Samborska. Climate Change. Available at https://ourworldindata.org/climate-change#all-charts (2026).

17. Global Warming of 1.5°C. IPCC, 2019.

18. Nelles, D. & Serrer, C. *Kleine Gase – große Wirkung. Der Klimawandel* (KlimaWandel GbR, Friedrichshafen, 2018).

19. Wallace-Wells, D. *Die unbewohnbare Erde. Leben nach der Erderwärmung* (Ludwig, München, 2019).

20. *Übereinkommen von Paris* (2015).

21. *Paris Agreement* (2015).

22. Renewable Energy Statistics 2025. International Renewable Energy Agency (IRENA).

23. Osman, A. I. *et al.* Cost, environmental impact, and resilience of renewable energy under a changing climate: a review. *Environ Chem Lett* **21,** 741–764; 10.1007/s10311-022-01532-8 (2023).

24. MacKay, D. J. C. *Sustainable energy - without the hot air* (UIT Cambridge, Cambridge, 2009).

25. Holler, C. & Gaukel, J. *Erneuerbare Energien - ohne heiße Luft* (UIT Cambridge, Cambridge, 2019).

26. Sterner, M. & Stadler, I. (eds.). *Handbook of energy storage. Demand, technologies, integration* (Springer, Berlin, Heidelberg, 2019).

27. SG HoBA. Netztransparent.de. Available at https://www.netztransparenz.de/de-de/Erneuerbare-Energien-und-Umlagen/Freiwillige-Ver%C3%B6ffentlichungen/Wind-und-Solarenergie-Hochrechnung (2026).

28. Entsoe. Transparency Platform. Available at https://transparency.entsoe.eu/ (2026).

29. Luo, X., Wang, J., Dooner, M. & Clarke, J. Overview of current development in electrical energy storage technologies and the application potential in power system operation. *Applied Energy* **137,** 511–536; 10.1016/j.apenergy.2014.09.081 (2015).

30. Hossain, E., Faruque, H., Sunny, M., Mohammad, N. & Nawar, N. A Comprehensive Review on Energy Storage Systems: Types, Comparison, Current Scenario, Applications, Barriers, and Potential Solutions, Policies, and Future Prospects. *Energies* **13,** 3651; 10.3390/en13143651 (2020).

31. Sayed, E. *et al.* Renewable Energy and Energy Storage Systems. *Energies* **16,** 1415; 10.3390/en16031415 (2023).

32. Winter, M. & Brodd, R. J. What are batteries, fuel cells, and supercapacitors? *Chemical reviews* **104,** 4245–4269 (2004).

33. Zhao, Y. *et al.* A Review on Battery Market Trends, Second-Life Reuse, and Recycling. *Sustainable Chemistry* **2,** 167–205 (2021).

34. Armand, M. *et al.* Lithium-ion batteries – Current state of the art and anticipated developments. *Journal of Power Sources* **479,** 228708 (2020).

35. Zubi, G., Dufo-López, R., Carvalho, M. & Pasaoglu, G. The lithium-ion battery: State of the art and future perspectives. *Renewable and Sustainable Energy Reviews* **89,** 292–308; 10.1016/j.rser.2018.03.002 (2018).

36. Linden, D. (ed.). *Handbook of batteries.* 3rd ed. (McGraw-Hill, New York, NY, 2002).

37. Scrosati, B. (ed.). *Lithium batteries. Advanced technologies and applications* (Wiley, Hoboken, NJ, 2013).

38. Dahn, J. R., Sacken, U. von, Juzkow, M. W. & Al-Janaby, H. Rechargeable LiNiO2 / Carbon Cells. *J. Electrochem. Soc.* **138,** 2207–2211; 10.1149/1.2085950 (1991).

39. Scrosati, B. Lithium Rocking Chair Batteries: An Old Concept? *J. Electrochem. Soc.* **139,** 2776–2781; 10.1149/1.2068978 (1992).

40. Passerini, S., Bresser, D., Moretti, A. & Varzi, A. (eds.). *Batteries. Present and future energy storage challenges* (Wiley-VCH Verlag GmbH & Co. KGaA, Weinheim, 2020).

41. Boettcher, S. W. *et al.* Potentially Confusing: Potentials in Electrochemistry. *ACS Energy Lett.* **6,** 261–266; 10.1021/acsenergylett.0c02443 (2021).

42. Weiss, M. *et al.* Fast Charging of Lithium-Ion Batteries: A Review of Materials Aspects. *Advanced Energy Materials* **11**; 10.1002/aenm.202101126 (2021).

43. Usiskin, R. & Maier, J. Interfacial Effects in Lithium and Sodium Batteries. *Advanced Energy Materials* **11**; 10.1002/aenm.202001455 (2021).

44. Wang, L. *et al.* Identifying cathode and anode polarizations during practical high-rate charging/discharging in different Li-ion pouch batteries. *Battery Energy* **2**; 10.1002/bte2.20220025 (2023).

45. Miao, J. Review on Electrode Degradation at Fast Charging of Li-Ion and Li Metal Batteries from a Kinetic Perspective. *Electrochem* **4,** 156–180; 10.3390/electrochem4020013 (2023).

46. Pender, J. P. *et al.* Electrode Degradation in Lithium-Ion Batteries. *ACS nano* **14,** 1243–1295; 10.1021/acsnano.9b04365 (2020).

47. Waldmann, T., Hogg, B.-I. & Wohlfahrt-Mehrens, M. Li plating as unwanted side reaction in commercial Li-ion cells – A review. *Journal of Power Sources* **384,** 107–124; 10.1016/j.jpowsour.2018.02.063 (2018).

48. Liu, Q. *et al.* Understanding undesirable anode lithium plating issues in lithium-ion batteries. *RSC Adv.* **6,** 88683–88700 (2016).

49. Hogrefe, C., Waldmann, T., Hölzle, M. & Wohlfahrt-Mehrens, M. Direct observation of internal short circuits by lithium dendrites in cross-sectional lithium-ion in situ full cells. *Journal of Power Sources* **556,** 232391; 10.1016/j.jpowsour.2022.232391 (2023).

50. Legrand, N., Knosp, B., Desprez, P., Lapicque, F. & Raël, S. Physical characterization of the charging process of a Li-ion battery and prediction of Li plating by electrochemical modelling. *Journal of Power Sources* **245,** 208–216; 10.1016/j.jpowsour.2013.06.130 (2014).

51. Gao, T. *et al.* Interplay of Lithium Intercalation and Plating on a Single Graphite Particle. *Joule* **5,** 393–414; 10.1016/j.joule.2020.12.020 (2021).

52. Vetter, J. *et al.* Ageing mechanisms in lithium-ion batteries. *Journal of Power Sources* **147,** 269–281; 10.1016/j.jpowsour.2005.01.006 (2005).

53. Deng, X. *et al.* A Comparative Investigation of Single Crystal and Polycrystalline Ni-Rich NCMs as Cathodes for Lithium-Ion Batteries. *Energy & Environ Materials* **6**; 10.1002/eem2.12331 (2023).

54. Fischer, S., Doose, S., Müller, J., Höfels, C. & Kwade, A. Impact of Spheroidization of Natural Graphite on Fast-Charging Capability of Anodes for LIB. *Batteries* **9,** 305; 10.3390/batteries9060305 (2023).

55. Li, J. *et al.* Comparison of Single Crystal and Polycrystalline LiNi 0.5 Mn 0.3 Co 0.2 O 2 Positive Electrode Materials for High Voltage Li-Ion Cells. *J. Electrochem. Soc.* **164,** A1534-A1544; 10.1149/2.0991707jes (2017).

56. Mancini, M. *et al.* Enabling Fast-Charging Lithium-Ion Battery Anodes: Influence of Spheroidization on Natural Graphite. *Batteries & Supercaps* **5**; 10.1002/batt.202200109 (2022).

57. Nisar, U. *et al.* Tailoring Co-Free LiNi 0.5 Mn 1.5 O 4 Material for High-Voltage Lithium-Ion Batteries: Particle Design & Grain Boundary Engineering. *Advanced Energy Materials* **14**; 10.1002/aenm.202403024 (2024).

58. Bläubaum, L. *et al.* Impact of Particle Size Distribution on Performance of Lithium-Ion Batteries. *ChemElectroChem* **7,** 4755–4766; 10.1002/celc.202001249 (2020).

59. Zhang, W.-J. Comparison of the Rate Capacities of LiFePO[sub 4] Cathode Materials. *J. Electrochem. Soc.* **157,** A1040; 10.1149/1.3460840 (2010).

60. Pham, T. A. *et al.* Intercalation of Lithium into Graphite: Insights from First-Principles Simulations. *J. Phys. Chem. C* **124,** 21985–21992; 10.1021/acs.jpcc.0c06842 (2020).

61. Raj, H. & Sil, A. Effect of carbon coating on electrochemical performance of LiFePO4 cathode material for Li-ion battery. *Ionics* **24,** 2543–2553; 10.1007/s11581-017-2423-0 (2018).

62. Nisar, U. *et al.* Borate modified Co-free LiNi0.5Mn1.5O4 cathode material: A pathway to superior interface and cycling stability in LNMO/graphite full-cells. *Chemical Engineering Journal* **493,** 152416; 10.1016/j.cej.2024.152416 (2024).

63. Buqa, H., Goers, D., Holzapfel, M., Spahr, M. E. & Novák, P. High Rate Capability of Graphite Negative Electrodes for Lithium-Ion Batteries. *J. Electrochem. Soc.* **152,** A474; 10.1149/1.1851055 (2005).

64. Parikh, D., Christensen, T. & Li, J. Correlating the influence of porosity, tortuosity, and mass loading on the energy density of LiNi0.6Mn0.2Co0.2O2 cathodes under extreme fast charging (XFC) conditions. *Journal of Power Sources* **474,** 228601; 10.1016/j.jpowsour.2020.228601 (2020).

65. Landesfeind, J., Eldiven, A. & Gasteiger, H. A. Influence of the Binder on Lithium Ion Battery Electrode Tortuosity and Performance. *J. Electrochem. Soc.* **165,** A1122-A1128; 10.1149/2.0971805jes (2018).

66. Scheck, V., Memm, M., Hölzle, M. & Wohlfahrt-Mehrens, M. Improving the Fast Charging Capability of Lithium-Ion Battery Graphite Anodes by Implementing an Alternative Binder System. *J. Electrochem. Soc.* **170,** 120514; 10.1149/1945-7111/ad0667 (2023).

67. Scheck, V. *et al.* Laser-structured anodes for high-power lithium-ion batteries: A journey from coin cells to 21700-type cylindrical cells. *Journal of Power Sources* **624,** 235528; 10.1016/j.jpowsour.2024.235528 (2024).

68. Park, J., Hyeon, S., Jeong, S. & Kim, H.-J. Performance enhancement of Li-ion battery by laser structuring of thick electrode with low porosity. *Journal of Industrial and Engineering Chemistry* **70,** 178–185; 10.1016/j.jiec.2018.10.012 (2019).

69. Kang, S.-W. *et al.* Improve the Overall Performances of Lithium Ion Batteries by a Facile Method of Modifying the Surface of Cu Current Collector with Carbon. *Electrochimica Acta* **176,** 604–609; 10.1016/j.electacta.2015.06.107 (2015).

70. Wu, H.-C., Wu, H.-C., Lee, E. & Wu, N.-L. High-temperature carbon-coated aluminum current collector for enhanced power performance of LiFePO4 electrode of Li-ion batteries. *Electrochemistry Communications* **12,** 488–491; 10.1016/j.elecom.2010.01.028 (2010).

71. Waldmann, T., Geramifard, G. & Wohlfahrt-Mehrens, M. Influence of current collecting tab design on thermal and electrochemical performance of cylindrical Lithium-ion cells during high current discharge. *Journal of Energy Storage* **5,** 163–168; 10.1016/j.est.2015.12.007 (2016).

72. Waldmann, T., Scurtu, R.-G., Brändle, D. & Wohlfahrt-Mehrens, M. Effects of Tab Design in 21700 Li-Ion Cells: Improvements of Cell Impedance, Rate Capability, and Cycling Aging. *Energy Tech* **11**; 10.1002/ente.202200583 (2023).

73. Zhao, W., Luo, G. & Wang, C.-Y. Effect of tab design on large-format Li-ion cell performance. *Journal of Power Sources* **257,** 70–79; 10.1016/j.jpowsour.2013.12.146 (2014).

74. Waldmann, T. *et al.* A Direct Comparison of Pilot-Scale Li-Ion Cells in the Formats PHEV1, Pouch, and 21700. *J. Electrochem. Soc.* **168,** 90519; 10.1149/1945-7111/ac208c (2021).

75. Waldmann, T., Scurtu, R.-G., Richter, K. & Wohlfahrt-Mehrens, M. 18650 vs. 21700 Li-ion cells – A direct comparison of electrochemical, thermal, and geometrical properties. *Journal of Power Sources* **472,** 228614; 10.1016/j.jpowsour.2020.228614 (2020).

76. Ahmed, S. *et al.* Electrode balancing as a key factor in lithium-ion batteries: From fundamentals to ultrafast charging. *Journal of Power Sources* **667,** 239188; 10.1016/j.jpowsour.2025.239188 (2026).

77. Ding, M. S. *et al.* Change of Conductivity with Salt Content, Solvent Composition, and Temperature for Electrolytes of LiPF[sub 6] in Ethylene Carbonate-Ethyl Methyl Carbonate. *J. Electrochem. Soc.* **148,** A1196; 10.1149/1.1403730 (2001).

78. Du, Z., Wood, D. L. & Belharouak, I. Enabling fast charging of high energy density Li-ion cells with high lithium ion transport electrolytes. *Electrochemistry Communications* **103,** 109–113; 10.1016/j.elecom.2019.04.013 (2019).

79. Kremer, L. S. *et al.* Influence of the Electrolyte Salt Concentration on the Rate Capability of Ultra-Thick NCM 622 Electrodes. *Batteries & Supercaps* **3,** 1172–1182; 10.1002/batt.202000098 (2020).

80. Kasnatscheew, J. *et al.* A Tutorial into Practical Capacity and Mass Balancing of Lithium Ion Batteries. *J. Electrochem. Soc.* **164,** A2479-A2486; 10.1149/2.0961712jes (2017).

81. Tang, M., Albertus, P. & Newman, J. Two-Dimensional Modeling of Lithium Deposition during Cell Charging. *J. Electrochem. Soc.* **156,** A390; 10.1149/1.3095513 (2009).

82. Li, J., Fleetwood, J., Hawley, W. B. & Kays, W. From Materials to Cell: State-of-the-Art and Prospective Technologies for Lithium-Ion Battery Electrode Processing. *Chemical reviews* **122,** 903–956 (2022).

83. Mizushima, K., Jones, P. C., Wiseman, P. J. & Goodenough, J. B. LixCoO2 (0<x<-1): A new cathode material for batteries of high energy density. *Materials Research Bulletin* **15,** 783–789; 10.1016/0025-5408(80)90012-4 (1980).

84. Lin, Z. *et al.* Decoding High-voltage LiCoO2: From Degradation to Stabilization Toward Durable Li-ion Batteries. *Advanced materials*; 10.1002/adma.202523570 (2026).

85. An, S. J. *et al.* The state of understanding of the lithium-ion-battery graphite solid electrolyte interphase (SEI) and its relationship to formation cycling. *Carbon* **105,** 52–76 (2016).

86. Peled, E. The Electrochemical Behavior of Alkali and Alkaline Earth Metals in Nonaqueous Battery Systems - The Solid Electrolyte Interphase Model. *Journal of The Electrochemical Society* (1979).

87. Peled, E. & Menkin, S. Review—SEI: Past, Present and Future. *Journal of The Electrochemical Society* **164,** A1703-A1719 (2017).

88. Xu, K. Interfaces and interphases in batteries. *Journal of Power Sources* **559,** 232652 (2023).

89. Holtstiege, F., Wilken, A., Winter, M. & Placke, T. Running out of lithium? A route to differentiate between capacity losses and active lithium losses in lithium-ion batteries. *Physical chemistry chemical physics : PCCP* **19,** 25905–25918; 10.1039/c7cp05405j (2017).

90. Edge, J. S. *et al.* Lithium ion battery degradation: what you need to know. *Physical chemistry chemical physics : PCCP* **23,** 8200–8221; 10.1039/d1cp00359c (2021).

91. Goodenough, J. B. & Park, K.-S. The Li-ion rechargeable battery: a perspective. *Journal of the American Chemical Society* **135,** 1167–1176; 10.1021/ja3091438 (2013).

92. Liu, J. *et al.* Aging mechanisms and thermal stability of aged commercial 18650 lithium ion battery induced by slight overcharging cycling. *Journal of Power Sources* **445,** 227263; 10.1016/j.jpowsour.2019.227263 (2020).

93. Mathieu, R., Briat, O., Gyan, P. & Vinassa, J.-M. Comparison of the impact of fast charging on the cycle life of three lithium-ion cells under several parameters of charge protocol and temperatures. *Applied Energy* **283,** 116344; 10.1016/j.apenergy.2020.116344 (2021).

94. Preger, Y. *et al.* Degradation of Commercial Lithium-Ion Cells as a Function of Chemistry and Cycling Conditions. *J. Electrochem. Soc.* **167,** 120532; 10.1149/1945-7111/abae37 (2020).

95. Hou, J. *et al.* Transforming Materials into Practical Automotive Lithium-Ion Batteries. *Adv Materials Technologies* **6**; 10.1002/admt.202100152 (2021).

96. Hawley, W. B. & Li, J. Electrode manufacturing for lithium-ion batteries—Analysis of current and next generation processing. *Journal of Energy Storage* **25,** 100862; 10.1016/j.est.2019.100862 (2019).

97. Bryntesen, S. N. *et al.* Opportunities for the State-of-the-Art Production of LIB Electrodes—A Review. *Energies* **14,** 1406; 10.3390/en14051406 (2021).

98. Reddy, M. V., Mauger, A., Julien, C. M., Paolella, A. & Zaghib, K. Brief History of Early Lithium-Battery Development. *Materials* **13** (2020).

99. Winter, M., Besenhard, J. O., Spahr, M. E. & Novák, P. Insertion Electrode Materials for Rechargeable Lithium Batteries. *Adv. Mater.* **10,** 725–763 (1998).

100. Tarascon, J.-M. & Armand, M. Issues and challenges facing rechargeable lithium batteries. *Nature* (2001).

101. Li, M., Lu, J., Chen, Z. & Amine, K. 30 Years of Lithium-Ion Batteries. *Advanced materials (Deerfield Beach, Fla.),* e1800561; 10.1002/adma.201800561 (2018).

102. Nölle, R. *et al.* A reality check and tutorial on electrochemical characterization of battery cell materials: How to choose the appropriate cell setup. *Materials Today* **32,** 131–146; 10.1016/j.mattod.2019.07.002 (2020).

103. Heubner, C. *et al.* Electrochemical Characterization of Battery Materials in 2-Electrode Half-Cell Configuration: A Balancing Act Between Simplicity and Pitfalls. *Batteries & Supercaps* **4,** 1310–1322; 10.1002/batt.202100075 (2021).

104. Zhang, S. S. Is Li/Graphite Half-Cell Suitable for Evaluating Lithiation Rate Capability of Graphite Electrode? *J. Electrochem. Soc.* **167,** 100510; 10.1149/1945-7111/ab945e (2020).

105. Yoshino, A. The birth of the lithium-ion battery. *Angewandte Chemie (International ed. in English)* **51,** 5798–5800; 10.1002/anie.201105006 (2012).

106. Whittingham, M. S. History, Evolution, and Future Status of Energy Storage. *Proceedings of the IEEE* **100,** 1518–1534 (2012).

107. Crabtree, G., Kócs, E. & Trahey, L. The energy-storage frontier: Lithium-ion batteries and beyond. *MRS Bulletin* **40,** 1067–1078 (2015).

108. Chung, D. D. L. Review Graphite. *Journal of Materials Science* **37,** 1475–1489; 10.1023/A:1014915307738 (2002).

109. LIPSON, H. & STOKES, A. R. A New Structure of Carbon. *Nature* **149,** 328; 10.1038/149328a0 (1942).

110. J. D. Bernal. The structure of graphite. *Royal Society,* 750–773 (1924).

111. Shi, H., Barker, J., Saïdi, M. Y. & Koksbang, R. Structure and Lithium Intercalation Properties of Synthetic and Natural Graphite. *J. Electrochem. Soc.* **143,** 3466–3472; 10.1149/1.1837238 (1996).

112. Asenbauer, J. *et al.* The success story of graphite as a lithium-ion anode material – fundamentals, remaining challenges, and recent developments including silicon (oxide) composites. *Sustainable Energy & Fuels* **4,** 5387–5416 (2020).

113. Hofmann, U. & Rüdorff, W. The formation of salts from graphite by strong acids. *Trans. Faraday Soc.* **34,** 1017–1021; 10.1039/TF9383401017 (1938).

114. Billaud, D., McRae, E. & Hérold, A. Synthesis and electrical resistivity of lithium-pyrographite intercalation compounds (stages I, II and III). *Materials Research Bulletin* **14,** 857–864; 10.1016/0025-5408(79)90149-1 (1979).

115. Song, X. Y., Kinoshita, K. & Tran, T. D. Microstructural Characterization of Lithiated Graphite. *J. Electrochem. Soc.* **143,** L120-L123; 10.1149/1.1836896 (1996).

116. Hogrefe, C. *et al.* Cross-Sectional In Situ Optical Microscopy with Simultaneous Electrochemical Measurements for Lithium-Ion Full Cells. *J. Electrochem. Soc.* **169,** 50519; 10.1149/1945-7111/ac6c57 (2022).

117. Maire, P., Evans, A., Kaiser, H., Scheifele, W. & Novák, P. Colorimetric Determination of Lithium Content in Electrodes of Lithium-Ion Batteries. *J. Electrochem. Soc.* **155,** A862; 10.1149/1.2979696 (2008).

118. Winter, M., Novák, P. & Monnier, A. Graphites for Lithium-Ion Cells: The Correlation of the First-Cycle Charge Loss with the Brunauer-Emmett-Teller Surface Area. *J. Electrochem. Soc.* **145,** 428–436; 10.1149/1.1838281 (1998).

119. Yao, X. L. *et al.* Comparisons of graphite and spinel Li1.33Ti1.67O4 as anode materials for rechargeable lithium-ion batteries. *Electrochimica Acta* **50,** 4076–4081; 10.1016/j.electacta.2005.01.034 (2005).

120. Sandhya, C. P., John, B. & Gouri, C. Synthesis and electrochemical characterisation of electrospun lithium titanate ultrafine fibres. *J Mater Sci* **48,** 5827–5832; 10.1007/s10853-013-7375-9 (2013).

121. Ohzuku, T., Ueda, A. & Yamamoto, N. Zero-Strain Insertion Material of Li [Li1 / 3Ti5 / 3] O 4 for Rechargeable Lithium Cells. *J. Electrochem. Soc.* **142,** 1431–1435; 10.1149/1.2048592 (1995).

122. Chen, C. H. *et al.* Studies of Mg-Substituted Li[sub 4−x]Mg[sub x]Ti[sub 5]O[sub 12] Spinel Electrodes (0≤x≤1) for Lithium Batteries. *J. Electrochem. Soc.* **148,** A102; 10.1149/1.1344523 (2001).

123. Kavan, L. *et al.* Li Insertion into Li[sub 4]Ti[sub 5]O[sub 12] (Spinel). *J. Electrochem. Soc.* **150,** A1000; 10.1149/1.1581262 (2003).

124. Rho, Y. H. & Kanamura, K. Li+ ion diffusion in Li4Ti5O12 thin film electrode prepared by PVP sol–gel method. *Journal of Solid State Chemistry* **177,** 2094–2100; 10.1016/j.jssc.2004.02.018 (2004).

125. Wagemaker, M., van Eck, E. R. H., Kentgens, A. P. M. & Mulder, F. M. Li-ion diffusion in the equilibrium nanomorphology of spinel Li(4+x)Ti(5)O(12). *The journal of physical chemistry. B* **113,** 224–230; 10.1021/jp8073706 (2009).

126. Bresser, D. *et al.* The importance of “going nano” for high power battery materials. *Journal of Power Sources* **219,** 217–222; 10.1016/j.jpowsour.2012.07.035 (2012).

127. Birrozzi, A. *et al.* Scaling up “Nano” Li 4 Ti 5 O 12 for High-Power Lithium-Ion Anodes Using Large Scale Flame Spray Pyrolysis. *J. Electrochem. Soc.* **162,** A2331-A2338; 10.1149/2.0711512jes (2015).

128. Lin, Y.-S., Tsai, M.-C. & Duh, J.-G. Self-assembled synthesis of nanoflower-like Li4Ti5O12 for ultrahigh rate lithium-ion batteries. *Journal of Power Sources* **214,** 314–318; 10.1016/j.jpowsour.2012.04.072 (2012).

129. Wang, Y.-Q. *et al.* Rutile-TiO2 nanocoating for a high-rate Li4Ti5O12 anode of a lithium-ion battery. *Journal of the American Chemical Society* **134,** 7874–7879; 10.1021/ja301266w (2012).

130. Zhao, L., Hu, Y.-S., Li, H., Wang, Z. & Chen, L. Porous Li4 Ti5 O12 coated with N-doped carbon from ionic liquids for Li-ion batteries. *Advanced materials (Deerfield Beach, Fla.)* **23,** 1385–1388; 10.1002/adma.201003294 (2011).

131. Sandhya, C. P., John, B. & Gouri, C. Lithium titanate as anode material for lithium-ion cells: a review. *Ionics* **20,** 601–620; 10.1007/s11581-014-1113-4 (2014).

132. Zhang, H. *et al.* Li 4 Ti 5 O 12 spinel anode: Fundamentals and advances in rechargeable batteries. *InfoMat* **4**; 10.1002/inf2.12228 (2022).

133. Beaulieu, L. Y., Hatchard, T. D., Bonakdarpour, A., Fleischauer, M. D. & Dahn, J. R. Reaction of Li with Alloy Thin Films Studied by In Situ AFM. *J. Electrochem. Soc.* **150,** A1457; 10.1149/1.1613668 (2003).

134. Boukamp, B. A., Lesh, G. C. & Huggins, R. A. All-Solid Lithium Electrodes with Mixed-Conductor Matrix. *J. Electrochem. Soc.* **128,** 725–729; 10.1149/1.2127495 (1981).

135. Obrovac, M. N. & Christensen, L. Structural Changes in Silicon Anodes during Lithium Insertion/Extraction. *Electrochem. Solid-State Lett.* **7,** A93; 10.1149/1.1652421 (2004).

136. Chae, S., Ko, M., Kim, K., Ahn, K. & Cho, J. Confronting Issues of the Practical Implementation of Si Anode in High-Energy Lithium-Ion Batteries. *Joule* **1,** 47–60; 10.1016/j.joule.2017.07.006 (2017).

137. Yoshio, M., Tsumura, T. & Dimov, N. Silicon/graphite composites as an anode material for lithium ion batteries. *Journal of Power Sources* **163,** 215–218; 10.1016/j.jpowsour.2005.12.078 (2006).

138. McDowell, M. T. *et al.* In situ TEM of two-phase lithiation of amorphous silicon nanospheres. *Nano letters* **13,** 758–764; 10.1021/nl3044508 (2013).

139. Liu, X. H. *et al.* Size-dependent fracture of silicon nanoparticles during lithiation. *ACS nano* **6,** 1522–1531; 10.1021/nn204476h (2012).

140. Dimov, N., Kugino, S. & Yoshio, M. Mixed silicon–graphite composites as anode material for lithium ion batteries. *Journal of Power Sources* **136,** 108–114; 10.1016/j.jpowsour.2004.05.012 (2004).

141. Holzapfel, M., Buqa, H., Scheifele, W., Novák, P. & Petrat, F.-M. A new type of nano-sized silicon/carbon composite electrode for reversible lithium insertion. *Chemical communications (Cambridge, England),* 1566–1568; 10.1039/b417492e (2005).

142. Dou, F., Shi, L., Chen, G. & Zhang, D. Silicon/Carbon Composite Anode Materials for Lithium-Ion Batteries. *Electrochem. Energ. Rev.* **2,** 149–198; 10.1007/s41918-018-00028-w (2019).

143. Jo, Y. N. *et al.* Si–graphite composites as anode materials for lithium secondary batteries. *Journal of Power Sources* **195,** 6031–6036; 10.1016/j.jpowsour.2010.03.008 (2010).

144. Kasavajjula, U., Wang, C. & Appleby, A. J. Nano- and bulk-silicon-based insertion anodes for lithium-ion secondary cells. *Journal of Power Sources* **163,** 1003–1039; 10.1016/j.jpowsour.2006.09.084 (2007).

145. Lee, J.-H., Kim, W.-J., Kim, J.-Y., Lim, S.-H. & Lee, S.-M. Spherical silicon/graphite/carbon composites as anode material for lithium-ion batteries. *Journal of Power Sources* **176,** 353–358; 10.1016/j.jpowsour.2007.09.119 (2008).

146. Kloker, G., Vrankovic, D., Arya, N., Diemant, T. & Anjass, M. Enabling Si-Dominant Anodes: Influence of Neutralization Degree of Polyacrylic Acid on Low-Cost Micron-Sized Silicon Anode in High-Energy Li-Ion Full Cell. *Batteries & Supercaps* **7**; 10.1002/batt.202400330 (2024).

147. Li, J., Lewis, R. B. & Dahn, J. R. Sodium Carboxymethyl Cellulose. *Electrochem. Solid-State Lett.* **10,** A17; 10.1149/1.2398725 (2007).

148. Parikh, P. *et al.* Role of Polyacrylic Acid (PAA) Binder on the Solid Electrolyte Interphase in Silicon Anodes. *Chem. Mater.* **31,** 2535–2544; 10.1021/acs.chemmater.8b05020 (2019).

149. Dalavi, S., Guduru, P. & Lucht, B. L. Performance Enhancing Electrolyte Additives for Lithium Ion Batteries with Silicon Anodes. *J. Electrochem. Soc.* **159,** A642-A646; 10.1149/2.076205jes (2012).

150. Yoon, T., Nguyen, C. C., Seo, D. M. & Lucht, B. L. Capacity Fading Mechanisms of Silicon Nanoparticle Negative Electrodes for Lithium Ion Batteries. *J. Electrochem. Soc.* **162,** A2325-A2330; 10.1149/2.0731512jes (2015).

151. McDowell, M. T., Lee, S. W., Nix, W. D. & Cui, Y. 25th anniversary article: Understanding the lithiation of silicon and other alloying anodes for lithium-ion batteries. *Adv. Mater.* **25,** 4966–4985; 10.1002/adma.201301795 (2013).

152. Flügel, M., Richter, K., Wohlfahrt-Mehrens, M. & Waldmann, T. Detection of Li Deposition on Si/Graphite Anodes from Commercial Li-Ion Cells: A Post-Mortem GD-OES Depth Profiling Study. *J. Electrochem. Soc.* **169,** 50533; 10.1149/1945-7111/ac70af (2022).

153. Whittingham, M. S. The Role of Ternary Phases in Cathode Reactions. *J. Electrochem. Soc.* **123,** 315–320; 10.1149/1.2132817 (1976).

154. Whittingham, M. Chemistry of intercalation compounds: Metal guests in chalcogenide hosts. *Progress in Solid State Chemistry* **12,** 41–99; 10.1016/0079-6786(78)90003-1 (1978).

155. Olivetti, E. A., Ceder, G., Gaustad, G. G. & Fu, X. Lithium-Ion Battery Supply Chain Considerations: Analysis of Potential Bottlenecks in Critical Metals. *Joule* **1,** 229–243; 10.1016/j.joule.2017.08.019 (2017).

156. Al Barazi, S. Rohstoffrisikobewertung - Kobalt. DERA Rohstoffinformationen, 2018.

157. Szurlies, M. Rohstoffrisikobewertung - Nickel. DERA Rohstoffinformationen, 2021.

158. Dahn, J. Structure and electrochemistry of Li1±yNiO2 and a new Li2NiO2 phase with the Ni (OH)2 structure. *Solid State Ionics* **44,** 87–97; 10.1016/0167-2738(90)90049-W (1990).

159. Ohzuku, T., Ueda, A. & Nagayama, M. Electrochemistry and Structural Chemistry of LiNiO2 (R3m) for 4 Volt Secondary Lithium Cells. *J. Electrochem. Soc.* **140,** 1862–1870; 10.1149/1.2220730 (1993).

160. Yamada, S., Fujiwara, M. & Kanda, M. Synthesis and properties of LiNiO2 as cathode material for secondary batteries. *Journal of Power Sources* **54,** 209–213; 10.1016/0378-7753(94)02068-E (1995).

161. Padhi, A. K., Nanjundaswamy, K. S. & Goodenough, J. B. Phospho-olivines as Positive-Electrode Materials for Rechargeable Lithium Batteries. *J. Electrochem. Soc.* **144,** 1188–1194; 10.1149/1.1837571 (1997).

162. Huang, H., Yin, S.-C. & Nazar, L. F. Approaching Theoretical Capacity of LiFePO[sub 4] at Room Temperature at High Rates. *Electrochem. Solid-State Lett.* **4,** A170; 10.1149/1.1396695 (2001).

163. Prosini, P. Determination of the chemical diffusion coefficient of lithium in LiFePO4. *Solid State Ionics* **148,** 45–51; 10.1016/S0167-2738(02)00134-0 (2002).

164. Morgan, D., van der Ven, A. & Ceder, G. Li Conductivity in Li[sub x]MPO[sub 4] (M = Mn, Fe, Co, Ni) Olivine Materials. *Electrochem. Solid-State Lett.* **7,** A30; 10.1149/1.1633511 (2004).

165. Liu, J., Wang, Z., Zhang, G., Liu, Y. & Yu, A. Size-Controlled Synthesis of LiFePO4/C Composites as Cathode Materials for Lithium Ion Batteries. *International Journal of Electrochemical Science* **8,** 2378–2387; 10.1016/S1452-3981(23)14316-1 (2013).

166. Satyavani, T., Srinivas Kumar, A. & Subba Rao, P. Methods of synthesis and performance improvement of lithium iron phosphate for high rate Li-ion batteries: A review. *Engineering Science and Technology, an International Journal* **19,** 178–188; 10.1016/j.jestch.2015.06.002 (2016).

167. Kasnatscheew, J. *et al.* The truth about the 1st cycle Coulombic efficiency of LiNi1/3Co1/3Mn1/3O2 (NCM) cathodes. *Physical chemistry chemical physics : PCCP* **18,** 3956–3965; 10.1039/c5cp07718d (2016).

168. Entwistle, J., Ge, R., Pardikar, K., Smith, R. & Cumming, D. Carbon binder domain networks and electrical conductivity in lithium-ion battery electrodes: A critical review. *Renewable and Sustainable Energy Reviews* **166,** 112624; 10.1016/j.rser.2022.112624 (2022).

169. Spahr, M. E., Goers, D., Leone, A., Stallone, S. & Grivei, E. Development of carbon conductive additives for advanced lithium ion batteries. *Journal of Power Sources* **196,** 3404–3413; 10.1016/j.jpowsour.2010.07.002 (2011).

170. Medvedev, O. S., Wang, Q., Popovich, A. A. & Novikov, P. A. Comparison of conductive additives for high-power applications of Li-ion batteries. *Ionics* **26,** 4277–4286; 10.1007/s11581-020-03631-4 (2020).

171. Gaikwad, A. M. & Arias, A. C. Understanding the Effects of Electrode Formulation on the Mechanical Strength of Composite Electrodes for Flexible Batteries. *ACS applied materials & interfaces* **9,** 6390–6400; 10.1021/acsami.6b14719 (2017).

172. Solef® PVDF. Solef® PVDF for Li-Ion Batteries. Available at https://www.syensqo.com/en/brands/solef-pvdf/li-ion-batteries.

173. GESTIS-Stoffdatenbank. N-Methyl-2-pyrrolidon. Available at https://gestis.dguv.de/data?name=013700.

174. Bundesministerium für Umwelt, Klimaschutz, Naturschutz und nukleare Sicherheit. Per- und polyfluorierte Chemikalien (PFAS). Available at https://www.bundesumweltministerium.de/faqs/per-und-polyfluorierte-chemikalien-pfas.

175. Lee, J.-H., Lee, S., Paik, U. & Choi, Y.-M. Aqueous processing of natural graphite particulates for lithium-ion battery anodes and their electrochemical performance. *Journal of Power Sources* **147,** 249–255; 10.1016/j.jpowsour.2005.01.022 (2005).

176. Li, J.-T. *et al.* Water Soluble Binder, an Electrochemical Performance Booster for Electrode Materials with High Energy Density. *Advanced Energy Materials* **7**; 10.1002/aenm.201701185 (2017).

177. Porcher, W., Lestriez, B., Jouanneau, S. & Guyomard, D. Design of Aqueous Processed Thick LiFePO[sub 4] Composite Electrodes for High-Energy Lithium Battery. *J. Electrochem. Soc.* **156,** A133; 10.1149/1.3046129 (2009).

178. Loeffler, N. *et al.* Performance of LiNi1/3Mn1/3Co1/3O2/graphite batteries based on aqueous binder. *Journal of Power Sources* **248,** 915–922; 10.1016/j.jpowsour.2013.10.018 (2014).

179. Hawley, W. B. *et al.* Lithium and transition metal dissolution due to aqueous processing in lithium-ion battery cathode active materials. *Journal of Power Sources* **466,** 228315; 10.1016/j.jpowsour.2020.228315 (2020).

180. Radloff, S., Carbonari, G., Scurtu, R.-G., Hölzle, M. & Wohlfahrt-Mehrens, M. Fluorine-free water-based Ni-rich positive electrodes and their performance in pouch- and 21700-type cells. *Journal of Power Sources* **553,** 232253; 10.1016/j.jpowsour.2022.232253 (2023).

181. Radloff, S. *et al.* Mitigating water-induced surface degradation in water-based Ni-rich Li-ion battery electrodes. *Journal of Power Sources* **580,** 233314; 10.1016/j.jpowsour.2023.233314 (2023).

182. Radloff, S., Scurtu, R.-G., Hölzle, M. & Wohlfahrt-Mehrens, M. Water-Based LiNi 0.83 Co 0.12 Mn 0.05 O 2 Electrodes with Excellent Cycling Stability Fabricated Using Unconventional Binders. *J. Electrochem. Soc.* **169,** 40514; 10.1149/1945-7111/ac6324 (2022).

183. Reynolds, C. D., Walker, H., Mahgoub, A., Adebayo, E. & Kendrick, E. Battery electrode slurry rheology and its impact on manufacturing. *Energy Adv.* **4,** 84–93; 10.1039/D4YA00380B (2025).

184. Huber, K., Adam, A., Grießl, D. & Kwade, A. Understanding slurry mixing effects on the fast charging capability of lithium-ion battery cells: Methodology and case study. *Journal of Power Sources* **536,** 231455; 10.1016/j.jpowsour.2022.231455 (2022).

185. Wang, M., Dang, D., Meyer, A., Arsenault, R. & Cheng, Y.-T. Effects of the Mixing Sequence on Making Lithium Ion Battery Electrodes. *J. Electrochem. Soc.* **167,** 100518; 10.1149/1945-7111/ab95c6 (2020).

186. Bitsch, B. *et al.* A novel slurry concept for the fabrication of lithium-ion battery electrodes with beneficial properties. *Journal of Power Sources* **265,** 81–90; 10.1016/j.jpowsour.2014.04.115 (2014).

187. Ouyang, L. *et al.* The effect of solid content on the rheological properties and microstructures of a Li-ion battery cathode slurry. *RSC advances* **10,** 19360–19370; 10.1039/d0ra02651d (2020).

188. Carl D. Reynolds, Sam D. Hare, Peter R. Slater, Mark J. H. Simmons & Emma Kendrick. Rheology and Structure of Lithium-Ion Battery Electrode Slurries.

189. Lee, S. C., Lee, J. S. & Lee, S. J. Influence of carboxymethyl cellulose molecular weight on anode slurry rheology for lithium-ion batteries. *Korea-Aust. Rheol. J.* **37,** 273–285; 10.1007/s13367-025-00129-1 (2025).

190. Zhu, P. *et al.* A review of current collectors for lithium-ion batteries. *Journal of Power Sources* **485,** 229321 (2021).

191. Park, M., Zhang, X., Chung, M., Less, G. B. & Sastry, A. M. A review of conduction phenomena in Li-ion batteries. *Journal of Power Sources* **195,** 7904–7929; 10.1016/j.jpowsour.2010.06.060 (2010).

192. Liu, Y.-K. *et al.* Research Progresses of Liquid Electrolytes in Lithium-Ion Batteries. *Small (Weinheim an der Bergstrasse, Germany)* **19,** e2205315; 10.1002/smll.202205315 (2023).

193. Kawamura, T., Okada, S. & Yamaki, J. Decomposition reaction of LiPF6-based electrolytes for lithium ion cells. *Journal of Power Sources* **156,** 547–554; 10.1016/j.jpowsour.2005.05.084 (2006).

194. Lux, S. F. *et al.* The mechanism of HF formation in LiPF6 based organic carbonate electrolytes. *Electrochemistry Communications* **14,** 47–50; 10.1016/j.elecom.2011.10.026 (2012).

195. Stich, M., Pandey, N. & Bund, A. Drying and moisture resorption behaviour of various electrode materials and separators for lithium-ion batteries. *Journal of Power Sources* **364,** 84–91; 10.1016/j.jpowsour.2017.08.009 (2017).

196. Xu, K. Li-ion battery electrolytes. *Nat Energy* **6,** 763; 10.1038/s41560-021-00841-6 (2021).

197. Chen, S. *et al.* Practical evaluation of prelithiation strategies for next-generation lithium-ion batteries. *Carbon Energy* **5** (2023).

198. Holtstiege, F., Bärmann, P., Nölle, R., Winter, M. & Placke, T. Pre-Lithiation Strategies for Rechargeable Energy Storage Technologies: Concepts, Promises and Challenges. *Batteries* **4,** 4 (2018).

199. Jin, L. *et al.* Pre-Lithiation Strategies for Next-Generation Practical Lithium-Ion Batteries. *Advanced science* **8** (2021).

200. Lau, V., Kuo, C. & Lan, C. Objective Review on Commercially Viable Prelithiation Techniques for Lithium-ion Batteries. *ChemElectroChem* **11** (2024).

201. Mancini, M. *et al.* A High-Voltage and High-Capacity Li1+x Ni0.5 Mn1.5 O4 Cathode Material: From Synthesis to Full Lithium-Ion Cells. *ChemSusChem* **9,** 1843–1849; 10.1002/cssc.201600365 (2016).

202. Peramunage, D. & Abraham, K. M. Preparation and Electrochemical Characterization of Overlithiated Spinel LiMn2 O 4. *J. Electrochem. Soc.* **145,** 1131–1136; 10.1149/1.1838428 (1998).

203. Betz, J., Nowak, L., Winter, M., Placke, T. & Schmuch, R. An Approach for Pre-Lithiation of Li 1+ x Ni 0.5 Mn 1.5 O 4 Cathodes Mitigating Active Lithium Loss. *J. Electrochem. Soc.* **166,** A3531-A3538; 10.1149/2.1221914jes (2019).

204. Park, K., Yu, B.-C. & Goodenough, J. B. Li 3 N as a Cathode Additive for High-Energy-Density Lithium-Ion Batteries. *Advanced Energy Materials* **6**; 10.1002/aenm.201502534 (2016).

205. Shanmukaraj, D. *et al.* Sacrificial salts: Compensating the initial charge irreversibility in lithium batteries. *Electrochemistry Communications* **12,** 1344–1347; 10.1016/j.elecom.2010.07.016 (2010).

206. Sun, Y. *et al.* High-capacity battery cathode prelithiation to offset initial lithium loss. *Nat Energy* **1**; 10.1038/nenergy.2015.8 (2016).

207. Wang, X. *et al.* Dual-Functional Cathodic Prelithiation Reagent of Li 3 P in Lithium-Ion Battery for Compensating Initial Capacity Loss and Enhancing Safety. *ACS Appl. Energy Mater.* **4,** 5246–5254; 10.1021/acsaem.1c00773 (2021).

208. Scott, M. G., Whitehead, A. H. & Owen, J. R. Chemical Formation of a Solid Electrolyte Interface on the Carbon Electrode of a Li-Ion Cell. *J. Electrochem. Soc.* **145,** 1506–1510; 10.1149/1.1838511 (1998).

209. YOSHIDA, S. *et al.* Li Pre-doping of Amorphous Silicon Electrode in Li-Naphthalene Complex Solutions. *Electrochemistry* **83,** 843–845; 10.5796/electrochemistry.83.843 (2015).

210. Zhang, X. *et al.* An electrode-level prelithiation of SiO anodes with organolithium compounds for lithium-ion batteries. *Journal of Power Sources* **478,** 229067; 10.1016/j.jpowsour.2020.229067 (2020).

211. Li, Y. & Fitch, B. Effective enhancement of lithium-ion battery performance using SLMP. *Electrochemistry Communications* **13,** 664–667; 10.1016/j.elecom.2011.04.003 (2011).

212. Yang, C. *et al.* Roll-to-roll prelithiation of lithium-ion battery anodes by transfer printing. *Nat Energy* **8,** 703–713; 10.1038/s41560-023-01272-1 (2023).

213. Tsuda, T. *et al.* Fabrication of Porous Graphite Anodes with Pico-Second Pulse Laser and Enhancement of Pre-Doping of Li + Ions to Laminated Graphite Anodes with Micrometre-Sized Holes Formed on the Porous Graphite Anodes. *ECS Transactions* **77,** 1897–1903 (2017).

214. Watanabe, T. *et al.* An improved pre-lithiation of graphite anodes using through-holed cathode and anode electrodes in a laminated lithium ion battery. *Electrochimica Acta* **324,** 134848 (2019).

215. Zensen, N. *Development of a Prelithiation Method on Cell Stack Level for Implementing Silicon Anodes.* Dissertation, Universität Ulm (2020).

216. Winter, M., Barnett, B. & Xu, K. Before Li Ion Batteries. *Chemical reviews* **118,** 11433–11456 (2018).

217. Grohol, M. & Veeh, C. *Study on the critical raw materials for the EU 2023. Final report* (Publications Office of the European Union, Luxembourg, 2023).

218. Patrick S Grant et al. Roadmap on Li-ion battery manufacturing research. *Journal of Physics: Energy* **4,** 42006 (2022).

219. Singh, M., Kaiser, J. & Hahn, H. Thick Electrodes for High Energy Lithium Ion Batteries. *J. Electrochem. Soc.* **162,** A1196-A1201; 10.1149/2.0401507jes (2015).

220. Yamada, M., Watanabe, T., Gunji, T., Wu, J. & Matsumoto, F. Review of the Design of Current Collectors for Improving the Battery Performance in Lithium-Ion and Post-Lithium-Ion Batteries. *Electrochem* **1,** 124–159 (2020).

221. Naskar, P., Saha, A., Biswas, B. & Banerjee, A. Review—Current Collectors for Rechargeable Batteries: State-of-the-Art Design and Development Strategies for Commercial Products. *Journal of The Electrochemical Society* **171,** 10515 (2024).

222. Tsuda, T. *et al.* Study on Li Metal Deposition, SEI Formation on Anodes and Cathode Potential Change during the Pre-Lithiation Process in a Cell Prepared with Laminated Porous Anodes and Cathodes. *ECS Transactions* **85,** 1507–1515 (2018).

223. Caizán-Juanarena, L. *et al.* Unraveling the Technology behind the Frontrunner LIC ULTIMO to Serve as a Guideline for Optimum Lithium-Ion Capacitor Design, Assembly, and Characterization. *Advanced Energy Materials* **11** (2021).

224. Matsumoto, F. *et al.* Review of the structure and performance of through-holed anodes and cathodes prepared with a picosecond pulsed laser for lithium-ion batteries. *International Journal of Extreme Manufacturing* **5,** 12001 (2023).

225. Elmer, M., Ensling, D. & Pytlik, E. *Lithium-ionen-Zelle mit hoher spezifischer Energiedichte. Europäische Patentschrift* (2020).

226. Xiao, J., Shi, F., Glossmann, T., Burnett, C. & Liu, Z. From laboratory innovations to materials manufacturing for lithium-based batteries. *Nat Energy* **8,** 329–339; 10.1038/s41560-023-01221-y (2023).

227. Zou, Q. *et al.* Enhancing the Capacity and Cycling Performance of Lithium Ion Batteries Through Perforated Current Collectors. *Acta Mech. Solida Sin.* **38,** 539–548; 10.1007/s10338-024-00519-y (2025).

228. Moretti, A. *et al.* A Comparison of Formation Methods for Graphite//LiFePO 4 Cells. *Batteries & Supercaps* **2,** 240–247; 10.1002/batt.201800109 (2019).

229. Chevrier, V. L. *et al.* Design and Testing of Prelithiated Full Cells with High Silicon Content. *J. Electrochem. Soc.* **165,** A1129-A1136; 10.1149/2.1161805jes (2018).

Table of Figures

Figure 2.1 *Schematic illustration of a Graphite||LFP LIB cell. The graphite electrode acts as the negative electrode, and the LFP electrode acts as the positive one. The electron and lithium-ion flow during charging is shown in red; during discharging, it's shown in blue.* _____ *6*

Figure 2.2 *Simplified illustration of the theoretical specific capacity evolution from the material level to the electrode level to cell level. The calculations are based on double-sided coated LFP electrodes with an areal capacity of 2.6 mAh cm^{-2} per side, double-sided coated graphite electrodes with an areal capacity of 3.0 mAh cm^{-2} per side, together with the use of standard current collector foils (10 µm copper foil, 15 µm aluminum foil) and coating compositions (92 wt.% LFP, 94 wt.% graphite).* *10*

Figure 2.3 *Simplified block diagram illustrating the basic LIB manufacturing process, from materials to cells (based on Li et al., 2021[82]).* _____ *14*

Figure 2.4 *2032-coin half-cell (Li||Electrode) formation data of graphite and SiC electrodes: a, b) voltage profile and c) derivative analysis. The formation protocol involves three CCCV-lithiation and CC-delithiation cycles of the electrode AMs at a current density of C/50 in the potential window 0.05 – 1.50 V. All cells contain electrodes with an areal capacity of ~3.0 mAh cm^{-2}. The electrolyte formulation depends on the anode AM, with LP10VC02 used for graphite and LP10VC02FEC10 for SiC.* _____ *17*

Figure 2.5 *2032-coin half-cell (Li||Electrode) formation data of LFP and NMC811 electrodes: a, b) voltage profile and c) derivative analysis. The formation protocol involves three CC-delithiation and CC-lithiation cycles of the electrode active materials at a current density of C/10 in the potential window 2.5 – 3.7 V and 3.0 – 4.3 V for LFP and NMC811 electrodes, respectively. All cells contain electrodes with an areal capacity of ~2.55 mAh cm^{-2} and LP10VC02 as electrolyte.* _____ *19*

Figure 2.6 *Schematic illustration of anodic SEI formation and its function in LIBs.* _____ *24*

Figure 2.7 *Single-layer pouch cell (Anode||Cathode) formation data of a, b) Graphite||LFP, c, d) Graphite||NMC811, and d, e) SiC||LFP cell chemistries: a, c, e) voltage profile and b, d, e) derivative analysis. The formation protocol involves five CCCV-charge and CC-discharge cycles at a current density of C/10 in the voltage window 2.5 – 3.7 V and 3.0 – 4.2 V for LFP and NMC811 cathode AM chemistries, respectively. All cells include a total initial cathode capacity of ~60 mAh, with a cathodic reversible areal capacity of ~2.5 mAh cm^{-2} and a N/P-balancing of ~1.15. The electrolyte formulation depends on the anode AM, with LP10VC02 used for graphite and LP10VC02FEC10 for SiC.* _____ *25*

Figure 2.8 *Simplified illustration of prelithiation strategies at the material level on the cathode side.* ___ *28*

Figure 2.9 *Simplified illustration of prelithiation strategies at the material or at the electrode level on the anode side.*_____ *29*

Figure 2.10 *Simplified illustration of prelithiation strategy at the cell level using lithium-ion permeable electrodes and a sacrificial lithium donor electrode.* _____ *30*

Figure 3.1 *A comparison of different strategies to increase the specific capacity of graphite electrodes, focusing on electrode design: a) reference, b) increase of AM content in the coating layer, c) reduction of current collector mass/volume, and d) the color legend. The calculations are based on a double-sided coated graphite electrode with an areal capacity of 2.9 mAh cm $^{-2}$ per side.* *33*

Figure 6.1 *Photographs and microscopic images of the perforated current collector coil and foil.* _____ *42*

Figure 6.2 *2D and 3D microscopic images of a single perforation in the copper current collector foil, shown from the front and back sides in both the initial and flattened states.* _____ *43*

Figure 6.3 *2D and 3D microscopic images of a single perforation in the aluminum current collector foil, shown from the front and back sides in both the initial and flattened states.* _____ *43*

Figure 6.4 *Photographs of the initial scale up of the foil flattening pretreatment process: process visualization (left), resulting coil of perforated current collector foil with a flattened surface (center), and subsequent roll-to-roll processing of the pretreated coil (right).*_____ *44*

Figure 6.5 *Photographs of the advanced scale-up of the foil-flattening pretreatment process using the ZSW roll-to-roll pilot-line calender with edge and tension control.* _____ *45*

Figure 6.6 *Illustration of a double-sided coated electrode used to calculate specific and volumetric capacity values at the electrode level.*_____ *46*

Figure 6.7 *Calculated specific and volumetric capacity as a function of areal capacity per side of double-sided coated a, b) LFP and c, d) NMC811 electrodes. The black and blue lines represent electrodes with standard and perforated current collectors, respectively.* _____ *47*

Figure 6.8 *Calculated specific and volumetric capacity as a function of areal capacity per side of double-sided coated a, b) graphite and c, d) SiC electrodes. The black and blue lines represent electrodes with standard and perforated current collectors, respectively.* _____ *48*

Figure 6.9 *Illustration of a LIB cell-unit used to calculate specific energy and energy density values at the cell level.*_____ *49*

Figure 6.10 *Calculated specific energy as a function of cathode areal capacity per side of a) Graphite||LFP, b) SiC||LFP, c) Graphite||NMC811, and d) SiC||NMC811 cell-units.*_____ *50*

Figure 6.11 *Illustration of the LIB prelithiation approach at the cell level. This approach requires lithium-ion permeable electrodes and an extra Li-donor source.*_____ *50*

Figure 6.12 *Calculated a) specific energy and b) energy density of different anode||cathode cell-units, assuming a cathode areal capacity of 2.5 mAh cm^{-2} per side.* _____ *51*

Figure 6.13 *Schematic overview of the processing steps and instruments used to manufacture graphite electrodes.* _____ *53*

Figure 6.14 *Rheological flow curves of the pre-mix and graphite slurries, together with images of their coating process on standard and perforated current collector foils, and a photograph of a single-sided coated graphite electrode with a perforated current collector wound around a cylinder of ~10 mm diameter.* _____ *54*

Figure 6.15 *2D and 3D microscopic images of a graphite coating on a perforated copper current collector foil in the initial and calendered states.* _____ *54*

Figure 6.16 *Illustration of the formation of distinct coating loading and density segments, depending on the current collector design and applied coating technique.* _____ *55*

Figure 6.17 *Graphite slurry and electrode properties: a, b) Rheological flow curves and c) amplitude sweep of different pre-mix and graphite slurries. d) Linear relationship between coating wet thickness and areal capacity for all slurries.* _____ *57*

Figure 6.18 *Photographs and microscopic images of a graphite coating and cut pouch electrodes with a) standard and b) perforated current collector foils.* _____ *58*

Figure 6.19 *Schematic overview of the processing steps and instruments used to manufacture LFP electrodes.* _____ *59*

Figure 6.20 *LFP slurry and electrode properties: a, b) Rheological flow curves and c) amplitude sweep of different pre-mix and LFP slurries. d) Linear relationship between coating wet thickness and areal capacity for all slurries.* _____ *60*

Figure 6.21 *Photographs and microscopic images of a LFP coating and stamped pouch electrodes with a) standard and b) perforated current collector foils.* _____ *61*

Figure 6.22 *Graphite||LFP single-layer pouch cell setups, along with the electrode connections during their formation and cycling protocols. Black-marked electrodes are active in the respective protocol, while white-marked electrodes remain inactive.* _____ *62*

Figure 6.23 *Initial charge voltage profiles of Graphite||LFP single-layer pouch cells. In the PreLi setup, the Li-donor electrode is connected to the anode, while the sandwiched lithium-ion permeable cathode remained inactive.* _____ *63*

Figure 6.24 *First and fifth anode||cathode cycle voltage profiles of different Graphite||LFP single-layer pouch cell setup. Two cells of each setup are shown: a, b) Standard, c, d) Perforated, and e, f) PreLi. In the PreLi setup, the sandwiched cathode is connected to the anode, while the Li-donor electrode remained inactive.* _____ *65*

Figure 6.25 *a) Voltage profiles and b) derivative analysis of Graphite||LFP single-layer pouch cells, which contain at least one perforated current collector electrode.* _____ *66*

Figure 6.26 *Formation data of Graphite||LFP single-layer pouch cells: a) LFP specific capacity as a function of cycle number, and b) accumulated capacity after formation. In the PreLi cell, the Li-donor electrode is connected to the anode, while the sandwiched lithium-ion permeable cathode remained inactive.* _____ *68*

Figure 6.27 *Cycling data of Graphite||LFP single-layer pouch cells. The cycling protocol involves a CCCV-charge and CC-discharge in the potential window 2.5 – 3.7V* _____ *69*

Figure 6.28 *Specific capacity at the electrode level* as a function of the cathode's areal capacity of all single-layer pouch cell setups under investigation (*total mass includes the anode and cathode). Comparison of theoretical calculated values (lines) and real cell data (dots).* _____ *70*

Figure 7.1 *Illustration of three distinct Graphite||LFP LIB systems that differ only in the size of their initial active lithium inventory: Standard (top), where ICL are not compensated; PreLi (center), where*

ICL are compensated; Li-Reservoir (bottom), where ICL are compensated and an additional anodic lithium reservoir equivalent to 10% of the cell's capacity is provided. _____ *71*

Figure 7.2 *Illustration of electrode lithiation/delithiation behavior of Standard Graphite||LFP cell system during a) initial charge, b) initial discharge, and c) subsequent cycling. A N/P-ratio of 1.25 and a ICL of 10% is considered.* _____ *72*

Figure 7.3 *Illustration of electrode lithiation/delithiation behavior of PreLi Graphite||LFP cell system during a) initial charge, b) initial discharge, and c) subsequent cycling. A N/P-ratio of 1.25 is considered.* _____ *73*

Figure 7.4 *Illustration of electrode lithiation/delithiation behavior of Li-Reservoir Graphite||LFP cell system during a) initial charge, b) initial discharge, and c) subsequent cycling. A N/P-ratio of 1.25 and an anodic Li-Reservoir of 10% of the total cell capacity is considered.* _____ *74*

Figure 7.5 *Schematic overview of the processing steps and instruments used to manufacture graphite electrodes.* _____ *78*

Figure 7.6 *Rheological data (flow curve and amplitude sweep) of a, b) pre-mixes and c, d) graphite slurries from different batch sizes.* _____ *79*

Figure 7.7 *a) 2032-coin half-cell (Li||Graphite) formation data of graphite electrodes. The protocol involves three CCCV-lithiation and CC-delithiation cycles of the electrode AM at a current density of C/50 in the potential window 0.05 – 1.50 V. b) Linear relationship between coating wet thickness and areal capacity.* _____ *80*

Figure 7.8 *SEM micrographs of graphite coating deposited on a standard copper current collector foil: a) top-view image at 150× magnification, b) top-view image at 1,000× magnification, c) cross-sectional image at 1,000× magnification, d) top-view image at 3,000x magnification, and e) cross-sectional image at 3,000x magnification.* _____ *81*

Figure 7.9 *Schematic overview of processing steps and instruments used to manufacture LFP electrodes. 82*

Figure 7.10 *Rheological data of a, b) pre-mix and c, d) LFP slurry from different batch sizes.* _____ *83*

Figure 7.11 *a) 2032-coin half-cell (Li||LFP) data of LFP electrodes. The protocol involves three CCCV-lithiation and CC-delithiation cycles of the electrode AM at a current density of C/50 and C/10 in the potential window 2.5 – 3.7 V. b) Linear relationship between coating wet thickness and areal capacity.* _____ *84*

Figure 7.12 *SEM micrographs of LFP coating deposited on a standard aluminum current collector foil: a) top-view image at 150× magnification, b) top-view image at 1,000× magnification, c) cross-sectional image at 1,000× magnification, d) top-view image at 3,000x magnification, and e) cross-sectional image at 2,250x magnification.* _____ *85*

Figure 7.13 *SEM micrographs of LFP coating deposited on a perforated aluminum current collector foil: a) top-view image at 150× magnification, b) top-view image of hole region at 1,000× magnification, c) top-view image of transition region at 1,000× magnification, d) top-view image of land region at 1,000× magnification, e) cross-sectional image at 1,000× magnification, f) cross-sectional image of transition region at 2,250x magnification, and g) cross-sectional image of hole region at 2,250x magnification.* _____ *86*

Figure 7.14 *Illustration of various Graphite||LFP single-layer pouch cell setups, along with the electrode connections during the formation/prelithiation and cycling protocols. Black-marked electrodes are active in the respective protocol, while white-marked electrodes remain inactive.* _____ *88*

Figure 7.15 *Formation data of Standard, PreLi and Li-Reservoir Graphite||LFP single-layer pouch cell setups. a) Measurement protocol overview, b) voltage profiles of the initial charge and discharge, c) capacity as a function of protocol step, and d) accumulated capacity as a function of protocol step. All cells contain a postive electrode with an areal capacity of ~2.40 mAh cm^{-2}, a N/P-ratio of 1.25, and LP10VC02 as electrolyte. In the PreLi and Li-Reservoir cells, the Li-donor electrode is connected to the anode, while the sandwiched lithium-ion permeable cathode remains inactive.* _____ *89*

Figure 7.16 *Discharge rate capability data of Standard, PreLi and Li-Reservoir Graphite||LFP single-layer pouch cell setups: a) LFP specific capacity as a function of cycle number, and b) capacity retention as a function of C-rate. The measurement is performed in the voltage window 2.5 – 3.7 V. All cells contain a positive electrode with an areal capacity of ~2.40 mAh cm^{-2}, a N/P-ratio of 1.25 and LP10VC02 as electrolyte.* _____ *92*

Figure 7.17 *Voltage profile (a), derivative analysis (dQ/dV-plot) (b), and comparison of the corresponding dQ/dV-plot peak activities (c) of the 12th rate capability test cycle at C/20 for Standard, PreLi and Li-Reservoir Graphite||LFP single-layer pouch cells.* _____ *94*

Figure 7.18 *Voltage profiles as a function of the graphite lithiation degree of the 12th rate capability charge at C/20 for Standard, PreLi and Li-Reservoir Graphite||LFP single-layer pouch cells.* _____ *95*

Figure 7.19 *Long-term cycling data – LFP specific capacity as a function of cycle number – of Standard, PreLi and Li-Reservoir Graphite||LFP single-layer pouch cell setups. The measurement is performed in the voltage window 2.5 – 3.7 V. All cells contain a positive electrode with an areal capacity of ~2.40 mAh cm^{-2}, a N/P-ratio of 1.25 and LP10VC02 as electrolyte.*_____ *97*

Figure 7.20 *Evolution of the C/10 check-up cycle voltage profiles in long-term cycling protocol of a) Standard, b) PreLi, and c) Li-Reservoir Graphite||LFP single-layer pouch cells.* _____ *98*

Figure 7.21 *Evolution of the C/2 charge voltage profiles following the check-up cycle in long-term cycling protocol of a) Standard, b) PreLi, and c) Li-Reservoir Graphite||LFP single-layer pouch cells.* __ *99*

Figure 7.22 *Long-term cycling data – SOH as a function of cycle number – of Standard, PreLi and Li-Reservoir Graphite||LFP single-layer pouch cell setups. The measurement is performed in the voltage window 2.5 – 3.7 V. All cells contain a positive electrode with an areal capacity of ~2.40 mAh cm^{-2}, a N/P-ratio of 1.25 and LP10VC02 as electrolyte.*_____ *100*

Figure 7.23 *Long-term cycling data – a) capacity loss as a function of cycle number and b) Li-reservoir-adjusted capacity loss as a function of cycle number – of Standard, PreLi and Li-Reservoir Graphite||LFP single-layer pouch cell setups*_____ *101*

Figure 7.24 *Voltage profiles and dQ/dV plots of Standard, PreLi, and Li-Reservoir Graphite||LFP single-layer pouch cells at different cycle lives, corresponding to similar active lithium inventory levels: a, b) active lithium inventory size equivalent to ~90% of maximum reversible cell capacity and c, d) active lithium inventory size equivalent to ~85% of maximum reversible cell capacity.*_____ *102*

Figure 7.25 *Long-term cycling data of a PreLi single-layer pouch cell setup in its initial and relithiated state. a) LFP specific capacity as a function of cycle number, b) comparison of initial and relithiated long-term cycling stability, c) voltage profiles at C/10, and d) voltage profiles at C/2.* _____ *104*

Figure 7.26 *Long-term cycling data of a Li-Reservoir single-layer pouch cell setup in its initial and relithiated state. a) LFP specific capacity as a function of cycle number, b) comparison of initial and relithiated long-term cycling stability, c) voltage profiles at C/10, and d) voltage profiles at C/2.* _____ *105*

Figure 8.1 *Schematic comparison of the conventional roll-to-roll coating process and the modified simultaneous roll-to-roll coating approach.* _____ *106*

Figure 8.2 *Roll-to-roll coating of low and high viscosity graphite slurries onto standard copper foil: a) photographs of the coating process, b) flow curves of graphite slurry batches prepared under different mixing conditions, and c) adhesion test results of roll-to-roll manufactured graphite electrodes.* _____ *108*

Figure 8.3 *Schematic of the modified copper current collector coil and representative photographs of the coil preparation process.* _____ *110*

Figure 8.4 *Schematic of the A-side coated coil and representative photographs of the coating process. 111*

Figure 8.5 *Schematic of the B-side coated coil and representative photographs of the coating process. 112*

Figure 8.6 *SEM micrographs of pilot line graphite coating deposited on standard and perforated copper current collector foil: a,b) top-view image at 150× magnification, c,d) top-view image at 1,000× magnification, and e,f) top-view image at 3,000x magnification.* _____ *113*

Figure 8.7 *SEM micrographs of pilot line graphite coating deposited on perforated copper current collector foil: a) top-view image at 500× magnification, b,c) top-view image at 1,000× magnification, and d,e) top-view image at 3,000x magnification.* _____ *114*

Figure 8.8 *SEM micrographs of pilot line graphite coating deposited on standard and perforated copper current collector foil: a-d) cross-section at 1,000× magnification.* _____ *115*

Figure 8.9 *Schematic of the modified aluminum current collector coil and representative photographs of the coil preparation process.* _____ *117*

Figure 8.10 *Schematic of the A-side coated coil and representative photographs of the coating process. 118*

Figure 8.11 *Schematic of the B-side coated coil and representative photographs of the coating process. 119*

Figure 8.12 *SEM micrographs of pilot line LFP coating deposited on standard and perforated aluminum current collector foil: a,b) top-view image at 150× magnification, c,d) top-view image at 1,000× magnification, and e,f) top-view image at 3,000x magnification.* _____ *120*

Figure 8.13 *SEM micrographs of pilot line LFP coating deposited on perforated copper current collector foil: a) top-view image at 500× magnification, b,c) top-view image at 1,000× magnification, and d,e) top-view image at 3,000x magnification.* _____ *121*

Figure 8.14 *SEM micrographs of pilot line LFP coating deposited on standard and perforated copper current collector foil: a-d) cross-section at 1,000× magnification and e) cross-section at 3,000× magnification* _____ *122*

Figure 8.15 *Illustration of the final roll-to-roll coating setup for processing perforated current collector foils using state-of-the-art equipment.* 124

Figure 8.16 *Schematic of the copper current collector coil, the A-side coated coil, and the B-side coated coil together with representative photographs of the overall coating process.* 125

Figure 8.17 *Formation data of Graphite||LFP 2032-coin cells with standard or perforated current collector systems within the electrodes: a) LFP specific capacity as a function of cycle number, b) initial cycle voltage profile, and c) final cycle voltage profile.* 127

Figure 8.18 *Rate capability data of Graphite||LFP 2032-coin cells with standard or perforated current collector systems within the electrodes: a) discharge LFP specific capacity as a function of cycle number, b) discharge capacity retention as a function of C-rate, and c) charge LFP specific capacity as a function of cycle number.* 128

Figure 8.19 *Long-term cycling data of Graphite||LFP 2032-coin cells with standard or perforated current collector systems within the electrodes a) LFP specific capacity as a function of cycle number and b) SOH as a function of cycle number.* 129

Figure 8.20 *Illustration of various bi-layer and stacked pouch cell setups, along with the electrode connections during the formation, relithiation and cycling protocols. Black-marked electrodes are active in the respective protocol, while white-marked electrodes remain inactive.* 130

Figure 8.21 *Photographs of bi-layer and stack pouch cell assemblies.* 131

Figure 8.22 *Formation data of Graphite||LFP bi-layer and stacked pouch cells with standard or perforated current collector systems within the electrodes: a) cell capacity as a function of cycle number, b) LFP specific capacity as a function of cycle number c) initial cycle voltage profile (cell capacity), d) initial cycle voltage profile (LFP specific capacity), e) final cycle voltage profile (cell capacity) and f) final cycle voltage profile (LFP specific capacity).* 133

Figure 8.23 *Illustration of the relithiation procedure applied to stacked pouch cells.* 134

Figure 8.24 *Comparison of voltage profiles of the final formation cycle charge and the relithiation charge in stacked Graphite||LFP pouch cells.* 135

Figure 8.25 *Rate capability of Graphite||LFP bi-layer and stack pouch cells: a) discharge performance, b) charge performance, c) discharge voltage profile at 1C, and d) charge voltage profile at 1C.* 137

Figure 8.26 *Comparison of the discharge rate capability performance of different Graphite||LFP cell formats in a) prelithiated and b) standard state. The cell's capacity retention is shown as a function of the C-rate.* 138

Figure 8.27 *12th Cycle at C/20 of Graphite||LFP bi-layer and stack pouch cells: a) voltage profile, b) derivative analysis, c) zoomed derivative analysis, and d) comparison of the corresponding dQ/dV-plot peak activities.* 139

Figure 8.28 *Voltage profiles as a function of the graphite lithiation degree of the 12th rate capability charge at C/20 for Graphite||LFP bi-layer and stacked pouch cells.* 140

Figure 8.29 *Long-term cycling of Graphite||LFP pouch cells: a) bi-layer cells with centered anode, b) bi-layer cells with centered cathode, c) relithiated stack pouch cells, and d) all pouch cells in one plot.* 141

Figure 8.30 *Long-term cycling of Graphite||LFP pouch cells: a) SOH as a function of cycle number and b) LFP specific capacity loss as a function of cycle number.* _____ *142*

Figure 8.31 *Voltage profile and derivative analysis of Graphite||LFP cells at different SOHs: a,b) Initial capacity of non-relithiated pouch cells, c,d) 5% capacity loss of non-relithiated pouch cells, and e,f) 10% capacity loss of non-relithiated pouch cells.* _____ *143*

Figure 9.1 *Illustration of three distinct LIB SiC||LFP systems that differ only in the size of their initial active lithium inventory: Standard (top), where ICL are not compensated; ReLi (center), where ICL are compensated; Li-Reservoir (bottom), where ICL are compensated and an additional anodic lithium reservoir equivalent to 10% of the cell's capacity is provided.* _____ *146*

Figure 9.2 *Illustration of various SiC||LFP single-layer pouch cell setups, along with the electrode connections during the formation, relithiation and cycling protocols. Black-marked electrodes are active in the respective protocol, while white-marked electrodes remain inactive.* _____ *147*

Figure 9.3 *Formation data of SiC||LFP single-layer pouch cell systems: a) cell capacity as a function of cycle number, b) LFP specific capacity as a function of cycle number, c) initial cycle voltage profile, and d) final cycle voltage profile. All cells contain a positive electrode with an areal capacity of ~2.45 mAh cm^{-2}, a N/P-ratio of 1.20 – 1.25, and LP10VC02FEC10 as electrolyte.* _____ *148*

Figure 9.4 *Illustration of the relithiation procedure applied to SiC||LFP single-layer pouch cells.* _____ *149*

Figure 9.5 *Comparison of voltage profiles of the final formation cycle charge and the relithiation charge of a) ReLi and b) Li-Reservoir SiC||LFP single-layer pouch cells.* _____ *150*

Figure 9.6 *Rate capability of SiC||LFP single-layer pouch cells: a) discharge performance, b) charge performance. All cells contain a positive electrode with an areal capacity of ~2.45 mAh cm^{-2}, a N/P-ratio of 1.20 – 1.25, and LP10VC02FEC10 as electrolyte.* _____ *151*

Figure 9.7 *SOH as a function of cycle number of C/10 cycles before and after rate performance testing: a) SiC||LFP cells from the current chapter, b) Graphite||LFP cells from chapter 7, and Graphite||LFP cells from chapter 8.* _____ *152*

Figure 9.8 *12th Cycle at C/20 of SiC||LFP single-layer pouch cells: a) voltage profile, b) derivative analysis, and c) comparison of the different dQ/dV-plot zone activities.* _____ *153*

Figure 9.9 *Schematic summary of the qualitative analysis method used to estimate the size of a cell's active lithium inventory by means of derivative analysis during low C-rate charging of the studied cell compared to a suitable reference cell. A suitable reference cell is one that has similar electrode design and balancing (N/P-ratio at the electrode level) to that of the studied cell. An arbitrary dQ/dV-plot shape is used to emphasize that the analysis is expected to be valid regardless of the anode and cathode chemistry of the studied cell.* _____ *154*

Figure 9.10 *Voltage profiles as a function of the anodic lithiation degree of the 12th rate capability charge at C/20 for Standard, ReLi and Li-Reservoir SiC||LFP single-layer pouch cells.* _____ *155*

Figure 9.11 *Schematic summary of the quantitative analysis method used to quantify the size of a cell's active lithium inventory, as well as the size of the anodic lithium reservoir, if present, by means of the cell's voltage profile as a function of anodic lithiation degree during low C-rate charging of the studied cell compared to a suitable reference cell. A suitable reference cell is one that has similar*

electrode design and balancing (N/P-ratio at the electrode level) to that of the studied cell. An arbitrary voltage profile shape is used to emphasize that the analysis is expected to be valid regardless of the anode and cathode chemistry of the studied cell. _____ *156*

Figure 9.12 *Cycling data of SiC||LFP cells: a) LFP specific capacity as a function of cycle number, b) capacity retention as a function of cycle number, and c) capacity loss as a function of cycle number. All cells contain a positive electrode with an areal capacity of ~2.45 mAh cm^{-2}, a N/P-ratio of 1.20 – 1.25, and LP10VC02FEC10 as electrolyte.* _____ *157*

Figure 9.13 *Evolution of the C/10 cycle voltage profiles in the cycling protocol of a) Standard, b) ReLi, and c) Li-Reservoir SiC||LFP single-layer pouch cells.* _____ *158*

Figure 10.1 *Illustration of the perforated current collector design investigated in this thesis.* _____ *160*

Figure 10.2 *Illustration of the prelithiation approach at the cell level investigated in this thesis.* _____ *161*

Figure 10.3 *Illustration of the adaptions in pilot-line electrode fabrication procedure.* _____ *162*

Figure 10.4 *Illustration and differentiation of the concepts of a) prelithiation and b) relithiation at the cell level.* _____ *165*

Figure 15.1 *2032-coin half-cell (Li||Electrode) data of LFP electrodes used in* ***Chapter 6*** *(page 42). The measurement protocol involves CCCV-delithiation and CC-lithiation cycles in the potential window 2.5 – 3.7 V. All cells contain electrodes with a loading of ~16.7 mg cm^{-2} and LP10VC02 as electrolyte.* _____ *186*

Figure 16.1 *Rheological data of a, b) pre-mix and c, d) slurry at different storage times (****Chapter 7.2.1*** *on page 78).* _____ *187*

Figure 16.2 *Rheological data of pre-mix at different storage times (****Chapter 7.2.2*** *on page 82).* _____ *187*

Figure 17.1 *Additional photographs of the graphite electrode pilot-line coating process (****Chapter 8.1.1*** *on page 110).* _____ *188*

Figure 17.2 *Additional photographs of the LFP electrode pilot-line coating process (****Chapter 8.1.2*** *on page 117).* _____ *188*

Figure 18.1 *Rate capability data of SiC||LFP single-layer pouch cells: a) voltage profile at 1C discharge, b) dQ/dV-plot at 1C discharge, c) voltage profile at 1C charge, and d) dQ/dV-plot at 1C charge (****Chapter 9.1.4*** *on page 151).* _____ *189*

Table of Tables

Table 6.1 *Comparison of the maximum anticipated specific energy and energy density of LIB chemistries of this study with state-of-the-art (2020) and target (2030) values for automotive applications, as reported by Armand et al. (2020)[34].* _____ *52*

Table 7.1 *Overview of the anticipated effects of different sizes of active lithium inventory (Standard, PreLi, and Li-Reservoir) on Graphite||LFP cell performance characteristics. *Considering only reversible capacity of anode and cathode **Considering also ICL, prelithiation, and anodic lithium reservoir ***EOL.* _____ *75*

Table 12.1 *Electrode material overview.*_____ *170*

Table 12.2 *Cell material overview.* _____ *171*

Table 14.1 *Material parameters considered for theoretical calculations.*_____ *175*

Table 14.2 *Electrode paramaters considered for theoretical calculations.* _____ *176*

List of Abbreviations

ALL	active lithium loss
AM	active material
CA	conductive additive
CB	carbon black
CC	constant-current
CE	coloumbic efficiency
CMC	carboxymethyl cellulose
CNT	carbon nanotubes
CV	constant-voltage
DEC	diethyl carbonate
DMC	dimethyl carbonate
EC	ethylene carbonate
EMC	ethyl methyl carbonate
EOL	end of life
FEC	fluoroethylene carbonate
GHG	greenhouse gas
ICL	initial capacity loss
LCO	lithium cobalt oxide
LFP	lithium iron phosphate
LIB	lithium-ion battery
LIC	lithium-ion capacitor
Li-Naph	lithium naphthalene
LNO	lithium nickel oxide
n-BuLi	n-butyl lithium
NCA	lithium nickel cobalt aluminium oxides
NMC	lithium nickel manganese cobalt oxides
NMP	N-methyl-2-pyrrolidone
OCV	open-circuit voltage
PAA	poly(acrylic acid)
PC	propylene carbonate
PE	polyethylene
PFAS	per- and polyfluoroalkyl substances
PP	polypropylene
PTFE	polytetrafluoroethylene
PVDF	polyvinylidene fluoride
rpm	revolutions per minute
SBR	styrene-butadiene rubber
SEI	solid-electrolyte interphase
SHE	standard hydrogen electrode
SiC	silicon-carbon composite
SLMP	stabilized lithium metal powder
SOC	state of charge
TSC	total solid content
VC	vinylene carbonate

Curriculum Vitae

Personal Details

Name	Jan Hettig
Date of Birth	1994
Place of Birth	Frankfurt am Main
Nationality	German

Education

2022 – 2026	**Dr. rer. nat. Chemie** Ulm University & ZSW (89081 Ulm)
2019 – 2022	**M.Sc. in Chemistry and Management** Ulm University & HIU (89081 Ulm)
2016 – 2019	**B.Sc. in Chemistry and Management** Ulm University (89081 Ulm)
2013 – 2016	**Apprenticeship as a Chemical Laboratory Technician** Evonik Industries (63457 Hanau)
2004 – 2013	**Abitur** Georg-Büchner-Gymnasium (61118 Bad Vilbel)

Professional Experience

05/2022 – 07/2025 3 Years	**Research Associate** Zentrum für Sonnenenergie- und Wasserstoffforschung (ZSW, 89081 Ulm)
11/2021 – 03/2022 5 Month	**Intern** VARTA AG (73479 Ellwangen)
03/2020 – 08/2021 1.5 Years	**Research Assistant** Helmholtz-Institut Ulm (HIU, 89081 Ulm)
2018 - 2020	**Working Student Jobs** Ulm University (89081 Ulm)

Conference Contributions

Poster Contribution	
14. – 15. June 2023	**18th Ulm ElectroChemical Talks 2023 (UECT 2023)** 89073 Ulm *Title:* "Design of current collectors to enable pre-lithiation and increase energy density of Li-ion cells" *Authors:* J. Hettig, M. Hoffmann, M. Mancini, M. Wohlfahrt-Mehrens, P. Axmann
4. – 5. June 2025	**19th Ulm ElectroChemical Talks 2025 (UECT 2025)** 89073 Ulm *Title:* "Rethinking Current Collectors in LIBs: Small Holes, Big Impact" *Authors:* J. Hettig, L. Bender, K. Bender, P. Axmann, M. Mancini
Oral Presentation	
7. – 8. November 2023	**Zeiss Young Researcher Award Final** 73447 Oberkochen *Topic:* "Visualization of the electrode microstructure and investigation of its impact on the electrode kinetics" *Author:* J. Hettig

Declaration of Authorship

I hereby declare that I have written this dissertation independently and without unauthorized assistance. All sources and materials used are properly acknowledged and cited.

Furthermore, I confirm that language enhancement tools, such as DeepL or ChatGPT, were used exclusively to improve the English spelling, wording, and grammar of this work. The intellectual content and research findings remain solely my own.

This dissertation has not been submitted in the same or similar form to any other university or examination board.

Date

Signature

This thesis was prepared within the framework of the BMBF-funded project *PERFORMANZ* (03XP0411A-D) at the Center for Solar Energy and Hydrogen Research Baden-Württemberg and Ulm University, from 05/2022 to 05/2026.

I would like to thank everyone who supported and accompanied me along the way.